Corrosion and Hydrogen Pickup Mechanisms of Zirconium Alloys



SYLVESTER BRIAN SETIADINATA

Hertford College

A thesis submitted for the degree of Doctor of Philosophy

Department of Materials, University of Oxford

ABSTRACT

Zirconium alloy cladding isolates the nuclear fuel rods from water coolant in a nuclear fission reactor, but in this harsh environment experience high temperature aqueous corrosion and hydrogen pickup (HPU). The segregation of minor elements such as iron, niobium and antimony greatly affects the corrosion and HPU of Zr alloys, but often this segregation occurs at a scale too small for most characterisation techniques to observe. Atom probe tomography (APT) enables the 3D analysis of elemental distributions on the atomic scale using time-of-flight spectroscopy.

The corrosion and HPU of Zr-Nb alloys with 0.5-2.5 wt% Nb were examined using APT. The oxygen-saturated metal region at the oxide/metal (O/M) interface increases with instantaneous oxidation rate and deuterium segregation to oxide grain boundaries and pores that probably contain hydrogen have been observed. The ratio of hydrogen isotopes showed that where the D-containing signal was higher, deuterium segregation to grain boundaries was more likely.

Fe around β-Nb particles and on metal grain boundaries is redistributed during oxidation. This redistribution results in Fe enrichment in the oxide which would correlate with the space charge compensation predicted to decrease HPU. During oxidation, Nb leaches out from the β-Nb precipitates to the oxide matrix. Preliminary analysis on Sb-containing samples has been carried out and weak Sb segregation to metal grain boundaries has been observed. Irradiation also causes redistribution of Fe and Nb, particularly Fe in the vicinity of oxide grain boundaries and Nb leaving the β-Nb particles under irradiation, resulting in the formation of small Nb clusters. The results of this study show that APT can observe changes of elemental distributions on the atomic scale which is vital to understanding how Zr alloys behaves during corrosion.

ACKNOWLEDGEMENTS

This thesis would not have been possible without the contributions and help from many people whom I would like to acknowledge.

I would like to express my sincere gratitude to my main supervisor, Prof. Chris Grovenor. His support, guidance and vast knowledge have been very instrumental for the completion of my study. I would like to thank my co-supervisors Prof. Michael Moody and Dr. Paul Bagot who have helped me in understanding the APT data analysis and interpretations. I would like to acknowledge the contributions from Westinghouse Electric LLC who have made this project possible by providing the financial support and materials.

I am grateful for the constant support that I have received from the Atom Probe Group and in particular, I would like to thank Dr. Tomas Martin for his inputs in designing the experiments in general and training in specimen preparation and APT instrumentation as well as Dr. Daniel Haley in statistical and deuterium analyses. I would like to thank Jing Hu and Thomas Aarholt who also represented Oxford in MUZIC-2, for information sharing and engaging discussions about zirconium corrosion and HPU.

I am privileged to have been taken part of MUZIC-2 programme and to meet colleagues in this consortium. I would like to thank Dr. Robert Comstock, Dr. Javier Romero and Jonna Partezana from Westinghouse for providing materials, Prof. Hans-Olof Andren, Dr. Matthias Thuvander and Dr. Gustav Sundell from Chalmers for hosting me for my visits to Sweden. Also, Dr. Pia Tejland from Studsvik for irradiated sample preparation and Dr. Heidi Nordin from AECL for providing deuterated samples.

Finally, I would like to thank my family and my best friend, Desy for supporting me throughout my study.

PREFACE

Part of the work in this thesis has been or will be published in the following publications:

Conference proceedings:

Hu, J., Setiadinata, B., Aarholt, T., Garner, A., Partezana, J., Bagot, P., Lozano-Perez, S., Preuss, M., Moody, M., Grovenor, C. (2016) High-resolution characterization of Zr nuclear fuel cladding alloys. Zirconium in the nuclear industry: Eighteenth international symposium. American Society of Testing Materials (unpublished).

Hu, J., Setiadinata, B., Aarholt, T., Bagot, P., Moody, M., Grovenor, C., Garner, A., Harte, A., Moore, K., Frankel, P., Preuss, M., Ni, N. (2015) High-resolution characterization of corrosion and hydrogen pickup of Zr cladding alloys. Proceedings of TopFuel.

Oral presentations:

Setiadinata, S. B., Tejland, P., Barroo, C., Magyar, A., Moody, M. P., Bagot, P. A. J., Martin, T. L., Grovenor, C. R. M. (2016) Investigation on the role of iron in zirconium-niobium cladding corrosion. Atom Probe Tomography and Microscopy Conference, Gyeongju, South Korea.

Setiadinata, B, Moody, M. P., Bagot, P. A. J., Martin, T. L., Grovenor, C. R. M. (2016) Understanding the iron impurity redistribution during the oxidation of Zr-Nb alloys cladding. International Conference of Hexagonal Materials, Oxford, UK.

Poster presentations:

Setiadinata, S. B., Moody, M. P., Bagot, P. A. J., Martin, T. L., Haley, D., Grovenor, C. R. M. (2016) Deuterium and hydrogen analysis on zirconium oxide. Atom Probe Tomography and Microscopy International Conference, Gyeongju, South Korea.

Setiadinata, S. B., Moody, M. P., Bagot, P. A. J., Martin, T. L., Grovenor, C. R. M. (2015) Redistribution of Nb during oxidation of Zr-Nb alloys. Gordon Research Conference in Physical Metallurgy, Biddeford, MN, US.

Setiadinata, S. B., Tejland, P., Barroo, C., Magyar, A., Moody, M. P., Bagot, P. A. J., Martin, T. L., Grovenor, C. R. M. (2015) The effects of irradiation on niobium and iron redistributions during zirconium-niobium waterside corrosion. MFFP Workshop on the Irradiation Effects to Materials, Oxford, UK.

Setiadinata, S. B., Moody, M. P., Bagot, P. A. J., Martin, T. L., Grovenor, C. R. M. (2015) Initial oxidation of Zr-1Nb. Third Year Poster Session, University of Oxford, UK.

Setiadinata, S. B., Moody, M. P., Bagot, P. A. J., Grovenor, C. R. M. (2014) Examination on Zr-1Nb alloy using atom probe tomography. Hume Rothery Lecture Poster Session, University of Oxford, UK.

Two publications are currently in preparation:

Setiadinata, S. B., Hu, J., Romero, J., Partezana, J., Lozano-Perez, S., Moody, M. P., Bagot, P. A. J., Martin, T. L., Grovenor, C. R. M. (2016) What happens to iron during the corrosion of Zr-Nb alloys? (unpublished)

Setiadinata, S. B., Haley, D., Romero, J., Partezana, J., Moody, M. P., Bagot, P. A. J., Martin, T. L., Grovenor, C. R. M. (2016) Hydrogen analysis on zirconium oxide (unpublished)

TABLE OF CONTENTS

1. INTRODUCTION 1
   1.1. Background 1
   1.2. The current work 1
   1.3. Thesis structure 2
2. LITERATURE REVIEW 3
   2.1. Zirconium in the nuclear industry 3
   2.2. Physical metallurgy 5
      2.2.1. Pure zirconium 5
      2.2.2. Zirconium-niobium alloys 7
         2.2.2.1. Impurities 9
         2.2.2.2. Heat treatment 11
   2.3. Corrosion 13
      2.3.1. Zirconium oxide 13
      2.3.2. Kinetics 15
      2.3.3. Oxidation mechanisms 17
      2.3.4. Metallurgical considerations 25
   2.4. Hydrogen pickup (HPU) 31
      2.4.1. Kinetics 31
      2.4.2. HPU mechanism 32
      2.4.3. Metallurgical considerations 37
      2.4.4. Delayed hydride cracking (DHC) 43
   2.5. Irradiation effects 46
3. EXPERIMENTAL METHODS 50
   3.1. Atom probe tomography (APT) 50
      3.1.1. Introduction 50
      3.1.2. Instrument development 50
      3.1.3. Working principle 51
      3.1.4. Local Electrode Atom Probe (LEAP) 54
      3.1.5. Tomographic reconstruction 57
      3.1.6. Mass spectrum 60
   3.2. APT of zirconium and its oxide 61
      3.2.1. Specimen preparation 61
         3.2.1.1. Electropolishing 61
         3.2.1.2. Focussed ion beam (FIB) liftout 62

3.2.2. Experimental conditions 65
3.2.3. Data analysis 66
3.2.3.1. Reconstruction methods 66
3.2.3.2. Mass spectrum analysis 67
3.2.3.2.1. Element identification 67
3.2.3.2.2. Ranging 70
3.2.3.3. Interfaces 80
4. MATERIALS 86
4.1. General overview 86
4.2. Unoxidised metal 89
4.3. Oxidised materials 90
4.3.1. As-recrystallised Zr-1Nb 91
4.3.2. Annealed Zr-1Nb 95
4.3.3. X2 100
4.3.4. Zr-2.5Nb 103
4.3.5. Zr-0.5Nb-0.1Sb 106
4.4. Summary 109
5. OXYGEN 110
5.1. Introduction 110
5.2. Oxygen in the metal 110
5.3. Oxygen in the bulk oxide 111
5.4. Oxygen at the O/M interface 113
5.4.1. Layered oxide structure 113
5.4.2. Suboxide thickness measurements 114
5.4.3. Oxygen-saturated metal 117
5.4.4. Sawtooth-shaped interfaces 124
5.5. Discussion 127
5.6. Summary 133
6. HYDROGEN AND DEUTERIUM 134
6.1. Introduction 134
6.2. Detection of hydrogenic species 135
6.3. Hydrogen in the metal 138
6.4. Hydrogen and deuterium in the oxide 138
6.4.1. Ratio of hydrogenic peaks 138
6.4.2. Hydrogen and deuterium segregation 142
6.4.2.1. Oxide grain boundaries 142
6.4.2.2. Porosity 155

6.5. Discussion 158
6.6. Summary 161
7. IRON 162
7.1. Introduction 162
7.2. Iron in the metal 163
7.2.1. Metal matrix 163
7.2.2. Metallic β-Nb particles 164
7.2.3. Metal grain boundaries 166
7.3. Iron in the oxide 168
7.3.1. Oxide and suboxide matrices 168
7.3.2. Oxidised β-Nb particles 169
7.3.3. Oxide grain boundaries 172
7.4. Iron at the O/M interface 175
7.4.1. Metal adjacent to the O/M interface 175
7.4.2. Iron-containing features 188
7.4.3. Grain boundary oxidation 191
7.5. Irradiation effects 194
7.6. Discussion 196
7.7. Summary 207
8. NIOBIUM 209
8.1. Introduction 209
8.2. Niobium in the metal 209
8.2.1. Metal matrix 209
8.2.2. Metallic β-Nb particles 210
8.2.3. Metal grain boundaries 211
8.3. Niobium in the oxide 213
8.3.1. Oxide matrix 213
8.3.2. Oxidised β-Nb particles 214
8.4. Niobium at the O/M interface 216
8.4.1. Metal adjacent to the O/M interface 216
8.4.2. Grain boundary oxidation 219
8.5. Irradiation effects 220
8.6. Discussion 222
8.7. Summary 228
9. ANTIMONY 230
9.1. Introduction 230
9.2. Antimony in the metal 230

9.2.1. Metal matrix 230
9.2.2. Metal grain boundaries 232
9.3. Antimony in the oxide 235
9.4. Discussion 235
9.5. Summary 236
10. CONCLUSIONS 237
10.1. Conclusions 237
10.1.1. Oxidation mechanisms 237
10.1.2. HPU mechanism 238
10.1.3. Effect of alloying elements 238
10.1.3.1. Iron 238
10.1.3.2. Niobium 239
10.1.3.3. Antimony 240
10.1.3.4. Comparison between alloying elements 240
10.1.4. Irradiation effects 242
10.2. Overall contribution of this thesis 244
10.3. Future directions 245
REFERENCES 246

1. INTRODUCTION

1.1. Background

Zirconium alloys are widely used in nuclear reactors as a cladding material, separating the nuclear fuel and water coolant. However, the cladding lifetime is limited by high temperature aqueous corrosion and hydrogen pickup (HPU) that occur at the reactor temperature (~320°C). Both corrosion and HPU can lead to the failure of the cladding and therefore, have to be understood.

1.2. The current work

The work described in this thesis is a part of the MUZIC-2 (Mechanistic Understanding of Zr HPU) programme led by Westinghouse Electric LLC. The MUZIC-2 programme is a continuation of MUZIC-1 that focused on the oxidation mechanism, and aimed at understanding the HPU process using various experimental techniques such as atom probe tomography (APT), transmission electron microscopy (TEM), nanoscale secondary ion mass spectroscopy (nanoSIMS), electrochemical impedance spectroscopy (EIS), and x-ray absorption near edge spectroscopy (XANES) in addition to density functional theory (DFT) modelling. The collaborators include universities (Imperial College London, University of Manchester, Chalmers University of Technology and Pennsylvania State University), laboratories (NNL, PSI and Studsvik), and other companies (EPRI, AMEC, Rolls-Royce, EdF and Standvik).

This thesis uses atom probe tomography (APT) as the characterisation technique. A substantial amount of work has been done to analyse the atomic scale chemical distribution of elements including oxygen, hydrogen/deuterium, iron, niobium and antimony in unoxidised

metal, oxide and at the oxide/metal (O/M) interface of specimens corroded in both light and heavy water autoclaves. To do that, sample preparation using advanced focussed ion beam (FIB) liftout has been carried out to produce more than 200 samples. The materials studied are Zr-Nb (Zr-1Nb and Zr-2.5Nb) and Zr-0.5Nb-0.1Sb alloys. In addition, Zr-1Nb corroded in-reactor has also been examined.

1.3. Thesis structure

Following this introduction, this thesis contains a literature review in Chapter 2 that focuses on the metallurgy of Zr-Nb alloys, the corrosion and HPU mechanisms as well as how alloying elements can influence these properties. An overview of APT, specimen preparation techniques and data analysis are discussed in Chapter 3, while Chapter 4 details the materials studied.

Chapters 5-9 are the results chapters that are divided according to the elements studied. In each chapter, there is a brief introduction, observations, discussion and summary. Chapters 5 and 6 focus on corrosion and HPU mechanisms respectively. Chapters 7, 8 and 9 discuss the iron, niobium and antimony distributions in the metal, oxide and at the O/M interface to study how these elements are redistributed upon oxidation. These chapters also include preliminary results from samples corroded in a nuclear reactor. The conclusions of all the result chapters and suggestions for future directions are presented in Chapter 10.

2. LITERATURE REVIEW

2.1. Zirconium in the nuclear industry

In nuclear fission reactors, Zr alloys are one of the most common fuel cladding materials (Figure 2.1) [1-3]. As well as their application in boiling water reactors (BWRs), Zr alloys are used in the pressurised water reactors (PWRs) that comprises about 60% of all nuclear reactors worldwide [1,4]. The basic principle of these reactors is the nuclear fission reaction involving a large fissile nucleus (e.g. ^{235}U, $^{235}UO_2$ and ^{239}Pu) and neutrons [1,4]. The nucleus is then decomposed into lighter nuclei, releasing large amounts of energy.

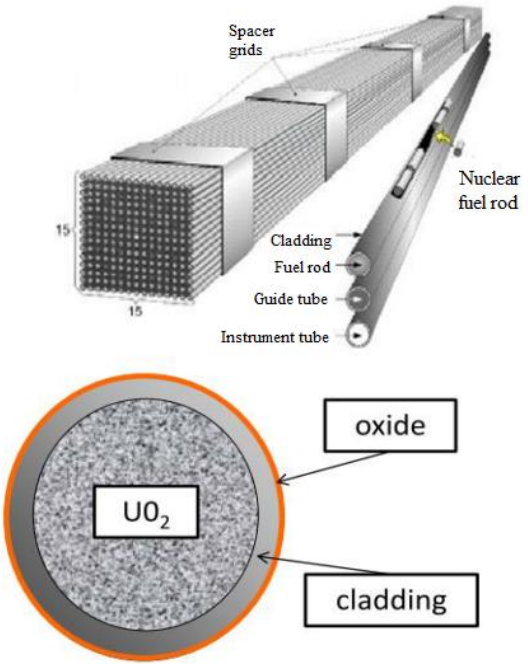


Figure 2.1: A fuel rod assembly and the cross section of a fuel rod [5].

Cladding plays an important role as it separates the nuclear fuel and the water or steam, and hence inevitably also retains most of the radioactive fission products. The main advantage of using Zr alloys as cladding material is the low thermal neutron absorption cross section (~0.18 barns) [6,7]. In addition, Zr also has moderate corrosion resistance in water at high temperatures [1].

Light (H_2O) and heavy water (D_2O) are usually used as a coolant that enables heat conduction away from the nuclear fuel [1,3]. However, the presence of water leads to the major problems of high temperature aqueous corrosion and HPU [3,5,6,8-11]. Uncontrolled oxide growth can limit the cladding lifetime [6,10]. Hydrogen atoms from the water can be absorbed to the Zr matrix during normal corrosion, resulting in the formation of brittle hydrides [12-14]. Eventually, this can cause delayed hydride cracking (DHC) and catastrophic mechanical failure (Figure 2.2).

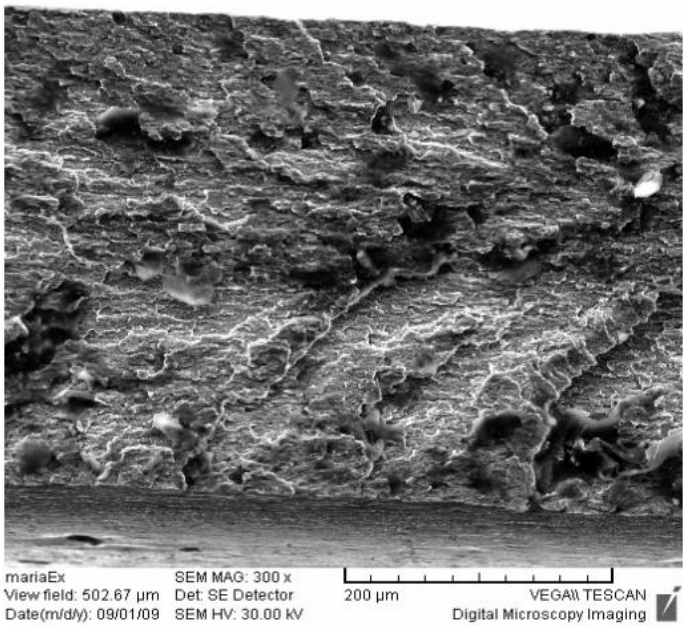


Figure 2.2: DHC on a CANDU Zircaloy sample tested at 250ºC [12]. Cracking is from right to left.

There is a trade-off between neutron absorption cross section and maximum operating temperature (Figure 2.3) [1]. Although Zr alloys have a low neutron absorption cross section, their maximum service temperature is only around 400°C [1,15]. This is another challenge for the development of new Zr alloys because the next generation of reactor designs (Generation IV/GIV reactors) will probably operate at higher temperatures and the burnup requirement has also increased from ~60GWd/tU to ~200GWd/tU from GII and GIII to GIV reactors [1,15]. Consequently, these conditions demand alloys with higher service temperatures and improved corrosion and creep resistance [15].

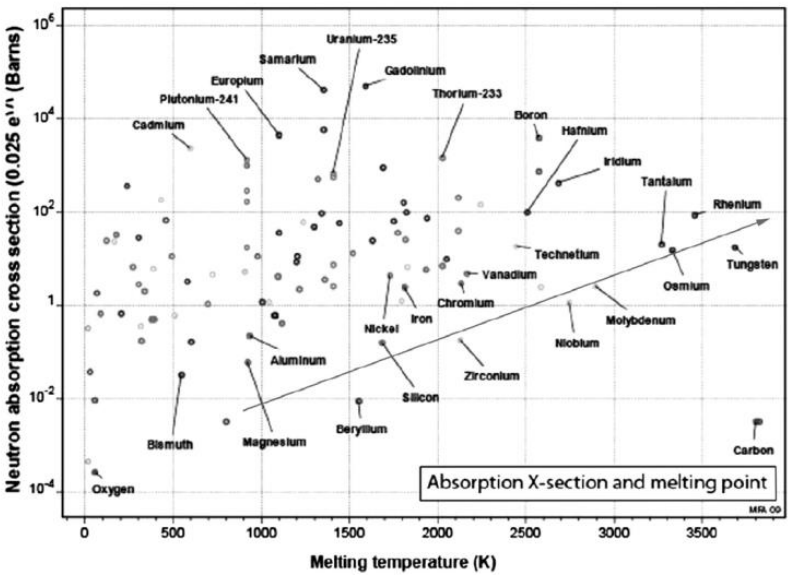


Figure 2.3: Temperature resistance (given as melting temperature) versus neutron absorption cross section for pure elements [1].

2.2. Physical metallurgy

The first Zr metal, a high purity crystal bar Zr was produced by van Arkel and de Boer in 1925 [16]. In late 1940s, the Kroll process to produce Zr with low neutron absorption cross section and good mechanical properties was developed [16]. Since then Zr products have been available in both alloyed and unalloyed, but Zr for claddings are alloyed. There are two main variants of Zr alloy systems: Zr-Sn and Zr-Nb. The Zr-Sn system (e.g. the Zircaloys) was developed in the US and Western Europe [17] while the Zr-Nb system was introduced by Russian scientists in 1958 [18,19].

2.2.1. Pure zirconium

At low temperatures, Zr exists as the α-Zr phase with a hexagonal close-packed (hcp) structure with lattice parameters: a=0.323nm, c=0.515nm [11,20]. An allotropic transformation can occur at 865°C where α-Zr transforms to β-Zr that has a body-centered

cubic (bcc) structure [11,21]. If β-Zr is cooled down below 865°C, either martensitic or bainitic transformation will occur, depending on the cooling rate. During this transformation, there is an orientation relationship between α-Zr and β-Zr; $[110]_\beta$ //$[0001]_\alpha$ and $(111)_\beta$ //$(11\bar{2}0)_\alpha$ (Figure 2.4) [3].

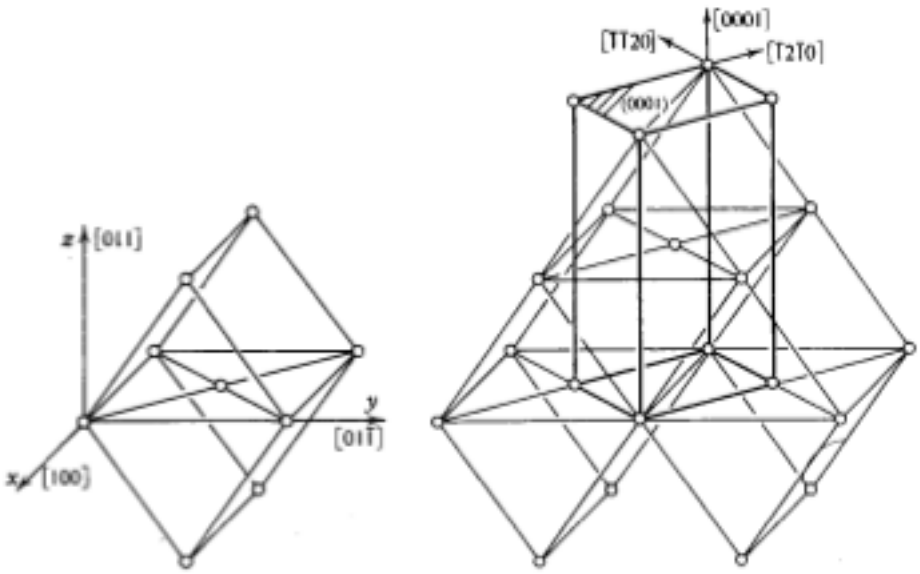
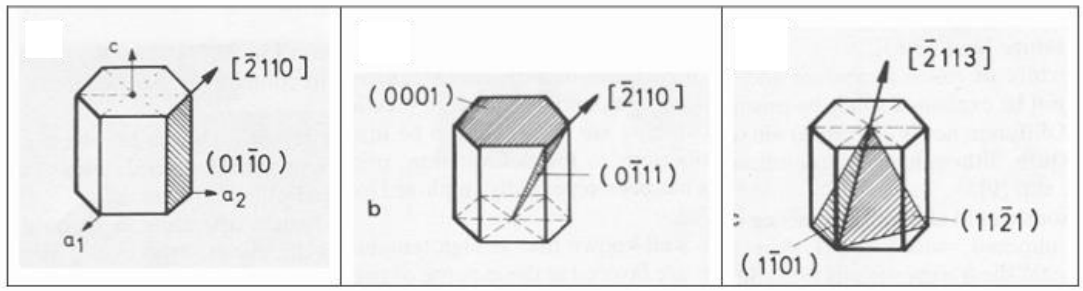


Figure 2.4: Orientation relationship between α-Zr and β-Zr [20].

There are not many slip systems in hcp structure and these slip systems are distributed asymmetrically (Figure 2.5). Because the c/a ratio of hexagonal α-Zr is 1.593 (slightly lower than the ideal value of 1.633), the plane with highest atomic density is the prismatic plane instead of the basal plane and hence prismatic slip is favoured [20,22]. This indicates a directional dependency of mechanical properties.



(a) (b) (c)

Figure 2.5: Possible slip systems in hcp materials (a) prismatic slip $\{01\bar{1}0\}(11\bar{2}0)$, (b) basal slip $\{0001\}(11\bar{2}0)$ and (c) pyramidal slip $\{11\bar{2}1\}(\bar{2}113)$ [22].

2.2.2. Zirconium-niobium alloys

The addition of Nb in general can improve corrosion resistance as well as mechanical properties [9,18,23]. Nb also has a smaller neutron absorption cross section (~1.1 barns) than some of other common alloying elements in Zr alloys such as Fe, Cr and Ni [19]. Zr-Nb alloys are usually binary and do not have many varieties as most are based on Zr-1Nb and Zr-2.5Nb compositions (Table 2.1). Note that O could be introduced deliberately as an alloying element as it is beneficial for the mechanical properties.

Table 2.1: Compositions of commercial Zr-Nb alloys [24].

Alloys	**wt%Nb**	**wt%Fe**	**wt%Cr**	**wt%Ni**	**wt%O**	**Application**
M5	0.8-1.2	0.015-0.06	-	-	0.09-0.12	PWR
E110 (Zr-1Nb)	0.9-1.1	0.014	<0.003	0.0035	0.05-0.07	VVER*, RBMK**
E125	2.5	-	-	-	0.06	VVER*, RBMK**
Zr-2.5Nb	2.4-2.8	<0.15	-	-	0.09-0.13	CANDU

*VVER = Voda Voda Energo Reactor

**RBMK = Reaktor Bolshoi Mozhnosti Kalanov (large boiling water channel type reactor)

Nb is a β-stabiliser, and hence its solubility in β-Zr (25-50wt%) is greater than in α-Zr (maximum ~0.6wt% at 610°C) [18,19,25-27]. As illustrated in Figure 2.6, for a Nb content less than 2.5wt%, different heat treatment methods can result in different phases where a phase called β-Nb can exist after heat treatments lower than 610°C. The possible phases constituting Zr-Nb alloys are given in Table 2.2. In the content range for commercial claddings (0.8-2.8wt%), Nb addition is mechanically beneficial as it can improve hardness and tensile strength (Figure 2.7) [28]. This is due to the reduction of grain size as Nb content increases (Figure 2.8) [29].

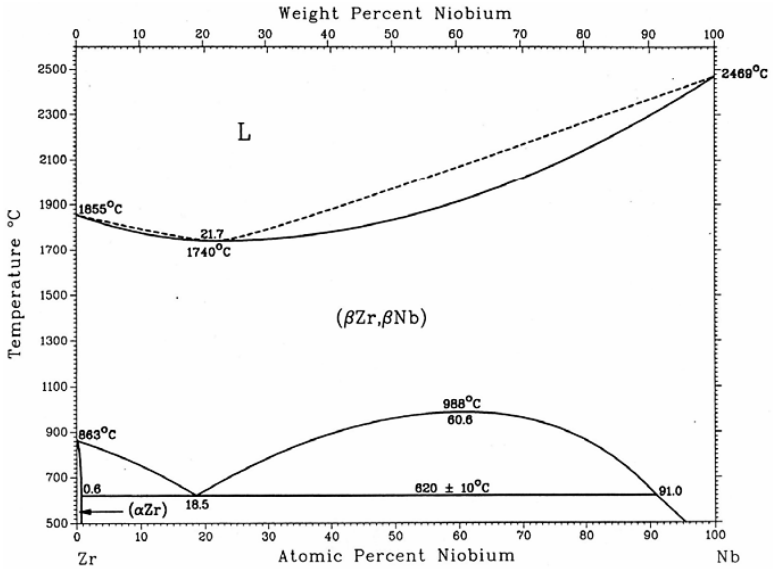


Figure 2.6: Zr-Nb phase diagram [5].

Table 2.2: Crystal structures of the phases in Zr-Nb alloys.

Phases	Structure	Unit cell size		References
		a (nm)	c (nm)	
α-Zr	hcp	0.323	0.515	[6,11]
β-Nb	bcc	0.331	-	[6,20]
β-Zr	bcc	0.361	-	[6]

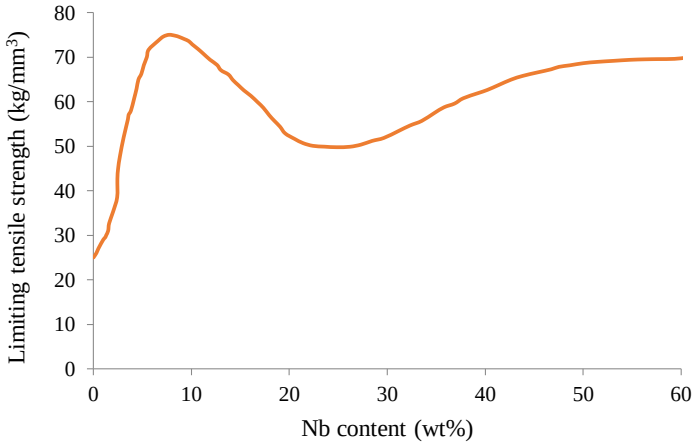
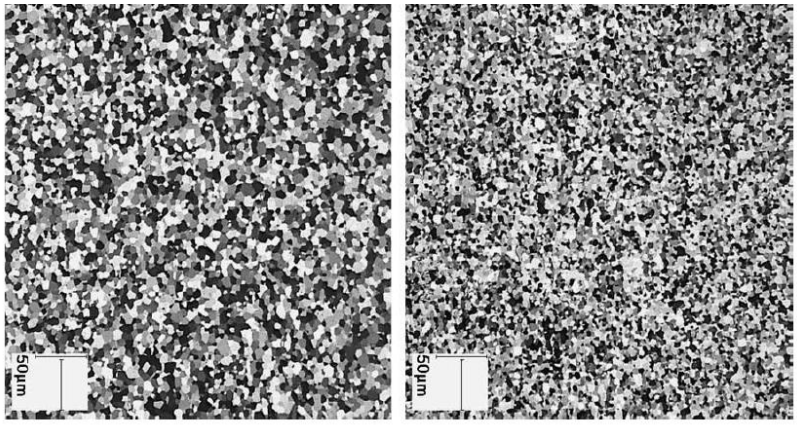


Figure 2.7: The relationship between Nb content and limiting tensile strength for Zr-Nb alloys annealed at 700°C [28].



(a) (b)

Figure 2.8: Optical micrographs of Zr claddings with (a) 0.07wt% and (b) 0.56wt% Nb [29].

2.2.2.1. Impurities

It is not possible to manufacture pure Zr or binary Zr-Nb because there are impurities in Zr sponge introduced during processing [16,30,31]. There are a lot of impurities in Zr-Nb alloys but in this section only some of them are discussed. One of the most important impurities is Fe [23,31,32]. Like Nb, Fe is also a β-stabiliser but, as illustrated in Figure 2.9, Fe has a much lower solubility in α-Zr (~120 wtppm) [20].

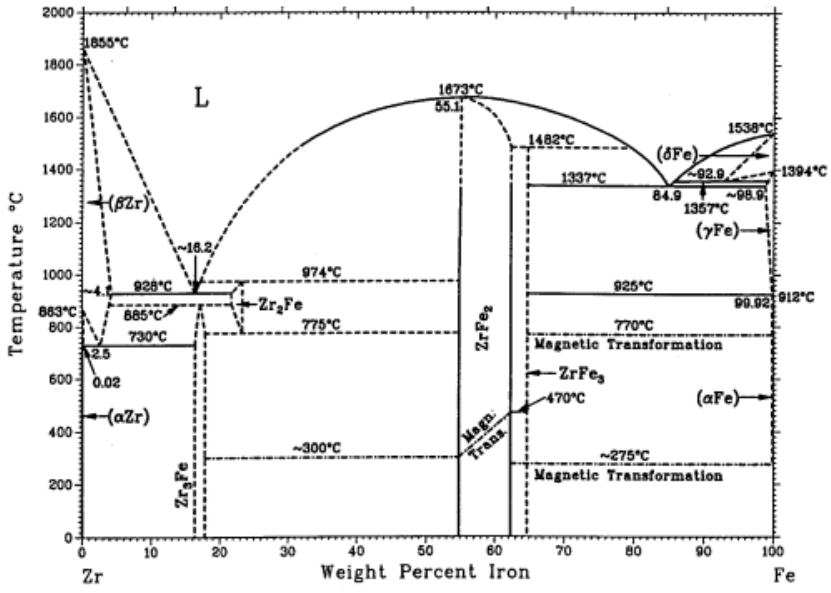


Figure 2.9: Zr-Fe phase diagram [5].

Due to its low solubility, Fe tends to segregate to grain boundaries or form intermetallics [23,31,33-35]. Several Fe-containing intermetallics in Nb-containing alloys are shown in Table 2.3. For most alloys heat treated at the typical recrystallisation temperature (~580°C), the most common intermetallics are Zr_3Fe and $Zr(Nb,Fe)_2$. However, Zr_3Fe only forms if the Nb content is very low (<0.5wt%) [23,35] while $(Zr,Nb)_2Fe$ forms at low Nb/Fe ratios [36,37]. In addition, Fe has been found inside bulk β-Nb (0.86-1.04wt%) and β-Zr (0.30-0.46wt%) [31].

Apart from Fe, other notable metallic impurities include Cr, Hf, Ni, Ti and Al [16,20,30,31,38]. Like Fe, Cr is also a β-stabiliser and has an extremely low solubility in α-Zr (~200 wtppm) [20]. Cr is also added as an alloying element in Zr-Sn alloys as it can improve mechanical properties by grain refinement [39-41]. Hf exists in the zircon ore used to extract Zr sponge and is detrimental for nuclear applications because of its high neutron absorption cross section (~105 barns) [6,16,20]. Ni is also not desirable as it can increase HPU, while Ti and Al have deleterious effects on corrosion properties [6,9,42,43].

Table 2.3: Fe-containing intermetallics in Zr-Nb and Zr-Sn-Nb systems.

Intermetallics	**Alloys**	**Structure**	**Unit cell size**			**References**
			a (nm)	**b (nm)**	**c (nm)**	
Zr_3Fe	Zr-0.1Nb, Zr-0.3Nb, Zr-0.5Nb	Orthorhombic	0.33	1.10	0.88	[20,23,35]
Zr_2Fe	Zr-2.5Nb	bct	0.66	-	0.56	[44,45]
$Zr(Nb,Fe)_2$	Zr-1Nb, ZIRLO*, E635**	Hexagonal	0.54	-	0.88	[29]
$(Zr,Nb)_2Fe$	E635**, Zr-0.3Nb-0.5Fe, Zr-0.5Nb-0.3Fe. Zr-0.7Nb-0.1Fe	fcc	1.21	-	-	[36,37]
$(Zr,Nb)_3Fe$	E635**	Orthorhombic	0.88	1.10	0.33	[36]

*ZIRLO = Zr-1Sn-1Nb-0.1Fe, **E635 = Zr-1Sn-1Nb-0.4Fe

Non-metallic impurities mainly include O, H, N, C and Si [6,30,38]. O is sometimes also added as an alloying element as O is an α-stabiliser beneficial for mechanical properties because it occupies the octahedral interstices of α-Zr and can act as an obstacle for dislocation motion [24,46]. H is not an alloying element by design but because it has a low solubility in α-Zr, excess H can result in brittle hydrides [20]. N is a harmful impurity as it can decrease corrosion resistance and cause embrittlement [6,47]. C incorporation is also not desirable as it can increase the susceptibility to both uniform and nodular corrosion [38,48]. Si can increase corrosion resistance between 80-140 ppm but additions >140ppm results in the opposite effect [38].

2.2.2.2. Heat treatment

The corrosion resistance of Zr-Nb alloys are very sensitive to the heat treatment because different heat treatment methods result in different microstructure, intermetallics and other secondary phases [23,35,49]. To study this, a typical manufacturing route for Zr-Nb alloys is discussed (Figure 2.10).

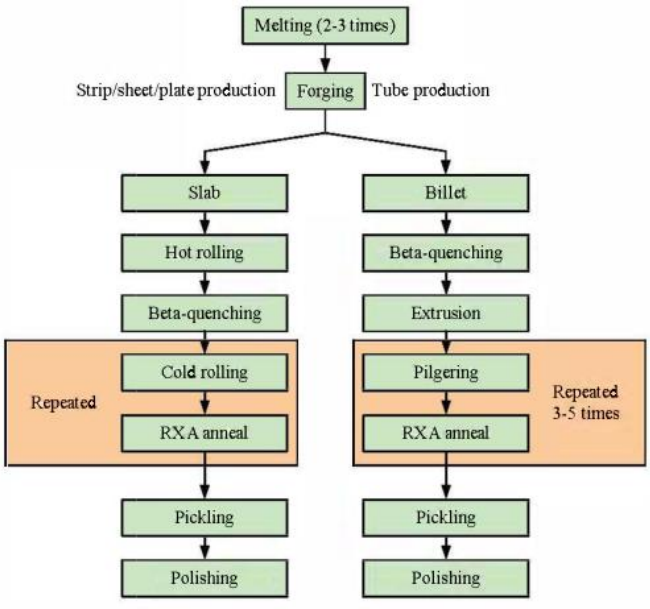


Figure 2.10: Manufacturing route of Zr-Nb alloys from the ingot stage [19].

The term β quenching refers to cooling from the β-phase region to homogenise the composition after hot forging because β-stabilisers are soluble in the β-matrix (Figure 2.6) [20,50]. The transformation from the β-phase may involve intermediate formation of Nb-depleted metastable ω-Zr and Nb-rich β-Zr [26,27]:

$$\beta \rightarrow \omega Zr + \beta Zr \quad (2.1)$$

Both ω-Zr and β-Zr can further decompose into β-Nb:

$$\beta Zr \rightarrow \omega Zr + \beta Nb \quad (2.2)$$

$$\omega Zr \rightarrow \alpha Zr + \beta Nb \quad (2.3)$$

As illustrated in Figure 2.6, if the material is annealed in the (αZr+βZr) region, β-Zr can be retained, while annealing in the (αZr+βNb) region encourages β-Zr decomposition into α-Zr and β-Nb according to Reactions 2.2-3 (Figure 2.11).

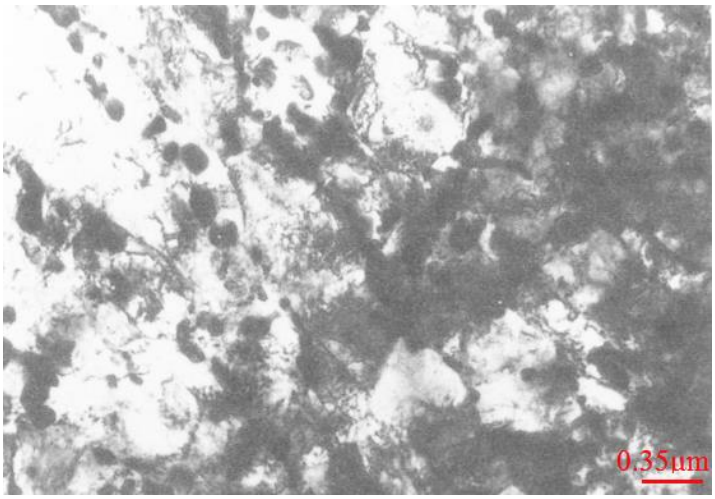
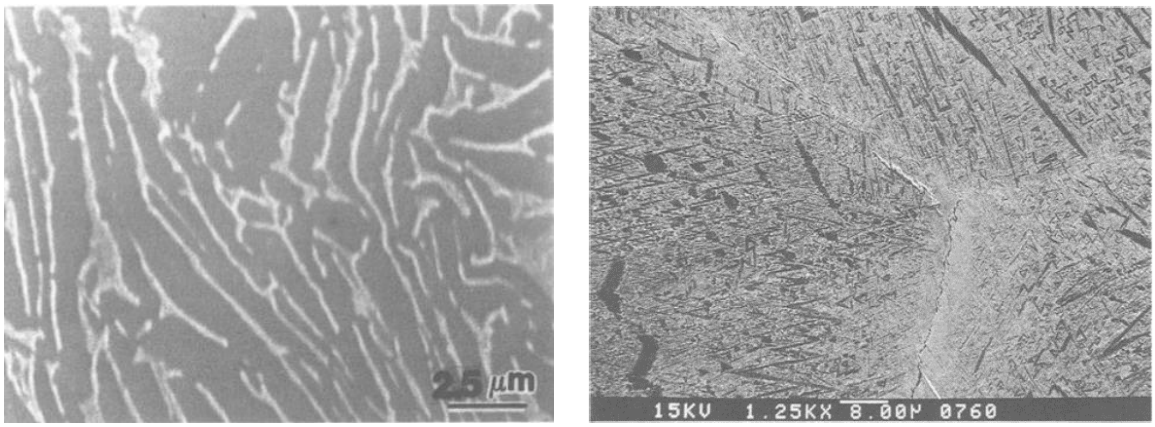


Figure 2.11: A TEM image showing β-Nb particles formed from decomposition of β-Zr [44].

A typical α+β microstructure consists of elongated α-Zr grains with β-Zr usually found at α-Zr grain boundaries (Figure 2.12a) [44,51]. Furthermore, martensitic transformation can occur at a high cooling rate [51,52]. Martensite (α'-Zr) is characterised by parallel plates inside the parent β-phase grains (Figure 2.12b).



(a) (b)

Figure 2.12: SEM micrographs of Zr-2.5Nb showing (a) elongated α-Zr grains (dark) bounded with β-phase at the grain boundaries (white) [44] and (b) parallel plates of martensite α'-Zr forms inside β-phase grains at the vicinity of a triple junction after water quenching from 1015°C [51].

2.3. Corrosion

There are several types of corrosion in Zr alloys, but this in this chapter the focus is on uniform corrosion. Uniform corrosion refers to the formation of uniform oxide layer when Zr alloys are exposed to a corrosive environment [24,53]. Other types of corrosion include nodular corrosion and shadow corrosion [9,39].

2.3.1. Zirconium oxide

Zirconium dioxide (ZrO_2) is the only thermodynamically stable phase of zirconium oxide [6]. With a bandgap of 5-6 eV, work function of 4.0 eV and relative permittivity of 22, ZrO_2 is known to be a good insulator [6,39]. ZrO_2 can exist in three different structures; monoclinic (α-ZrO_2 or m-ZrO_2), tetragonal (β-ZrO_2 or t-ZrO_2) and cubic (γ-ZrO_2 or c-ZrO_2) (Table 2.4 and Figure 2.13) [54,55]. Under atmospheric conditions, Zr alloys have a passive ZrO_2 film with ~2nm in thickness [56].

Table 2.4: The crystal structures of ZrO_2 phases [54].

Phase	Structure	Unit cell size		
		a (Å)	b (Å)	c (Å)
α-ZrO_2	Monoclinic (β=99.38°)	5.148	5.203	5.316
β-ZrO_2	Tetragonal	5.148	-	5.270
γ-ZrO_2	Cubic	5.090	-	-

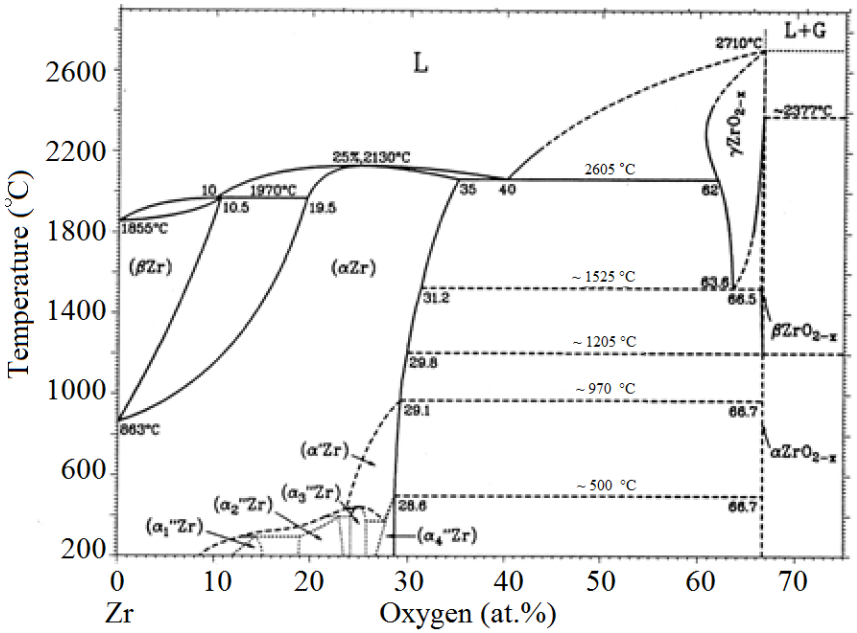


Figure 2.13: Zr-O phase diagram [57].

Apart from ZrO_2, there are also sub-stoichiometric oxide phases called the suboxides that have been observed experimentally in various publications (Table 2.5) [6,8,10,58-64]. At reactor (~300°C) or autoclave temperatures for corrosion experiments (~350°C), the suboxide phases that can exist are ZrO, Zr_3O, Zr_2O and Zr_6O (Figure 2.14) [65]. The most commonly observed suboxide phase is ZrO, probably because its enthalpy of reaction is the most negative [66].

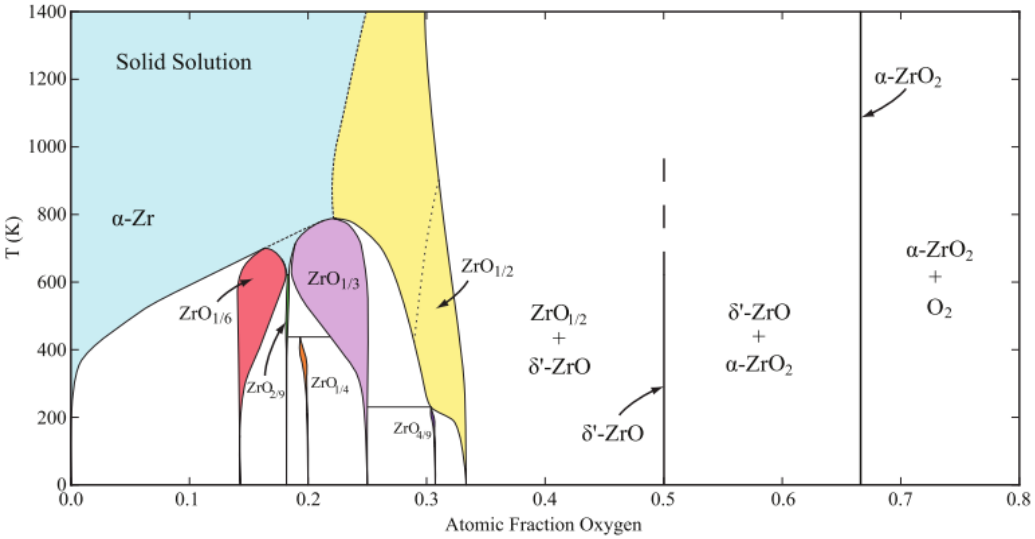


Figure 2.14: Modified calculated Zr-O phase diagram showing the regions where suboxides can be stabilised [65].

Table 2.5: Crystal structures of different suboxide phases.

Phase	**Structure**	**Unit cell size**		**Methods**	**References**
		a (Å)	**c (Å)**		
ZrO	Hexagonal	5.31	3.20	DFT	[67]
ZrO	Cubic	2.65	-	XRD	[68]
Zr_2O_3	Tetragonal	3.13	5.74	DFT	[65]
Zr_3O	Rhombohedral	5.56	31.19	XRD	[61]
Zr_3O	Rhombohedral	5.67	15.70	DFT	[66]
Zr_2O	Rhombohedral	5.65	5.25	DFT	[66]
Zr_6O	Rhombohedral	5.65	15.64	DFT	[66]

2.3.2. Kinetics

The initial oxidation kinetics (Figure 2.15) shows a sub-parabolic relationship that can be defined as [5,61,69]:

$$\Delta m = (k_c t)^n \quad (2.6)$$

Δm is the weight gain, k_C is a rate constant in the pre-transition regime, and t is time. The n-value (~0.2-0.4) is determined experimentally and good corrosion resistance is associated with large n-values.

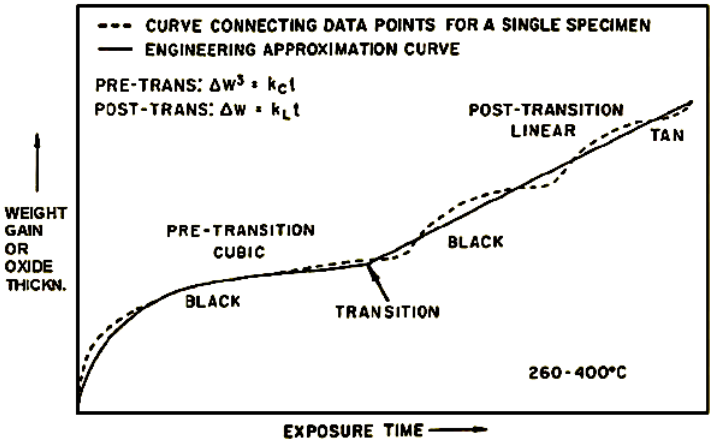


Figure 2.15: Typical oxidation kinetics of a Zr alloy [9,43].

The sub-parabolic relationship is only valid until a critical oxide thickness (typically ~1.5-3μm) where a change of kinetics known as transition occurs [9]. In the post-transition regime, oxide passivation disappears and the oxidation kinetics has a cyclic, quasi-linear characteristic that can be expressed as [3,6,9,43]:

$$\Delta m = k_L t \tag{3.4}$$

$$k_L = \frac{dm}{dt} = Ce^{\left(\frac{-Q}{RT}\right)} \tag{3.5}$$

k_L is the rate constant in post-transition regime, dm/dt is the corrosion rate, C is a constant that depends on heat treatment and alloy composition, Q is activation energy, R is gas constant, and T is absolute temperature.

In post transition, depending on the alloying composition and microstructure, some Zr alloys can still regain protectiveness (Figure 2.16 example 3). On the other hand, some alloys can exhibit a phenomenon called breakaway where the loss of protectiveness is irreversible (Figure 2.16 examples 1 and 2) [70,71]. In the breakaway regime the oxide changes from black or grey to white and becomes powdery, followed by spallation [71,72].

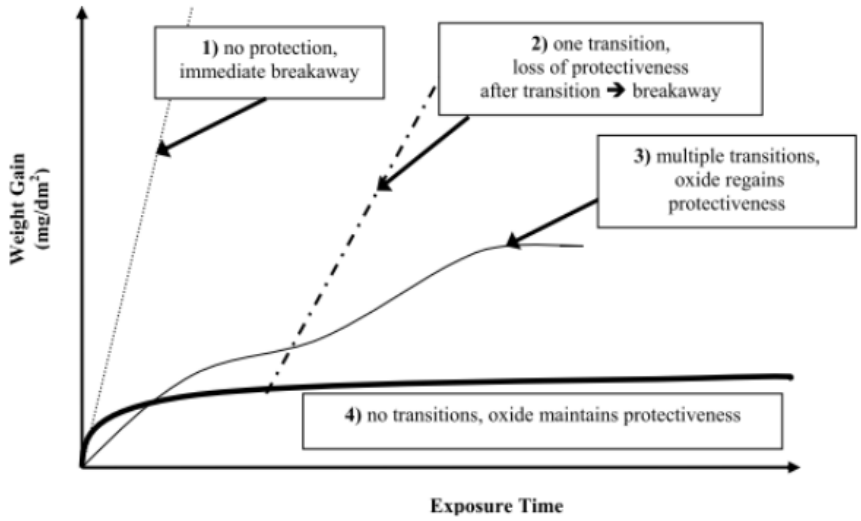


Figure 2.16: Schematic diagram showing different corrosion kinetics of Zr alloys [5,43].

2.3.3. Oxidation mechanisms

The oxidation reaction can be written as follows [53]:

Anodic: $$Zr + 2O^{2-} \rightarrow ZrO_2 + 2V_O + 4e^- \quad (2.4)$$

Cathodic: $$2V_O + 2H_2O + 4e^- \rightarrow 2O^{2-} + 4H \quad (2.5)$$

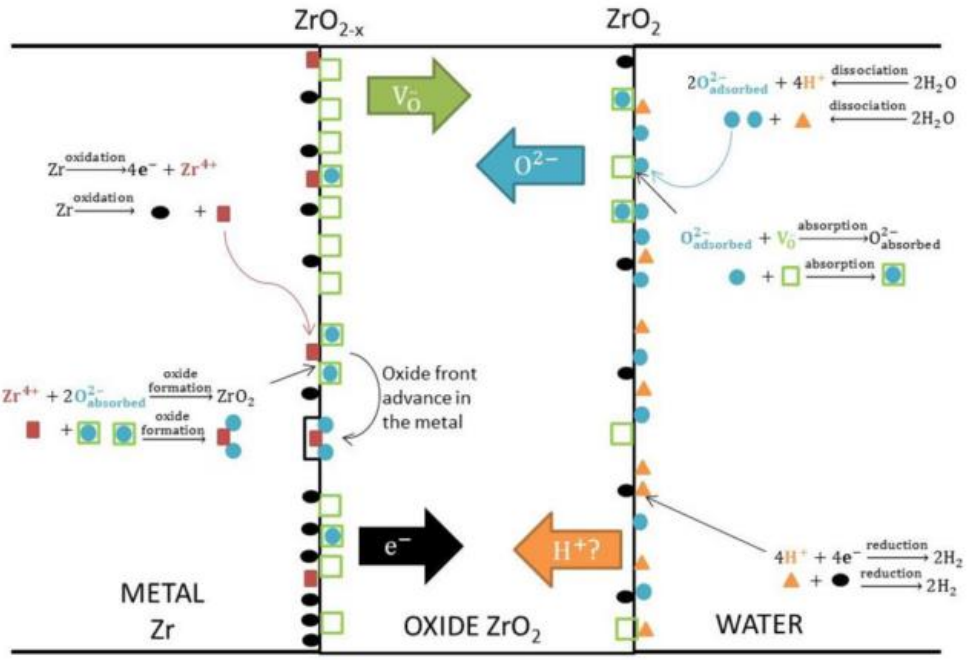
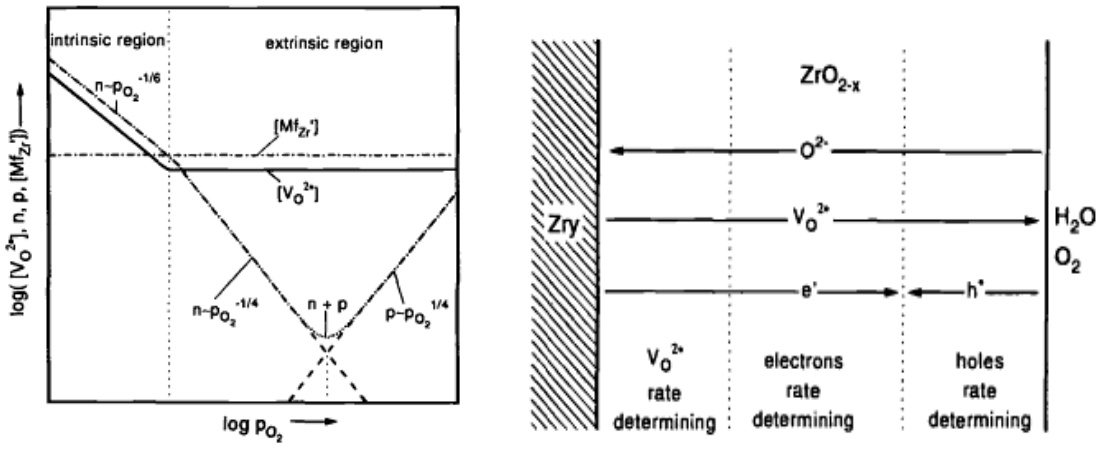


Figure 2.17: Schematic diagram of Zr oxidation adapted from [5].

As illustrated in Figure 2.17, Reactions 2.4 and 2.5 occur at the O/M (oxide/metal) and W/O (water/oxide) interfaces respectively. Oxidation requires both oxygen vacancy and electron transport from the O/M to W/O interface accompanied by oxygen ion and proton transport in the opposite direction. However, in actual materials this process is more complex because of the microstructure evolution and the redistribution of alloying elements upon oxidation. Considering that the oxide is a poorer electronic conductor than it is an oxygen diffusion barrier, and that oxygen ions can diffuse even faster via oxide grain boundaries (~10^8x faster than in the bulk), the rate-determining step of oxidation is presumed to be the electron transport [39,73-75]. Alloying additions can influence oxide conductivity, and change the rate-determining process to the ionic current [76]. This implies that changing electronic conductivity can influence the corrosion behaviour.

EIS experiments have shown that only the innermost part of the oxide, called the barrier layer, controls the overall oxidation kinetics [5,77-81]. According to Beie et al., inside the barrier layer the rate-determining process is the transport of oxygen vacancies, while it is electron transport at the outer oxide (Figure 2.18a-b) [77].



(a) (b)

Figure 2.18: (a) Concentration of charge carriers in the oxide as a function of oxygen pressure and (b) the corresponding barrier layer [77].

The barrier layer is highly resistive and impervious to electrolyte [78,82,83]. The barrier layer resistivity is at least 4 orders of magnitude higher than the outer oxide [82]. Although the barrier layer thickness is approximately equal to the overall oxide thickness in pre transition, there is a sudden decrease of thickness immediately after transition corresponding to the loss of protectiveness, and the barrier layer can regrow again in the second transition (Figure 2.19) [78,79]. Note that the barrier layer resistance increases with thickness and vice versa.

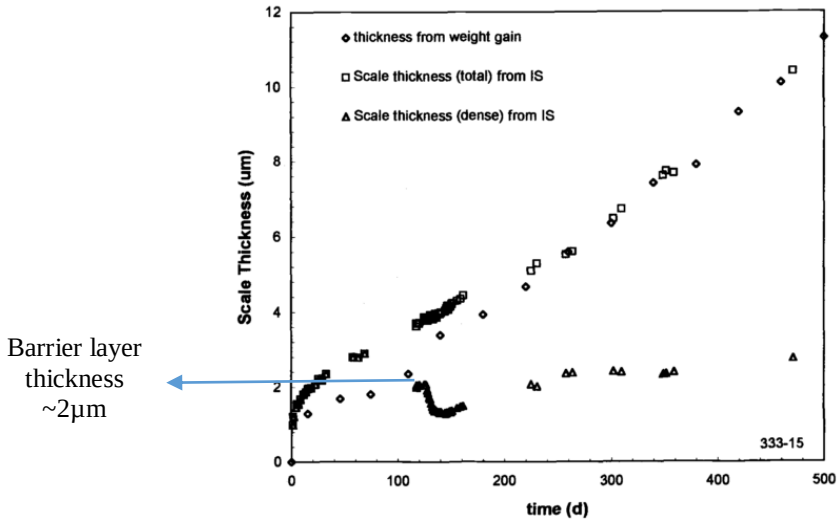
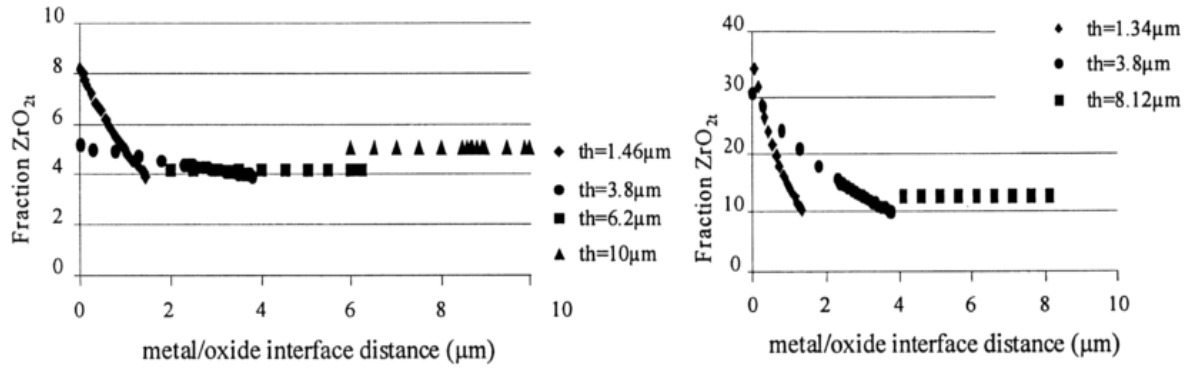


Figure 2.19: The evolution of overall oxide layer (◊: from weight gain measurement, □: from impedance spectroscopy) and dense barrier layer (Δ) over the course of oxidation of Zr-1.55Sn-0.2Fe-0.1Cr [79].

The evolution of this barrier layer can be correlated with microstructure evolution during transition. Apart from the electrochemical barrier layer explained above, this barrier layer can be regarded as a dense layer at the innermost part of the oxide. To understand this, the microstructure evolution during the oxide growth process is discussed below.

Although the thermodynamically stable ZrO_2 phase at ~300-360°C is m-ZrO_2 (Figure 2.13), there is a mixture of t-ZrO_2 and m-ZrO_2 in the innermost part of oxide layer [61,84-86]. The t-ZrO_2 grains are thought to be stabilised by compressive stress near the O/M interface (~1GPa), and are equiaxed in shape and 15-50nm in size [77,85,87-89]. Compressive stress due to the volume expansion on transforming metal to oxide is known to exist in the oxide as the Pilling-Bedworth (P-B) ratio of ZrO_2 is ~1.56 [90-93].



(a) (b)

Figure 2.20: The fraction of t-ZrO_2 through the oxide layer of (a) Zr-1Nb and (b) Zircaloy-4 with different oxide thicknesses [86].

The fraction of t-ZrO_2 decreases with time in the pre-transition regime as the t-ZrO_2 transforms to m-ZrO_2 [61,73,85,94,95]. Motta et al. proposed that the t-ZrO_2 transformation to m-ZrO_2 is accompanied by the elongation of original equiaxed t-ZrO_2 grains such that the m-ZrO_2 grains are columnar until reaching a critical aspect ratio of 4-5 [61]. Transition occurs when a new group of equiaxed t-ZrO_2 grains nucleate and repeat this cycle (Figure 2.21). This is supported by XRD data showing the periodicity of t-ZrO_2 intensity through the oxide layer (Figure 2.22).

Considerable attention has been focused on the stress evolution in the oxide during transition [91-93,95-97]. Compressive stress in the oxide layer tends to accumulate during pre transition and is relieved at transition (Figure 2.23) [91,95-97]. If t-ZrO_2 is stabilised by this stress, the stress relaxation could be the cause of t-ZrO_2 transformation to m-ZrO_2.

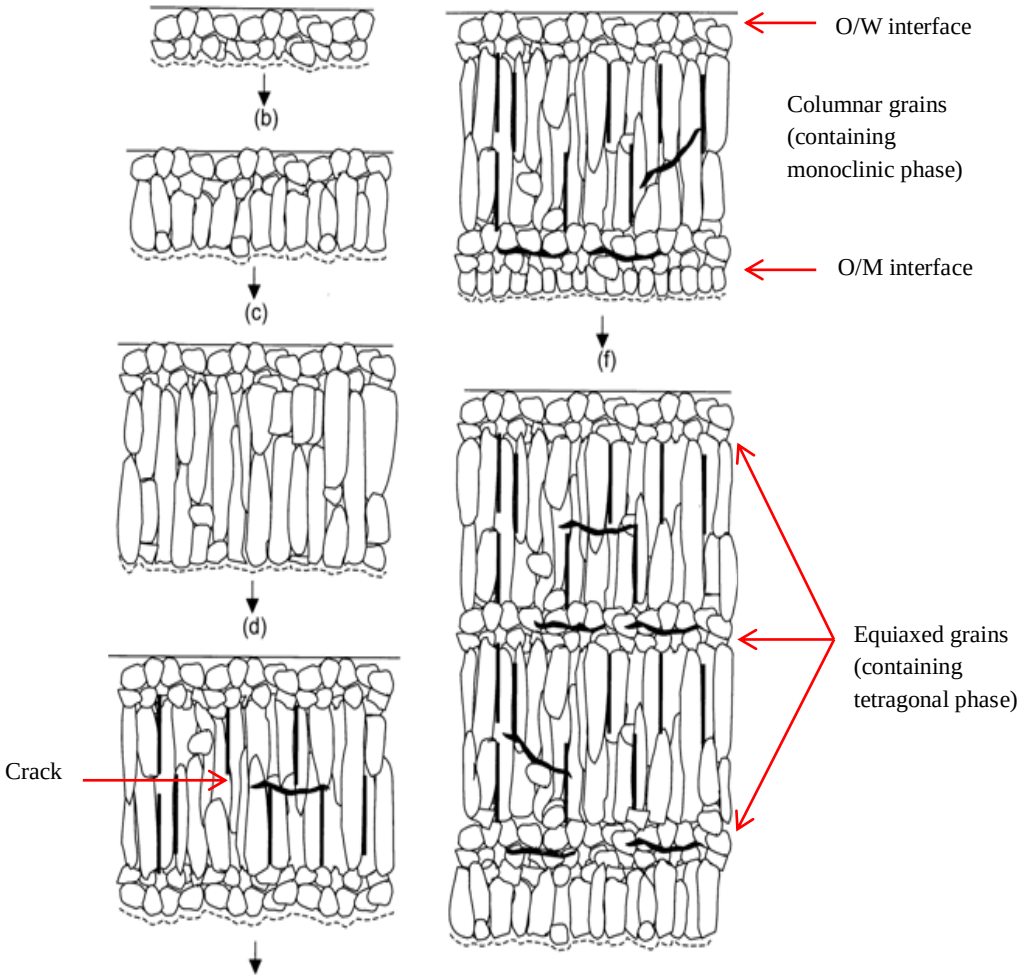


Figure 2.21: A schematic diagram showing the oxide growth mechanism proposed by Motta et al. [61].

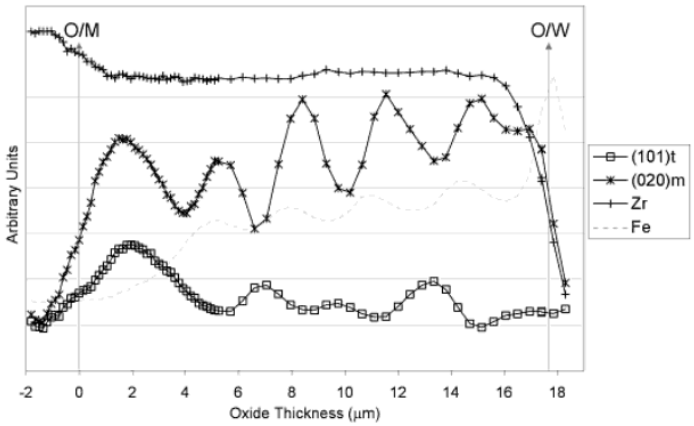


Figure 2.22: Variation of tetragonal (101)t and monoclinic (202)m diffracted peak intensities accompanied with Zr and Fe fluorescence counts as a function of oxide thickness on ZIRLO treated in 360°C lithiated water [61].

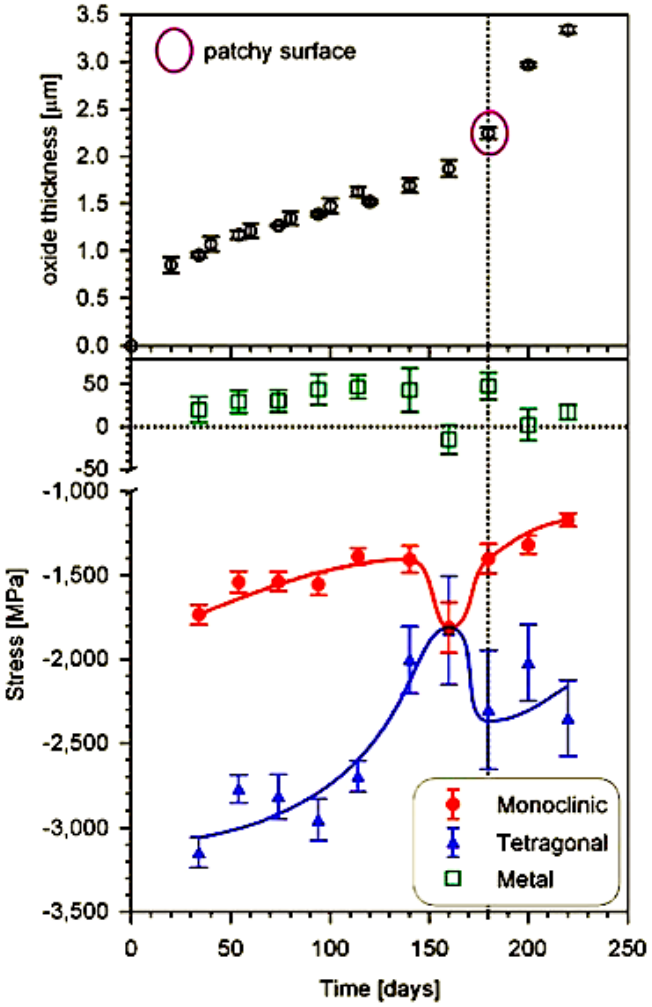


Figure 2.23: Evolution of through thickness oxide stress of Zircaloy-4 corroded at 360°C measured by synchrotron x-ray [97]. Dashed line corresponds to the transition point.

Other features that occur during transition are cracks and pores. Lateral cracks parallel to the O/M interface are only occasionally observed in pre transition oxide, but are common in post transition oxide where a network of cracks are always observed (Figure 2.24) [8,10,71,77,98-101]. The cracks are not only associated with the relaxation of compressive stress but also the cyclic nature of post transition kinetics [71,102]. These cracks are presumably the cause of oxide mechanical breakdown or spallation [103]. Vertical cracks are observed more rarely but they are normally located at the outer part of the oxide and do not reach the O/M interface (Figure 2.25) [83,100,104].

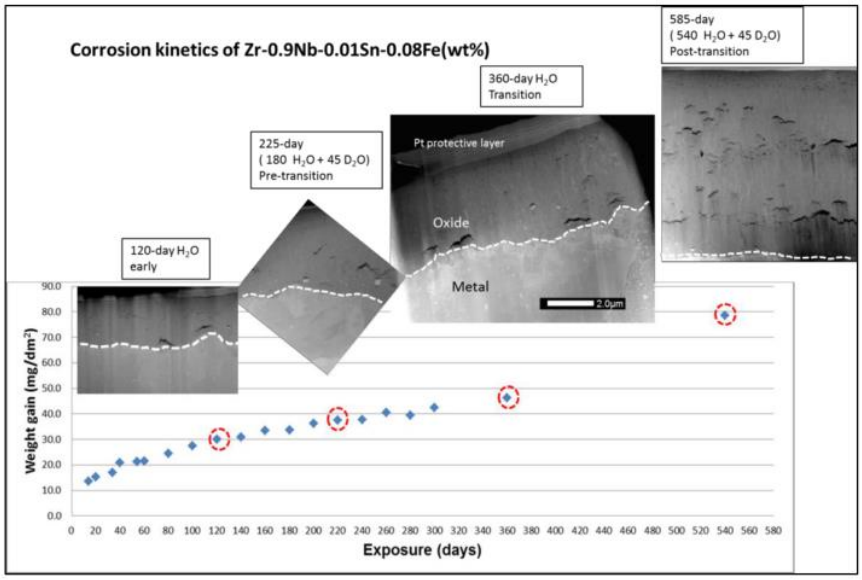


Figure 2.24: Corrosion kinetics of Zr-0.9Nb-0.01Sn-0.08Fe and the microstructure of the oxide near the O/M interface of the samples circled in red, taken from TEM HAADF [99].

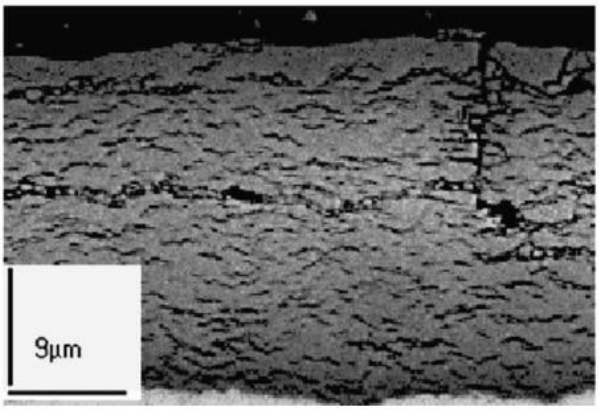


Figure 2.25: A cross section of the oxide of Zircaloy-4 corroded at 530°C showing a large vertical crack perpendicular to the O/M interface [100].

The existence of nanoporosity (a few nm in size) in the oxide layer is well-known as the outer part of the oxide layer is usually porous [9,10,77,82,100,105,106]. However, pores can also form even in pre transition where the whole oxide is relatively dense [70]. The pores are isolated in pre transition but become interconnected after transition; many of them were also found along grain boundaries (Figure 2.26 and Figure 2.27a-b) [10,106]. These pores originate from the coalescence of vacancies in the oxide due to the Kirkendall effect and are considered to be the cause of cracks associated with transition [70,71,106,107].

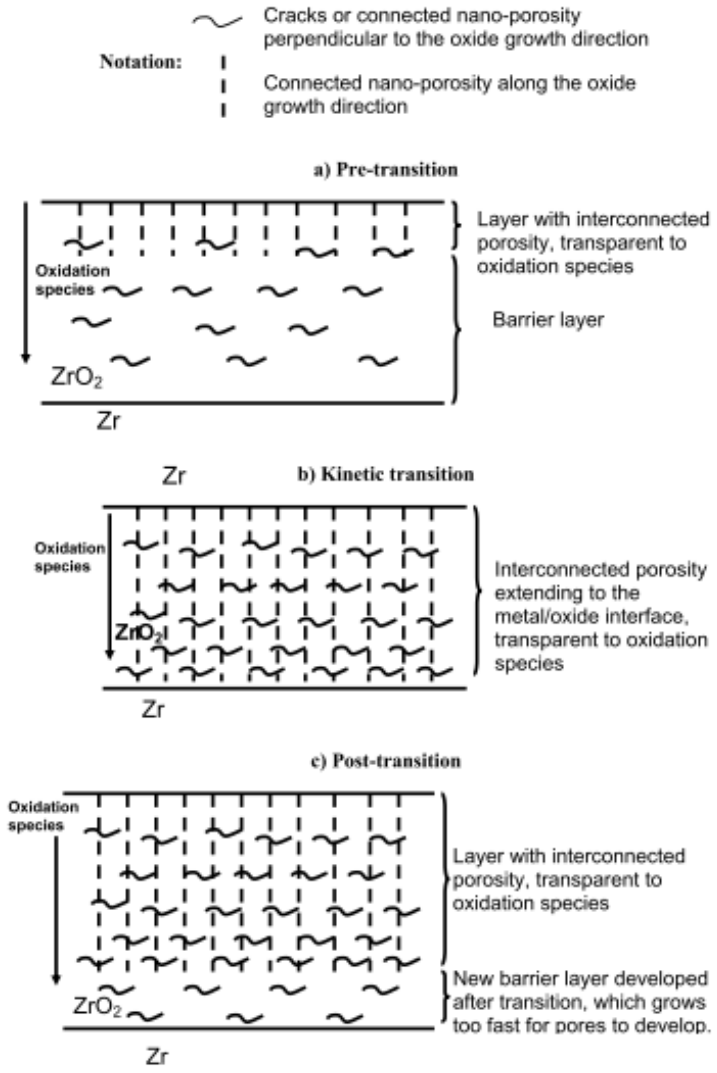


Figure 2.26: Microstructural change during transition proposed by Ni [10].

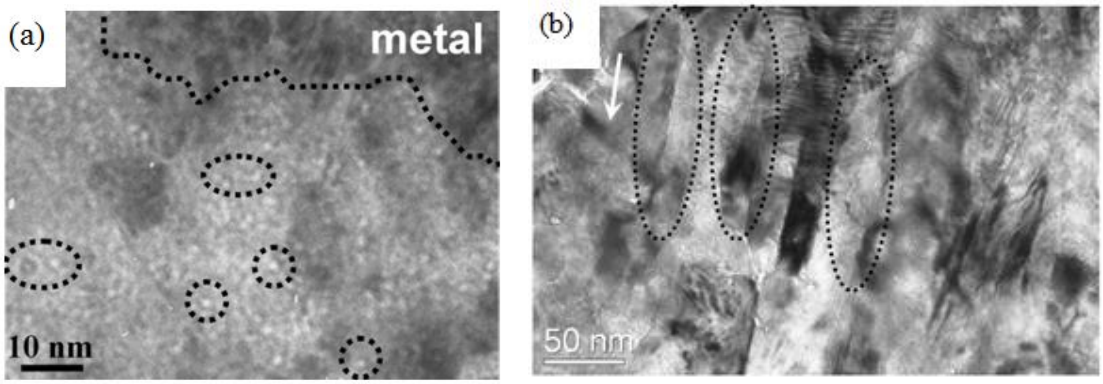


Figure 2.27: TEM micrographs showing (a) disconnected pores in the oxide of pre-transition Zircaloy-4 and (b) interconnected pores ~1.6μm from the O/M interface of post-transition ZIRLO [10]. Black circles show the location of the pores and the white arrow in (b) shows the oxide growth direction.

2.3.4. Metallurgical considerations

Alloys chemistry is an important factor determining the corrosion behaviour of Zr alloys. In general, Zr-Nb alloys show a better corrosion resistance compared to Zr-Sn and Zr-Sn-Nb because Zr-Nb usually shows a paralinear transition rather than the sudden transition in Zr-Sn (Figure 2.28) [79]. However, there is no clear understanding regarding the role of alloying elements on corrosion behaviour.

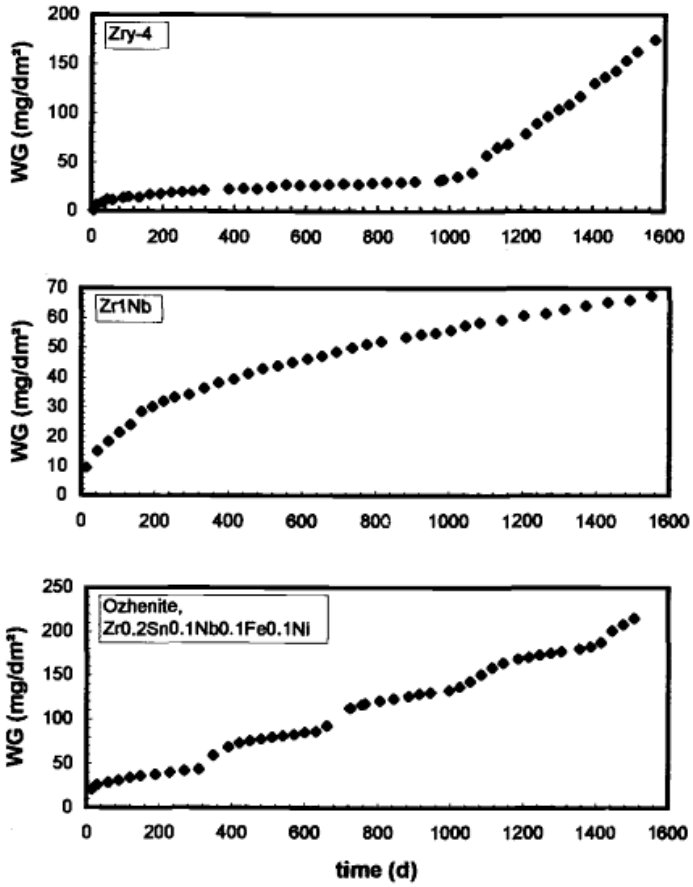


Figure 2.28: A comparison of corrosion kinetics of Zircaloy-4, Zr-1Nb and Ozhenite in 350°C water, 17MPa water [79].

The corrosion resistance has long been considered to be related to SPPs (second phase particles) [23,29,35,108-113]. Most SPPs have a higher P-B ratio compared to ZrO_2 and hence, there is a compressive stress inside the SPPs and tensile stress at the SPP/oxide interface [112]. The compressive stress could be high enough to stabilise t-ZrO_2 [113]. Furthermore, SPPs can also increase oxide electronic conductivity by providing a pathway

for electron diffusion, especially for large SPPs (Figure 2.29) [114]. In this case, the questions that should be addressed are if there is any correlation between SPP size and corrosion rate, and whether the SPPs remains metallic when incorporated into the oxide.

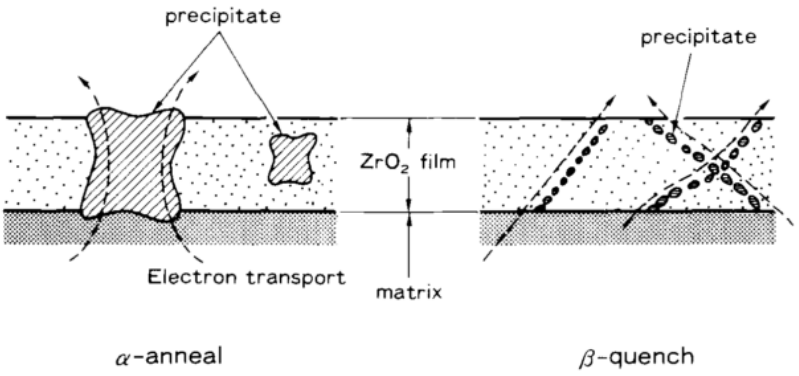
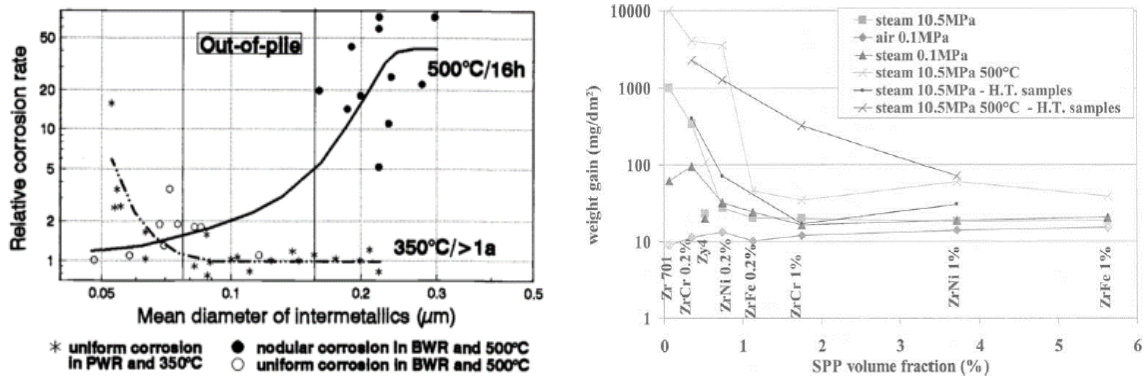


Figure 2.29: Schematic diagram showing the comparison between electron transport pathways via a large SPP obtained from α-annealing and small SPPs from β-quenching [114].

Pecheur et al. suggested that small SPPs (<400nm) have a greater tendency to remain unoxidised as opposed to large SPPs in Zircaloy-4 [115]. Increasing SPP size and volume fraction is beneficial for corrosion resistance because SPPs could be the cathodic sites for the oxidation reaction and hence increasing the total surface area by reducing SPP size can increase corrosion (Figure 2.30a-b) [29,108,116,117].



(a) (b)

Figure 2.30: The effects of (a) SPP size on the corrosion rate in the Zircaloys [117] and (b) SPP volume fraction on corrosion weight gain in various Zr alloys [116].

If SPPs are seen as an electron conduction pathway in the oxide, it is necessary to understand if the SPPs remain metallic upon oxidation. Redistribution of alloying elements has been

observed in oxidised SPPs [109-111,115]. Anada et al. pointed out that this redistribution is accompanied with oxygen diffusion from the surrounding ZrO_2 matrix into the SPPs (Figure 2.31) [113]. Obviously, the oxidation of SPPs depends on how easy it is to redistribute the alloying elements from SPPs. Some SPPs can undergo immediate oxidation once incorporated into the oxide, e.g. Zr_3Fe, $(Zr,Nb)_2Fe$ and β-Zr but some others exhibit delayed oxidation, e.g. β-Nb and $Zr(Nb,Fe)_2$ [29,37,110,112,116,118].

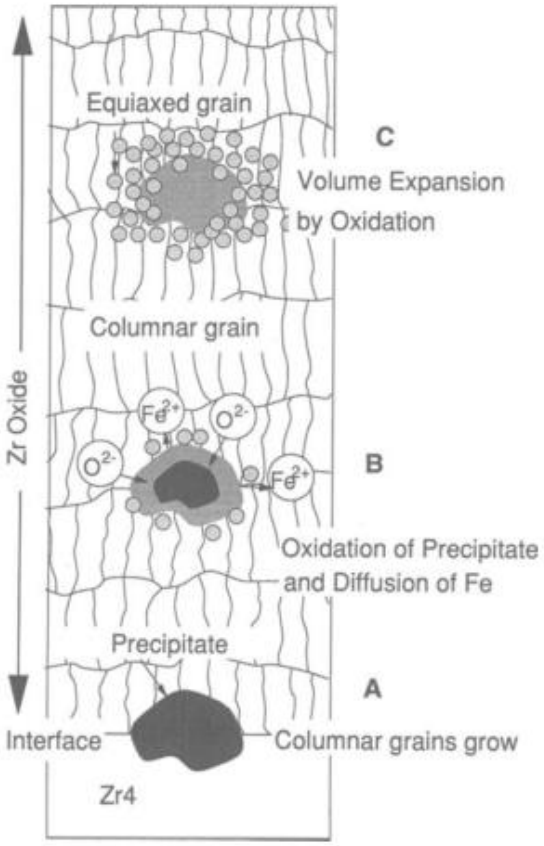


Figure 2.31: A model of $Zr(Fe,Cr)_2$ SPP oxidation proposed by Anada et al. [113].

Proff et al. stated that SPPs with delayed oxidation behaviour have higher free energy of oxide formation (Figure 2.32) [112]. Furthermore, upon oxidation they tend to form a crescent-shaped crack at the SPP/oxide interface facing the outer part of the oxide (SPPs in Figure 2.33) [88,99,119,120]. This is perhaps because of a volume change effect when Zr is oxidised to ZrO_2.

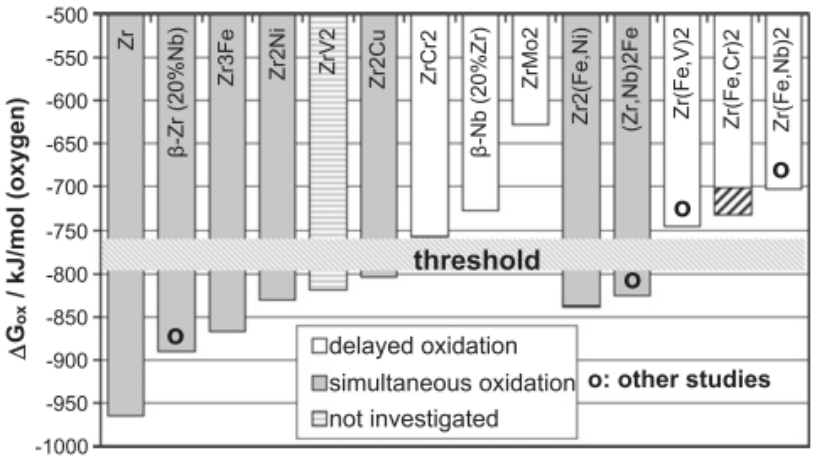


Figure 2.32: The free energy of oxide formation of different SPPs [112].

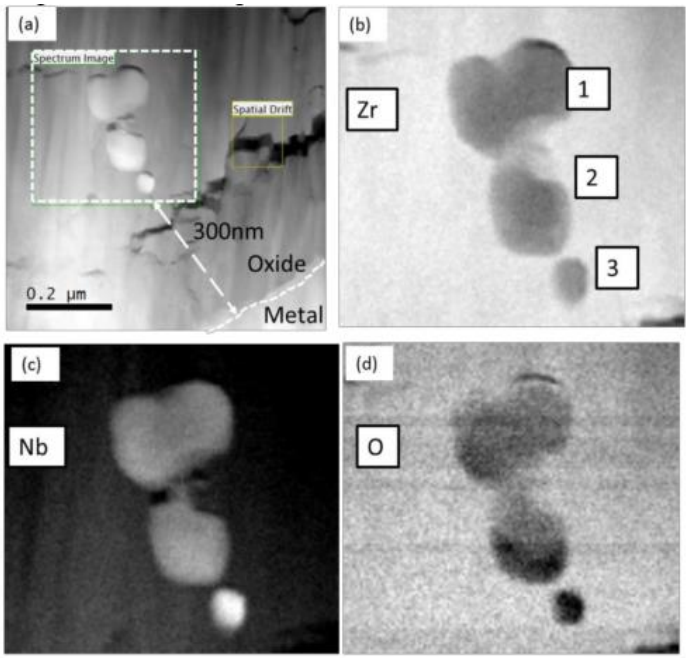


Figure 2.33: (a) STEM HAADF image of an area containing three SPPs about 300nm away from the metal-oxide interface, (b)-(d) core loss EELS mappings of Zr, Nb and O respectively taken from the white box in (a) [99]. There are 3 SPPs in this image; SPP1 is fully oxidised, SPP2 is partially oxidised and SPP3 is metallic.

The influence of Nb on corrosion behaviour depends on its distribution and the type of SPPs in the alloy. Under the solubility limit (~0.4wt%), increasing Nb content can slightly reduce corrosion [23,49]. Above ~0.4wt%, Nb is supersaturated and the corrosion behaviour can increase with Nb content if the major SPP is β-Zr but this trend is not observed if the major SPP is β-Nb (Figure 2.34 and Figure 2.35) [23,35,49]. Other observations also show that the corrosion resistance is improved in alloys with decomposed β-Zr, reinforcing that β-Zr is

detrimental and β-Nb beneficial for corrosion resistance [27,121]. This is probably because β-Zr corrodes faster than both α-Zr (Figure 2.36) and β-Nb, but there is no clear explanation as to why this is the case [27,121]. Furthermore, oxidised β-Zr is structurally different from α-Zr as it consists of fine (~15nm) equiaxed grains and probably also contains t-ZrO_2 [121].

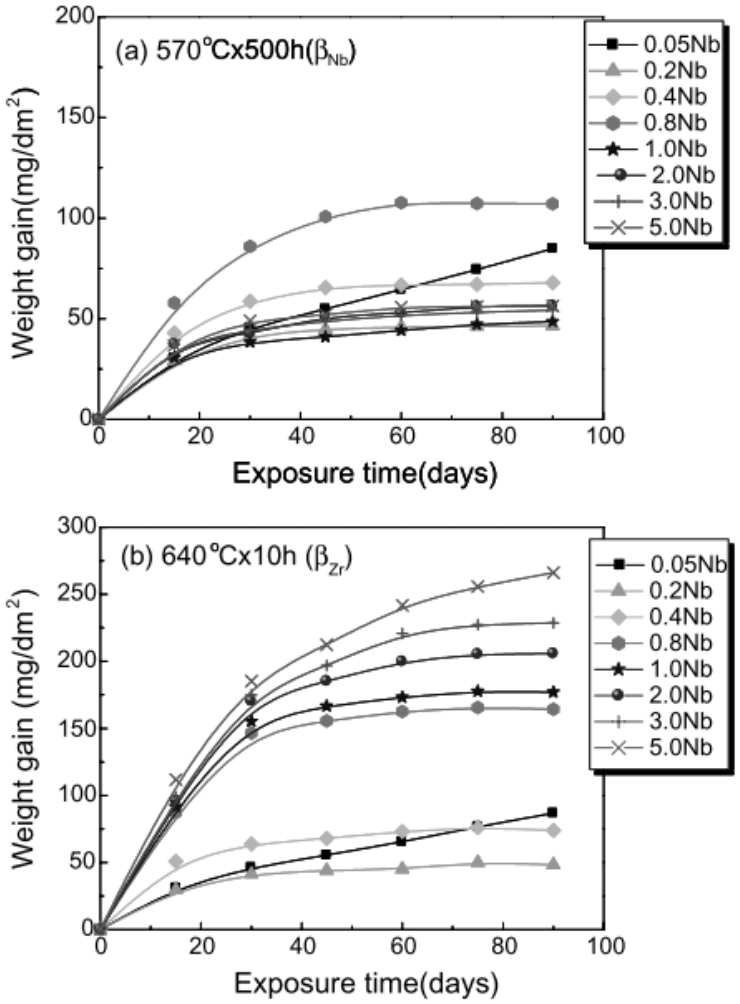


Figure 2.34: The corrosion kinetics of two types of Zr-xNb alloys (0.05<x<5wt%); where the first type has a major phase of β-Nb (annealed at 570°C) and the other type has a major phase of β-Zr (annealed at 640°C) [35]. These samples were corroded in water at 360°C.

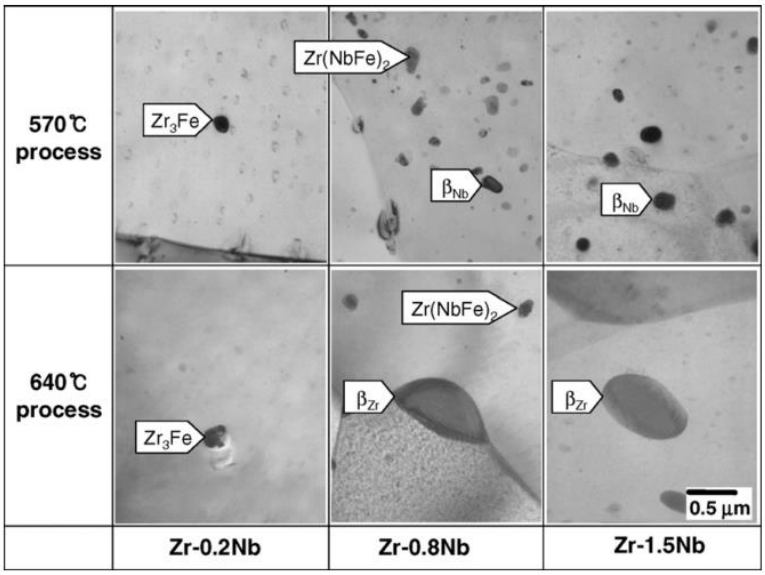


Figure 2.35: The microstructures of Zr-0.2Nb, Zr-0.8Nb and Zr-1.5Nb with two heat treatment methods from Figure 2.34 showing different SPPs observed in each sample [23]

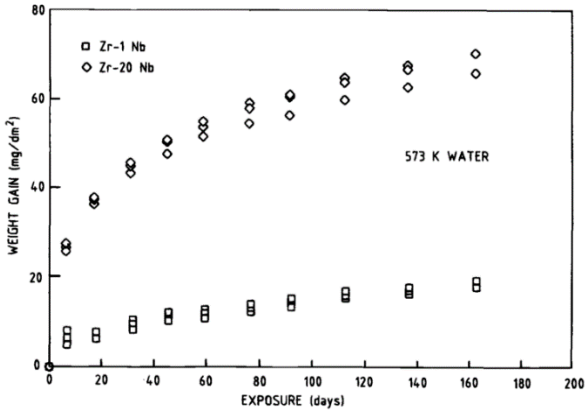


Figure 2.36: The corrosion kinetics of Zr-1Nb (representing α-Zr) and Zr-20Nb (containing a single phase of β-Zr) at 300°C lithiated water [121].

From the above information, the superior corrosion resistance of commercial Zr-Nb alloys may be related to β-Nb. However, other researchers have also proposed other theories regarding the beneficial effect of Nb. One of the most recent ones is the space charge compensation mechanism as Nb has multiple oxidation states and can affect the space charge in the oxide [5,122,123]. This is further discussed in Chapter 8.

Pecheur found that the Nb content of unoxidised β-Nb in the oxide is ~60%, and decreases to 10-50% in oxidised β-Nb [110]. When oxidised, the stoichiometry of β-Zr becomes $Nb_2Zr_{x-2}O_{2x+1}$ where $7.1<x<12$, indicating that Nb may or may not be leached out from the SPP upon

oxidation because the Nb/Zr ratio could be higher or lower than the theoretical value of ~0.25 [27]. Kim et al. observed that both Nb/Zr and Fe/Zr ratios decrease upon oxidation when $(Zr,Nb)_2Fe$ and $Zr(Nb,Fe)_2$ are oxidised (Figure 2.37) [37]. However, there is little information regarding the role of Fe in Zr-Nb alloys on corrosion behaviour.

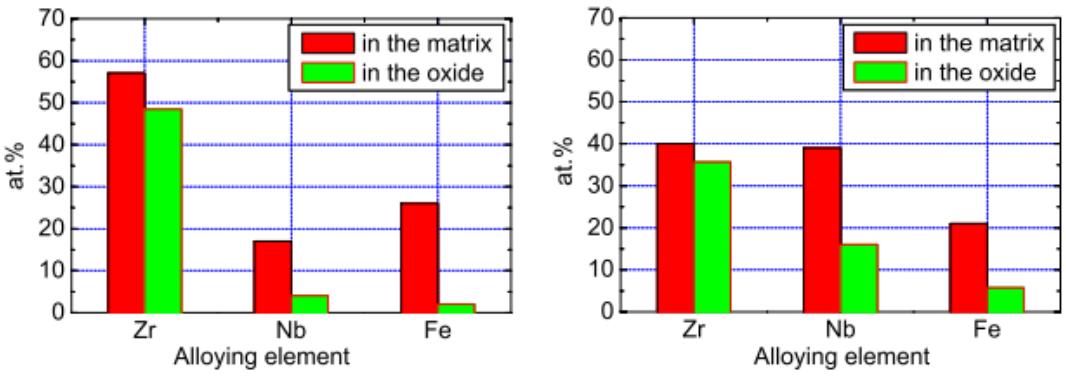


Figure 2.37: The compositions of (a) fcc $(Zr,Nb)_2Fe$ SPP in Zr-0.3Nb-0.5Fe and (b) hcp $Zr(Nb,Fe)_2$ hcp SPP in Zr-0.7Nb-0.1Fe in the metal and oxide [37].

2.4. Hydrogen pickup (HPU)

2.4.1. Kinetics

Because H atoms are much lighter than O, weight gain measurement is not a good parameter in describing the degree of HPU. Instead, H content (usually in wtppm) or a quantity called the hydrogen pickup fraction (HPUF) is often used. HPUF can be defined as the ratio between absorbed and generated hydrogen in the metal:

$$\mathrm{HPUF} = \frac{\mathrm{H_{absorbed}}}{\mathrm{H_{generated}}} \tag{2.6}$$

Because HPU is the consequence of corrosion, it is not surprising that the HPU kinetics is related to oxidation. As a kinetic change in HPU is observed during oxidation transition, the HPU periodicity follows that of oxidation (Figure 2.38). Note that this kinetic change is not called a transition, as transition only refers to the change in oxidation kinetics.

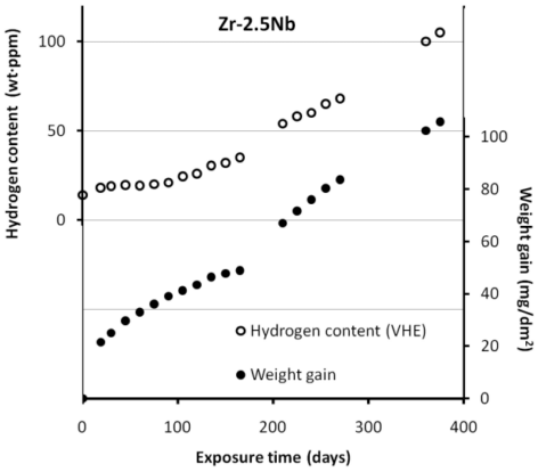


Figure 2.38: Corrosion and HPU kinetics of Zr-2.5Nb [5].

2.4.2. HPU mechanism

The anodic oxidation reaction (Reaction 2.4) results in the generation of electrons and oxygen vacancies. They both can react with water to produce H atoms at cathodic sites [9]:

$$V_O + H_2O \rightarrow O^{2-} + 2H^+ \quad (2.7)$$

$$2e^- + 2H^+ \rightarrow 2H \text{ or} \quad (2.8)$$

$$2e^- + H_2O \rightarrow O^{2-} + 2H \quad (2.9)$$

In nuclear reactors, water dissociation by radiolysis also results in H atoms [9]:

$$2H_2O \rightarrow 2OH + 2H \quad (2.10)$$

Some of these H atoms recombine to form gaseous H_2 which is subsequently released to the environment but the rest can penetrate to the Zr matrix, contributing to HPU as the absorbed hydrogen [5,9,124].

The HPU mechanism is not well-understood, especially how hydrogen can travel in the oxide from the W/O to O/M interface (Figure 2.17) and where cathodic reactions (Reaction 2.8, 2.9 or H_2 gas evolution) occur. Although several hypotheses have been introduced, there is a lack of experimental data that can support these hypotheses.

Because the H atom is much smaller than Zr, the possibility of interstitial diffusion should be considered. H diffusion coefficients at 600K in m-ZrO_2 and t-ZrO_2 are between 10^{-25}-10^{-24} m^2/s and 10^{-20}-10^{-17} m^2/s respectively, suggesting that H is not mobile in the bulk oxide [125]. This is probably because even though the interstice volume of ZrO_2 (~4.76Å^3) is large enough to accommodate a hydrogen atom or proton, the gap between O and Zr in ZrO_2 crystal (~0.15Å) is much smaller than the diameter of the H atom (~1.06Å) and thus, interstitial diffusion is unlikely [126].

SPPs are thought to affect the HPU properties [82,127-131]. A SIMS experiment also demonstrates that there is a possible correlation between the SPP and H/D distribution (Figure 2.39) [82]. Hatano et al. showed that Zircaloy-2 with coarse SPPs displays a higher HPU than alloys with finer SPPs (Figure 2.40a-b) [129]. A formula unit of $Zr(Cr,Fe)_2$ and $Zr(Ni,Fe)_2$ is capable of absorbing 3-4.5 H atoms, indicating that they can store H [127,132].

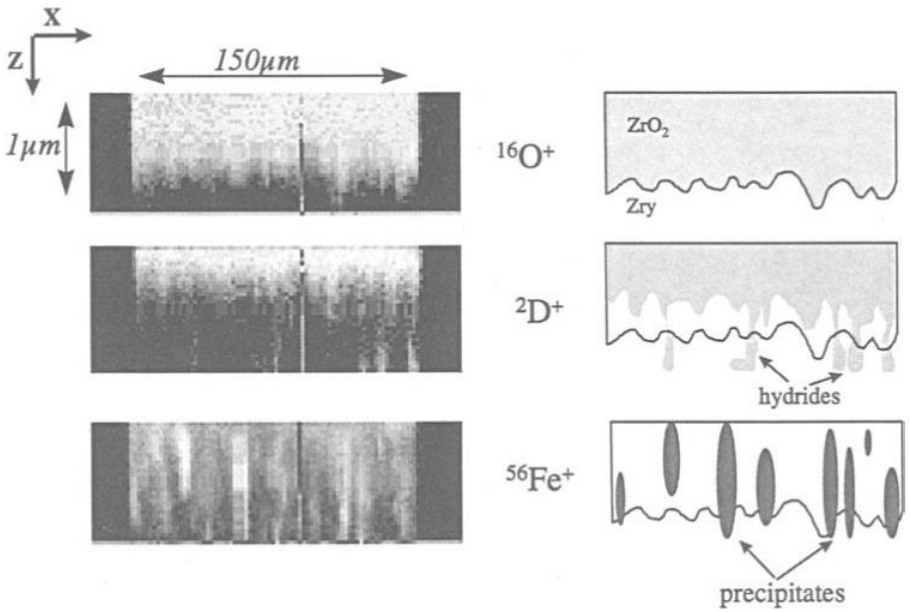
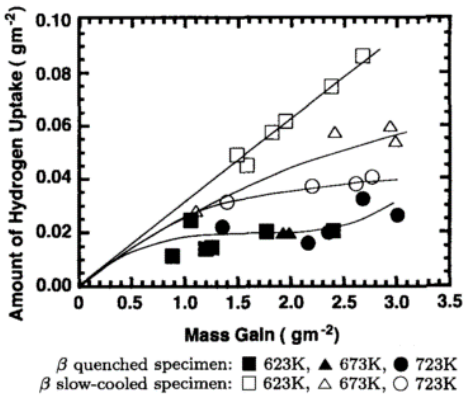
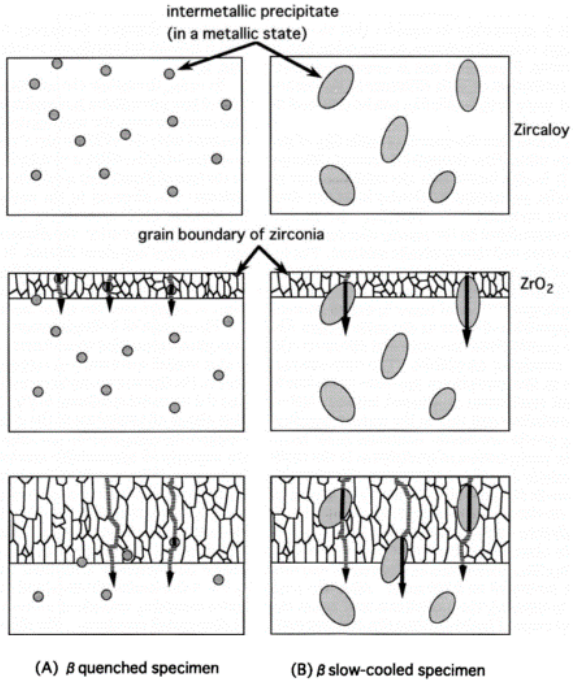


Figure 2.39: The maps (left) and schematic diagrams (right) of $^{16}O^+$, $^2D^+$ and $^{56}Fe^+$ distributions near the O/M interface of Zircaloy-4 corroded for 48 hours at 673K [82].



(a)



(b)

Figure 2.40: (a) A comparison between HPU of Zircaloy-2 with fine (β-quenched) and coarse (β-slow-cooled) SPPs and (b) the schematic diagram showing the proposed hypothesis of H transport in the oxide layer by Hatano et al. [129].

However, the hypothesis of H transport via SPPs was later disputed by Cox and Wong who deposited Cu balls as cathodes, demonstrating that the Cu balls are not the cathodic sites, but the cathodic sites instead are the cracks and pores adjacent to the balls (Figure 2.41) [133]. The capability of SPPs to absorb H is only valid at low temperatures, as segregation of H to the SPPs is similar to the deuterium redistribution when Zr liner is cooled down [133,134]. Inevitably, this leads to another hypothesis that H travels via cracks and pores. Although

these features are not present in the barrier layer, they are still considered the fastest pathways for H diffusion in the oxide layer.

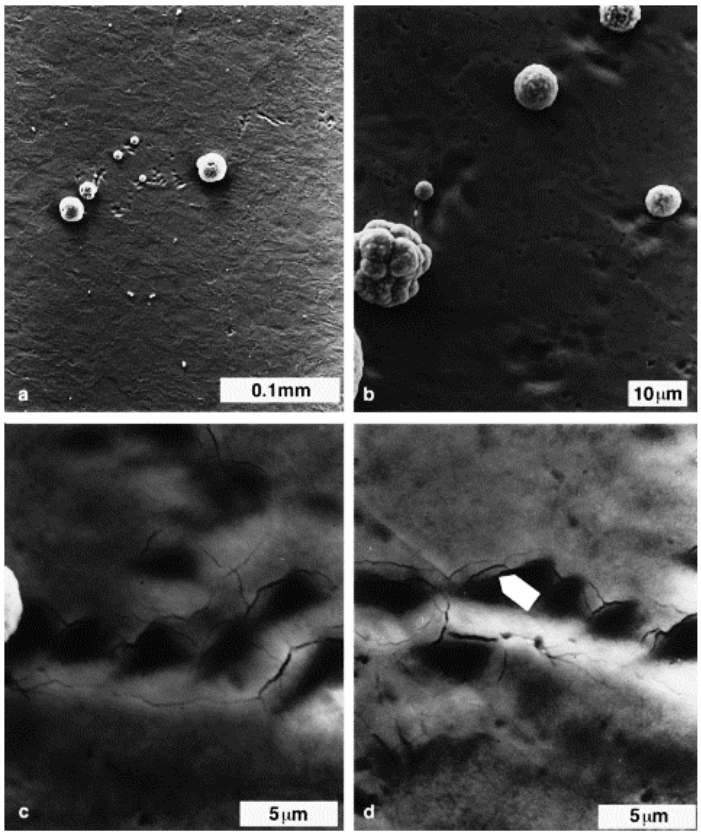


Figure 2.41: SEM images of Cu balls deposited cathodically on 1.2μm thick Zircaloy-2 oxide showing (a) the distribution of the balls and (b) a group of deposited Cu balls, (c) the crack pattern adjacent to a ball in (b) and (d) the nucleation site for the ball in (c) [135].

The presence of water molecules on the pore surface can induce the local dissolution of the oxide layer (Figure 2.42) [136]. The rest of H can then accumulate inside the pores such that pure gaseous H_2 can form there [135,137]. Cox speculated that this H can be absorbed by the metal, but there is no clear explanation regarding how the H can travel through a barrier layer that is free from pores [135]. However, there are suggestions that H can travel through a network of interconnecting pores [138,139].

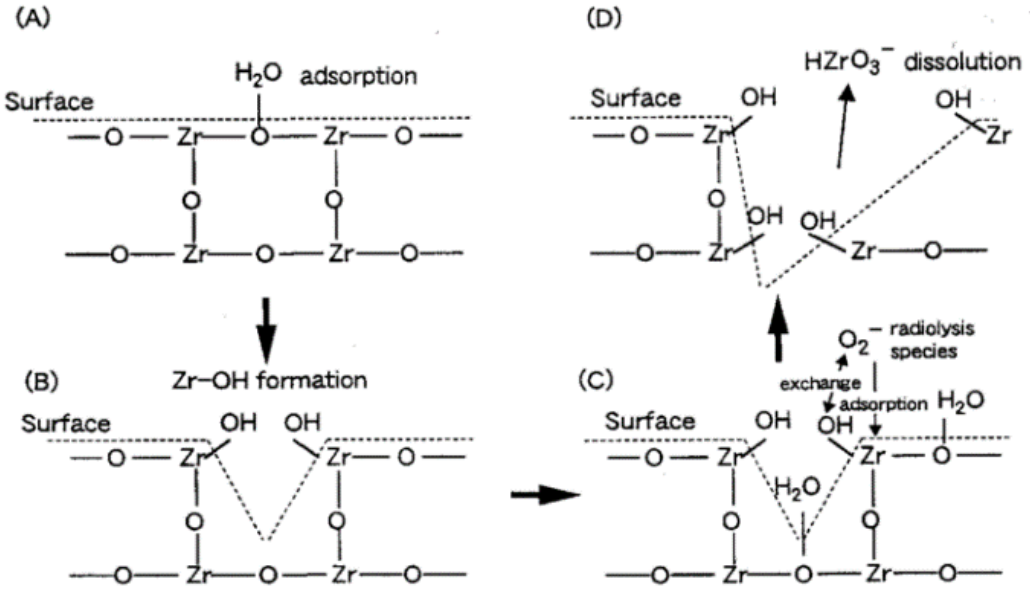


Figure 2.42: The oxide dissolution process [136].

The oxide breakdown results in the formation of hydroxyl on the oxide surface (Figure 2.42). Hydroxyl formation in the oxide has been predicted and experimentally observed by dissolution experiments, SIMS and FTIR [80,139,140]. This indicates that the H-carrying species is more likely to be OH^- rather than protons. Ramasubramanian et al. suggested that H transport is via an interconnected hydroxylated pathway (Figure 2.43) [80]. This hydroxylated pathway could either be interconnected porosity or oxide grain boundaries [42,124,138,139].

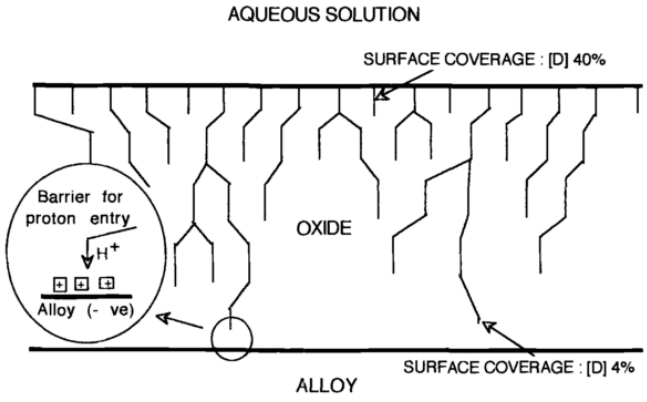
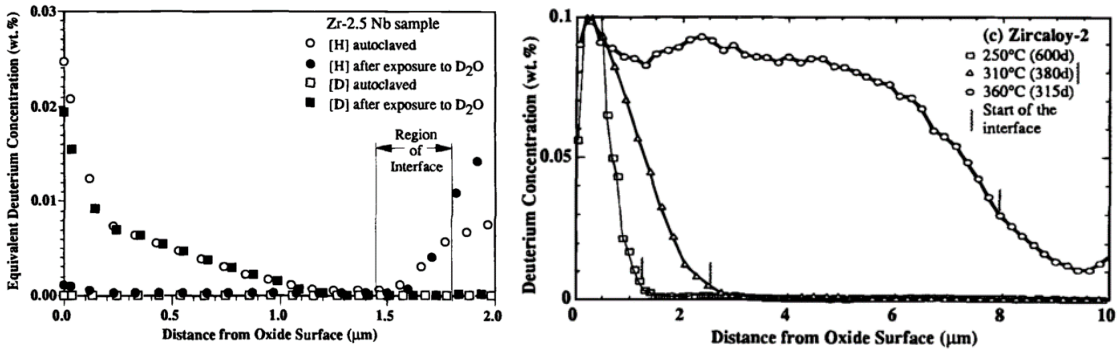


Figure 2.43: The interconnected hydrated pathways in the oxide layer [80].

How H can penetrate through the barrier layer is still not well understood. The barrier layer is highly resistive, impervious to electrolyte and contains almost no H [78,82,83]. According to

SIMS work on deuterated Zr-2.5Nb and Zircaloy-2, the pre-transition barrier layer is mostly free from D (Figure 2.44a) but in post transition, more significant D accumulation is observed in the oxide near to the O/M interface especially the sample corroded at 360°C/315 days (Figure 2.44b) [139]. Although this study does not provide the weight gain information for the samples, as Zircaloy-2 undergoes sudden transition it is reasonable to say that the barrier layer disappears completely after transition. In addition, it has been suggested that the presence of compressive stress inside the barrier layer can suppress H diffusion, and therefore H is not mobile in this region [141].



(a) (b)

Figure 2.44: Through-oxide-thickness deuterium and hydrogen concentration profile of (a) Zr-2.5Nb prefilmed by steam autoclaving at 400°C for 2 days and subsequently corroded in D_2O at 300°C for 7 days and (b) Zircaloy-2 corroded in D_2O at 250°C/600 days, 310°C/380 days and 360°C/315 days [139].

2.4.3. Metallurgical considerations

Alloying elements clearly can influence HPU behaviour (Figure 2.45) [5,9,42,69,142-144]. Results from DFT modelling work concerning the effect of transition metals (TMs) show that HPU can be suppressed by encouraging H_2 gas formation, but this depends on how stable the TM-H-Zr "hydride" bond is (Figure 2.49a-b) [42,124,144]. A stable "hydride" bond tends to favour HPU while unstable bond results in H atoms being released from the system and

recombining. This theory is successful in explaining the adverse effect of Ni on HPU resistance (Figure 2.45) but cannot be used to understand the effects of Nb.

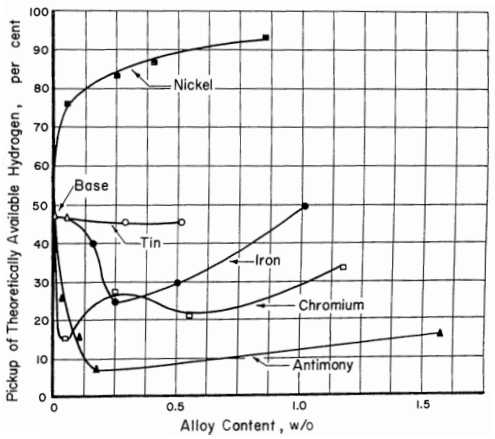
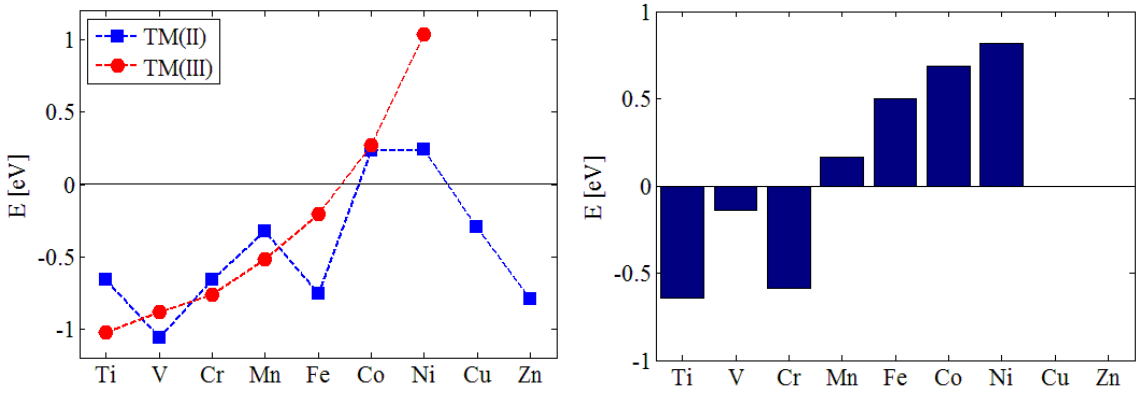


Figure 2.45: Effect of alloying elements on HPUF [142].



(a) (b)

Figure 2.46: (a) The energetics for H_2 formation from transition metal (TM) hydride for TM(II) (squares) and TM(III) (dots), respectively and (b) the energetics for formation of TM(III) hydrides, giving the feasibility of this channel for H_2 evolution [124]. Negative numbers are favourable, while positive numbers disfavour this channel.

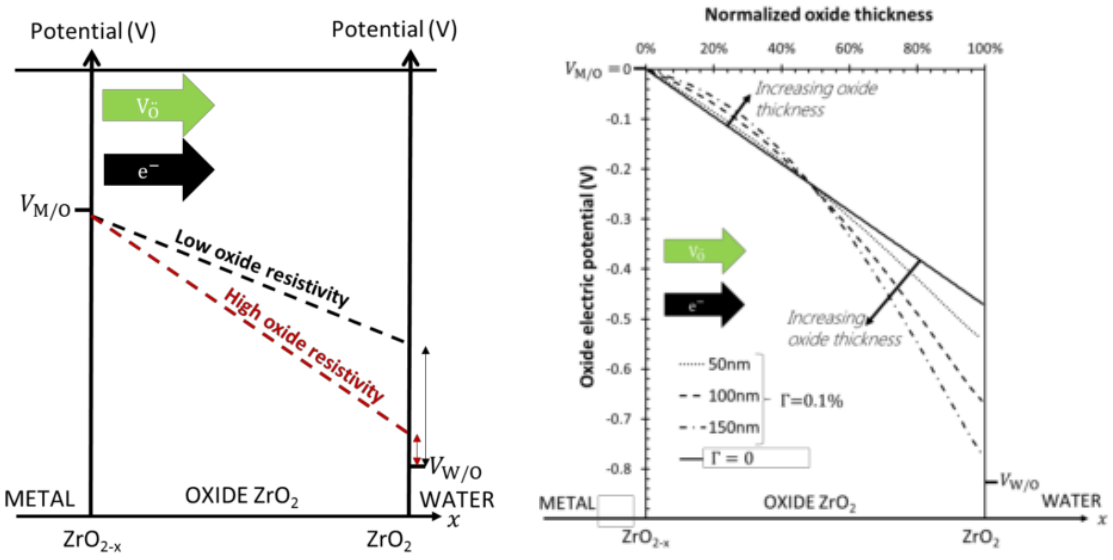
Another approach to examine the effects of alloying elements is by analysing space charge compensation [143,145,146]. The existence of space charge in oxidised Zr alloys has been predicted and evidenced before [77,143,145,147,148]. Space charge arises due to the transport and reorganisation of charged species in the oxide layer and its magnitude depends on oxide properties such as dielectric constant, how fast the charged species diffuse and the corrosion potential [143,148,149]. The space charge can be either reduced by ions with

oxidation states greater than +4 (corresponding to Zr^{4+}) such as Nb^{5+}, or compensated by ions with oxidation states less than +4 such as $Nb^{2,3+}$ and $Fe^{2,3+}$, with the space compensation factor (Γ), which is the fraction of diffusing charged species that is not compensated defined as [143]:

$$\Gamma = 1 - \frac{(\sum_i Z_i C_i(x))_{\text{aliovalent ions}}}{(\sum_i Z_i C_i(x))_{\text{diffusing charges}}} \quad (2.11)$$

with Z and C corresponding to the valence and concentration (in cm^{-3}) of the species of interest. Note that space charge compensation is beneficial for HPU but space charge increase has the opposite effect.

Space charge plays an important role in controlling oxidation and HPU by changing the oxide electronic resistivity that ultimately influences oxidation and HPU [77,79,143]. The term corrosion potential refers to the potential difference between the O/M and W/O interface and is thought to be the driving force for HPU as it reduces the probability of electrons diffusing towards the W/O interface and instead forces H to diffuse inwards [143]. If the resistivity is high, the electron transport is difficult and there is no electron supply to the outer part of the oxide to be involved in cathodic reactions, eventually resulting in a high oxide corrosion potential by reducing the potential at the W/O interfaces and vice versa (Figure 2.47a) [143]. In addition, the amount of space charge compensation in the same alloy can also alter the potential (Figure 2.47b).



(a) (b)

Figure 2.47: The effects of (a) resistivity and (b) space charge compensation factor on the corrosion potential [143].

Consequently, high resistivity is associated with good corrosion kinetics and bad HPU behaviour and vice versa (Figure 2.48 and Figure 2.49a-b). In the presence of space charge compensators, both resistivity and oxide electrical potential are suppressed (Figure 2.48 and Figure 2.49a-b) [143,150]. This eventually leads to an increase in oxidation kinetics and decrease of HPU.

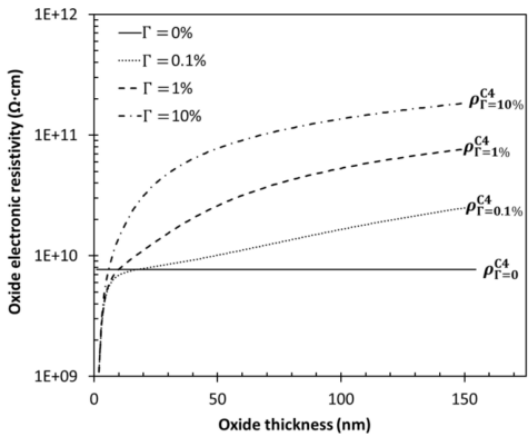
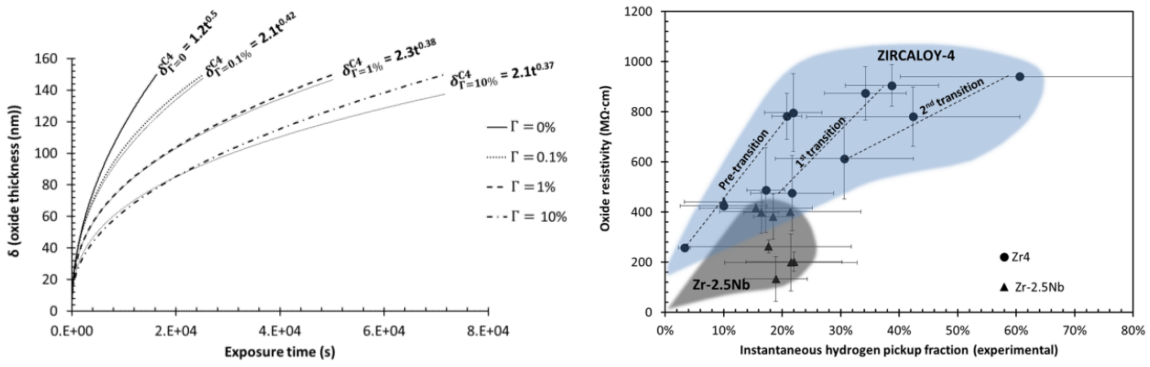
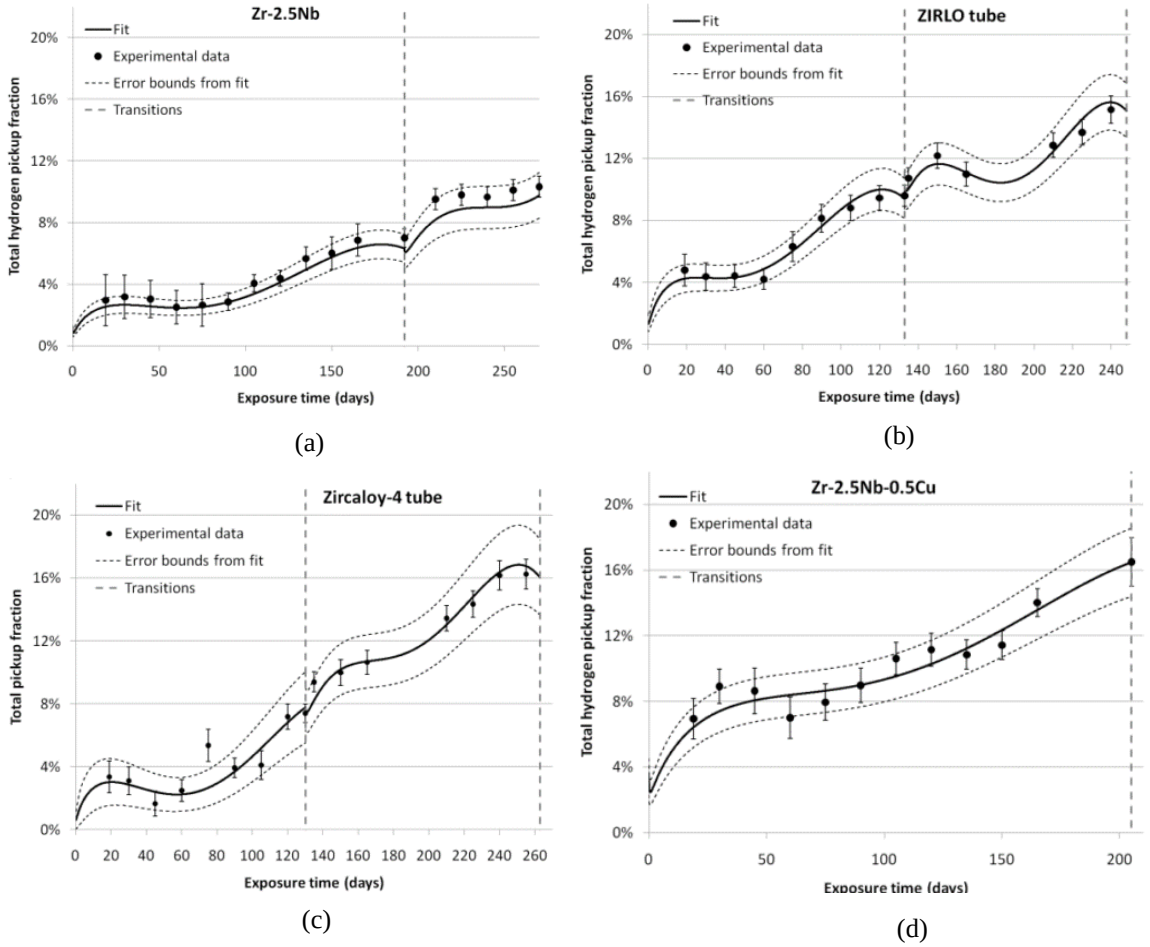


Figure 2.48: The relationship between oxide thickness, resistivity, and space charge compensation [143].



(a) (b)

Figure 2.49: The relationships between (a) oxidation kinetics and space charge compensation and (b) oxide resistivity and HPUF of Zircaloy-4 and Zr-2.5Nb [143].



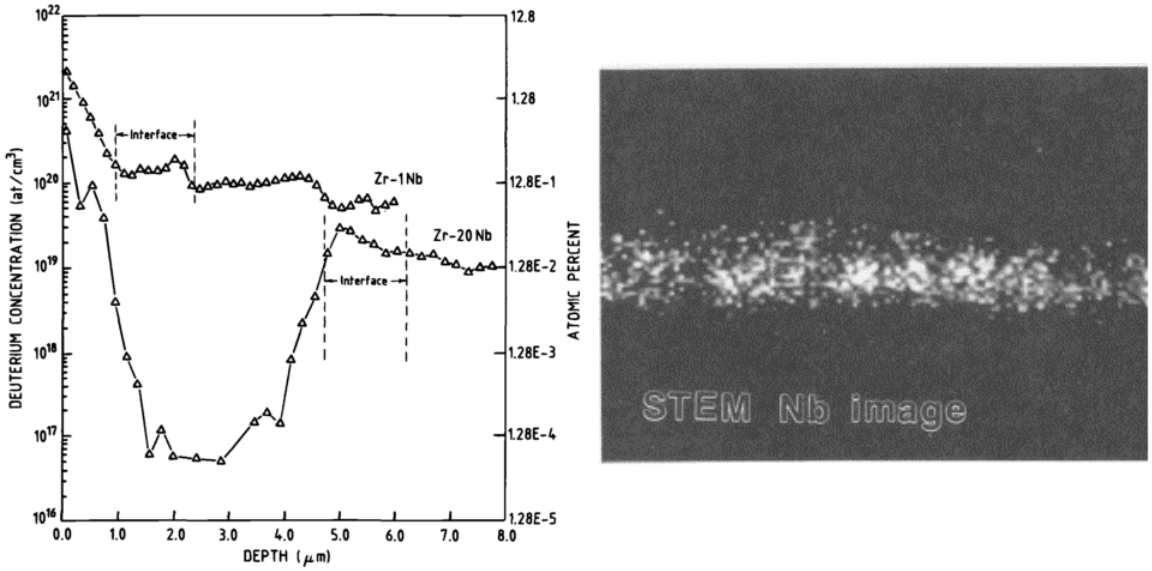
(a) (b)

(c) (d)

Figure 2.50: The comparison of HPUF in (a) Zr-2.5Nb, (b) ZIRLO, (c) Zircaloy-4 and (d) Zr-2.5Nb-0.5Cu corroded at 360°C [5].

In general, Zr-Nb alloys have lower HPU behaviour compared to the other Zr alloys (Figure 2.50a-d), probably because Nb is a good space charge compensator and the amount of Nb is

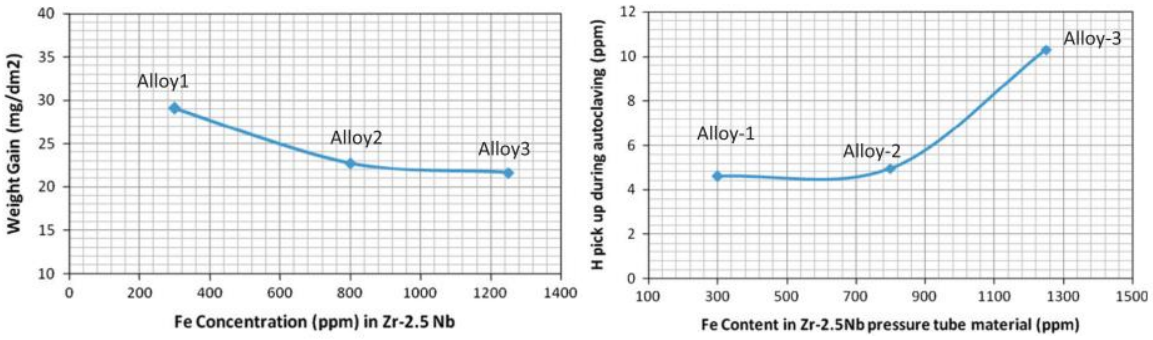
high enough to compensate the majority of space charge [5,143]. Regarding the effect of β-Zr, despite having worse corrosion properties β-Zr exhibits a lower HPU than α-Zr (Figure 2.51a) and this is possibly due to the higher concentration of Nb accumulation (probably still metallic) in the oxide of β-Zr that is not found in α-Zr (Figure 2.51b) [121].



(a) (b)

Figure 2.51: (a) The comparison of D profiles of Zr-1Nb (mimicking α-Zr) and Zr-20Nb (β-Zr) and (b) the accumulated Nb in oxidised Zr-20Nb [121].

Fe is also a good space charge compensator and has been proved to improve HPU resistance in Zircaloy-2 [150]. However, a discrepancy is found in a study conducted by Choudhuri et al. where Fe additions from 300-1250 wtppm in Zr-2.5Nb increase corrosion weight gain and reduces HPU (Figure 2.52) [151]. They further explained that this is due to the formation of Zr_2Fe that in the alloy containing 1250ppm Fe, as this SPP is thought to be detrimental for HPU [151].



(a) (b)

Figure 2.52: The (a) oxidation weight gain and (b) HPU of Zr-2.5Nb with 300ppm (Alloy 1), 800ppm (Alloy 2) and 1250ppm (Alloy 3) additions of Fe, all corroded at 415°C for 3 days [151].

2.4.4. Delayed hydride cracking (DHC)

Although in the bulk oxide diffusivity of hydrogen is slow, it is fast in α-Zr (~10^{-10} m^2/s at 335°C, compared to ~10^{-25}-10^{-24} m^2/s at 373°C in m-ZrO_2) [125,152]. The terminal solubility of H in α-Zr is extremely low at reactor temperatures (150 wtppm or 1.34 at% at 360°C) and decreases with temperature (Figure 2.53). H supersaturation leads to hydride (ZrH_2) formation (Figure 2.54) [153]. ZrH_2 is brittle, implying easy crack generation and a difficulty in dislocation motion compared to pure Zr [154].

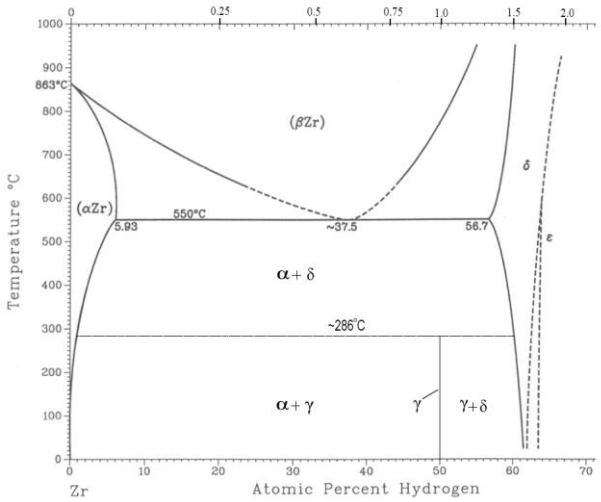
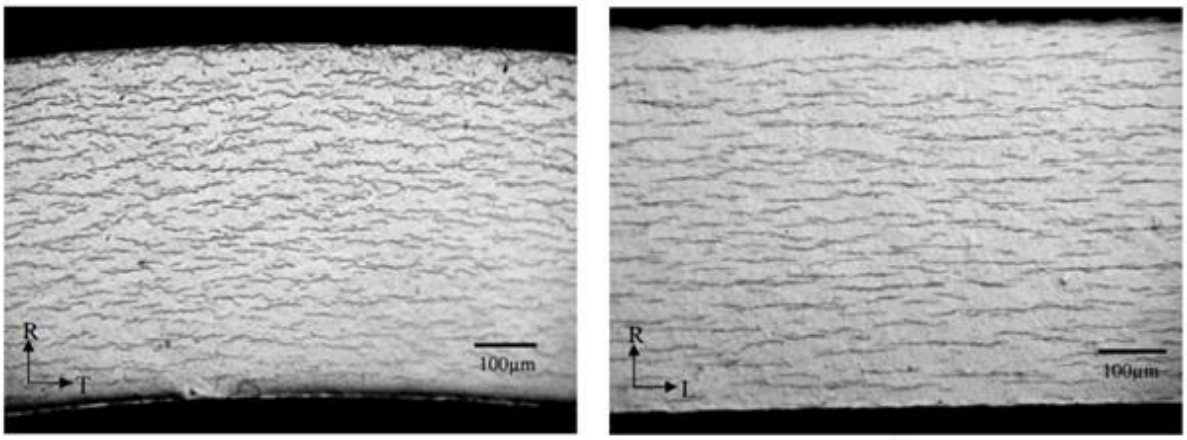


Figure 2.53: Zr-H phase diagram [152].



(a) (b)

Figure 2.54: Distribution of hydrides on (a) transverse-radial plane and (b) longitudinal-radial plane in a Zircaloy-4 sample [12].

Because hydrided Zr alloys can exhibit a brittle-to-ductile transition starting at ~130°C (Figure 2.55), the major implications of the presence of hydrides are reduction of fracture toughness and ductility when the reactor temperature is reduced during servicing and refuelling [154,155]. Hydrides can also influence corrosion. In 360°C PWR conditions, pre-hydrided Zircaloy-4 shows a greater oxidation rate and earlier transition compared to unhydrided Zry-4, due to ~2x increased O diffusivity in the presence of hydrides [60].

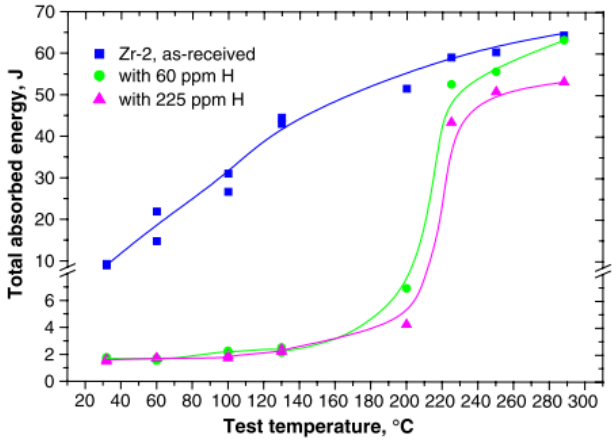


Figure 2.55: Ductile-brittle transition in hydrided Zircaloy-2 [155].

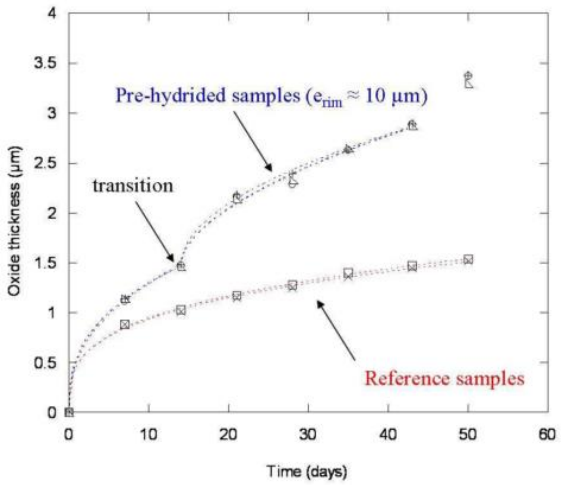
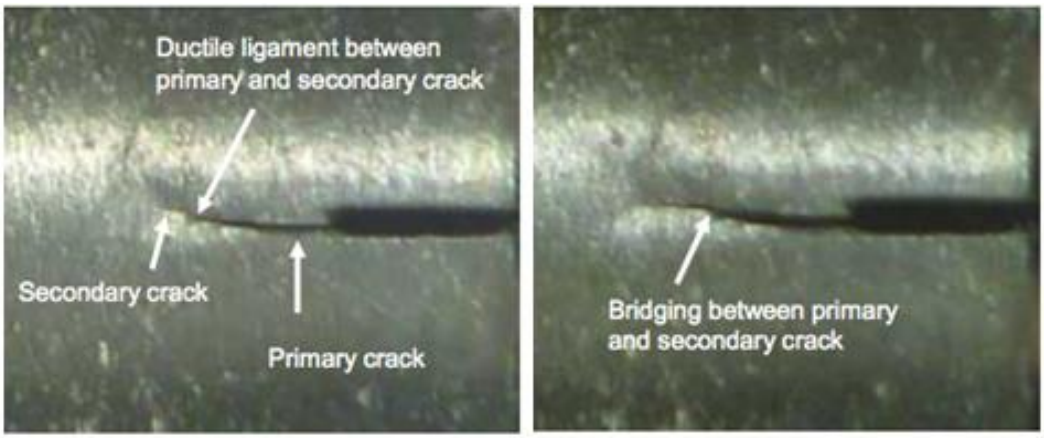


Figure 2.56: Comparison of corrosion kinetics between hydride and unhydrided reference Zircaloy-4 [60].

DHC occurs in a cyclic manner preceded by the precipitation of hydrides in the metal matrix [13,156]. Nucleation of hydrides is favoured near regions where tensile stress is high, e.g. defects or pre-existing crack tips and where they are dissolved and reprecipitate [1,13]. Hydride brittle fracture causes crack advancement and secondary crack (Figure 2.57a-b) and this cycle is repeated until the cracks are integrated and experience unstable growth where component failure occurs (Figure 2.58) [12].



(a) (b)

Figure 2.57: (a) Secondary crack in front of primary crack and (b) the bridging between primary and secondary cracks in Zircaloy-2 [156].

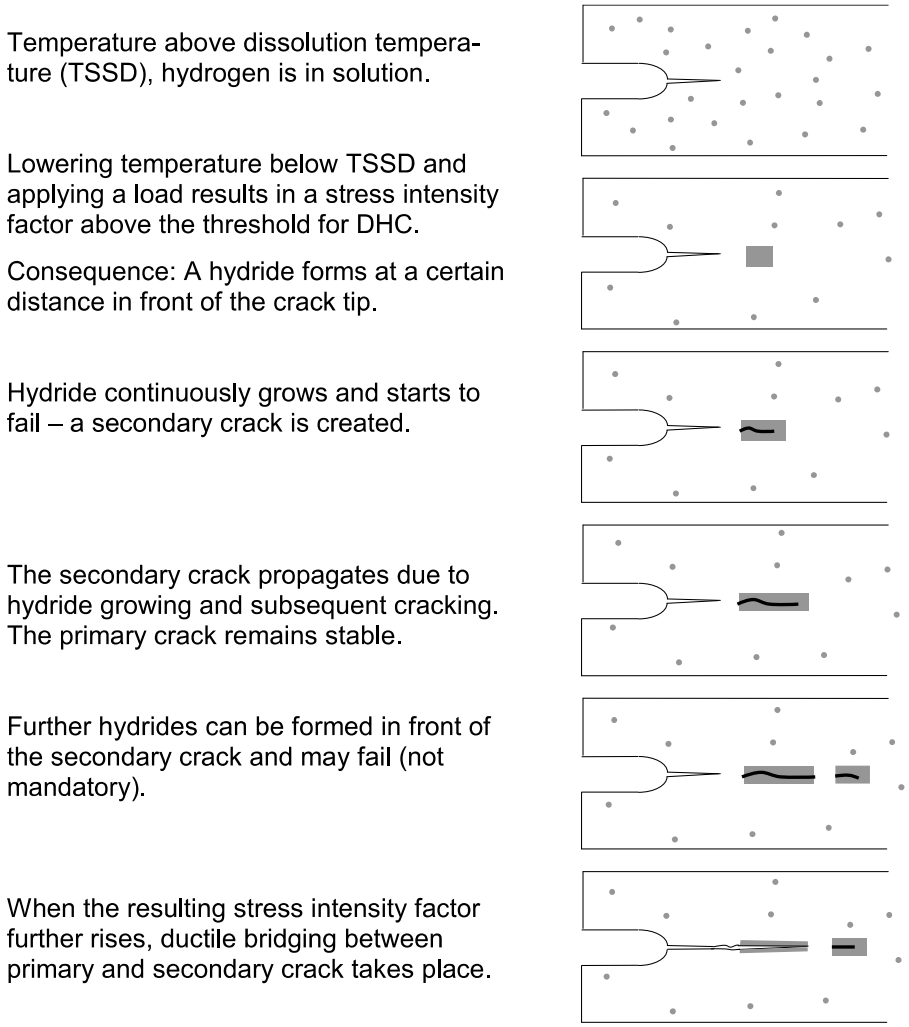


Figure 2.58: Schematic diagram showing a DHC process [156].

2.5. Irradiation effects

Irradiation changes material microstructure by the formation of various defects as an energetic particle (e.g. neutron) collides with atoms in the material and causes a displacement cascade (Figure 2.59) [2]. In the metal, the common defects include the formation of parallel dislocation lines or dislocation loops of <a>, <c> or <c+a> character (Figure 2.60a-b) [157-159].

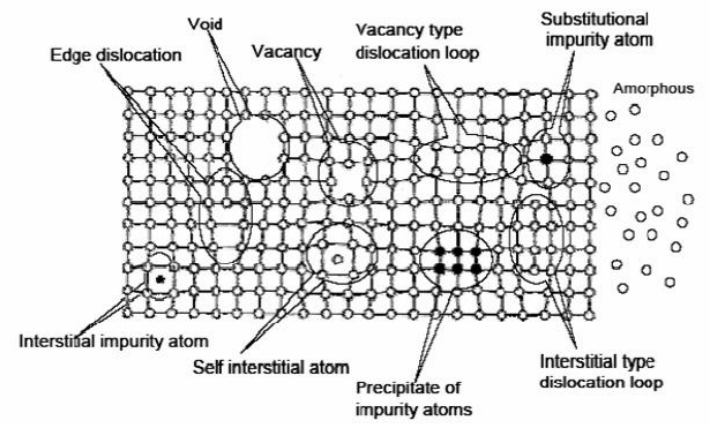


Figure 2.59: Defects in the lattice structure of materials that can change their material properties [2].

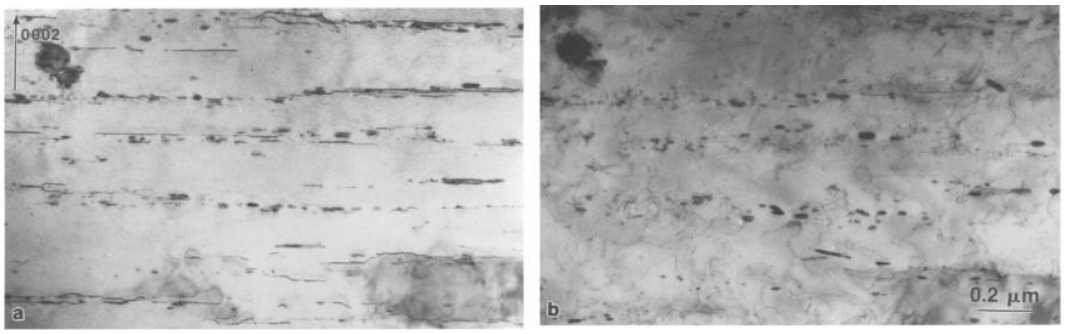


Figure 2.60: The microstructures of an impure sponge Zr sponge after irradiation to a fluence of 1.5×10^{25} m^{-2} at 700 K showing (a) Fe/Cr-rich SPPs aligned in bands lying on the basal plane, with parallel c-component dislocation lines and (b) <c>-loops [158].

Irradiation can also affect the alloying element distribution in the alloys [160-163]. Specifically for Zr-1Nb, Shishov et al. suggested that under irradiation of 20-30 dpa there is a depletion of Nb content in β-Nb (40-50nm) from 80-90 at% (unirradiated) to 50-60 at% (irradiated) as well as in the metal matrix from ~0.4 at% (unirradiated) to below 0.2 at% (irradiated) (Figure 2.61a,c) [161]. In addition, irradiation induces a precipitation of fine (5-10nm) β-Nb. Samples with β-Zr demonstrated that it decomposes to β-Nb containing 40-60 at% Nb during irradiation [161], but this decomposition depends on the temperature and flux [163].

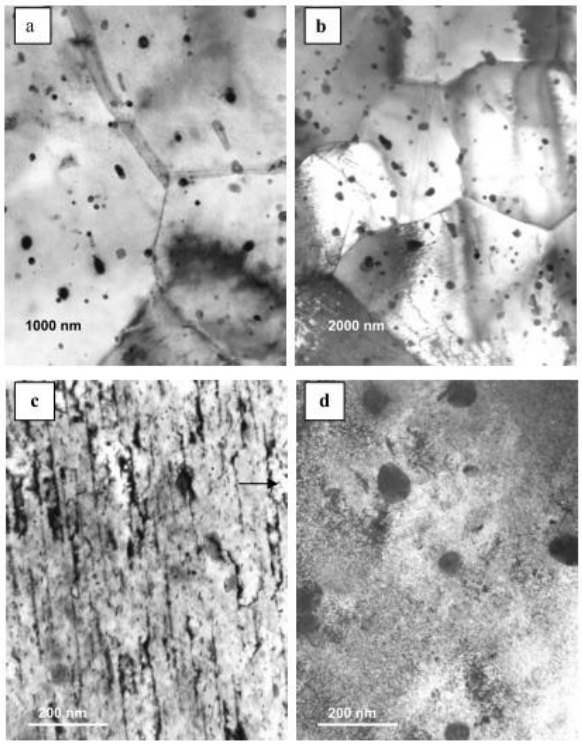


Figure 2.61: The microstructure of unirradiated (a) Zr-1Nb (containing β-Nb) and (b) E635 (containing $Zr(Nb,Fe)_2$); and (c) 23-dpa irradiated Zr-1Nb and (d) 22-dpa irradiated E635 [161].

Analyses on E635 containing predominantly $Zr(Nb,Fe)_2$ showed that this SPP transforms to β-Nb after irradiation, with the Nb content increasing from 35 at% to 50 at% while Fe decreases from 20 at% to 5-10 at% (Figure 2.61b,d) [161]. At the same time, the matrix Nb content decreases from ~0.3 at% to <0.2 at% while Fe increases from <0.1 at% to 0.3-0.4 at%. This implies that under irradiation the Nb content in the matrix decreases but almost all Fe is located in the metal matrix. It has been shown as well that Fe can decorate dislocation loops [164].

Irradiation enhances diffusivity of atoms in the oxide including O, and this is probably why it accelerates corrosion (Figure 2.62) [39,165,166]. In addition, it also introduces space charge as ions and electrons are displaced and therefore comparing the effect of alloying elements by space charge compensation is not straightforward [166]. Under irradiation, Zr-Nb alloys generally display a better corrosion and HPU resistance than Zr-Sn alloys (Figure 2.63)

[104,167,168]. However, the reason is not fully understood. Urbanic et al. hypothesised that this is associated with the decrease of Nb content in the metal matrix and reprecipitation of fine β-Nb particles [163,168]. This is somewhat counterintuitive because the out-of-pile corrosion resistance is improved by the increase of Nb content in the metal matrix (Section 2.3.4). Bossis et al. speculated regarding HPU that as Nb is homogeneously dispersed in the oxide layer, the presence of Nb^{5+} near W/O interface encourage the HPU cathodic reaction to occur in this region [104].

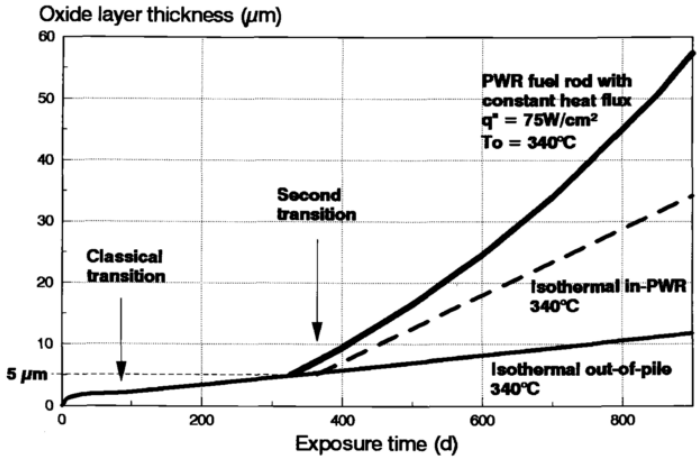


Figure 2.62: A schematic diagram comparing the corrosion kinetics of a Zr alloy corroded unirradiated in a PWR environment with constant temperature and with constant heat flux [117]. All at 340°C.

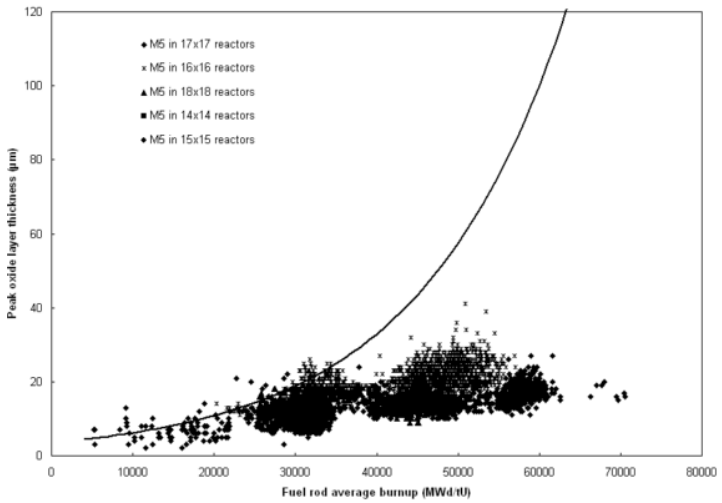


Figure 2.63: Peak oxide thickness of M5 (dots) and Zircaloy-4 (line) corroded in PWRs for 6 cycles [104].

3. EXPERIMENTAL METHODS

3.1. Atom probe tomography (APT)

3.1.1. Introduction

APT allows the three-dimensional atom-by-atom reconstruction of a needle-like specimen [6,169]. With very high spatial (~0.3nm) and chemical (~1ppm) resolutions, analyses on the atomic scale are possible [170]. Compared to other analytical techniques, this technique has several advantages (Figure 3.1). APT has a comparable spatial resolution but higher chemical detection ability than electron microscopy techniques (e.g. TEM and STEM). In comparison with SIMS and time-of-flight SIMS, despite having worse sensitivity, the capability to produce a nanometre scale 3D representation of the chemistry of the specimen is unique to APT.

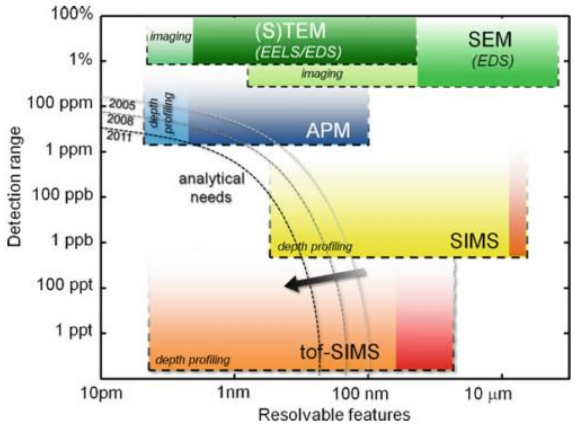


Figure 3.1: Detection range and spatial resolution limits of various analytical techniques [169].

3.1.2. Instrument development

The history of APT began in 1935 when Muller built the field electron emission microscope that provided nanoscale topographical information about the surface of the specimen [171]. A later development of this microscope was the invention of the field ion microscope (FIM) in

1955 [171,172]. FIM is based upon the phenomenon of field ionisation; the ionisation of atoms of an imaging gas from the surface of specimen by an intense electric field. The gas atoms that are attracted to the sawtooth-shaped specimen, field evaporate from sites of high local electric field and are projected onto a detector. Although this technique enables the detection of the position of surface atoms, chemical information is very limited [169].

To obtain the chemical identity of the sample atoms field evaporated from the surface by a higher applied field, the 1D atom probe was developed in 1967 by combining FIM and a time-of-flight mass spectrometer [173]. The next major advances were introduced in the second generation of atom probes by Cerezo et al.; the 3D atom probe (3DAP) in 1988 [174]. 3DAP uses a position-sensitive digital detector that enables the collection of millions of ions with both their chemical identity and original location in the sample recorded [174]. This enabled the first 3D atom-by-atom reconstruction of the data, or atom probe tomography. Initially the application of APT was limited to metals and alloys, but when reliable laser-pulsing was incorporated to the apparatus the analysis of non-metallic materials such as semiconductors was made possible [175]. The latest generation of atom probe microscope is the Local Electrode Atom Probe (LEAP^{TM}), which was commercially introduced in 2003 and has continued to develop since this time (Section 3.1.4) [171,176].

3.1.3. Working principle

In APT, a needle-like specimen is subjected to a potential sufficient to field evaporate atoms in the vicinity of the tip. Field evaporation refers to the ionisation and ejection of atoms from their lattice under a sufficiently intense electric field. The evaporation field (F) is given as [169]:

$$F = \frac{V}{kr} \tag{3.1}$$

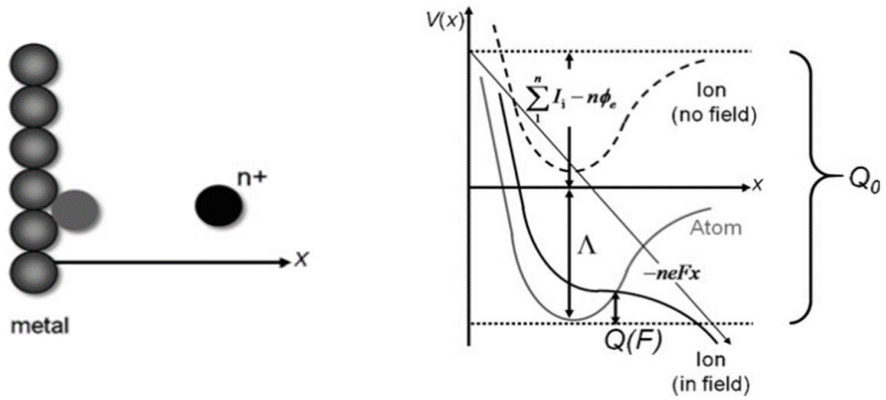
where V is applied voltage, k is a geometrical parameter that describes the shielding of the electrical field caused by the shank (typically ~3.3), and r is the radius at the apex of the tip.

Two models have been proposed to explain the field evaporation mechanism thermodynamically; the image hump and charge draining models [169,177,178]. The image hump model assumes that the atoms are ionised at a critical distance when leaving the surface [177]. The more widely accepted theory is the charge draining model which assumes that the the charge is progressively drained out of the atoms while they are evaporated [178].

Both models share a fundamental similarity whereby an activation energy barrier (Q(F)) has to be overcome in order for atoms to escape from the surface (Figure 3.2a-b) [169]:

$$Q(F) = Q_0 - \sqrt{\frac{n^3 e^3}{4\pi\varepsilon_0} F} \tag{3.2}$$

Q_0 is the energy of species under no electric field, n is the charge state, e is the electronic charge, and ε_0 is the dielectric permittivity of vacuum.



(a) (b)

Figure 3.2: (a) The field evaporation process according to the image hump process where an adatom (grey) is ionised (black) and (b) the atomic and ionic potential energy diagram with and without electric field [169].

In APT, field evaporation can be induced by two mechanisms, either voltage or laser pulsing [6,169]. The pulsing is done such that no more than 1 ion per pulse is evaporated in order to

enable the reliable detection of as many ions as possible by time-of-flight mass spectroscopy. In voltage mode, pulsed voltage is added to the standing DC voltage on the specimen, creating an electric field that results in field evaporation. On the other hand, laser pulsing utilises the laser to heat the specimen without changing the electric field (Figure 3.3). The laser pulse supplies an ultra-fast pulse of thermal energy for surface atoms to overcome the barrier to field evaporate [169,179].

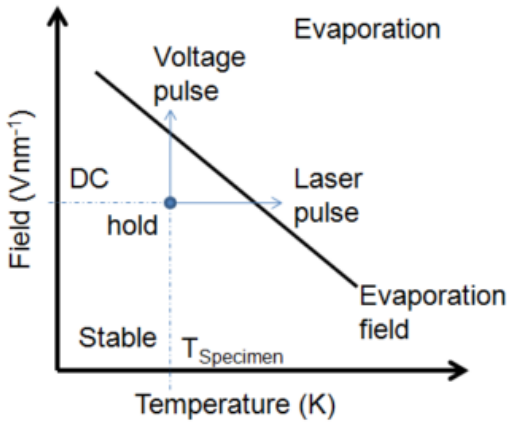


Figure 3.3: Schematic diagram of field- and temperature-induced evaporation. The evaporation field line is the minimum threshold for field evaporation. The blue dot corresponds to the standing voltage of the pulsing cycle, while the blue lines show the direction of voltage (vertical) and laser (horizontal) pulses [6].

Field ionisation is a quantum mechanical process [169]. As the ions travel away from the specimen as a singly-charged species, they can be further post-ionised, and so the same elemental (or molecular) ions can be created in different charge states [169,180]. One can use the Kingham diagram (Figure 3.4) to predict the ratio of ions with different charge states at a given evaporation field [180,181].

As ions are collected, the specimen becomes blunter and requires a higher voltage to maintain the intense electric field required for field evaporation. However, at constant evaporation rate (fraction of detected ions per pulse) the voltage increase can result in electrostatic pressure and eventually stress around the apex of the tip [182,183]. This stress can be several GPa

[182,183]. This build-up of the stress could ultimately result in mechanical failure of the specimen [169].

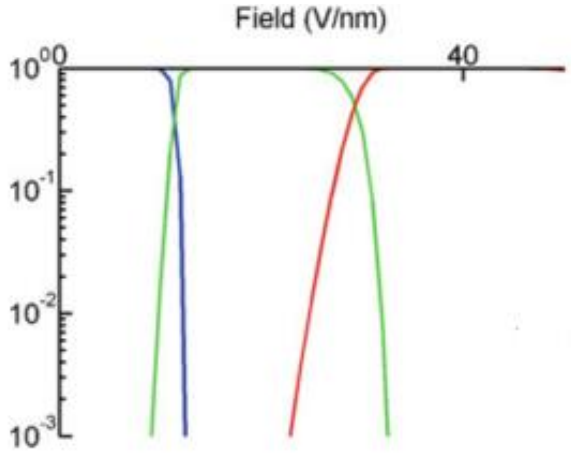


Figure 3.4: Kingham diagram of Zr metal. The blue, green, and red curves correspond to +1, +2, and +3 states respectively [169,181]. The y-axis is the fraction of total evaporated ions with a given charge state.

3.1.4. Local Electrode Atom Probe (LEAP)

In this study, most experiments were carried out using a CAMECA LEAP 3000HR. The instrument consists of three main chambers where specimens are stored at decreasing pressures. The first chamber is a load lock that pumps down the pressure from atmospheric to $<5x10^{-6}$ torr. After that, the specimen is transferred to a buffer chamber until the pressure is $<5x10^{-8}$ torr, and subsequently to the analysis chamber where the experiment is carried out at a vacuum of $\sim10^{-11}$ torr. The ultra-high vacuum pressure is necessary to minimise the gaseous atoms in the analysis chamber that can be attracted to the tip and detected as noise. Furthermore, the sample is typically cooled to cryogenic temperature (~20-60K) to minimise diffusion of atoms on the specimen surface.

There are several key components in the LEAP instrument (Figure 3.5). Firstly, the local electrode is 20-50 μm in diameter and the specimen is positioned less than one aperture diameter away from it [171]. Because the distance between local electrode and specimen is so

short, the path over which ions are accelerated is also short and therefore this arrangement can improve both the mass resolution and field of view to ~100nm [6,171]. This configuration also decreases the standing voltage required for field evaporation and results in less stress being generated on fragile specimens [6].

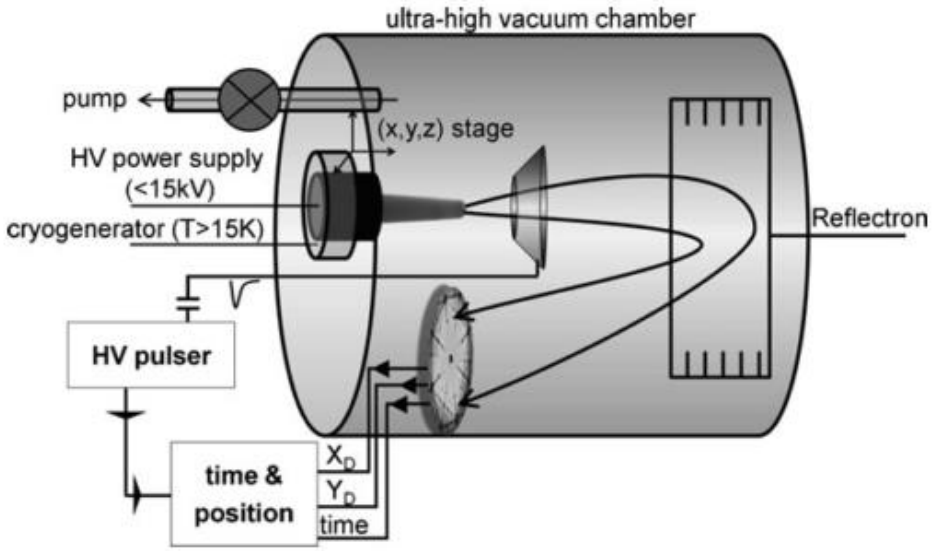
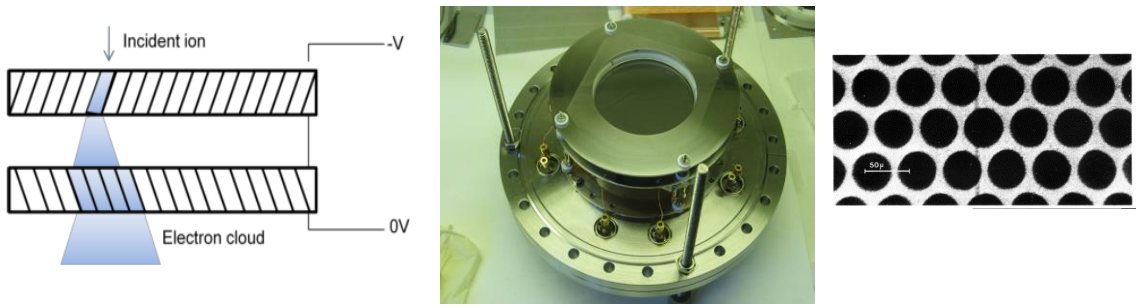


Figure 3.5: Simplified schematic of a LEAP incorporating a reflectron [169].

Another important feature is an electrostatic lens called the reflectron which deflects the ion flight path such that ions with the same mass-to-charge-state ratio but different initial kinetic energies can hit the detector at the same time [169,184]. In the voltage mode, ions with the same mass-to-charge-state ratio can acquire different energies from the voltage pulse, and therefore have different velocities and time-of-flight to the detector. This is compensated by the reflectron as ions with greater energy travel further than the ones with lower energy. In laser mode, this is not the case because the specimen voltage remains constant. Although reflectron can also alter the spatial position of ions, this problem is overcome in the LEAP system where a large angle reflectron compensator (LARC) with long flight path is used [171]. The long flight path is beneficial in improving the mass resolution in both voltage and laser modes. For illustration, consider two ions with slightly different mass-to-charge-state ratios that should hit the detectors at different times. The time difference is important because

if it is too small, the atoms might be detected as the same species, with the same mass-to-charge-state ratio. The longer flight path will lengthen the time difference of these ions resulting in sharper peaks and therefore, improve mass resolution in laser mode [185].

The LEAP detectors consist of two parallel microchannel plates (MCPs) that serve as a signal amplifiers, situated behind delay-line detectors (DLDs) (Figure 3.6a-b) [6,176]. MCPs contain an array of electron-multiplier channels where cascades of electrons are generated by an incident ion. An electron cloud is created at the gap between the two MCPs to amplify the incident ion signal. However, the drawback of this design is that ions arriving at the open area of the MCP between the channels are not detected. This is a stochastic process independent of the chemical identity of the ions. The MCP itself has an efficiency of 57%, but the mesh used in the detector design decreases the efficiency further to ~38% for a reflectron-fitted LEAP (Figure 3.6c) [6,169].



(a) (b) (c)

Figure 3.6: (a) A schematic diagram of chevron MCP arrangement [6] and (b) the physical appearance of APT detectors, and (c) the mesh of an individual MCP detector (courtesy of Oxford APT group).

There are three DLDs to determine the coordinates of incident ions, each containing of parallel delay lines (Figure 3.7). The first two are stacked in orthogonal fashion such that four signals are obtained from an individual ion at the end of the pair of delay line, which are used to calculate the x and y coordinates of the ion of interest [176]. The third DLD is assigned to correct multiple hit events where more than one ion hits the detector from the same evaporation pulse [176].

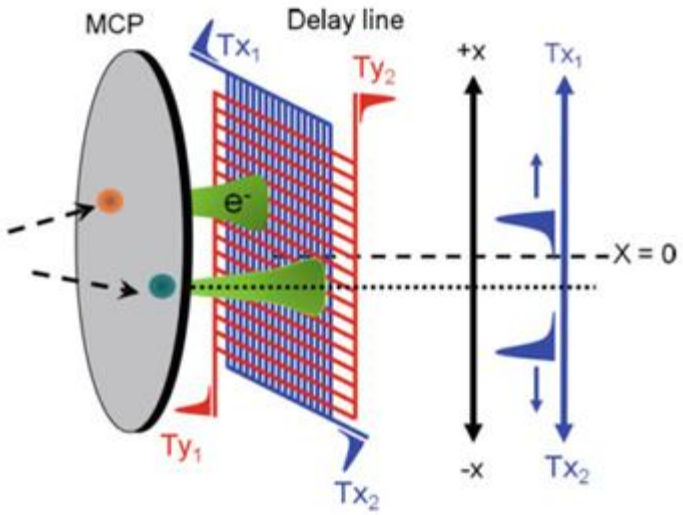


Figure 3.7: DLDs configuration showing the principle by which the position of an ion impact is detected [169].

3.1.5. Tomographic reconstruction

Once evaporated, ions are accelerated by an electric field and strictly follow the electric field lines [169]. Although there are several proposed hypotheses regarding the model of ion projection, the point-projection model is commonly used [169,186,187] (Figure 3.8). This model assumes that the ion trajectories are straight lines originated from a single point inside the tip beneath the centre of a hemispherical cap (O) with radius R, and this point is called the projection point (P). The distance between this point and the apex of the tip is expressed in terms of a fraction of the tip radius: ξR, known as the image compression factor. It depends on the local electric field and tip geometry.

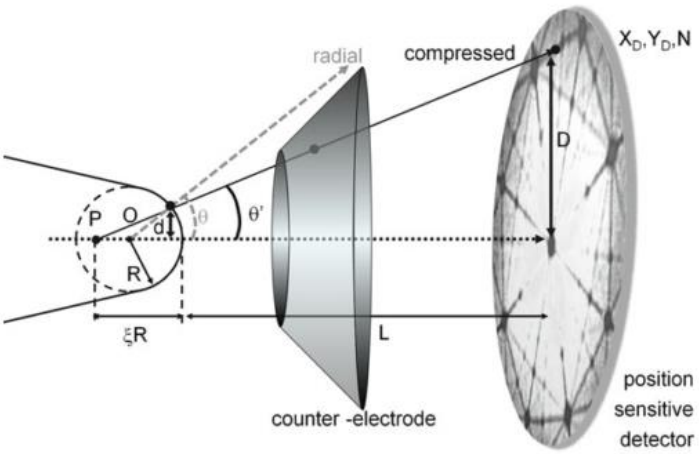


Figure 3.8: Point-projection model schematic diagram.

The reconstruction turns the 2D detector information into a 3D atomic image and is carried out atom-by-atom by the reverse projection of the detected position onto a surface of the reconstructed specimen [169]. There are several assumptions in tomographic reconstruction. Firstly, that the tip geometry is hemispherical, which is not always the case in actual specimens. To account for this, an image compression factor is introduced. Secondly, it also assumes the shell model where only protruding atoms at the surface are evaporated, atom-by-atom and layer-by layer. The DLDs record the coordinates of each ion (X_D,Y_D) (Section 3.1.4) [176,188]. The z coordinate is obtained from the detection sequence of evaporated atoms [169].

Several artefacts in APT reconstructions are associated with how the atoms are evaporated, as illustrated in Figure 3.9. For example, the roll-up effect refers to the surface migration of atoms, resulting in atoms of interest detected at incorrect positions [189]. Trajectory aberrations are where atoms can be evaporated with paths that depend on local electric field differences, causing density variations across one dataset, e.g. at crystallographic poles.

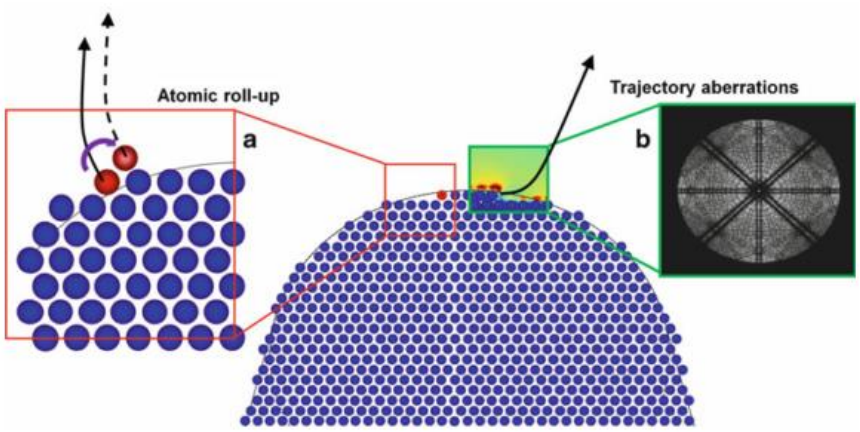


Figure 3.9: Schematic diagram of (a) roll-up effect and (b) trajectory aberrations [169].

Trajectory aberrations can also occur when evaporating precipitates that can have either higher or lower evaporation field compared to the matrix (Figure 3.9) [169]. In the former case, because the precipitate is easier to field evaporate a flattening of the hemispherical surface occurs, and ions are deflected inwards relative to the precipitate, resulting in an apparently higher density precipitate in the reconstruction. The opposite occurs for a high-field precipitate, where the apparent precipitate density is lower than the matrix.

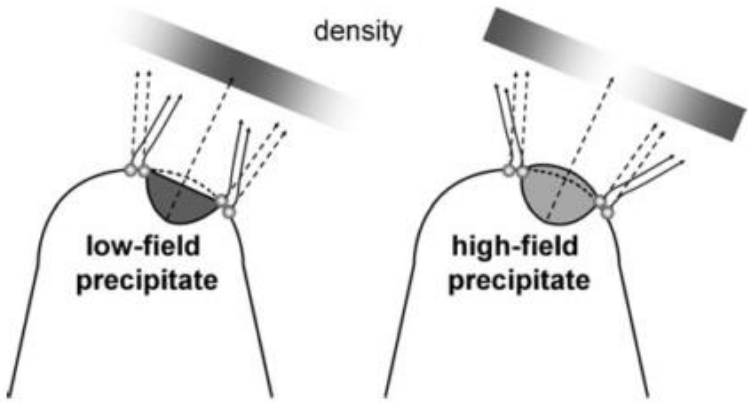


Figure 3.10: Trajectory aberrations occurring when field evaporating low- and high-field precipitates [169].

Another effect causing spurious local density variations is called preferential retention where atoms that requires higher field evaporation compared to their neighbours remain on the surface after the neighbouring atoms are already evaporated, e.g. at grain boundaries [169,190].

3.1.6. Mass spectrum

Each detected ion can be directly correlated to the voltage or laser pulse that triggered its evaporation. Hence its time of flight (t) can be measured for each detected event. By assuming that the potential energy is converted into kinetic energy, the mass-to-charge state ratio of each ion can be determined [169]:

$$\frac{m}{n} = \frac{2eVt^2}{d^2} \tag{3.3}$$

where m the mass of ion and d is the flight length. This allows element identification when a mass spectrum containing the mass-to-charge-state ratio of all ions is created.

The evaporated ions can be in the form of either elemental or molecular ions. When analysing a mass spectrum these ions form peaks at the position corresponding to their mass-to-charge-state ratios. The elements constituting the ions can be identified by the natural isotopic abundance ratios that act as a fingerprint for each ion. Because APT collects atoms from the specimen that are detected individually, very good isotopic abundance ratios can be achieved. Often one peak contains more than one species of ion with the same mass-to-charge-state ratio and in this case, the contribution of each species must be accounted for. This separation process is called deconvolution.

In mass spectrum examination, it is important to define where a peak starts and ends. This is called ranging. Ranging is a crucial part of the data analysis process because different ranging methods result in different compositional results. Consistent ranging is required to obtain the most accurate compositional analysis. Although there continues to be discussions about establishing standard ranging guidelines, agreement is yet to be reached [169]. Therefore, normally the ranging is determined by user experience. For specific materials, I describe the ranging used for my samples in Section 3.2.3.2.2.

3.2. APT of zirconium and its oxide

This section is about the experimental aspects of APT that are specific to the materials studied in this thesis; Zr-Nb alloys and oxide. The understanding of these aspects is crucial for interpreting the results in Chapters 5-9.

3.2.1. Specimen preparation

3.2.1.1. Electropolishing

Electropolishing was carried out only for unoxidised as-recrystallised and annealed Zr-1Nb metal samples. Initially, a matchstick-shaped specimen with square cross section ~0.3x0.3mm is prepared by low-speed saw cutting from a sheet sample. Attempts to prepare specimens by the drop polishing method using the electropolishing ring were unsuccessful, probably due to excessive preferential etching, resulting in blunt tips. Therefore, the modified double layer method was employed [169].

This method consists of two stages, both with the same configuration (Figure 3.11). The first stage is carried out where the mid-section of the blank specimen is exposed to 25% perchloric acid (60%) + 75% acetic acid (100%) electrolyte with an applied AC voltage of ~15V floating on top of Galden, a perflourinated polyether (PFPE) as an inert solution. An up and down motion is carried out such that a neck is created. In the second stage, the electrolyte is 10% perchloric acid (60%) + 90% acetic acid (100%). As perchloric is a stronger acid than acetic acid, the reduction of perchloric acid concentration is intended to achieve slower polishing. The voltage is also decreased to ~10V at the start and can go down further to ~5V depending on the thickness of the neck. An up and down motion is also required to prevent preferential etching, and the process is finished when the sample breaks into two halves.

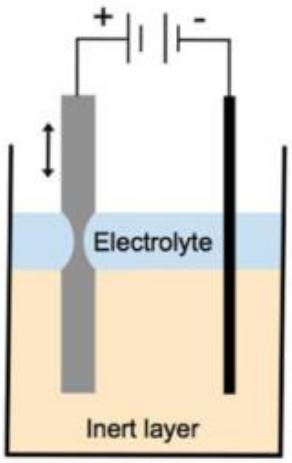
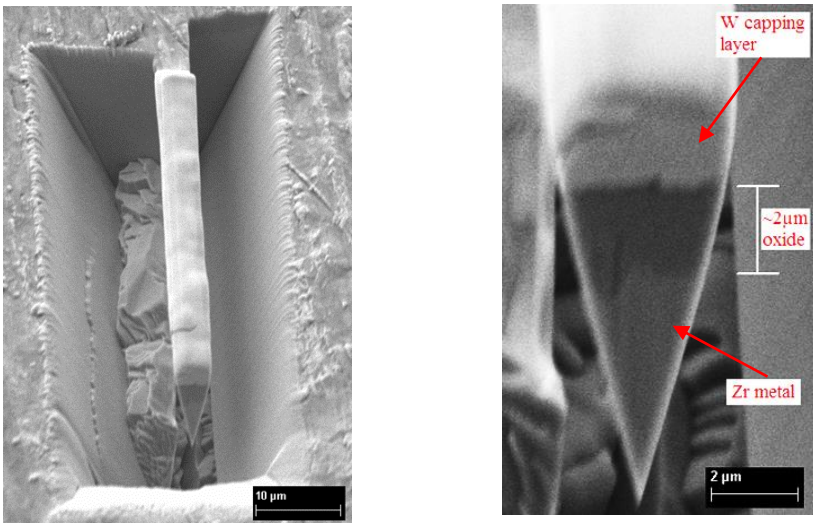


Figure 3.11: The configuration of double layer electropolishing method [169].

3.2.1.2. Focussed ion beam (FIB) liftout

This process was carried out using a Zeiss Nvision 40 FIB-SEM dual beam microscope mainly for oxide analyses [191]. The oxide, metal and O/M interface are of interest. Due to the presence of cracks and pores at the outer part of the oxide, oxide analyses are carried out within ~600nm of the O/M interface, and so sawtooth-shaped samples must be prepared with the apex in this region of the sample.

Specimens are manufactured with the interface perpendicular to the tip axis. The first step of this technique is to make a prism-shaped cantilever bar with triangular cross section (Figure 3.12). Initially, a tungsten capping layer ~1-2µm thick is deposited at the top of the oxide. Then trenches are milled such that the prism is 2-4µm wide, 35-55µm long and 2-12µm high. If the prism is too long or too high, it will be difficult to liftout and hence it is important to control the prism geometry.



(a) (b)

Figure 3.12: (a) A cantilever prism with O/M interface perpendicular to the normal axis and (b) its cross section containing an ~2µm oxide. The material is 30-day oxidised annealed Zr-1Nb.

When analysing the oxide, it is important to know the location of analysis relative to the O/M interface, and therefore the metal has to be included in the prism. However, this is difficult when the oxide is very thick (above ~7µm). In this instance, no capping layer is applied, and the outer part of the oxide can be milled down to leave 2-4µm oxide near the O/M interface. As a result of milling away microns of oxide, especially when using a relatively high milling current, the top of the prism can become uneven, but this should not cause problems because the region of interest is at least 1µm away from the top of the prism (Figure 3.13).

The prism is subsequently cut free from the remaining material and lifted out by a micromanipulator (Figure 3.14a-b). In this stage, an atom probe coupon is inserted into the microscope. This coupon is an array of 36 silicon posts, each having a circular cross section ~2µm in diameter. The prism is positioned in contact with the top of the post, welded and cut free to make a wedge. This procedure is repeated for the remainder of the prism until the desired number of samples is produced. After that, each wedge is welded again on the other side to fix it firmly to the post.

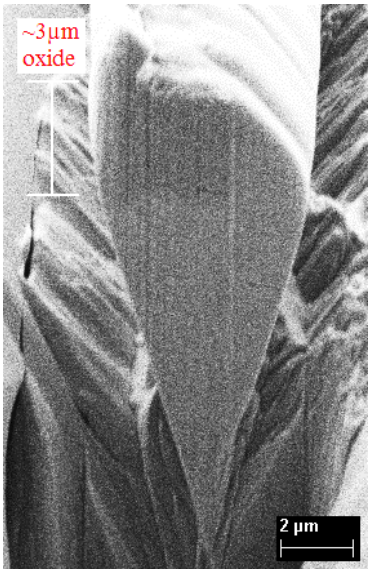
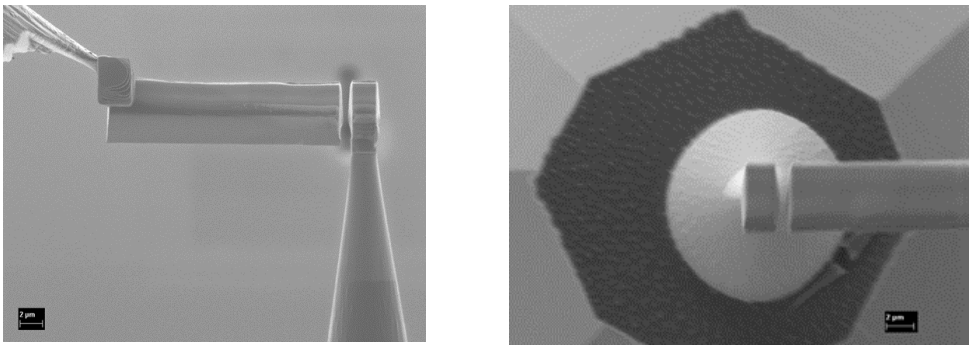


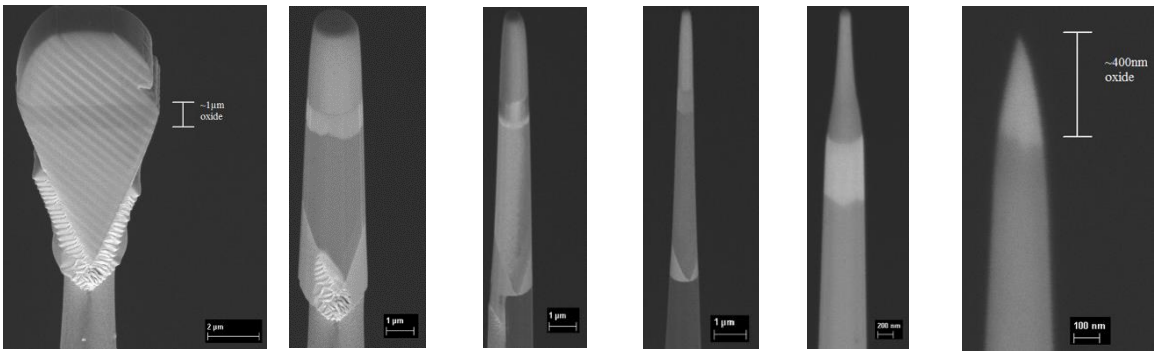
Figure 3.13: A cross section of cantilever prism containing ~3µm thick oxide. The material is 1040-day oxidised Zr-2.5Nb with original oxide thickness ~12µm.



(a) (b)

Figure 3.14: The mounting process taken by (a) the FIB and (b) SEM.

In the final stage, annular milling with decreasing inner diameter and milling current is carried out to create a needle with tip diameter ~100nm (Figure 3.15a-f and Table 3.1). This is then milled down until the desired oxide thickness is reached and the tip diameter is reduced further. Typically for oxide analysis, the remaining oxide thickness is ~500nm and for O/M interface analysis is ~100-200nm. At the end of the process, a final milling at 5kV then takes place to clean the sample from gallium contamination.



(a) (b) (c) (d) (e) (f)

Figure 3.15 An example of the sequence of tip sharpening for oxide analysis ~400nm away from O/M interface: (a) initial sample containing ~1µm oxide, and (b-e) sequential annular milling with decreasing inner diameter to produce (f) the final tip with ~400nm oxide. The material is 15-day oxidised Zr-1Nb-0.1Sb.

Table 3.1: Tip sharpening details.

Stage	Outer/inner diameter (µm)	FIB current (pA)	Voltage (kV)	Comments
1	6/2	700	30	Tip shaping
2	3/1	300	30	
3	2/0.7	150	30	
4	1.5/0.5	80	30	Tip sharpening, diameter ~100nm
5	1/0	40	30	Further sharpening and milling down the oxide
6	1/0	250	5	Cleaning

3.2.2. Experimental conditions

All datasets in this study are obtained from laser mode atom probe analyses. Most samples were run in the temperature range 50-55K and laser energy 0.4-0.55nJ, while the pulse frequency is maintained at 200 kHz. These conditions are similar to those reported for Zr sample in the literature [6,192].

When an analysis is carried out using a constant laser energy, the evaporation rate is increased by increasing the standing voltage. Because oxide is brittle, for oxide analysis the

evaporation rate has to be maintained at a relatively low value, no more than 0.2%. This means that 400 ions are expected to be detected per 200000 laser pulses in one second. Above 0.2% evaporation rate, the specimen is much more likely to fracture prematurely. On the other hand, metal samples can withstand a rate even up to 1.0%, but during my experiments the rate was controlled between 0.2-0.5% depending on the voltage.

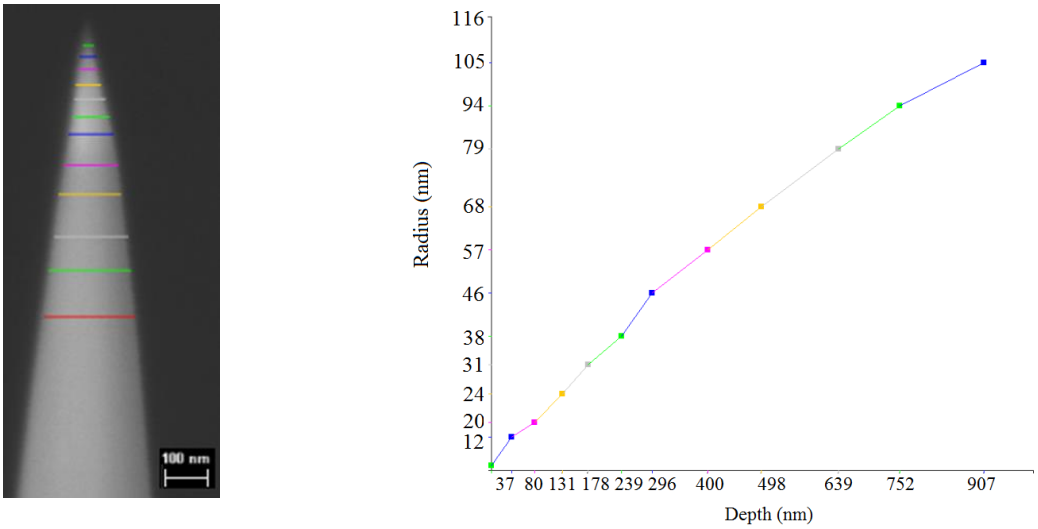
3.2.3. Data analysis

3.2.3.1. Reconstruction methods

In this study, the reconstruction process is done using IVAS software. Data are reconstructed using either the voltage-based method or using SEM images. The voltage-based method uses Equation 3.1 to estimate the instantaneous radius of curvature with k=3.3, which is a default value from IVAS. The latter method uses an SEM image of the tip from the FIB-SEM to model the reconstructed data. These techniques have their own limitations especially when analysing the O/M interface. As the evaporation approaches the interface, there is a voltage instability as the oxide has higher evaporation field than the metal. This is not taken into account in the voltage-based reconstruction. In addition, if during an experiment, the user manually changes the voltage, this will be regarded by the reconstruction software as a change of radius of curvature.

In general, the SEM-based reconstruction gives a reasonably good profile of the original tip (Figure 3.16a-b). The limitation of this method is that if the tip diameter is very small, the tip apex can be electron transparent and so not visible in the SEM image. Furthermore, the reconstruction assumes that the tip is always hemispherical throughout the experiment (Section 3.1.5) [169]. This is not necessarily the case in practice and hence, any deviation from the hemispherical shape can lead to artefacts in the 3D reconstruction of LEAP data. In

this study, most of O/M interface reconstructions are based on SEM images due to the change in evaporation field between the metal and oxide.



(a) (b)

Figure 3.16: An example of SEM-based reconstruction: (a) an SEM image of a tip with horizontal lines to model the tip profile and (b) the width of each line plotted against the corresponding depth. The line colours in (a) correspond to the data points in (b).

3.2.3.2. Mass spectrum analysis

3.2.3.2.1. Element identification

A mass spectrum contains information on the mass-to-charge-state ratios of all detected ions. Ions can have different charge states that each gives rise to individual peaks. All of these peaks are taken into account in the compositional analysis. When analysing the sample volume around the O/M interface, different regions in the datasets can be identified based on the nature of the evaporating ions (Figure 3.17). These ions can be either elemental or molecular, e.g. bulk ZrO_2 is mostly ionised as $ZrO^{1,2,3+}$ and O_2^+ with a ratio of roughly 2:1. This can be seen when analysing an O/M interface where in the oxide, the $ZrO^{1,2,3+}$ and O_2^+ signals dominate. This has been previously reported in ZrO_2 [192].

In the metal adjacent to O/M interface there is usually an O-saturated metal region ($Zr(O_{sat})$) where the O_2^+ signal rapidly decreases and $Zr^{1,2,3+}$ ions start to appear such that the $ZrO^{1,2,3+}$: $Zr^{1,2,3+}$ ratio is roughly 1:1. Moving away from the interface, the O_2^+ and ZrO^{2+} signals then gradually decrease, while $Zr^{1,2,3+}$ are the majority ions in the metal. Unlike in the oxide, the $Zr^{1,2,3+}$ signals from the bulk metal can exhibit low density regions at crystallographic poles due to trajectory aberrations (Section 3.1.5).

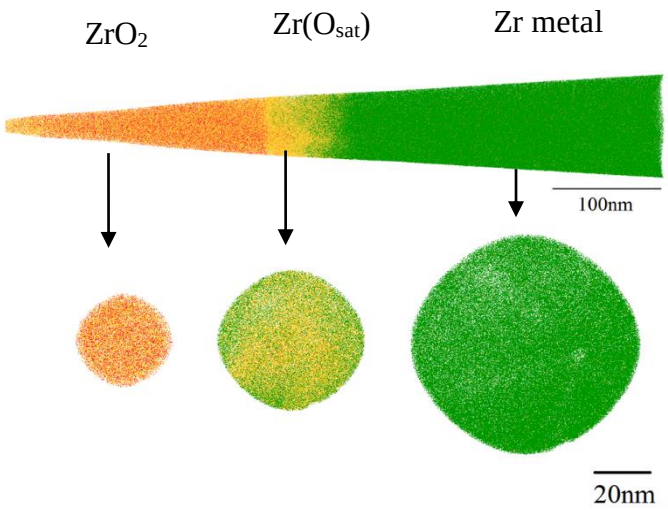


Figure 3.17: Evaporation of the matrix atoms across the O/M interface and thin slices of the tip in different regions. The red, yellow, and green dots correspond to O_2^+, $ZrO^{1,2,3+}$, and $Zr^{1,2,3+}$ ions respectively.

Zr has 5 isotopes: ^{90}Zr, ^{91}Zr, ^{92}Zr, ^{94}Zr and ^{96}Zr and all of them appear in the bulk metal mass spectrum with charge states +1, +2 and +3 (Figure 3.18) [6]. Apart from Zr- and Nb-containing signals, a typical bulk Zr-Nb metal mass spectrum also contains impurities such as H, O, Fe, C, Al, N and occasionally Cr (only inside SPPs). For specimen prepared by FIB, there are also $Ga^{1,2+}$ peaks. Data analysis concerning both the Fe and Nb signals is discussed in Section 3.2.3.2.2.

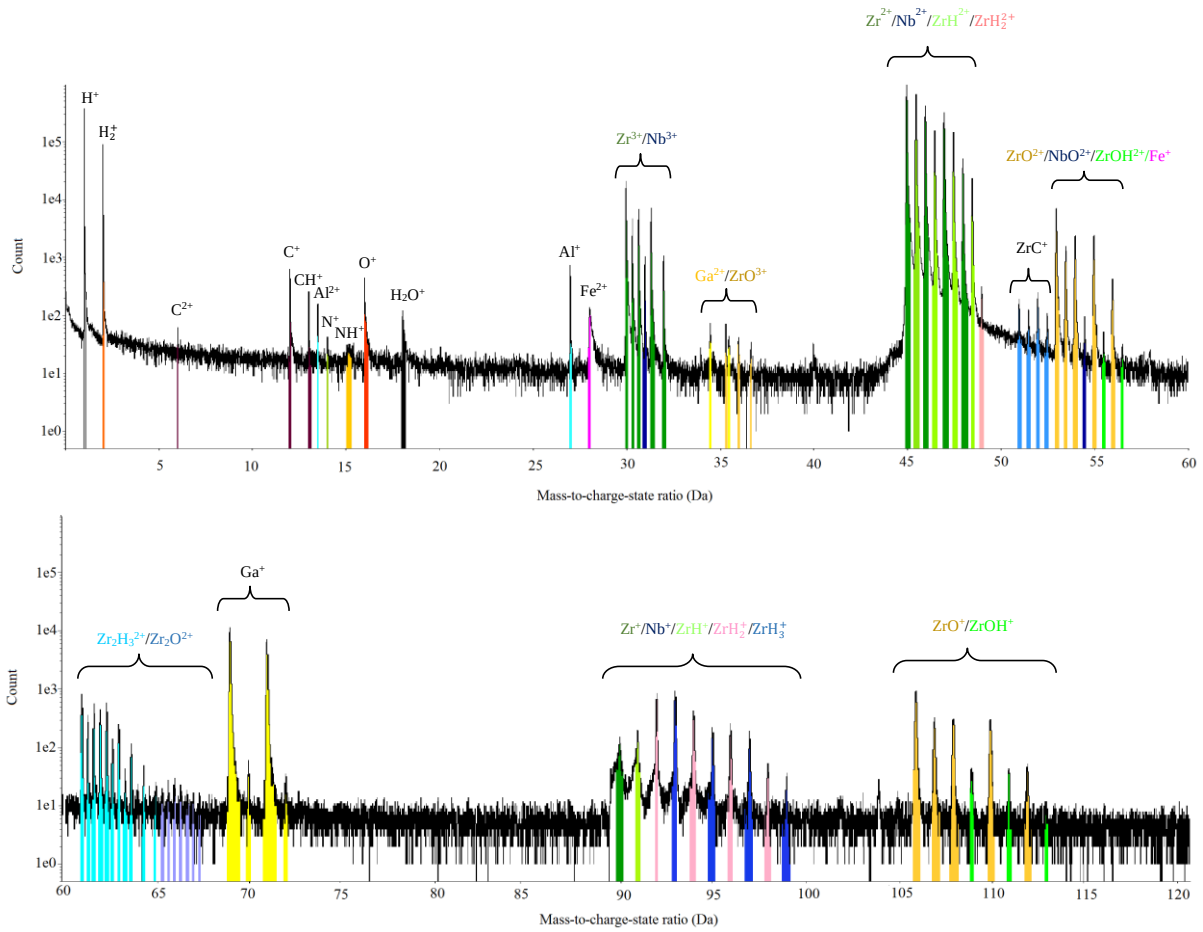


Figure 3.18: A typical Zr-Nb bulk metal mass spectrum from a sample prepared by FIB. Overlapping peaks are ranged as the majority species, and labelled according to their respective colours. The ranging system is used for a typical analysis according to the ranging guidelines in Section 3.2.3.2.2, with exceptions of H^+, H^{2+}, H_2O^+, and $Ga^{1,2+}$ that are ranged only for introduction purposes and the hydride peaks of which the hydrogen is excluded.

ZrO_2 is a poor thermal conductor and hence when exposed to a laser pulse the heat is not dissipated rapidly to the metal substrate [6]. As a result, the tip stays hotter for a longer duration such that field evaporation can still occur after the pulse. As shown in Equation 3.3, the detected mass-to-charge-state ratios of these ions is then higher than it should be. In the oxide mass spectrum, this effect is seen in the form of thermal tails, and usually is more pronounced in the matrix-atom-containing species (Figure 3.19). This gives rise to different ranging methods when analysing the oxide and metal (Section 3.2.3.2.2). Apart from $ZrO^{1,2,3+}$, the oxide matrix could be evaporated in different species but the quantity of these ions is relatively small.

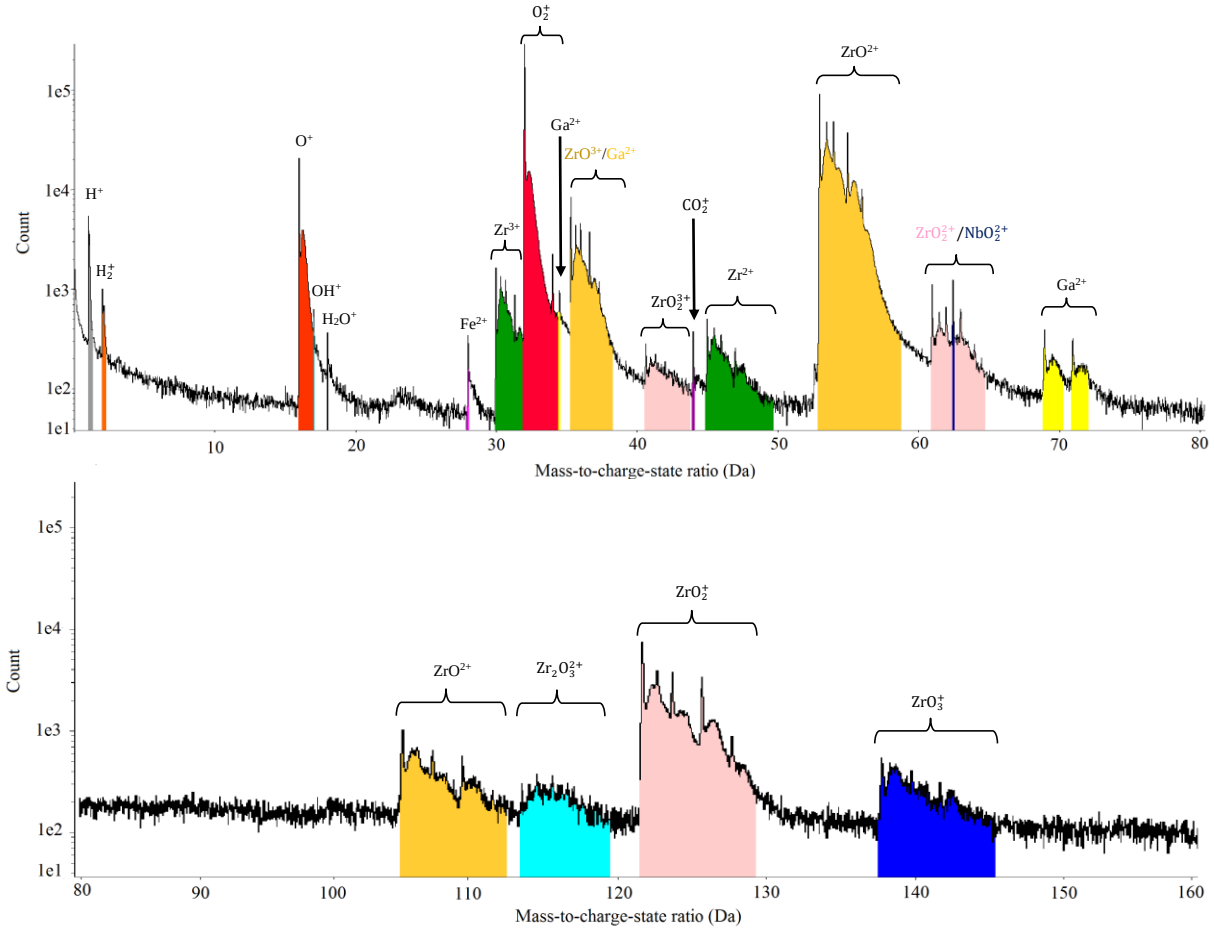


Figure 3.19: A typical mass spectrum of ZrO_2. Overlapping peaks are ranged as the majority species, and labelled according to their respective colours. The ranging system is used for a typical analysis according to the ranging guidelines in Section 3.2.3.2.2, with exceptions of H^+, H^{2+}, OH^+, H_2O^+, and $Ga^{1,2+}$ that are ranged only for introduction purposes.

3.2.3.2.2. Ranging

In both metal and oxide mass spectra, there are peak overlaps that need to be ranged and deconvoluted appropriately. In IVAS software, there is an automated peak decomposition feature that allows the deconvolutions of background-substracted peaks. The number of ions in each peak is calculated to satisfy the natural isotopic abundancy ratios.

If a peak contains more than two species, the majority species is chosen to represent the peak. For example, the 46Da peak containing both ZrH^{2+} and Nb^{2+} is ranged as either ZrH^{2+} or Nb^{2+} depending on consideration of the whole analysis. If the dataset of interest does not

contain Nb-rich features (clusters or precipitates), this peak normally contains mostly ZrH^{2+}, and will be ranged as such. However, if the dataset contains Nb-rich features that are usually metallic in nature, then this peak will likely to contain more Nb, and in this case it will be ranged as Nb^{2+} rather than ZrH^{2+}.

The atom map can only display atoms from the ranged peaks, and therefore it cannot separate the signals of different species occupying the same peak. If both species demonstrate different distribution, it is possible to partially differentiate them. This can be done by isolating the regions where one of the species segregates, and doing the necessary analysis on those regions. For example, if the 46Da peak shows segregation to an SPP, then the atoms that segregate are most likely to be Nb^{2+} rather than ZrH^{2+}. In this case, if a separate mass spectrum of the particle is created, then the 46Da signal will contain much more Nb^{2+} than ZrH^{2+}. However, such a method is not possible for analysing species with similar distributions. For example, in a dataset with no 46Da segregation, it is not possible to display with confidence the distribution of Nb^{2+} or ZrH^{2+} in separate atom maps.

As a general rule, only atoms originating from the specimen are included in the analyses. Because the H signal originating from gas in the vacuum system can be significant if all the H-containing signals are included, H is excluded in all analyses except when examining hydrogen/deuterium (Chapter 6). Ions from common adsorbate gases such as CO^{+} and CO_2^{+} are also not ranged because their atoms are more likely to be from the gases rather than the specimen. $Ga^{1,2+}$ peaks are not ranged either as they originate from the FIB sample preparation. Generally the Ga content in the specimen is below 1 at%.

Under the experimental conditions described in Section 3.2.2, a metal mass spectrum contains well-defined peaks, and except for Fe all peaks are windowed from beginning to the end of the peak (Figure 3.18). On the other hand, the bulk oxide mass spectrum has

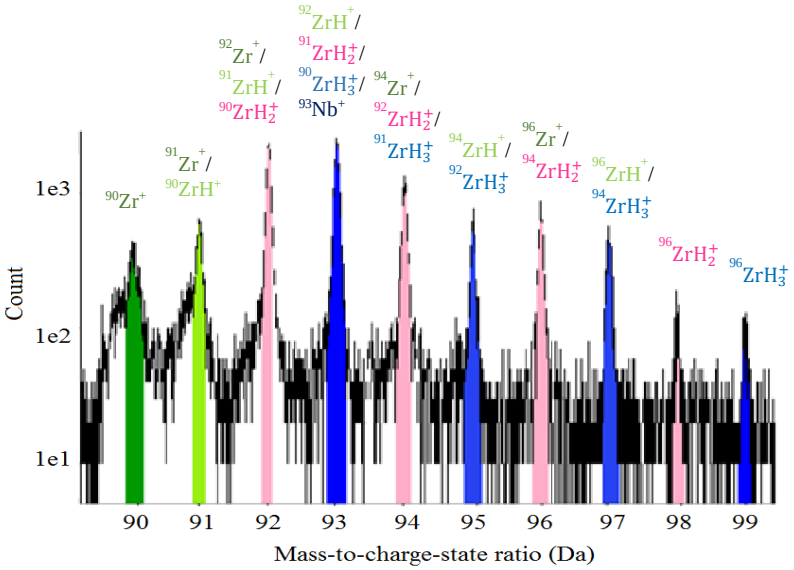
significant thermal tails that have to be treated differently (Figure 3.19). A more believeable composition with Zr:O ratio close to 1:2 is obtained when the tails are ranged. If only the peak area is ranged, this will give incorrect Zr:O ratio close to ~3:1, even though the bulk oxide must be close to ZrO_2 stoichiometry.

Nb is monoisotopic (^{93}Nb), but because Zr hydride molecular ion peaks occur in all datasets and overlap with $Nb^{1,2,3+}$, deconvolution is required to calculate its overall composition. In the metal, Nb is mainly detected as $Nb^{1,2,3+}$ and NbO^{2+}. However, only the Nb^{3+} peak contains entirely Nb. NbO^{2+} overlaps with $^{92}ZrOH^{2+}$, while both Nb^{+} and Nb^{2+} overlap with $^{92}ZrH^{+}$ and $^{92}ZrH^{2+}$ respectively. In some cases they can also be affected by the presence of $^{91}ZrH_2^+$ and $^{91}ZrH_2^{2+}$ ions. Therefore, deconvolution of these peaks is necessary to obtain more precise Nb concentrations.

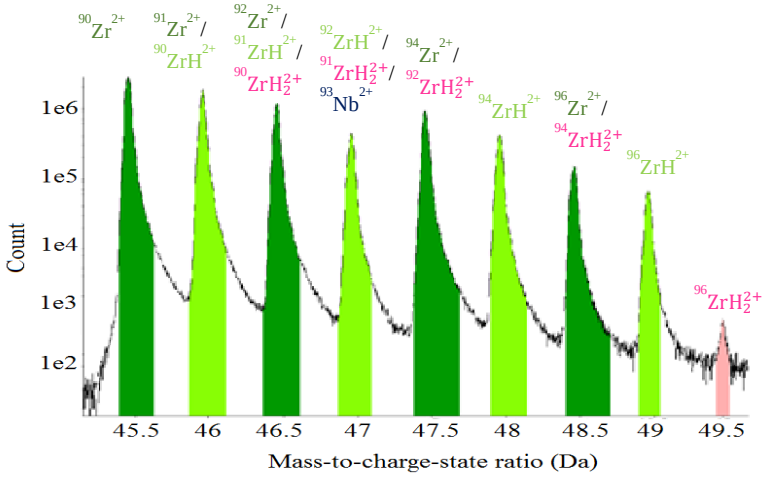
In this section, examples of analysis of typical data from the metal and oxide mass spectra from Figure 3.18 and Figure 3.19 are discussed. The overlapping of Nb^{+}, Nb^{2+}, and NbO^{2+} are illustrated in Figure 3.20a-c. The number of ions contributing to each peak is listed in Table 3.2, Table 3.3 and Table 3.4 respectively. The first set of peak deconvolutions involves 5 ions: Zr^{+}, ZrH^{+}, ZrH_2^+, ZrH_3^+, and Nb^{+} (Table 3.2). In 93Da, Nb^{+} overlaps with $^{92}ZrH^{+}$, $^{91}ZrH_2^+$, $^{90}ZrH_3^+$ and the ratio between these ions is Nb^{+}:$^{92}ZrH^{+}$:$^{91}ZrH_2^+$:$^{90}ZrH_3^+$ = 5.7:7.4:18.0:68.9, implying that Nb^{+} only constitutes 5.7% of the overall peak. Similar conditions are observed in the second peak deconvolutions of doubly-charged ions (Table 3.3), except in this case there is no ZrH_3^{2+} ion. The apparent Nb^{2+} signal (46.5Da) peak only contributes to 6.1% of that peak. In both cases, these peaks are ranged as ZrH_3^+. However, in the peak deconvolution of the doubly-charged oxide ions (

Table 3.4), the Nb-containing peak is the majority species. NbO^{2+} ions (54.5Da) overlap only with $ZrOH^{2+}$ and make up 88.4% of that peak. As $^{58}Fe^{+}$ peak does not appear, the overall contribution of Fe^{+} ions is probably insignificant and thus, is disregarded in

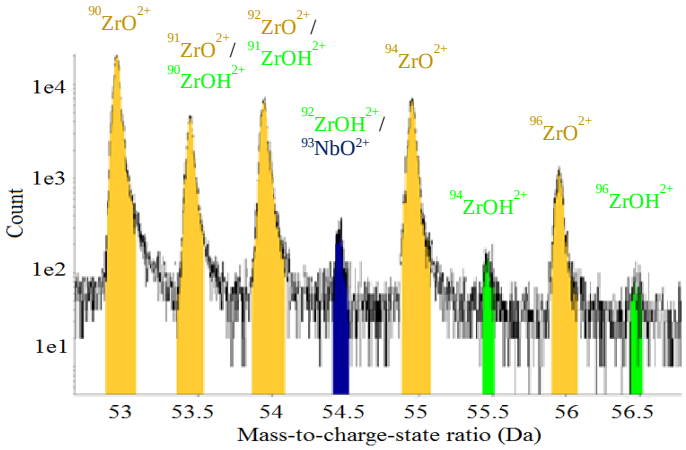
Table 3.4.



(a)



(b)



(c)

Figure 3.20: Typical overlaps of (a) Nb^{+}, (b) Nb^{2+} and (c) NbO^{2+} and Zr-containing peaks.

Table 3.2: Deconvolution of singly-charged ions.

Ions	Number of ions									
	90Da	**91Da**	**92Da**	**93Da**	**94Da**	**95Da**	**96Da**	**97Da**	**98Da**	**99Da**
Zr^+	3446	751	1149		1164		188			
ZrH^+		3125	681	1042		1055		170		
ZrH_2^+			11676	2546	3892		3944		635	
ZrH_3^+				9757	2128	3252		3296		531
Nb^+				806						
Total ions	3446	3876	13506	14151	7184	4308	4132	3466	635	531

Table 3.3: Deconvolution of doubly-charged ions.

Ions	Number of ions								
	45Da	**45.5Da**	**46Da**	**46.5Da**	**47Da**	**47.5Da**	**48Da**	**48.5Da**	**49Da**
Zr^{2+}	6413107	1396463	2136196		2169211		348088		
ZrH^{2+}		1986247	651391	996050		1017064		164390	
ZrH_2^{2+}			31131	7011	13580		10878		1684
Nb^{2+}				65570					
Total ions	6413107	3382710	2818718	1068631	2182791	1017064	358966	164390	1684

Table 3.4: Deconvolution of doubly-charged NbO ions.

Ions	Number of ions							
	53Da	**53.5Da**	**54Da**	**54.5Da**	**55Da**	**55.5Da**	**56Da**	**56.5Da**
ZrO^{2+}	58501	12740	19624		19824		3539	
$ZrOH^{2+}$		250	55	83		84		14
NbO^{2+}				635				
Total ions	58501	12990	19679	718	19824	84	3539	14

Using the deconvolution methods above, it is possible to include explicitly the contributions of all Nb-containing peaks when calculating the metal matrix composition, but this is not the case in the oxide matrix. Due to the overlapping and thermal tails it is not possible to fully deconvolute the overlapping peaks. $Nb^{1,2,3+}$ peaks are associated with metallic Nb and mainly found inside SPPs in the oxide, but are not normally observed from the oxide matrix. All Nb-containing species are included in these deconvolution methods and hence, we can expect reasonably accurate measurements of Nb content in the metal matrix.

Nb in the oxide matrix is evaporated as $NbO^{1,2+}$ and $NbO_2^{1,2+}$, occasionally also $Nb^{1,2,3+}$. $NbO^{1,2+}$, and NbO_2^+ peaks are not always present but overlap with the thermal tails of

$^{90,91,92}ZrO^{1,2+}$ and $^{90,91,92}ZrO_2^+$ respectively, usually making a minor contributions to these peaks. Although there is a mixture of signals inside the thermal tail, because the thermal effect only broadens the peak towards higher mass-to-charge-state ratios, the peaks overlapping with $NbO^{1,2+}$ and $NbO_2^{1,2+}$ are likely to be located in the lower mass-to-charge-state ratios, i.e. $^{90,91,92}ZrO^{1,2+}$ and $^{90,91,92}ZrO_2^+$ respectively. These Nb-containing peaks might overlap with $^{90,91,92}ZrOH^{1,2+}$ and $^{90,91,92}ZrO_2H^+$ ions as well but it is not possible to determine whether there are any H-containing peaks in the thermal tails. However, in most cases neither $NbO^{1,2+}$ nor NbO_2^+ form the majority of their respective peaks.

Fortunately, this is not the case for NbO_2^{2+}, even though it also overlaps with $^{90,91,92}ZrO_2^{2+}$and the thermal tail. This is because the peak height is significantly higher than the thermal tail background, and therefore the assumption is that the entire 62.5Da peak area consists of NbO_2^{2+} (Figure 3.19). Thus, any measured Nb content in the oxide matrix only comes from NbO_2^+. This can ultimately underestimate the measured Nb content in the oxide matrix.

Fe is mainly evaporated as $^{56}Fe^{2+}$ (28Da), from both the metal and oxide. Fe has three other minor isotopes ($^{54}Fe^{2+}$, $^{57}Fe^{2+}$, and $^{58}Fe^{2+}$) but clear peaks from them are not always present. $^{54}Fe^{2+}$ overlaps with monoisotopic Al^+ (27Da). This peak is not always present, but the contribution of $^{54}Fe^{2+}$ to this peak is usually very small as the ratio of $^{54}Fe^{2+}$:$^{56}Fe^{2+}$ = 5.8:91.7. However, the 27Da peak is usually higher than the 28Da one (Figure 3.18), and therefore this peak consists mostly of Al^+. $^{57}Fe^{2+}$ and $^{58}Fe^{2+}$ do not always appear in the mass spectra because the Fe overall concentration is very low (Chapter 7) and their natural isotopic abundances are only 2.1% and 0.28% respectively. Because only $^{56}Fe^{2+}$ is ranged, the Fe concentration values in this thesis is divided by 91.7% (the natural abundance of $^{56}Fe^{2+}$) to account for the contribution of Fe from the other (unranged) Fe^{2+} peaks.

The 28Da peak cannot be considered to entirely contain $^{56}Fe^{2+}$ [6]. In both the metal and oxide mass spectra, this peak is normally broader than the other metallic peaks due to the tail at the end of the peak that gradually decreases towards higher mass-to-charge-state ratios. The tail of the peak does not necessarily originate from thermal effects, because the thermal tails usually consist of a rather sharp first peak followed by a hump (e.g. the $ZrO^{1,2+}$ peaks in Figure 3.19). Obviously, this can also occur in the 28Da peak, especially when analysing oxide but the fact that the broad peak can occur even in the metal mass spectrum indicates that this peak does not only contain $^{56}Fe^{2+}$. Only the beginning of the peak contains significant amount of Fe and the end contains predominantly noise that is presumably CO^{+} (Figure 3.21) [6,192,193]. It is important to range Fe^{2+} as accurately as possible because the overall Fe concentration is very low and improper ranging might cause significant error in the results.

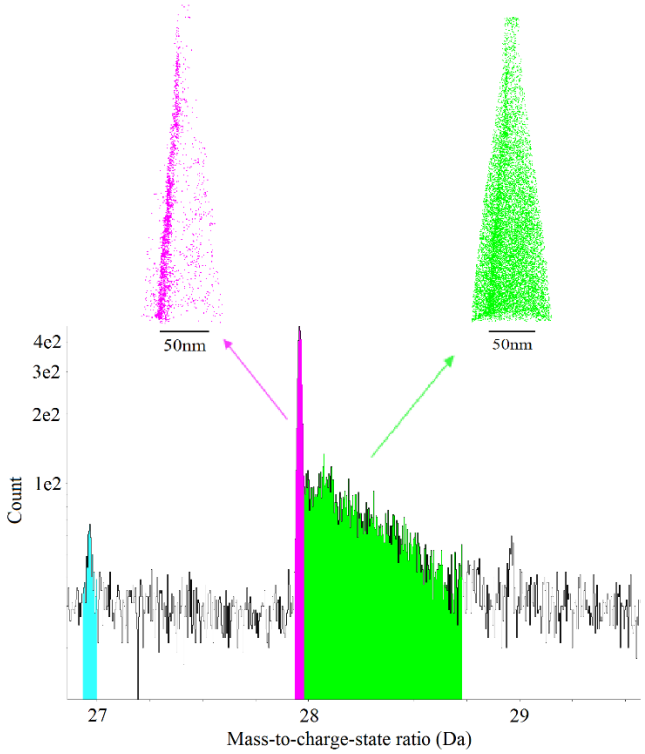
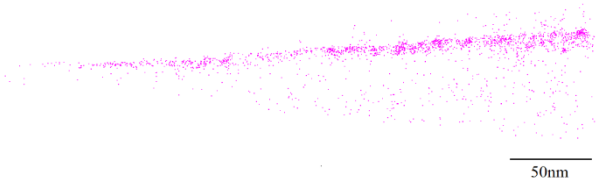
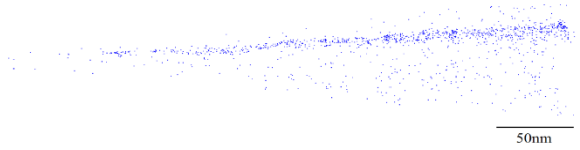


Figure 3.21: The distribution of the peak at 28Da (containing mostly Fe^{2+} (pink)) and tail (mostly CO^{+} (green)) and the different distribution of the 2 parts of the peak can be seen in the atom maps. This dataset contains an Fe-rich grain boundary

It is reported that the Fe from this peak mainly comes from single hit events and CO^+ from multiple hit events [6]. However, this is probably not true because reconstructions of single and multiple hit ions from a dataset where Fe segregates to a grain boundary show similar segregation (Figure 3.22a-b). This should not be the case if CO^+ only comes in multiple hit events as it is not expected to segregate because it is a gas phase contaminant.



(a)



(b)

Figure 3.22: Atom maps of 28Da peak showing the segregation of (a) all ions and (b) multiple-hit ions to a grain boundary. The ranging is similar to Figure 3.21 where only the beginning of the peak is ranged as Fe.

If the experiment is carried out at a sufficiently low temperature (<30K) so that the thermal tails are reduced, Fe^{2+} and CO^+ could be distinguished because they have mass-to-charge-state ratios of 27.97Da and 28.01Da respectively, requiring a mass resolution of 0.04Da to be separated (Figure 3.23). However, the success rate of running samples at this temperature is very low and hence this is not a practical solution to solve the Fe^{2+}/ CO^+ overlap.

To address this issue, two considerations should be taken into account. Firstly, whether the peak should be located at the precise mass-to-charge-state ratio for Fe^{2+}. $^{56}Fe^{2+}$ should be located at 27.97Da but if the 28Da peak contains more CO^+, the peak may shift towards a higher mass-to-charge-state ratio as CO^+ probably originates from gaseous molecules inside the analysis chamber. The second consideration is how the peak can be consistently ranged across different datasets.

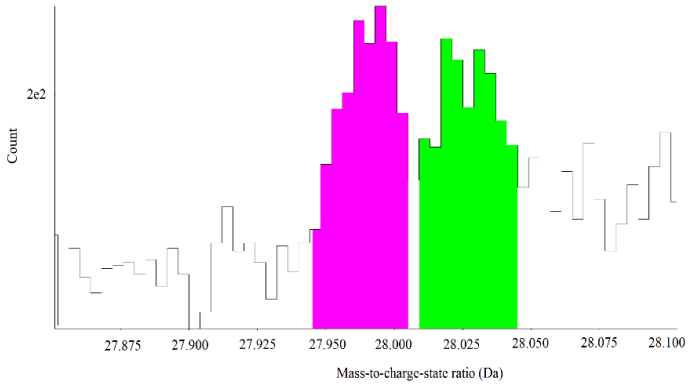
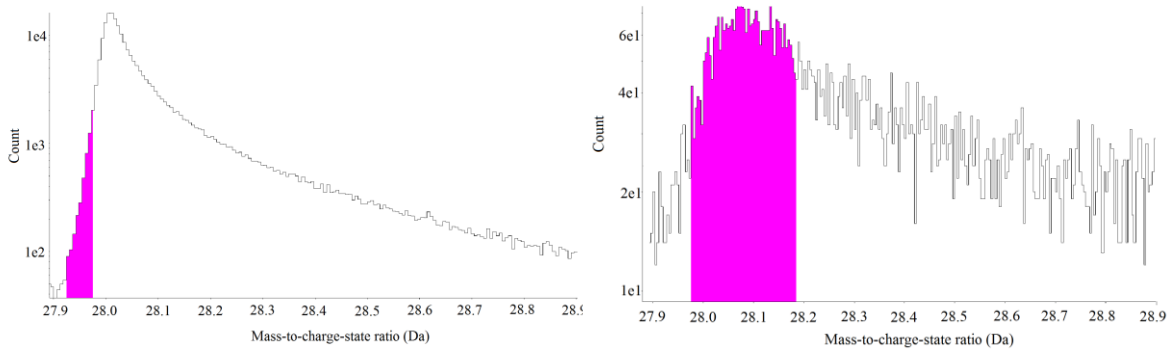


Figure 3.23: Separated Fe^{2+} (pink) and CO^{+} (green) peaks in an oxide mass spectrum of Zr-0.5Nb-0.1Sb run at 30K.

In this study, the Fe^{2+} ranging guidelines are as follows. If the peak is located at 27.97Da, only the peak area is ranged, even though the tail or end of the peak may also contain Fe^{2+} ions, on the assumption that the tail mostly contains CO^{+} (Figure 3.21). If the peak is located at a mass-to-charge-state ratio higher than 27.97Da but begins below 27.97Da, only the beginning of the peak is ranged until a point between 27.98-28.02Da (Figure 3.24a). In this case, most of the peak is not ranged on the assumption that this tail contains mostly CO^{+}. Another possibility is if the whole peak is located above 27.97Da due to issues in peak calibration, only the beginning of the peak is ranged (Figure 3.24b).

These guidelines underestimate the total amount of Fe^{2+} because they disregard the Fe^{2+} at the end of the peak. However, we can assume that we have avoided most of the contribution from CO^{+} because the CO^{+} peak is broadened towards the right hand side of the mass spectrum.



(a) (b)

Figure 3.24: Two examples of different 28Da ranging methods for Fe^{2+}. In (a), the peak starts before 27.97Da (27.92Da) but most of the peak is not ranged (ranging window: 27.92-27.98Da). In (b), the whole peak is located above 27.97Da (ranging window: 27.98-28.12Da). Note the change of vertical scales between (a) and (b).

3.2.3.3. Interfaces

Interface analysis can be carried out by two methods. The first one is by creating a region of interest (ROI) through an interface in a reconstructed dataset. In the IVAS software, ROIs can be of three different shapes; cylindrical, spherical or cuboidal. Once an ROI is created, a 1D concentration profile along the length of a cylinder or cuboid can be computed. The calculation includes all atoms inside the ROI. The concentration profile can be plotted in terms of concentration or density in a defined step size. In this thesis, the step size is normally 0.5nm or 1nm.

The second method is by creating a proximity histogram (proxigram). The 3D reconstruction data is partitioned into a grid of cubic or rectangular blocks known as voxels [169]. A collection of voxels containing a certain concentration of element form a surface called the isoconcentration surface (isosurface) in which the concentration between two neighbouring voxels is smoothed by delocalisation. To create a proxigram, an isosurface with a defined concentration is initially created. Then an average composition profile as a function of increasing distances normal to the surface can be generated. For comparison, consider an

oxidised β-Nb particle in the oxide layer (Figure 3.25). This particle can be examined by an isosurface at 25 at% Nb as well as a cylinder penetrating through the particle.

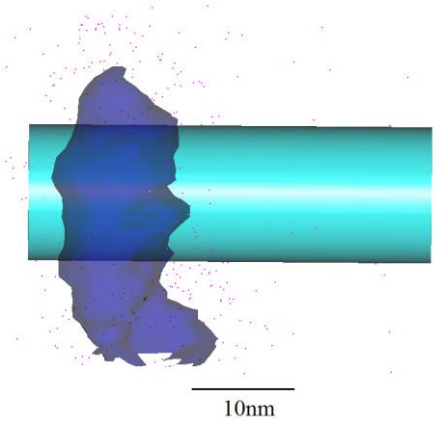


Figure 3.25: An oxidised β-Nb particle in the oxide containing Fe (pink dots). A 25 at% Nb isosurface (blue) covering the particle/oxide interface is created. There is a cylinder penetrating the particle, more less perpendicular to the isosurface.

The two methods have their own advantages and drawbacks. The profile produced by the ROI method depends on the number of atoms inside each section, and hence the ROI cross sectional area. Therefore when analysing an element with low concentration, it is important to ensure that the ROI is sufficiently large. However, the advantage of using ROI method is that the position and size of the ROI can be controlled easily and it is not computationally expensive. Examining the example from Figure 3.25, the ROI method gives similar concentration profiles to the proxigram (Figure 3.26a-b) in terms of Zr, Nb, and O, with half of the ROI 1D concentration profile resembling the proxigram profiles and the other half resembles its mirror image. However, discrepancies occur when comparing elements with low concentrations; Fe and Cr. The 1D concentration profile suggests a maximum Fe concentration ~0.7 at% which is greater than the ~0.3 at% calculated by proxigram. This is due to limited number of ions included in the analysis.

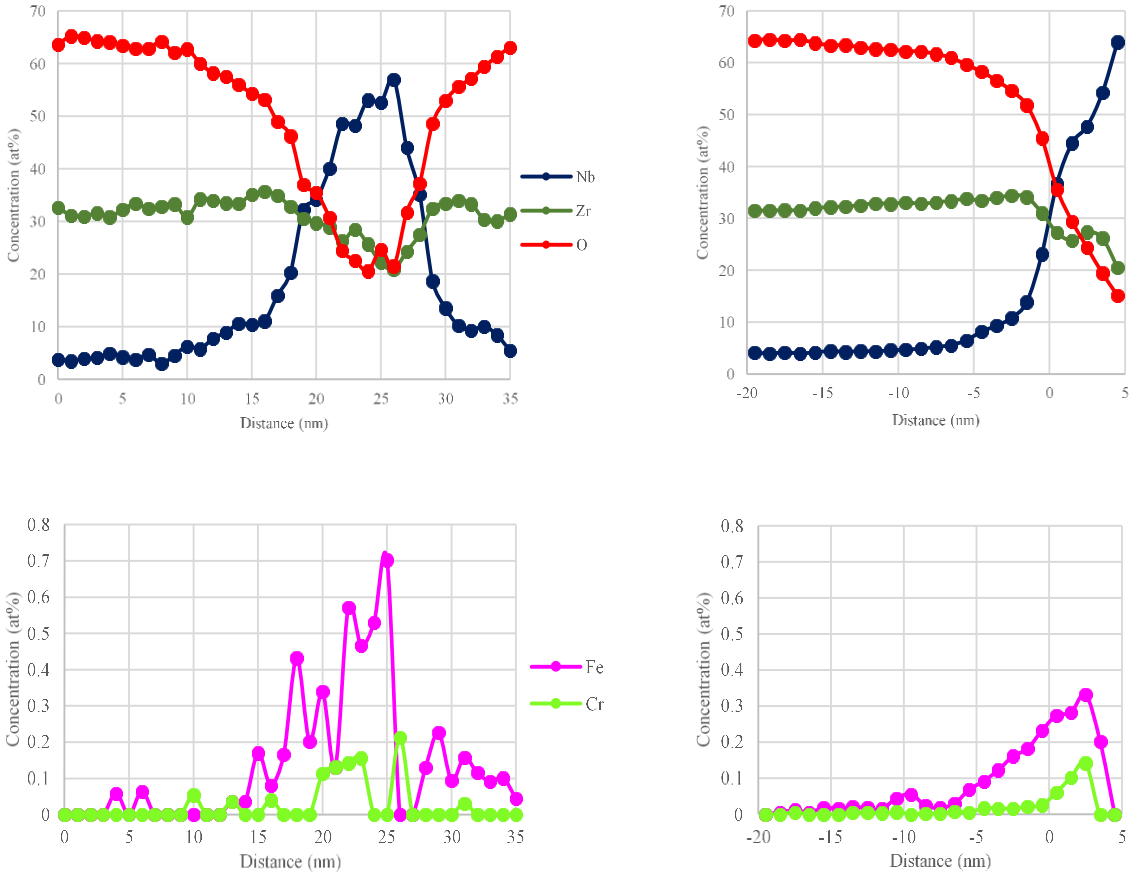


Figure 3.26: The composition profiles from the β-Nb particle from Figure 3.25 calculated by (a) cylinder and (b) 25 at% Nb proxigram.

The proxigram method is suitable for interfaces with complex shapes, but it is computationally expensive. Because this method uses an isosurface as a reference and creates a composition profile in all directions normal to the isosurface, it is not possible to determine the compositional profile along a specific direction. When doing an analysis over a long distance the proxigram tends to be unreliable because at greater distances (>50nm) as it averages data points of voxels constituting a surface with a very different shape (much flatter) compared to the shape of the original isosurface. In the example from Figure 3.25, the proxigram calculates the radial composition variations, and therefore the profiles end in a location where all points in the proxigram converge at the centre of the particle (right hand side of Figure 3.26b). The superiority of the proxigram compared to ROI method is that

proxigram include all atoms in the vicinity of particle which is especially important when analysing elements with low concentrations.

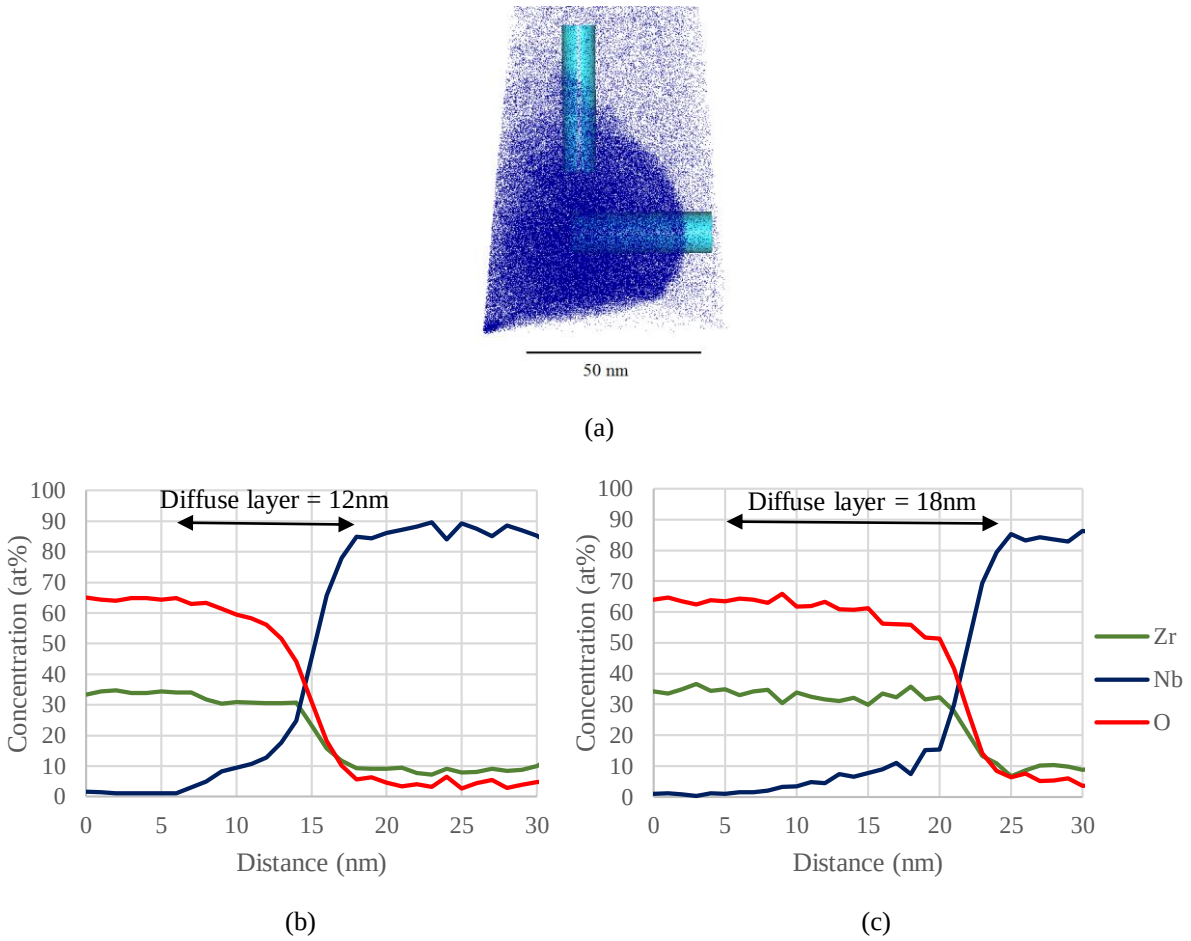


Figure 3.27: (a) A distribution of Nb in β-Nb particle in ZrO_2 and two cylinder ROIs penetrating through the particle in horizontal and vertical directions. (b) and (c) are the Nb profiles across the particle/oxide interface in horizontal and vertical directions respectively, taken from the ROIs in (a).

When using ROIs, they have to be positioned such that the angle between the axis of cylinder and horizontal line is minimised due to trajectory aberrations in the z direction (Section 3.1.5). This can be observed in Figure 3.27a-c where the Nb diffuse layer between the particle and matrix (oxide) is different in the horizontal and vertical directions. In the vertical direction, the Nb distribution is more diffuse (Nb diffuse layer = 18nm) compared to the horizontal direction (Nb diffuse layer = 12nm). This indicates that the β-Nb particle evaporates more easily compared to the matrix.

Quantitatively, the degree of interfacial segregation of an element can be described as the number of excess atoms per unit area of the interface. This is known as the interfacial excess (Γ):

$$\Gamma = \frac{N_{excess}}{e_D A} \tag{3.4}$$

where N_{excess} is the number of excess atoms, e_D is the LEAP detector efficiency (~0.38) and A is the interface area. When calculating the interfacial excess from a proxigram or 1D concentration profile, the concentration of excess atoms can be over a distance of a few nm, much wider than the expected width of a grain boundary or interface [169,190]. This could be due to local magnification effects where atoms on the interface are subjected to different electric field than the ones in the matrix, resulting in trajectory aberrations and preferential retention. In this case, the total excess atoms can be determined by the summation of all atoms on the interface substracted by the matrix concentration that serves as a background. In this case, Equation 3.4 can be modified to:

$$\Gamma = \frac{\sum_{i=1}^{n}(N_i C_i)_{interface} - (N_i C_i)_{matrix}}{e_D A} \tag{3.5}$$

where n is the step size or number of sections in the ROI containing the excess atoms, N and C are the total number of atoms in each section and the concentration of the element of interest respectively.

Elemental segregation can also be described in terms of the number of equivalent monolayers of excess solute, a quantity known as the Gibbsian excess. This can only be used for interfaces between the same material such as grain boundaries. The Gibbsian excess (Φ) is expressed as:

$$\Phi = \frac{\Gamma}{\rho\omega} \tag{3.6}$$

where ρ is the material average density and ω is the closest matrix plane spacing. For hcp α-Zr, the close-packed plane is the basal plane (0001) with ρ = 43.0 atoms/nm^3 and ω = 0.323nm [194]. For monoclinic ZrO_2, ρ = 85.3 atoms/nm^3 and ω = 0.515nm [54]. When calculating the interfacial excess of oxide grain boundaries, the interfacial excess calculated using Equation 3.5 is further divided by P-B ratio of ZrO_2 (1.56) to consider the volume expansion in the oxide growth direction.

In this study, cylinder ROIs with 1D concentration profiles have been used to analyse the Nb profiles across particle/matrix interfaces. The cylinder is positioned as perpendicularly as possible to the needle axis, and with the interface normal to minimise the trajectory aberration effect (Figure 3.25). Proxigrams were used to analyse the O/M interface due to the complexity of the interface shapes. The O-saturated metal layer thickness between the oxide and metal can be very thin and might be difficult to identify using a cylinder ROI, and therefore it is important to include as large area as possible. Analyses on elements with low concentration such as Fe have to be carried out by proxigrams because the greater number of atoms in the analyses, the lower the systematic compositional error. Quantitatively, interfacial excess is used to describe elemental segregations at the O/M interface as well as at particle/matrix interfaces, and the Gibbssian excess is used for grain boundary analysis.

4. MATERIALS

4.1. General overview

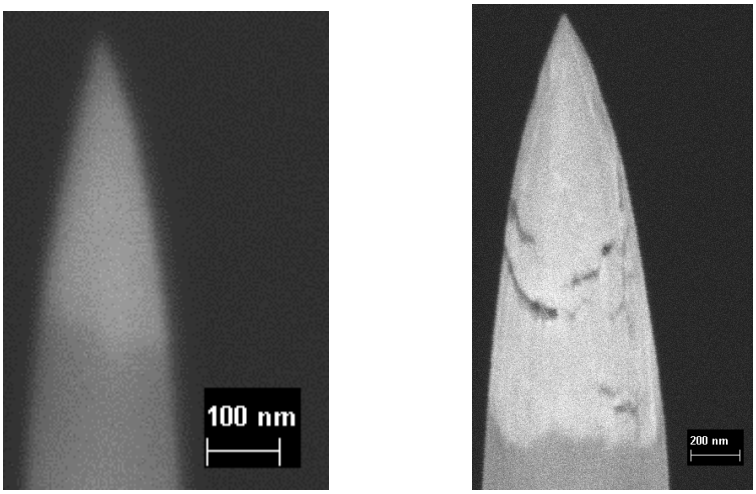
The materials studied in this thesis include both unoxidised and oxidised samples. Unoxidised specimens were prepared for APT analysis by electropolishing, while oxidised specimens by FIB liftout. Unoxidised materials include as-recrystallised and annealed Zr-1Nb. Oxidised materials include oxidised as-recrystallised and annealed Zr-1Nb, X2, Zr-2.5Nb, and Zr-0.5Nb-0.1Sb in various stages of oxidation; from early pre transition to late post transition. Irradiated X2 samples were also examined for comparison with the unirradiated alloys. Examinations were carried out in different regions; metal, oxide and at the O/M interface, but most experiments were to analyse the latter two. Considering that the outer part of the oxide contains cracks and pores, oxide analyses were mainly carried out 500-600 nm from the O/M interface. For oxidised samples, different materials were examined with different experimental objectives (Section 4.3).

In this project, over 268 APT samples were examined, with overall success rate ~44%. In general, pre-transition samples have a better success rate compared to post-transition ones, probably because the post-transition oxide contains many more cracks compared to pre-transition oxide (Figure 4.1a-b). The materials with the lowest success rate is Zr-2.5Nb, because most of these analyses were carried out in the oxide 500-600 nm from the O/M interface. Furthermore, the adhesion of O/M interface seems to be better in pre-transition compared to post-transition samples, as many post-transition samples fractured close to the interface.

Table 4.1: Summary of oxidised materials.

Materials	Oxidation duration (days)		State	Number of APT samples prepared	Number of successful experiments*	Success rate (%)
	Light water	Heavy water				
Annealed Zr-1Nb	3	0	Pre-transition	31	12	38.7
	30	0		10	8	80.0
	15	31		12	8	66.7
	60	31	Post-transition	32	11	34.3
	105	0		9	5	55.6
	225	0		12	6	50.0
As-rec'd Zr-1Nb	3	0	Pre-transition	12	5	41.7
	210	0	Post-transition	18	6	33.3
X2	180	45	Pre-transition	12	7	58.3
	540	45	Post-transition	11	5	45.5
Zr-2.5Nb	0	150	Unknown but most likely pre-transition	25	10	40.0
	0	1040	Post-transition	40	13	32.5
Zr-0.5Nb-0.1Sb	15	0	Pre-transition	23	16	69.6
	195	0		16	6	37.5
Irradiated X2	548	0	Unknown	5	2	40.0

*The number of successful analyses corresponds to the number of experiments with more than 2 million ions collected.



(a) (b)

Figure 4.1: (a) A typical APT sample of a pre-transition material containing ~400nm oxide and (b) an unfinished APT sample of a post-transition material containing ~800nm oxide showing cracks very close to O/M interface.

The oxidised annealed and as-recrystallised Zr-1Nb samples were supplied with the most complete information regarding oxidation weight gain as well as HPU. I carried out further analysis of this data in this project. The first term to be calculated is the instantaneous oxidation rate as the time derivative of the oxidation weight gain, calculated using numerical differentiation [195]:

$$\frac{dw}{dt} = \frac{w_{t+\Delta t} - w_{t-\Delta t}}{2\Delta t} \tag{4.1a}$$

$$\frac{dw}{dt} = \frac{w_{t-2\Delta t} - 4w_{t-\Delta t} + 3w_t}{4\Delta t} \tag{4.1b}$$

where w_t is the weight gain at oxidation time t. It was assumed that the initial weight gain is zero, and therefore Equation 4.1a is used at all t, except in the last oxidation time where Equation 4.1b is used instead.

HPU data from these samples was also collected, making it possible to do further analysis. From this information, we can calculate the HPUF using the following expression [5]:

$$\mathrm{HPUF} = \frac{10^{-6}(m_s^t C_H^t - m_s^i C_H^i)}{\frac{2(m_s^t - m_s^i)M_H}{M_O}} \tag{4.2}$$

where m_s^i and C_H^i are the initial specimen mass and hydrogen concentration (in ppm) respectively, m_s^t and C_H^t are the specimen mass and hydrogen concentration (in ppm) after oxidation time t respectively, and M_H and M_O refer to atomic mass of hydrogen and oxygen atoms respectively. The instantaneous rates of both HPU and HPUF are calculated using Equation 4.1a-b.

In addition, oxide thickness measurements were carried out by taking an SEM image of FIB milled cross sections, and averaging the thickness at five points in the image, including the points where the thickness is the greatest and smallest, as well as three other points selected randomly.

4.2. Unoxidised metal

Examinations of unoxidised metal samples were carried out only for baseline matrix composition determination. The unoxidised materials include both annealed and as-recrystallised Zr-1Nb. A typical metal mass spectrum can be found in Figure 3.16, and the measured composition of each material is given in Table 4.2 and Table 4.3.

The total number of collected atoms were 41 and 26 million for annealed and as-recrystallised Zr-1Nb material respectively, collected from 4 as-recrystallised and 5 annealed samples. The compositions across all samples show a good consistency. O, Nb, Fe, Al and C are present in all samples, while N is only present in some of them. H is excluded in this analysis because the H signals originate from various external sources (Chapter 6). Further details about O, Fe, and Nb levels measured in these samples are discussed in Chapters 5, 7 and 8 respectively.

Table 4.2: As-recrystallised Zr-1Nb matrix compositions.

Sample no.		**Zr**	**O**	**Nb**	**Fe**	**Al**	**C**	**N**	**Total**
1	No. of atoms	2010696	15473	8299	365	255	926		2036014
	Conc. (at%)	Balance	0.76	0.41	0.018	0.013	0.045		
2	No. of atoms	3235181	26331	13978	865	602	1933	458	3278891
	Conc. (at%)	Balance	0.80	0.43	0.026	0.018	0.059	0.014	
3	No. of atoms	1500167	17884	5508	175	279	901		1524914
	Conc. (at%)	Balance	1.28	0.43	0.011	0.073	0.015		
4	No. of atoms	18990061	303318	80411	2097	3177	9904	461	19388968
	Conc. (at%)	Balance	1.56	0.41	0.011	0.016	0.051	0.002	
Overall	No. of atoms	25736105	363007	108196	3502	4313	13664	918	26228788
	Conc. (at%)	Balance	1.38	0.41	0.013	0.016	0.052	0.004	

Table 4.3: Annealed Zr-1Nb matrix compositions.

Analysis no.		Zr	O	Nb	Fe	Al	C	N	Total
1	No. of atoms	28401062	239557	120525	2877	2470	18981		28785471
	Conc. (at%)	Balance	0.83	0.42	0.010	0.009	0.066		
2	No. of atoms	4632100	81729	18198	508	389	4122	357	4737046
	Conc. (at%)	Balance	1.73	0.38	0.011	0.008	0.087	0.008	
3	No. of atoms	4825443	78165	19743	1000	377	6562		4931290
	Conc. (at%)	Balance	1.59	0.40	0.020	0.008	0.13		
4	No. of atoms	1399562	18006	6480	205	141	2311		1426704
	Conc. (at%)	Balance	1.26	0.45	0.014	0.010	0.16		
5	No. of atoms	1207462	18972	4229	339	169	2654		1233824
	Conc. (at%)	Balance	1.54	0.34	0.027	0.014	0.22		
Overall	No. of atoms	40465629	436429	169174	4929	3545	34630	357	41114335
	Conc. (at%)	Balance	1.06	0.41	0.012	0.009	0.084	0.001	

4.3. Oxidised materials

All samples were tested in a static autoclave under simulated PWR conditions and summarised in Table 4.4. The information in Table 4.4 was supplied by the respective organisations that conducted the tests [196-199]. The HPU and DPU (for Zr-2.5Nb) data were provided by Westinghouse and AECL respectively, measured using inductively coupled plasma mass spectrometry (ICPMS).

Table 4.4: Alloy compositions, and autoclave experiment details [196-199].

Materials	**Minor alloying element contents**				**Oxidising water chemistry**	**T (°C)**	**Tested by**
	Nb (wt%)	Sb (wt%)	Fe (wtppm)	H (wtppm)			
As-recrystallised Zr-1Nb	1	-	753	13	Pure H_2O	360	Westinghouse
Annealed Zr-1Nb	1	-	596	10	Pure H_2O (and subsequent pure D_2O for partially-deuterated samples)	360	Westinghouse
X2	1	-	1000	-	Primary water (2 wtppm Li + 1000 wtppm B) and subsequent pure D_2O	360	EdF
Zr-2.5Nb	2.5	-	440	-	Lithiated D_2O	335	AECL
Zr-0.5Nb-0.1Sb	0.5	0.1	500	-	Pure H_2O	360	Westinghouse

4.3.1. As-recrystallised Zr-1Nb

All the Zr-1Nb material in this study was provided in the form of sheet. The sample fabrication and oxidation of as-recrystallised and annealed Zr-1Nb were carried out by Westinghouse in a method similar to Figure 2.10. The final heat treatment for as-recrystallised Zr-1Nb was carried out at 580ºC (Figure 4.2), resulting in the precipitation of spherical β-Nb particles (Chapter 8). Samples were weighed prior to oxidation, and put in a light water autoclave at 360ºC up to 225 days. Samples were removed after 1, 3, 7, 15, and then every 15 days to be weighed again before being heated up for hydrogen content measurement.

The studied materials include 3-day (pre-transition) and 210-day (post-transition) as-recrystallised samples, mainly to compare the local chemistry near O/M interface. Compared to the annealed sample, this material contains smaller SPPs and has better oxidation resistance but slightly worse HPU behaviour. This can be seen in the oxidation kinetics curve where it only undergoes one transition up to 225 days, between 135-150 days (Figure 4.3). In

comparison with the annealed Zr-1Nb, this alloy undergoes much less abrupt transition at a similar weight gain values, but ~90 days later; a significantly improved corrosion behaviour. There is a rapid change of HPU kinetics between 120-135 days that corresponds to, but occurs slightly before, the oxidation transition (Figure 4.4).

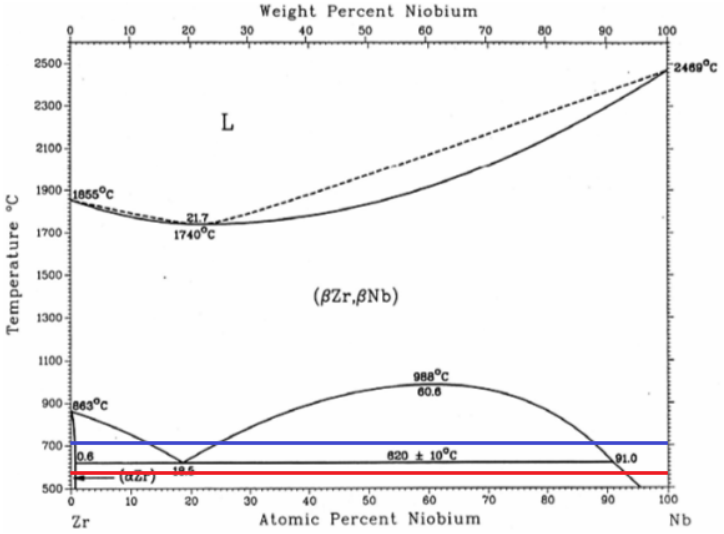


Figure 4.2: A Zr-Nb phase diagram showing the position of heat treatments at recrystallisation (580°C, red line) and annealed (720°C, blue line) temperatures [5]

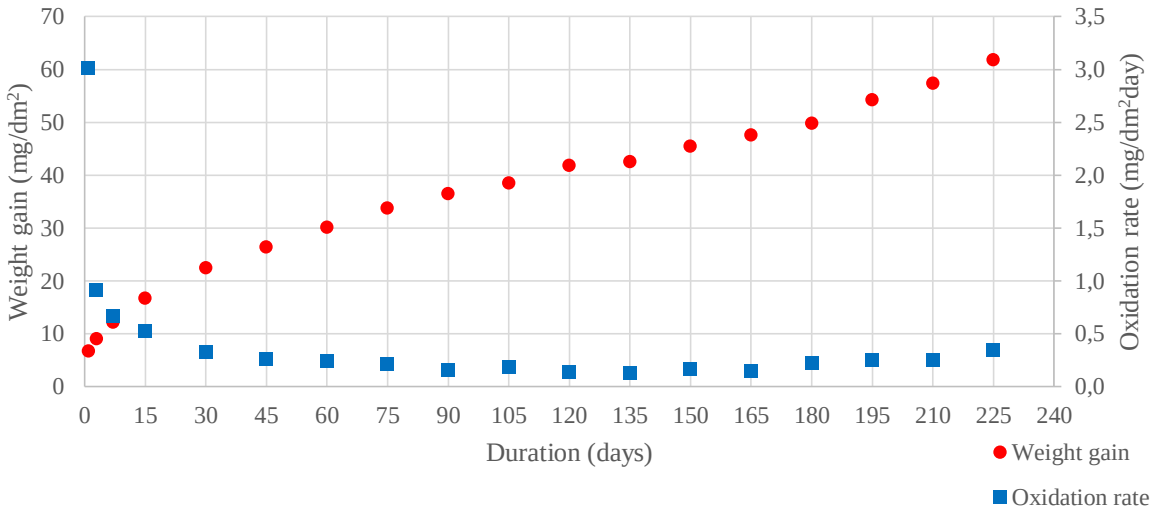


Figure 4.3: Oxidation kinetics and instantaneous rate of oxidation in as-recrystallised Zr-1Nb.

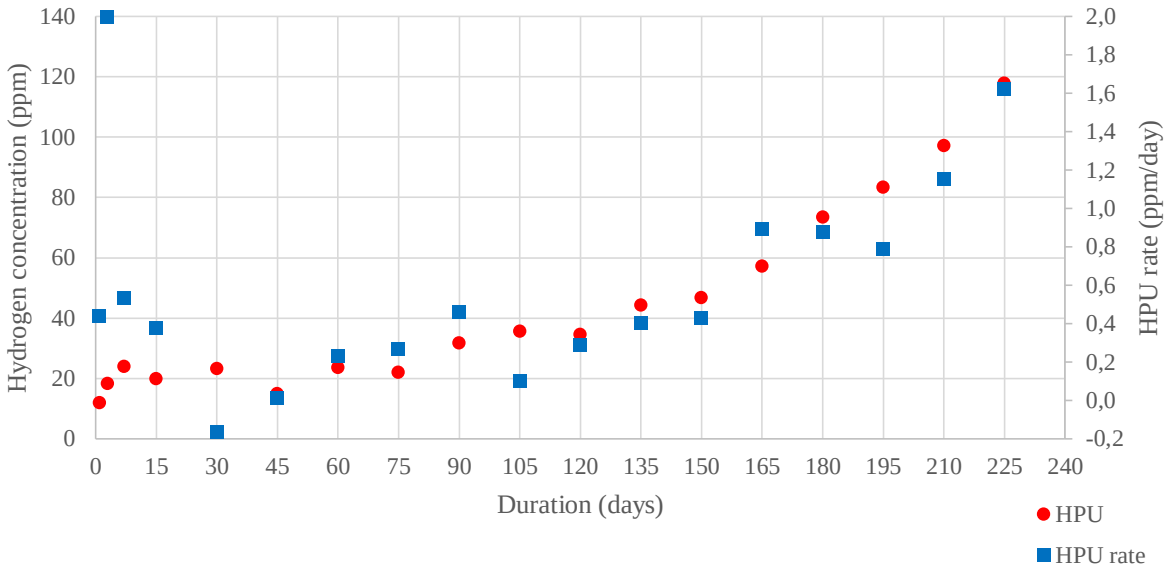


Figure 4.4: HPU kinetics and instantaneous HPU rate in as-recrystallised Zr-1Nb.

The C_H^i value in Equation 4.2 is obtained by extrapolating a polynomial fit from Figure 4.4, and for this material the extrapolated C_H^i value is 17ppm. This value results in an apparently negative HPUF value at 1 day, presumably a result of measurement errors or loss of initial H in solid solution to the corroding medium during warm up (Figure 4.5). The HPUF kinetics curve is similar to HPU, with a rapid change between 120-135 days (Figure 4.9).

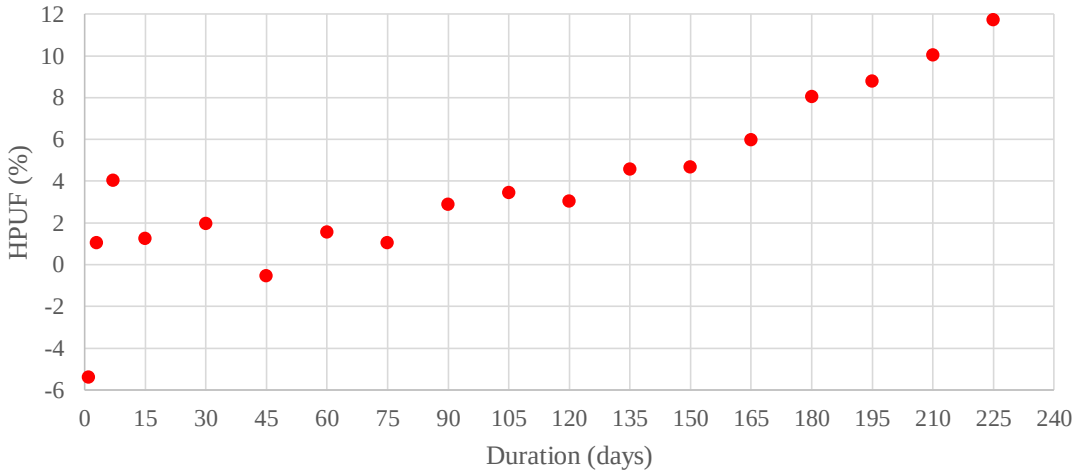


Figure 4.5: HPUF kinetics in as-recrystallised Zr-1Nb.

The O/M interface of 3-day sample is almost free of any cracks, while the 210-day sample exhibits a layer of small cracks associated with transition (Figure 4.6a-b). The 210-day sample is at least 60 days post transition, but compared to annealed samples with shorter

times after transition (i.e. 91-day and 105-day), the cracks in the oxide of this sample are smaller. This may be attributed to the slower oxidation rate measured in the post-transition regime.

(a)

(b)

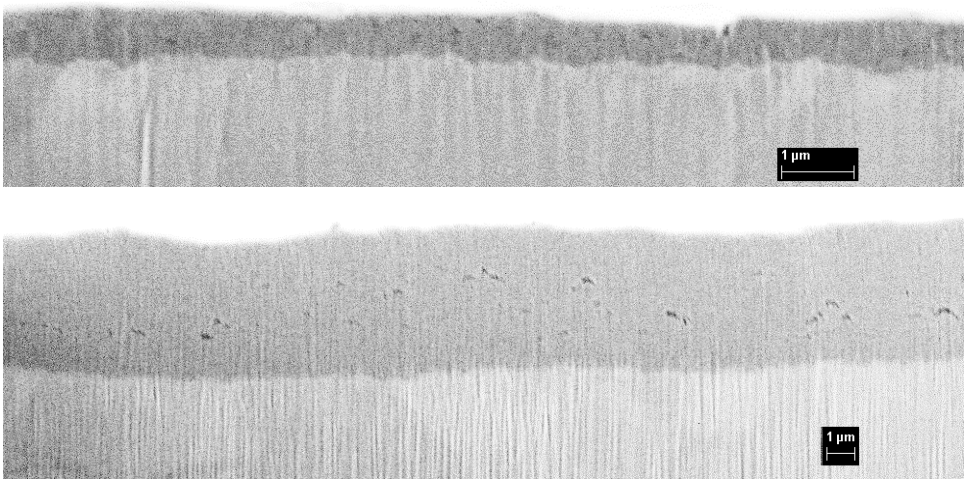


Figure 4.6: SEM micrographs of the O/M interface of as-recrystallised Zr-1Nb oxidised in: (a) 3 and (b) 210 days. The oxide has darker contrast at the top of each image, and the metal with lighter contrast at the bottom.

The oxide thickness variations are shown in Table 4.5. As a 1 mg/dm^2 weight gain corresponds to 0.06µm of new oxide, the theoretical oxide thickness of 3-day and 210-day samples are 0.60µm and 3.82µm. In comparison with these values, the measured 3-day sample oxide thickness is in a good agreement, but the measured value of 210-day sample is 31% higher, implying that although across the area examined by SEM (~20µm) the O/M interface is relatively flat (with thickness variation only ~4.9% average), but in the larger scale it may be uneven.

Table 4.5: Oxide thickness measurements from as-recrystallised Zr-1Nb.

Samples	**Measured thickness values (h) (µm)**		**Averaged thickness ($h_{average}$) (µm)**	**Theoretical oxide thickness (weight gain /15) (µm)***	**Thickness variation (h_{max}-h_{min}) (µm)**	**Thickness variation ($\frac{h_{max}-h_{min}}{h_{average}}$) (%)**
	Lowest (h_{min})	**Highest (h_{max})**				
3-day	0.49	0.73	0.63	0.60	0.23	36.6
210-day	4.83	5.07	4.98	3.82	0.24	4.9

*The weight gain is in mg/dm^2.

In comparison with the annealed samples (Table 4.7) with similar averaged oxide thickness, both 3-day and 210-day as-recrystallised Zr-1Nb have more uniform oxide thickness. In addition, the 210-day sample has the lowest thickness variation of all annealed samples, suggesting that the oxidation rate is relatively uniform across the sample surface in the post transition regime.

4.3.2. Annealed Zr-1Nb

At the latest stage of production, this annealed Zr-1Nb alloy was further heat treated at 720°C for 24 hours to precipitate β-Zr. Because precipitates in this sample are located far apart from each other, no precipitates were detected by APT from this material.

In this study, I selected 6 samples for APT analysis: 3-day, 30-day, and 46-day (pre-transition) as well as 91-day, 105-day, and 225-day (post-transition). This material is suitable for the study of the post-transition behaviour because there is sufficient data regarding oxidation weight gain and HPU in this regime. In addition, a considerable amount of time was committed to studying Fe distributions in this material (Chapter 7).

Two annealed samples were also deuterated for 31 days following oxidation in the autoclave (46-day and 91-day). The deuteration was designed to allow the analysis of the distribution of hydrogenic species in the oxide while avoiding the problems of by H contamination from the LEAP vacuum system and from FIB polishing (Chapter 6).

The weight gain of the 46-day sample (15 days H_2O + 31 days D_2O) is ~1.05x of the equivalent sample treated in light water only (sample oxidised for 45 days in H_2O), and both are still in pre transition (Table 4.6). Meanwhile, the weight gain ratio between 91-day (60 days H_2O + 31 days D_2O) and the equivalent sample treated in light water only (sample oxidised for 90 days in H_2O) is ~0.90. Theoretically, the weight gain from D_2O should be

1.11x greater than from exactly the same thickness of oxide in H_2O. Therefore, the deuterated samples should have a slightly more weight gain than samples oxidised in light water. This is the case for 46-day sample but not for 91-day sample where the discrepancy between the $\frac{w_h}{w_l}$ ratio and the theoretical value could be due to normal sample-to-sample variation.

Table 4.6: Deuteration details.

Samples	**Weight gain prior to deuteration (mg/dm^2)**	**Weight gain from deuteration (mg/dm^2)**	**Total weight gain after deuteration (w_h) (mg/dm^2)**	**Weight gain of equivalent samples oxidised in light water (w_l) (mg/dm^2)***	**$\frac{w_h}{w_l}$**
46-day (15 days H_2O + 31 days D_2O)	20.8	15.1	35.9	34.2	1.05
91-day (60 days H_2O + 31 days D_2O)	40.6	22.3	63.0	69.7	0.90

*The equivalent samples for 46- and 91-day samples are 45-day and 90-day samples treated in light water only.

The annealed alloy undergoes a transition between 45-60 days, and the post-transition regime shows two further transition points between 120-135 and 180-195 days respectively (Figure 4.7). The oxidation rate is very high initially, but after ~15 days the cycles of oxidation are clear where the rate reaches minima at transition points and maxima at the plateau region.

The first transition is at least ~45 days, while the second and third transitions are separated by at least 60 and 45 days respectively. Transition is a localised phenomenon and occurs at different locations in the same sample and is sensitive to microstructure variation [97,200]. Therefore, an inhomogeneous distribution of cracks in the oxide might be associated with the delay of the second transition.

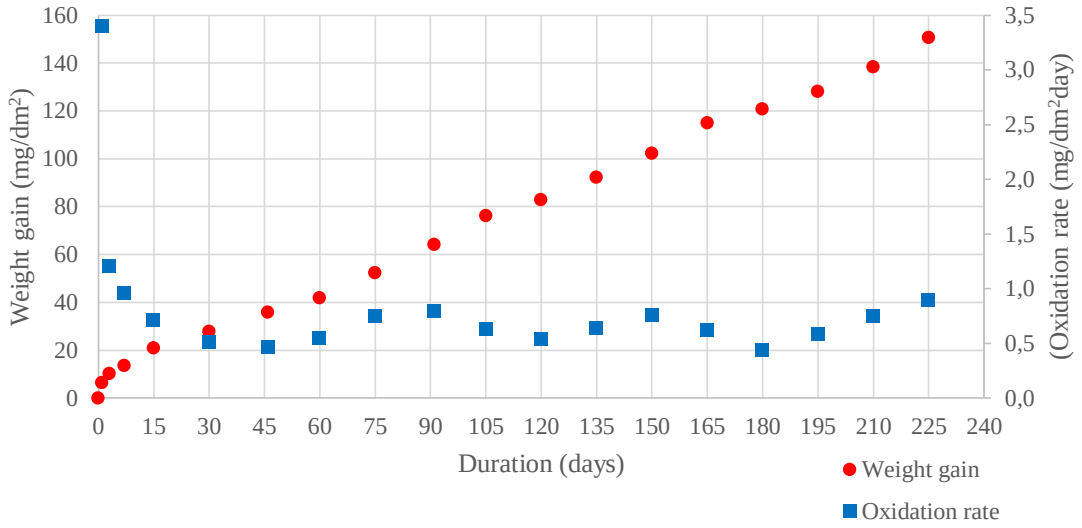


Figure 4.7: Oxidation weight gain evolution and instantaneous rate of oxidation in annealed Zr-1Nb.

The HPU periodicity seems slightly different; the first rapid increase of HPU rate occurs earlier (between 15-30 days) (Figure 4.8). This is also the case for the second and third minima in the HPU rate curve (between 105-120 and 165-180 days respectively). This HPU behaviour is similar to the as-recrystallised Zr-1Nb where HPU rate minima precede the weight gain minima, indicating that the increase of HPU rate is associated with the onset of the oxidation weight gain rate increase.

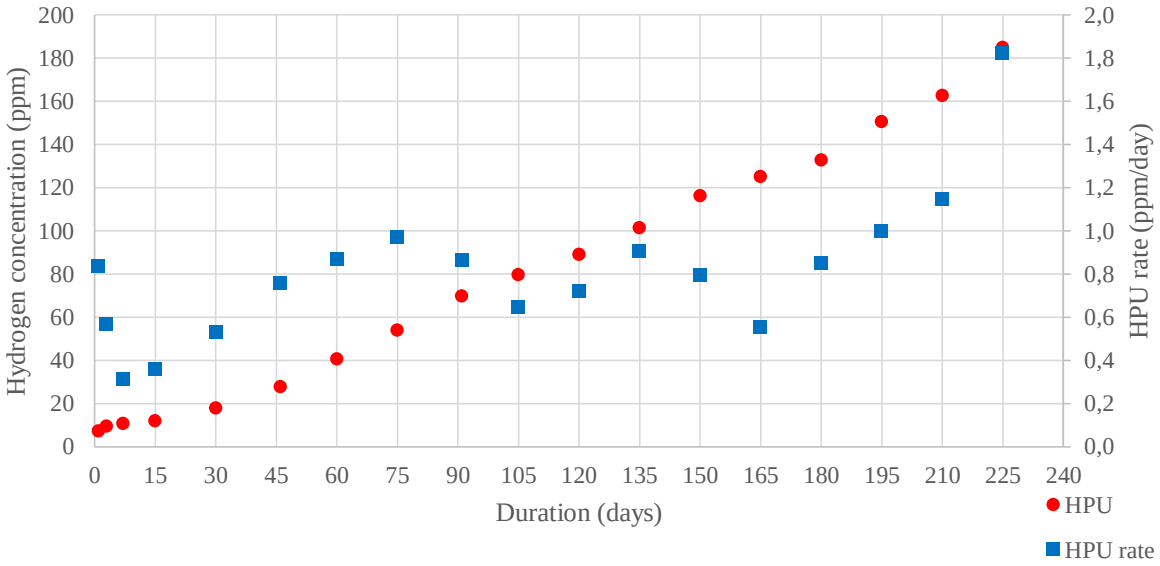


Figure 4.8: HPU kinetics in annealed Zr-1Nb.

For this sample, the C_H^i value is 7 ppm. The curve increases very significantly at the beginning of transition (Figure 4.9). After the second minimum, the HPUF only increases slightly from 7.1% (120 days) to 8.6% (225 days) even though HPU increases from 89ppm to 184ppm over the same period. It is clear that most of the hydrogen generated over this period is rejected to the environment in the form of gaseous H_2 rather than entering the metal.

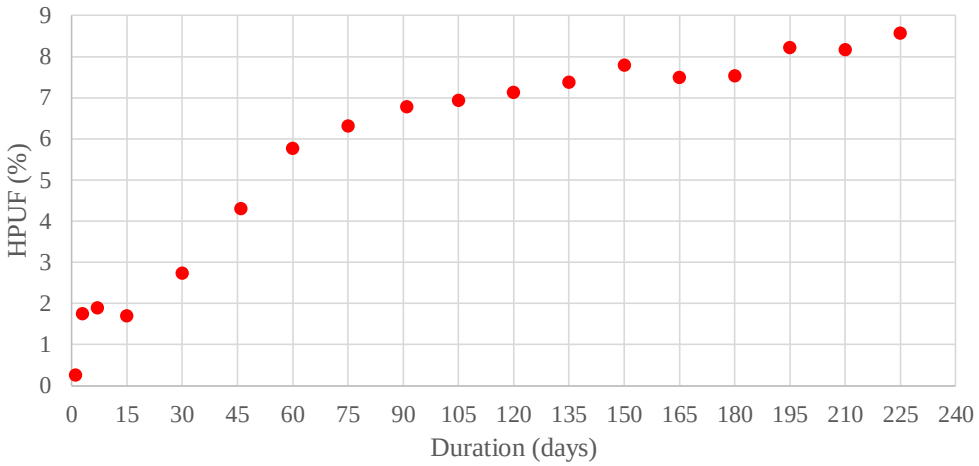


Figure 4.9: HPUF evolution in annealed Zr-1Nb.

The shape of the O/M interface changes over the course of oxidation (Figure 4.10a-f). In the pre-transition regime the oxide is dense and almost free of cracks, with the exception the 46-day sample. Although still in pre transition, this sample is very close to the transition point. Transition is a localised phenomenon and therefore the cracks may be associated with localised transitions. These cracks are located very close to the interface, suggesting that they were developed not long before the sample was taken out from the autoclave.

In the post-transition regime, cracking in the oxide layer is very obvious in some samples, but the crack size can be very different in different samples and locations, e.g. the cracks in the 105-day sample (Figure 4.10e) are not as large as in the 91-day ones (Figure 4.10d). Even within the same sample, different stages of transition can be observed, e.g. in the 91-day sample, an extra layer of cracks close to the O/M interface is observed where the oxide is

thicker (shown by the red circles), corresponding to a local second transition. The details of the oxide thickness measurements taken from FIB sections are given in Table 4.7.

Table 4.7: Oxide thickness measurement results from annealed Zr-1Nb.

Sample	**Measured thickness values (h) (μm)**		**Averaged thickness ($h_{average}$) (μm)**	**Theoretical oxide thickness (weight gain /15) (μm)***	**Thickness variation (h_{max}-h_{min}) (μm)**	**Thickness variation ($\frac{h_{max}-h_{min}}{h_{average}}$) (%)**
	Lowest (h_{min})	**Highest (h_{max})**				
3-day	0.26	1.09	0.61	0.68	0.82	135
30-day	1.17	2.55	1.86	1.85	1.37	73.9
46-day	1.37	2.90	2.32	2.39	1.53	65.9
91-day	4.40	6.20	5.07	4.27	1.80	35.5
105-day	4.40	6.29	5.34	5.07	1.89	35.4
225-day	9.38	10.41	9.98	10.04	1.02	10.3

*The weight gain is in mg/dm^2.

Compared to the weight gain values, the measured average thickness values show good agreement, except for 91-day and 105-day samples. This is possibly due to inhomogeneity of O/M interface in a larger scale. The oxide thickness values demonstrate as expected that the average oxide thickness increases with time and as the oxide grows, and that the thickness variation tends to increase as can be seen in the (h_{max}-h_{min}) values that increase up to 105 days. If the thickness variation is calculated in terms of percentage of the average value ($\frac{h_{max}-h_{min}}{h_{average}}$), this variation in thickness gradually decreases with oxidation time.

A comparison between samples with similar measured thickness from these two materials suggests that annealed Zr-1Nb probably has more uneven O/M interface compared to the as-recrystallised samples. 3-day annealed Zr-1Nb has greater thickness variation (0.82μm) compared to the 3-day as-recrystallised sample (0.23μm). 91-day annealed Zr-1Nb has ~7.4x higher thickness variation than 210-day as-recrystallised Zr-1Nb, despite having similar oxide thickness.

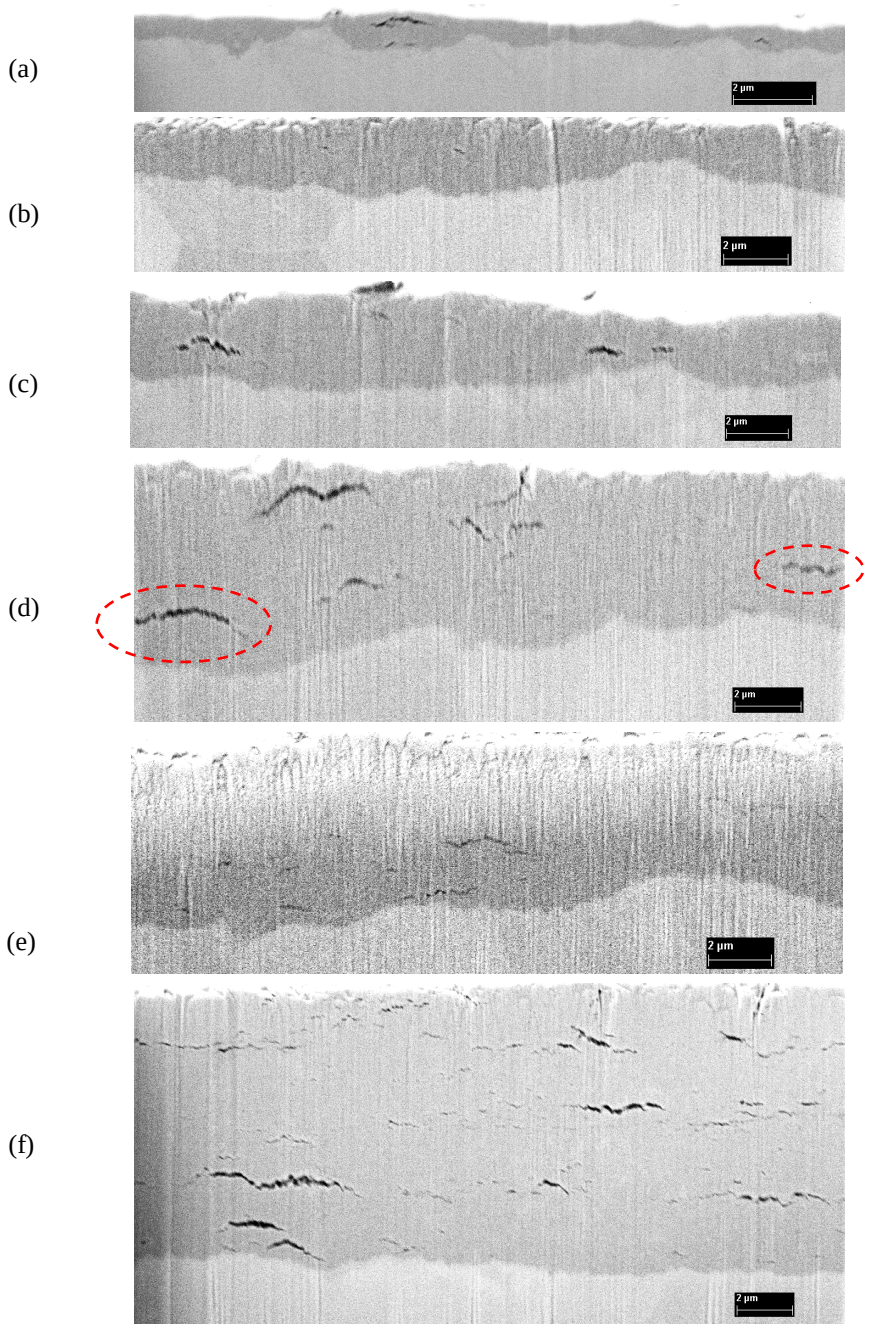


Figure 4.10: SEM micrographs of the O/M interface of annealed Zr-1Nb oxidised for: (a) 3, (b) 30, (c) 46, (d) 91, (e) 105 and (f) 225 days. The oxide has darker contrast at the top of each image, and the metal with lighter contrast at the bottom. The red circles in (d) show a crack that belongs to the second crack layer.

4.3.3. X2

X2 is a Westinghouse developmental alloy based on Zr-1Nb with deliberate addition of 0.1% Fe, and was supplied in an as-recrystallised state. The manufacturing process is similar to as-

recrystallised Zr-1Nb, but X2 was corroded in primary water containing lithium hydroxide and boric acid. Therefore, although its composition is very similar to Zr-1Nb, X2 displays different oxidation kinetics compared to the as-recrystallised Zr-1Nb samples studied here.

The selected X2 samples include 225-day (pre-transition) and 585-day (post-transition) samples. These samples were oxidised for 180 and 540 days in light water respectively, before further oxidation in a heavy water autoclave for 45 days. The samples were not weighed after the completion of the heavy water corrosion test.

Although determination of transition points is not straightforward from this data, it is likely that X2 is still in pre transition even at 360 days (Figure 4.11). Judging from the weight gain of the 540-day sample, the transition should have taken place somewhere between 360-540 days.

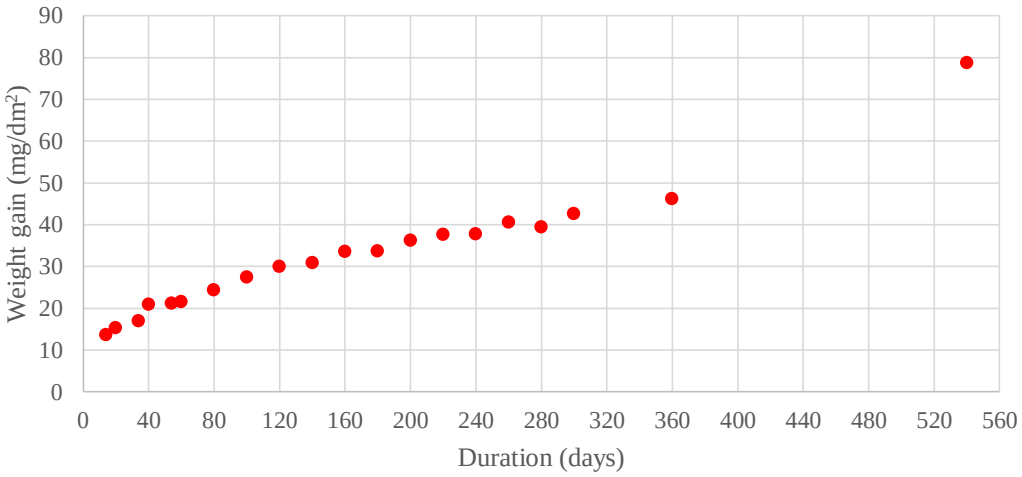


Figure 4.11: Oxidation kinetics of X2.

Although the 225-day sample is in pre transition, small cracks are found in the oxide layer (Figure 4.12a). These cracks may correspond to local transitions, but interestingly they are not located very close to the O/M interface. As expected from a post-transition sample, the 585-day X2 sample contains a lot of big cracks (Figure 4.12b). However, there are two distinct cracking layers indicating that 2 transitions may have occurred in this sample.

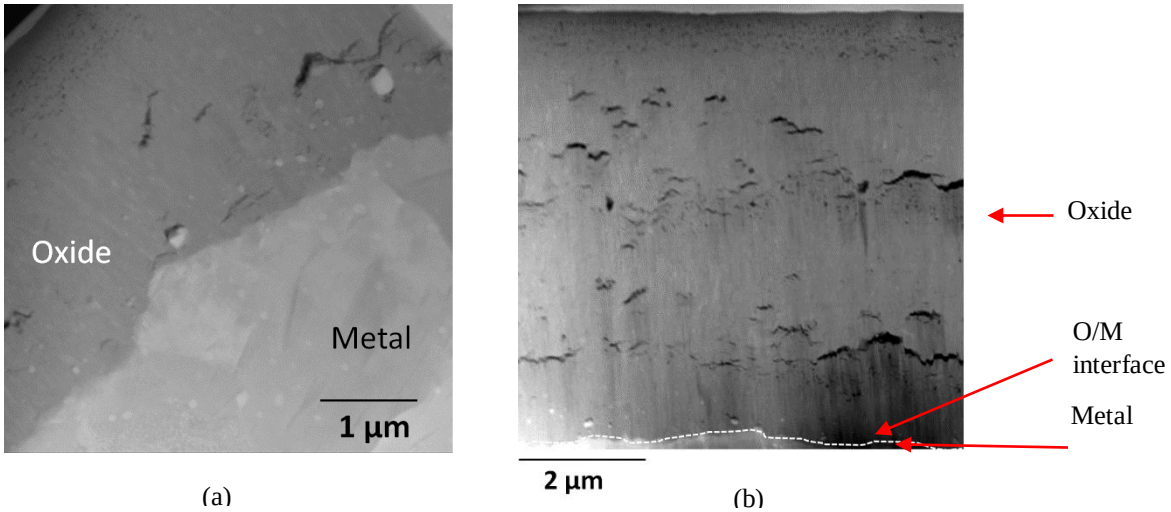


Figure 4.12: Images of (a) 225-day and (b) 585-day X2 oxide layers taken by STEM HAADF imaging in a JEOL 2100 TEM [201].

I was also provided with an irradiated X2 extracted from the Vogtle PWR (Figure 4.13). This sample was irradiated for 1 cycle (1.5 years) with a total neutron fluence of 4.35 10^{21} n/cm^2 with an energy >1 MeV. The oxide is almost free of cracks despite being oxidised for more or less the same duration as the 585-day sample, possibly because the oxidation took place at a lower temperature (305-315°C). There was no weight gain measurement on this material, but the fact that this sample does not contain big cracks shows that it has a structure characteristic of pre-transition samples.

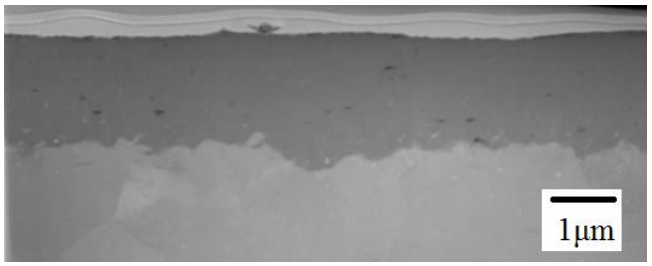


Figure 4.13: STEM HAADF TEM image of irradiated X2. The oxide has darker contrast at the top of the image, and the metal with lighter contrast at the bottom [201].

The examination of oxide thickness variations were taken only over ~4µm, ~8µm and ~7µm wide regions for the 225-day, 585-day and irradiated X2 samples, respectively (taken from Figure 4.12a-b and Figure 4.13), which is a relatively small analysis range compared to other materials described above (typically ~20µm) (Table 4.8). Comparing the 225-day and 585-

day samples, the oxide thickness variation is greater in the 225-day than in the 585-day sample, both in terms of unit length and percentage of average thickness. In comparison with Zr-1Nb samples, in terms of oxide thickness variation X2 seems to be in between annealed and as-recrystallised Zr-1Nb. However, X2 may have greater oxide thickness variations over a larger analysis area. Although the O/M interface of X2 seems to be relatively flat, this is clearly not the case on the atomic scale (Chapter 5).

Table 4.8: Oxide thickness measurement results from X2 samples.

Samples	**Measured thickness values (h) (µm)**		**Averaged thickness ($h_{average}$) (µm)**	**Thickness variation (h_{max}-h_{min}) (µm)**	**Thickness variation ($\frac{h_{max}-h_{min}}{h_{average}}$) (%)**
	Lowest (h_{min})	**Highest (h_{max})**			
225-day	2.61	3.17	2.96	0.55	18.8
585-day	6.53	6.86	6.69	0.32	4.9
Irradiated (1 cycle)	1.746	2.328	1.987	0.582	29.3

In comparison with unirradiated samples, irradiated X2 clearly has much lower oxidation rate in overall. The 585-day X2 sample has ~3.4x thicker oxide than the irradiated X2, and is also already in post transition regime (presumably third transition). Moreover, the O/M interface of irradiated sample is less uniform compared to both unirradiated ones.

Because there were no hydrogen measurements on this material, they are not suitable for studying HPU. APT analyses on X2 were aimed at the O/M interface as it has a relatively thick suboxide in comparison to Zr-1Nb materials with distinct morphology on the atomic scale (Chapter 5).

4.3.4. Zr-2.5Nb

The Zr-2.5Nb samples were Canada Deuterium Uranium (CANDU) pressurised tubes. These samples are the back of Tube F in [197]. They were processed by β-quenching followed by hot extrusion, cold working and stress relieving at 400ºC for 24 hours [196]. This heat

treatment results in elongated α-Zr grains partially surrounded by a thin network of filaments of β-Zr. During the stress relieving stage, β-Zr can decompose to β-Nb with Nb content in the β phase of ~62% [197].

This material was only exposed to heavy water with the addition of lithium oxide at 335°C [197], a slightly lower temperature than most of the oxidised samples. The selected samples include those after 150 and 1040 days, which are ideal to study deuterium in the oxide (Chapter 6). Moreover, the higher Nb content in this material in comparison to those described above makes it suitable to study the oxidation of numerous Nb-containing particles (Chapter 8). Although the autoclave testing was carried out until 1800 days, only 6 data points were taken and hence these specimens are not suitable to study oxidation rates in detail.

Due to the lack of data points, it is also not possible to determine the transition points in this material (Figure 4.14). Transition occurs somewhere between 600-1040 days where there is a steep gradient between 600 and 1040 days, corresponding to an acceleration of both oxidation and deuterium pickup (DPU) between these two points.

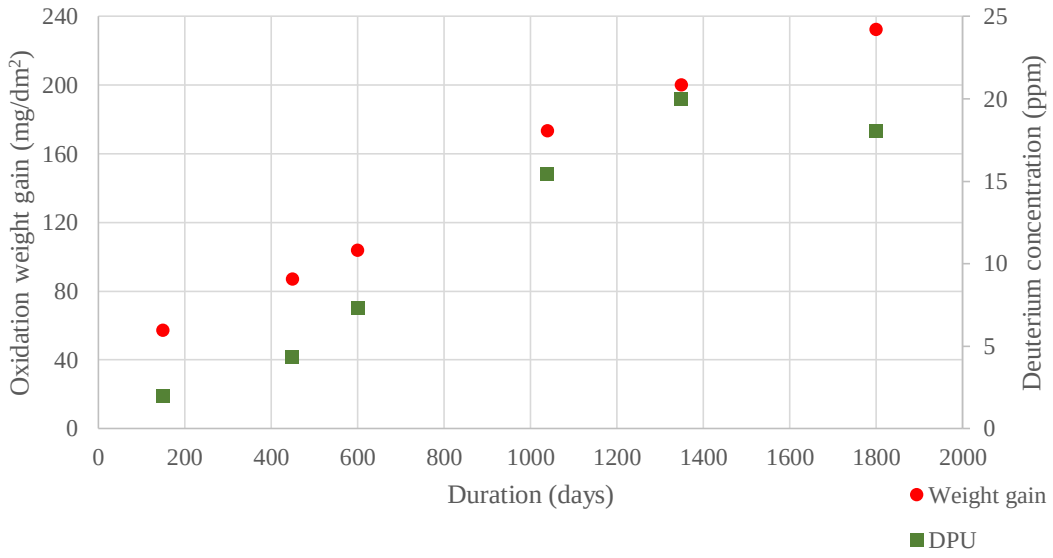


Figure 4.14: Oxidation weight gain and DPU of Zr-2.5Nb.

Based on the SEM micrographs, the oxide of the 150-day sample seems to have an absence of cracks, suggesting that this sample may be in the pre transition regime (Figure 4.15a). The 1040-day oxide contains at least one layer of big cracks parallel to the O/M interface, indicating that this sample is post-transition (Figure 4.15b). The 1040-day sample also contains another porous layer having ~2μm thickness at the top of ZrO_2 that gives a different contrast and distinct interface. According to EDX analysis using an EVO MA10 instrument, this oxide contains roughly ~20 at% Cr, ~10 at% Ni, and ~70 at% O that is most likely deposited from the stainless steel autoclave. Because this oxide layer does not appear in the 150-day sample and other samples analysed in this thesis, the deposition of such oxide could take hundreds of days. This oxide is not included in determining the oxide thickness of the 1040-day sample.

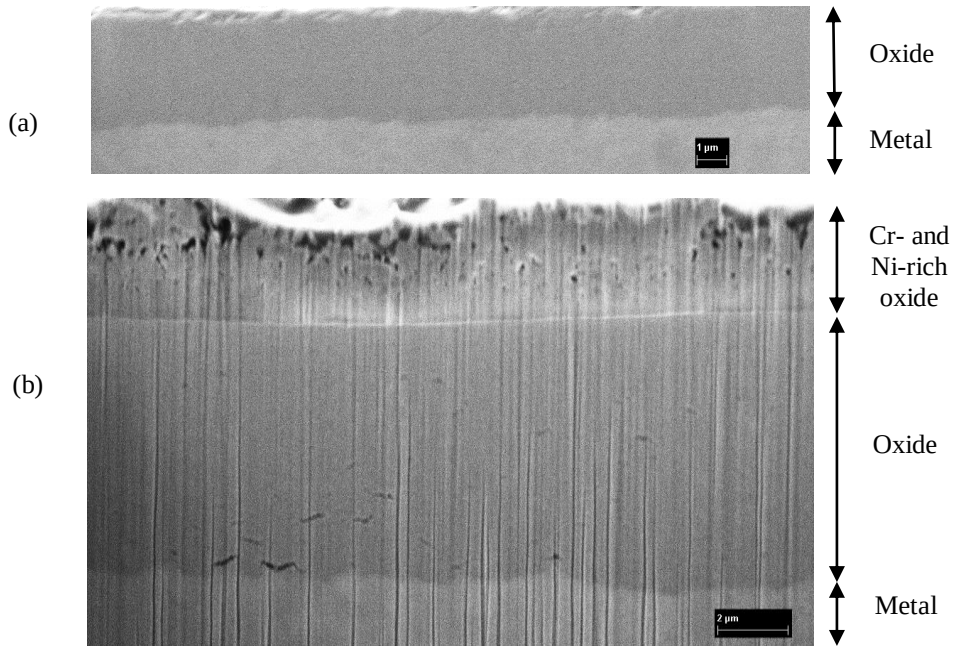


Figure 4.15: SEM micrographs of the O/M interface of Zr-2.5Nb oxidised for: (a) 150 and (b) 1040 days. The oxide has darker contrast at the top of each image, and the metal with lighter contrast at the bottom. For (b), the layer at the top is a Cr-rich oxide.

The thickness variation (in length) increases with oxidation (Table 4.9), which is also the case for the Zr-1Nb samples (Table 4.7). In comparison with the theoretical oxide thickness

values, the measured average oxide thickness of 150-day sample shows a good agreement, but this is not the case for 1040-day sample. The measured oxide thickness in the 1040-day sample is only ~72% of the weight gain value, indicating that this sample has inhomogeneous oxide thickness across the entire sample. Unlike the Zr-1Nb samples, this material shows that the thickness variation (as a fraction of total thickness) decreases with oxide thickness, suggesting that the interface of 150-day sample is very uniform, while the 1040-day one is much more uneven. Apart from local variations, the different oxidation behaviour between this material and Zr-1Nb might be attributed to other factors such as temperature and water chemistry.

Table 4.9: Oxide thickness measurement results from Zr-2.5Nb.

Samples	**Measured thickness values (h) (µm)**		**Averaged thickness ($h_{average}$) (µm)**	**Theoretical oxide thickness (weight gain /15) (µm)***	**Thickness variation (h_{max}-h_{min}) (µm)**	**Thickness variation ($\frac{h_{max}-h_{min}}{h_{average}}$) (%)**
	Lowest (h_{min})	**Highest (h_{max})**				
150-day	3.57	3.82	3.71	3.81	0.24	6.7
1040-day	7.22	10.09	8.31	11.55	2.87	34.5

*Weight gain is in mg/dm^2.

4.3.5. Zr-0.5Nb-0.1Sb

Zr-0.5Nb-0.1Sb alloy was provided in an as-recrystallised condition and tested in a light water autoclave in the same manner as Zr-1Nb but only for 195 days. A control material of Zr-0.5Nb was also tested for comparison, but was not analysed in this study because the main purpose of this sample is to analyse the Sb distribution during oxidation to try and explain the effect of Sb on the oxidation performance. The studied materials include 15-day and 195-day samples, both pre-transition.

In comparison with Zr-0.5Nb, Zr-0.5Nb-0.1Sb has a superior corrosion behaviour, presumably due to the presence of Sb (Figure 4.16). These two alloys have the best corrosion

performance of all materials studied in this work, and still in pre transition after 195 days. HPU was not measured in all data points (Figure 4.17), but both materials are still in pre transition and demonstrate extremely low HPU up to 105 days. However, between 105-120 days there is a significant HPU increase for Zr-0.5Nb that continues until 165 days. In contrast, Zr-0.5Nb-0.1Sb does not show this increase and maintains low HPU throughout the test.

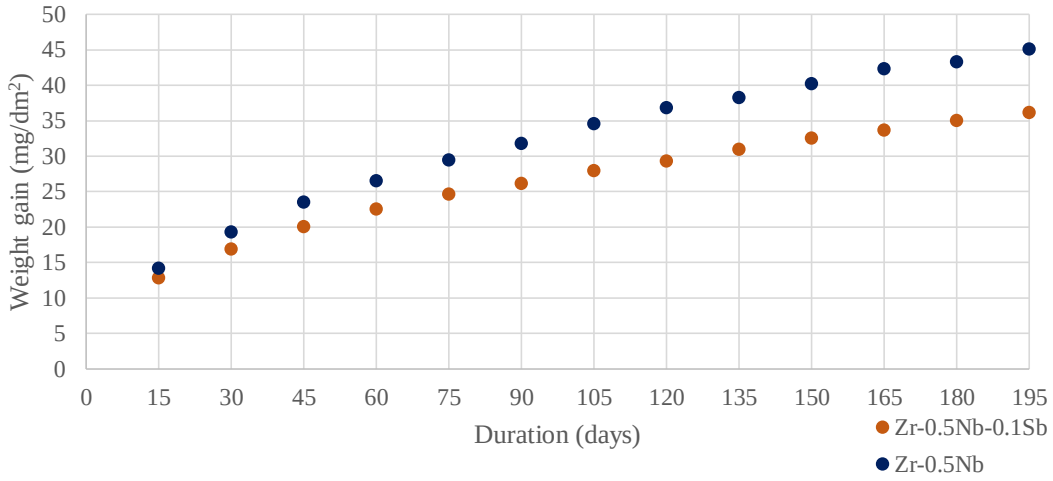


Figure 4.16: Oxidation kinetics of Zr-0.5Nb-0.1Sb and Zr-0.5Nb.

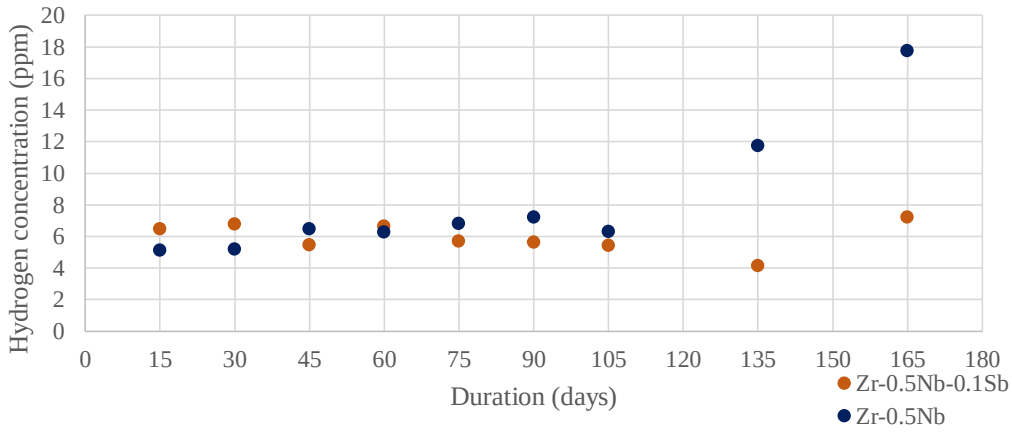


Figure 4.17: HPU kinetics of Zr-0.5Nb-0.1Sb and Zr-0.5Nb alloys.

These two materials have very low HPU rates, and even show apparently negative values (Figure 4.18). Similar to the HPU kinetics, the difference between samples at 135 days can also be observed in HPU rate curves, where the HPU rate of Zr-0.5Nb (0.19 ppm/day) is ~6.4x higher than for Zr-0.5Nb-0.1Sb (0.03 ppm/day).

The oxide layers of 15-day and 195-day Zr-0.5Nb-0.1Sb appear similar; there is almost no sign of cracks even at 195 days, implying that the oxide is still in pre transition (Figure 4.19a-b). The sample with thinner oxide (15-day) has closer measured average thickness to the weight gain oxide thickness value than the sample with thicker oxide (195-day). Over the course of 180 days (from 15 to 195 days), the oxide of this alloy only grows ~1.5µm (Table 4.10). This is relatively small compared to other alloys in this study as the oxide on as-recrystallised and annealed Zr-1Nb grow ~2.5µm and ~7.2µm respectively during the same period. However, the O/M interfaces in both Zr-0.5Nb-0.1Sb and Zr-0.5Nb samples are non-uniform as the thickness variation value of 67.4% of average thickness at 195 days is very large in comparison with Zr-1Nb samples oxidised for a similar duration.

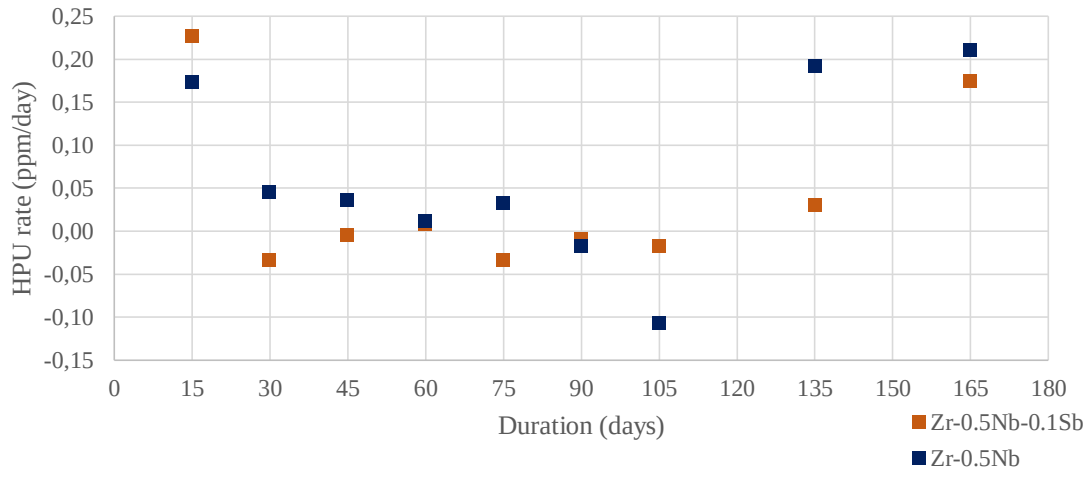


Figure 4.18: HPU rate of Zr-0.5Nb-0.1Sb and Zr-0.5Nb alloys.

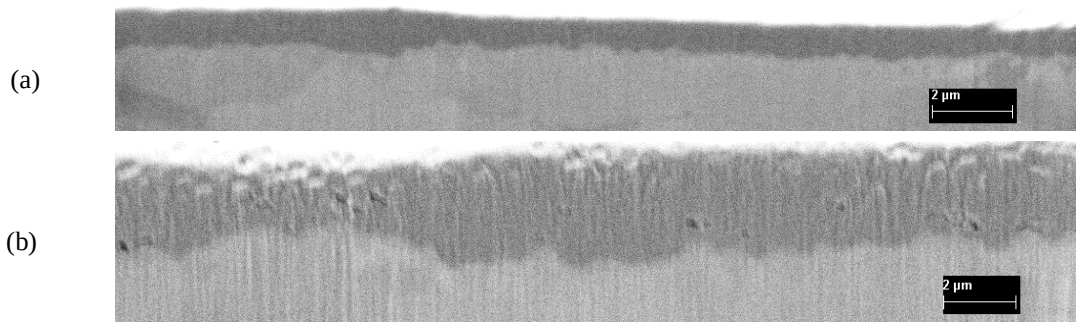


Figure 4.19: SEM micrographs of the O/M interface of Zr-0.5Nb-0.1Sb oxidised in: (a) 15 and (b) 195 days. The oxide has darker contrast at the top of each image, and the metal with lighter contrast at the bottom.

Table 4.10: Oxide thickness measurement results for Zr-0.5Nb-0.1Sb.

Samples	Measured thickness values (h) (µm)		Average thickness ($h_{average}$) (µm)	Theoretical oxide thickness (weight gain /15) (µm)*	Thickness variation (h_{max}-h_{min}) (µm)	Thickness variation ($\frac{h_{max}-h_{min}}{h_{average}}$) (%)
	Lowest (h_{min})	Highest (h_{max})				
15-day	0.56	1.20	0.88	0.85	0.63	72.5
195-day	1.45	3.03	2.35	3.00	1.58	67.4

*Weight gain is in mg/dm^2.

4.4. Summary

Table 4.11: Summary of sample information.

Materials	Important information	Analysis objective
Unoxidised metals (annealed and as-recrystallised Zr-1Nb)	Metal only.	Metal matrix composition determinations, with a focus on Fe and Nb contents.
Annealed Zr-1Nb	Bad oxidation behaviour: three transition points within 225 days.	• Understanding the O/M interface of samples at different transition stages: including O and Fe profiles. • To investigate Fe redistribution upon oxidation.
As-recrystallised Zr-1Nb	Better oxidation behaviour than annealed Zr-1Nb: only one transition point within 225 days.	Comparison with annealed Zr-1Nb regarding O and Fe profiles near the O/M interface.
X2	Transitions 360-540 days. Also have irradiated X2.	• Understanding suboxide and different O/M interface morphologies. • Irradiated sample is for comparison with unirradiated samples in terms of Fe and Nb redistribution.
Zr-2.5Nb	Only treated in heavy water.	Oxide analysis for understanding deuterium distribution and oxidation of Nb-rich particles.
Zr-0.5Nb-0.1Sb	Excellent oxidation and HPU behaviour.	Study Sb distribution and comparison with Zr-Nb system.

5. OXYGEN

5.1. Introduction

This chapter discusses the oxygen distribution in the oxide, metal and at the O/M interface, but the focus is aimed at understanding the O/M interface. This region is complex both in terms of microstructure and chemistry and information about the O distribution is crucial in studying the oxidation process because it can be used to relate the microstructure, morphology, and chemistry of the O/M interface to the overall oxidation behaviour described in Chapter 4.

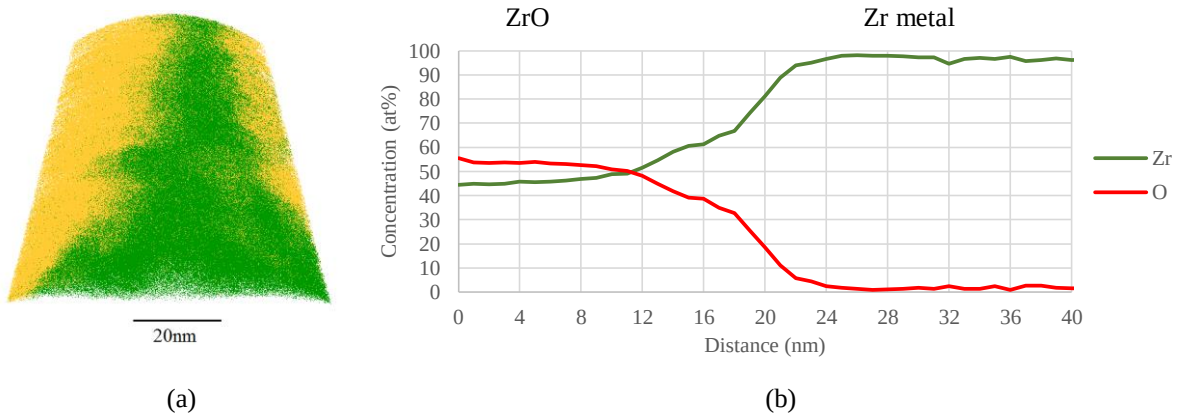
The materials used for this analysis included annealed and as-recrystallised Zr-1Nb, and unirradiated X2. In the former two I analysed the content of O in all regions, while in X2 I studied the suboxide and sawtooth-shaped O/M interface.

5.2. Oxygen in the metal

O in the bulk metal is an impurity from the manufacturing process due to the high affinity of Zr for O [24]. The choice of laser energy can affect the amount of O detected in the metal in APT analysis, but the measurements in this study are in a good agreement with Hudson who suggested that between 0.3-0.6nJ laser energy the apparent O content remains roughly constant at ~0.65 at% in ZIRLO [6]. The overall O concentrations in the metal samples of both as-recrystallised and annealed Zr-1Nb are 1.06 at% (~0.19wt%) and 1.38 at% (~0.24wt%) respectively, well below the O solubility limit in α-Zr, (~28.6 at%) at any temperature below ~1525°C [34,57,65,202]. These values are not significantly different between samples; the measured standard deviations were 0.35 at% and 0.39 at% for the annealed and as-recrystallised samples respectively (Table 4.2 and Table 4.3). In none of the

datasets was any sign of O segregation observed, suggesting that the O distribution in the bulk metal is very uniform.

O can be introduced from external sources such as exposure to open air (during handling) or from the residual gases inside the LEAP analysis chamber [203]. For electropolished samples, O from the electropolishing solution could diffuse into the sample, resulting in increased O concentration and the formation of metastable ZrO layer with a Zr/O ratio of ~45:55 (Figure 5.1a-b). Although this ratio is slightly lower than the previous APT results [6,204], this value is very close to the ZrO composition. The native oxide forms immediately on an atomically clean Zr specimen surface within the first 5 minutes of exposure, followed by a linear oxide growth rate up to 1 hour but this only results in 0.1 at% O concentration variation in the metal [6,205].



(a) (b)

Figure 5.1: (a) An atom map of an electropolished sample containing the ZrO suboxide (yellow) and Zr metal (green) and the concentration profile across the O/M interface obtained from a cylinder ROI perpendicular to the interface.

5.3. Oxygen in the bulk oxide

There is an assumption that the bulk oxide is stoichiometric ZrO_2 with Zr/O atomic ratio 1:2. However, despite the inclusion of all the O-containing ions in the oxide mass spectrum, the Zr/O ratio in all oxide sample is always above 1:2 (Table 5.1: Zr/O ratios in different

materials.). With 3σ confidence, the lower limits of the measured Zr/O ratios are 0.52, 0.53 and 0.53 for annealed, as-recrystallised Zr-1Nb and X2 materials respectively, implying that APT analysis of bulk ZrO_2 systematically results in Zr/O ratio above 0.5.

Table 5.1: Zr/O ratios in different materials.

Materials	Average concentration (at%)		Zr/O ratio	Standard deviation	Number of observations
	Zr	O			
Annealed Zr-1Nb	35.51	64.35	0.55	0.017	28
As-recrystallised Zr-1Nb	35.66	64.17	0.56	0.011	7
X2	34.96	64.74	0.54	0.007	5

A possible explanation for this systematic error is that the oxide matrix is evaporated in the form of molecular ions (Section 3.2.3.2). Molecular ions can be unstable under the effect of the intense electric field and prone to dissociation, a process by which molecular ions dissociate into either two daughter ions or in some cases a charged ion and a neutral species [206]. If the dissociation occurs relatively far from the specimen such that there is insufficient field to post-ionise the neutral species, it will not be detected. This could be due to two main reasons. Firstly, because the neutral species is not further accelerated by the field, it may not accumulate sufficient energy to trigger the detection [207]. Secondly, it may not hit the detector due to taking a radial trajectory as it is unaffected by the electric field (Figure 3.8) [208]. Whether the neutral species can be subsequently ionised is still a matter of debate, but there is a strong indication that this is possible if the dissociation occurs very close to the specimen surface such that the ionised neutral species acts like an imaging gas molecule in FIM [208].

This loss of stoichiometry in ZrO_2 analysis has been reported [209] but there is limited information regarding the extent of which the neutral species generation affects the stoichiometry and the ions that dissociate into neutral species. There is a discrepancy between

the stoichiometry measured in this thesis with the results from Dong et al. where they reported Zr/O ratios of ~0.50 and ~0.47 in the oxides on crystal bar Zr and Zircaloy-4 respectively [210]. This could be due to different instrumentation and, more importantly, the type of laser used in those experiments. Kirchhofer et al. postulated that the correct stoichiometry can be achieved at a low temperature and laser energy, as increasing laser energy can also increase the number of complex molecular ions that could subsequently dissociate into neutral species [207,208,211]. Although the loss of stoichiometry is inevitable but the results in this thesis show a good agreement with EELS where the measured O concentration within ±1-5 at% was reported [10,212].

5.4. Oxygen at the O/M interface

5.4.1. Layered oxide structure

At the beginning of aqueous oxidation, the oxidation rate is extremely high and therefore there is a high influx of O injection from the water to fresh metal. However, in the later stage of pre transition the oxidation rate decreases, corresponding to restricted O supply, resulting in the formation of suboxides (Section 2.3.1) [6,10,61].

Although APT can measure the composition of a suboxide, it is not possible to determine its crystallography, i.e. whether it is one of the known suboxide phases. Because the peak O solubility in α-Zr is ~30 at%, the assumption in this study is that if the O content of a region is ~30 at% (remainder Zr), it is considered to be an O-saturated metal. Under a layer of this stoichiometry, it is normal to see the O concentration decrease gradually to a bulk metal value well below 30 at%. The suboxides in Section 2.3.1 have O contents ranging from ~14-66%, but the only phase in this study that is considered a suboxide is ZrO because it is the only one usually identified by electron microscopy based techniques for mapping crystal structures

[10,63,99]. Therefore, the layered structure with decreasing O content analysed at the O/M interface is: ZrO_2-ZrO-Zr(O_{sat})-bulk metal.

5.4.2. Suboxide thickness measurements

A well-defined ZrO suboxide layer is only occasionally detected in the as-recrystallised and annealed Zr-1Nb specimens (Table 5.2). Because the suboxides are generally very thin, and in some datasets are located at the beginning of the analyses, the mass spectrum contains a high background level due to high level of contamination being evaporated from the specimen surface, that reduces the accuracy of compositional analysis.

There is no obvious trend regarding the growth of suboxide at different oxidation stages in either as-recrystallised or annealed Zr-1Nb (Table 5.2). Firstly, this could be due to a lack of datasets containing suboxide. This is important considering that due to the local variations of oxide thickness and oxidation rate, more data are required for a more thorough analysis. Furthermore, if a dataset contains only suboxide and metal, or oxide and suboxide, the whole suboxide thickness in the specimen is not accurately measured. It is difficult to engineer a sample containing a specific thickness of suboxide, as during specimen preparation the suboxide gives the same contrast as the oxide under SEM. In addition, some datasets contain unusual sawtooth-shaped O/S (oxide/suboxide) or S/M (suboxide/metal) interfaces (Section 5.4.4) and in this case, the determination of the suboxide thickness is not straightforward.

The only datasets with adequate information about the suboxide are from X2. As there are only two samples from this material, it is not possible to study suboxide layer growth as a function of oxidation time. An example of a sample with ~320nm ZrO suboxide is presented in Figure 5.2. The Zr/O ratio is not constant throughout the suboxide; there are two regions with slightly different Zr/O ratio; one region is richer in O (ZrO') and the other in Zr (ZrO''). The Zr:O ratio of ZrO' and ZrO'' is roughly ~47:52 and ~51:48 respectively. ZrO' and ZrO''

regions have been observed previously [6,210]. Apart from neutral species generation (Section 5.3), the reason for this is possible associated with the sample geometry and thermal conductivity differences between these regions [6]. As the stoichiometries of ZrO' and ZrO'' are very close to ZrO, they are both best described as the ZrO phase.

Table 5.2: Suboxide in annealed, as-recrystallised Zr-1Nb and X2.

Materials	**Oxidation duration (days)**	**Total number of analyses with O/M interface**	**Total number of analyses containing suboxide**	**Total number of analyses containing the whole suboxide**	**Minimum suboxide thickness (nm)**	**Maximum suboxide thickness (nm)**
Annealed Zr-1Nb	3	8	2	2	30	60
	30	6	1	1	120	120
	46	6	3	1	70	300*
	91	6	2	2	30	45
	105	4	2	1	10	40
	225	3	2	0	50	120
As-recrystallised Zr-1Nb	3	4	2	0	30	30
	210	5	2	1	10	10
X2	225	3	2	0	250	320
	585	4	4	0	30	380*

*The suboxide in these datasets is very narrow and has a sawtooth-shaped O/S or S/M interface.

The S/M interface (Figure 5.2) is sharp since there is an abrupt decrease of O concentration from ZrO to the bulk metal across the interface. In the global scale, the suboxide is non-uniform throughout the sample (Figure 5.3a-b) where the O/S and S/M interfaces are undulated, and in the extreme case could form sawtooth-shaped interfaces (Section 5.4.4). There is also a ~10nm $Zr(O_{sat})$ layer between the suboxide and metal before the O concentration drops gradually from ~30 at% to the impurity concentration level in the bulk metal.

The ZrO behaves more like a metal during the APT experiments, except that it is mostly evaporated as $ZrO^{1,2,3+}$ ions, in that its mass spectrum does not contain big thermal tails. Out

of three X2 samples containing a significant suboxide, the average Zr:O ratio in the suboxide is ~51.1:48.4. This is very close to reports in the literature; ~51.1:48.1 and ~51.1:48.8 in Zircaloy-4 and Zr-Fe-Cr suboxides respectively [210].

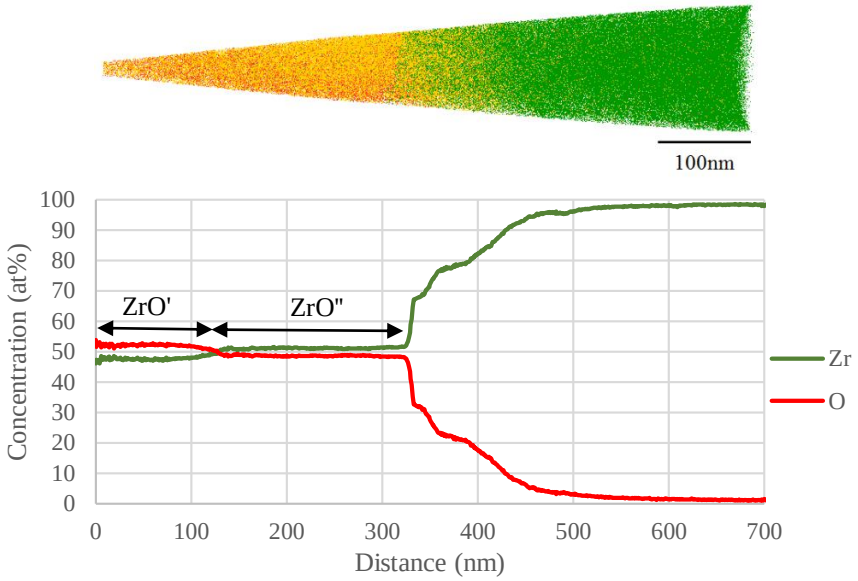
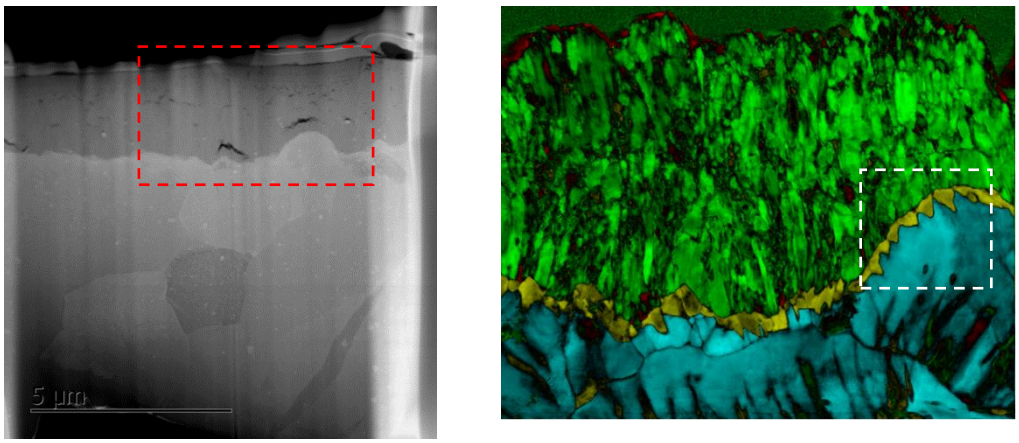


Figure 5.2: Atom map and the concentration profile across the S/M interface of a 225-day X2 sample. The red, yellow and green dots in the atom map correspond to O_2^+, $ZrO^{1,2,3+}$ and $Zr^{1,2,3+}$ ions respectively. The suboxide (left) is dominated by $ZrO^{1,2,3+}$ ions and the metal (right) by $Zr^{1,2,3+}$ ions. The concentration profile is obtained from a cylinder ROI penetrating perpendicular to the S/M interface and includes the entire sample length.



(a) (b)

Figure 5.3: (a) An SEM image of O/M interface of 120-day X2 and (b) the precession diffraction TEM image of the area inside the red box from (a) showing the sawtooth-shaped S/M interface (especially clear inside the white box) [201]. The red, green, yellow, and blue colours in (b) refer to t-ZrO_2, m-ZrO_2, ZrO, and Zr metal respectively.

The thicknesses of the detected suboxide are quite large; 250nm (225-day), 320nm, and 360nm (both 585-day) (Table 5.2). TEM results on the same material suggest that the averaged suboxide thickness in the 225-day and 585-day samples are 200nm and 30nm respectively [201]. While my value for 225-day sample is close to the average thickness measured by TEM, this is not the case for the 585-day sample, probably due to the local thickness variations.

5.4.3. Oxygen-saturated metal

When O is injected into the metal, an O-saturated layer ($Zr(O_{sat})$) containing ~30 at% O forms and the layer thickness evolves throughout the course of oxidation. Obtaining specimens containing the $Zr(O_{sat})$ regions is easier than ZrO because $Zr(O_{sat})$ is essentially a metal that gives different contrast to the oxide under SEM. Therefore, all samples containing the O/M or S/M interface contain $Zr(O_{sat})$, unless this layer does not exist in the sample. Because the APT analysis volume is very small, it is important to obtain more than one such dataset containing the entire length of the $Zr(O_{sat})$ region from each material.

I have achieved more than one dataset from each material (Table 5.3). There is a significant thickness variation in the $Zr(O_{sat})$ layer between samples from the same material, indicating that the local oxidation rate variation also affects this layer. There is no obvious correlation between the thickness variation and the averaged thickness, but it appears that the absolute thickness variation increases with average $Zr(O_{sat})$ layer thickness (Figure 5.4). In the pre-transition regime of annealed Zr-1Nb there is a trend of increasing $Zr(O_{sat})$ thickness over time, but this is not the case for the post transition samples. In all samples except 210-day as-recrystallised Zr-1Nb, the thickness variation is greater than 100% of the average values (last row in Table 5.3), suggesting that the $Zr(O_{sat})$ layer is rough.

Table 5.3: O-saturated metal region in annealed and as-recrystallised Zr-1Nb.

Materials	**Annealed Zr-1Nb**						**As-recrystallised Zr-1Nb**	
State of transition	Pre transition			Post transition			Pre transition	Post transition
Oxidation duration (days)	3	30	46	91	105	225	3	210
Number of analyses with O(S)/M interface	8	6	6	6	4	3	4	5
Number of analyses containing the whole Zr(O_{sat})	5	6	4	2	2	2	4	3
Minimum Zr(O_{sat}) thickness (h_{min}) (nm)*	0	6	18	0	10	11	5	49
Maximum Zr(O_{sat}) thickness (h_{max}) (nm)*	24	79	92	22	59	42	62	101
Averaged Zr(O_{sat}) thickness ($h_{average}$) (nm)*	9	29	48	11	35	27	21	69
Zr(O_{sat}) thickness variation (h_{max}-h_{min}) (nm)	24	73	74	22	49	31	57	52
Zr(O_{sat}) thickness variation ($\frac{h_{max}-h_{min}}{h_{average}}$) (%)*	266	251	154	200	140	115	271	75

*Data only taken from datasets containing the whole Zr(O_{sat}) layer.

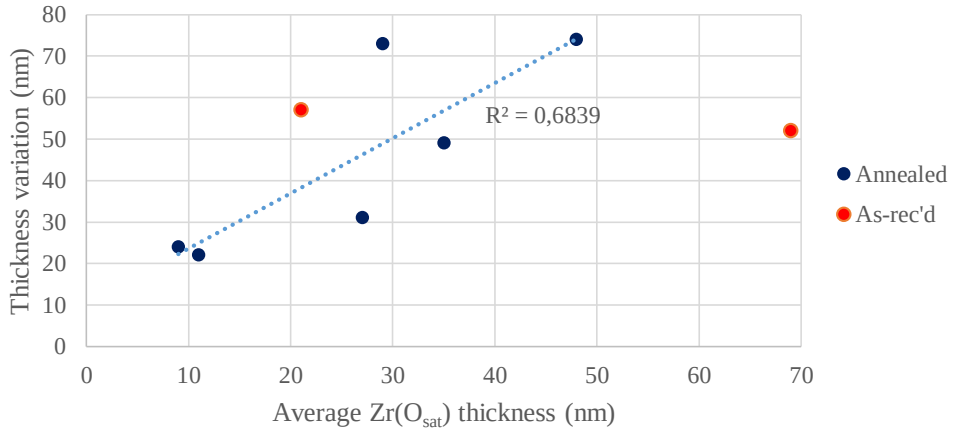


Figure 5.4: The average Zr(O_{sat}) layer thickness vs thickness variation in nm.

In the early pre-transition stage (3 days), 2 out of 8 samples do not have a detectable Zr(O_{sat}) layer where there is an abrupt O concentration decrease from the bulk oxide to metal (Figure 5.5a). However, the dataset with the thickest Zr(O_{sat}) layer shows ~24nm of constant ~30 at% O (Figure 5.5b), indicating that there is a local Zr(O_{sat}) layer thickness variation between different locations in the same sample. The 3-day annealed Zr-1Nb sample has a very high oxidation rate (~80.5 nm/day) and oxide thickness variation (~135% average thickness), the

highest among all the annealed Zr-1Nb samples. This is also seen in the Zr(O_{sat}) by with thickness variation of ~266% average, greater than all other samples despite having the second least absolute thickness variation (in unit length) due to having a very small average Zr(O_{sat}) thickness.

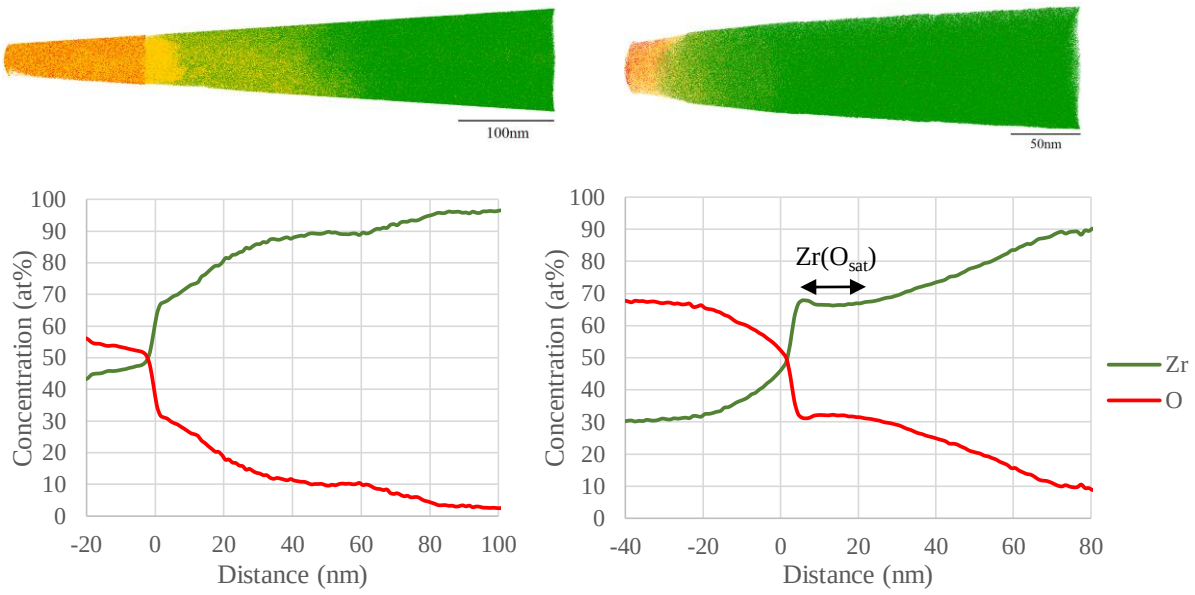
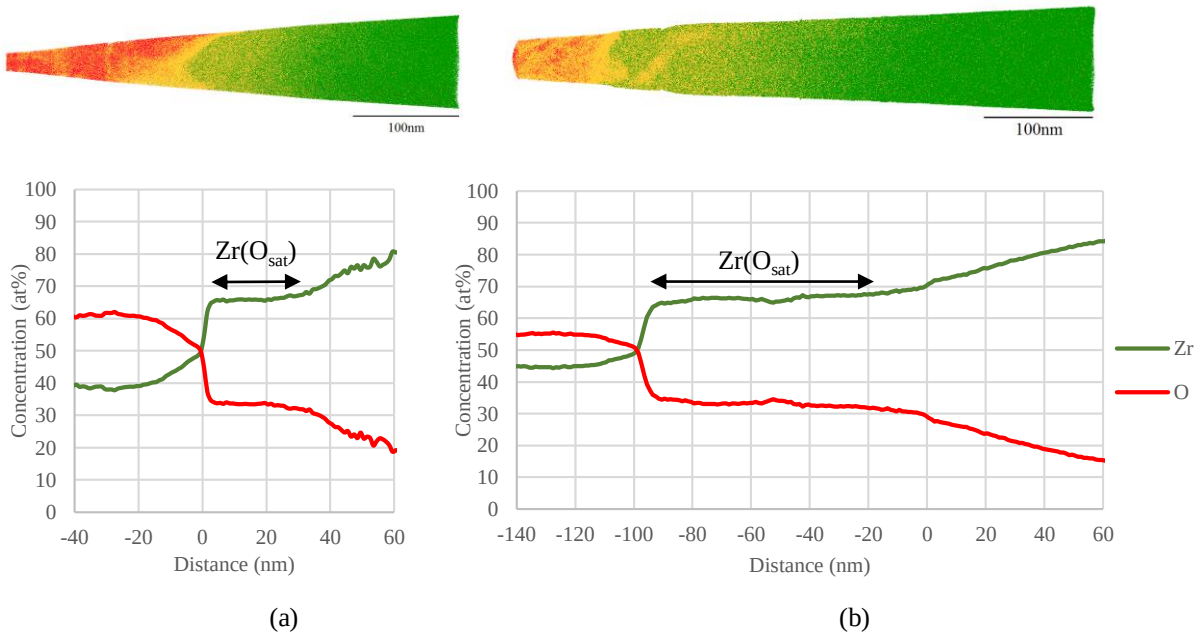


Figure 5.5: Atom maps and concentration profiles of Zr and O across the O/M interface of 3-day annealed Zr-1Nb samples taken by proxigrams at 40 at% and 50 at% O isosurfaces from datasets with (a) 0 and (b) ~24nm thick Zr(O_{sat}) layer. The red, yellow and green dots in the atom maps correspond to O_2^+, $ZrO^{1,2,3+}$ and $Zr^{1,2,3+}$ ions respectively.

At the latter stages of pre transition the oxidation rate decreases and there is not enough O to form ZrO_2, resulting in the build-up of O in the metal adjacent to O/M interface (Figure 5.6a-b). Despite some local variations, from 3 to 46 days there is an increase of average Zr(O_{sat}) thickness from 11nm (3 days) to 29nm (30 days) and finally to 48nm (46 days). The thickness variation also decreases during this period of time from 34nm/309% average (3 days) to 73nm/251% average (30 days) and 74nm/154% average (46 days).



(a) (b)

Figure 5.6: Atom maps and concentration profiles of Zr and O across the O/M and S/M interfaces of (a) 30-day and (b) 46-day annealed Zr-1Nb samples taken by proxigrams at 47 at% and 29 at% O isosurfaces respectively. The red, yellow and green dots in the atom maps correspond to O_2^+, $ZrO^{1,2,3+}$ and $Zr^{1,2,3+}$ ions respectively.

Although the pre-transition samples demonstrate a clear trend of Zr(O_{sat}) thickening with time, this does not continue in the post-transition samples (Figure 5.7a-c). After the transition point, there is a significant decrease of Zr(O_{sat}) thickness from 48nm (46 days) to 11nm (91 days) perhaps due to the accelerating rate of oxidation in the post transition regime. However, it is not clear exactly when the decrease of Zr(O_{sat}) thickness starts. This is in good agreement with de Gabory et al. [64] stating that both ZrO and Zr(O_{sat}) layers grow in thickness during the pre transition stage and are consumed by ZrO_2 shortly after transition.

After the first transition, the annealed Zr-1Nb undergoes 2 further transitions and therefore, the oxidation rate in this region does not decrease steadily as in the pre transition region but fluctuates several times. Because the O supply is responsible for the build-up of Zr(O_{sat}), it is the transient oxidation rate that should be taken into account rather than simply the total oxidation duration.

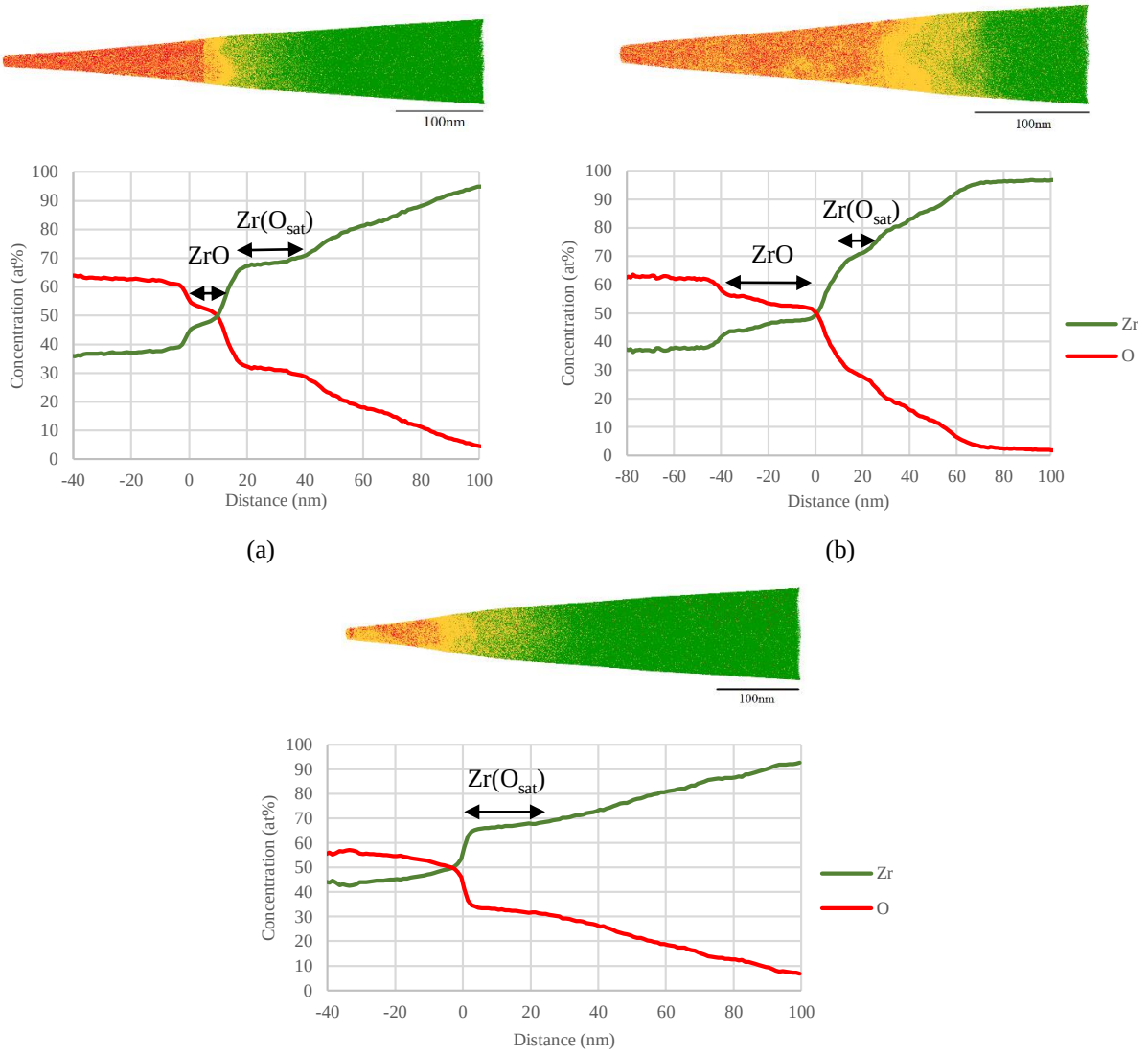


Figure 5.7: Atom maps and concentration profiles of Zr and O across the O/M and S/M interfaces of (a) 91-day, (b) 105-day and (c) 225-day annealed Zr-1Nb taken by proxigrams of 55 at%, 52 at% and 41 at% O isosurfaces respectively. The red, yellow and green dots in the atom maps correspond to O_2^+, $ZrO^{1,2,3+}$ and $Zr^{1,2,3+}$ signals respectively.

Even in the post-transition region, the Zr(O_{sat}) thickness evolution can still be seen, e.g. when comparing the 91-day and 105-day samples (both in the second transition stage). The 105-day sample has a lower oxidation rate (0.62 mg/dm^{2}day) compared to the 91-day sample (0.79 mg/dm^{2}day). Between these two points, the average Zr(O_{sat}) thickness increases from 11nm (91-day) to 35nm (105-day). This follows the trend in the pre transition sample; the Zr(O_{sat}) thickens as oxidation rate decreases from 91 to 105 days. In Figure 5.7a-b, there is a ZrO

suboxide layer between the ZrO_2 and $Zr(O_{sat})$ layer both in 91-day and 105-day samples that increases in thickness from 8nm (91-day) to 30nm (105-day). At the same time, the $Zr(O_{sat})$ thickness decreases from 22nm (91-day) to 10nm (105-day), indicating that there is a consumption of $Zr(O_{sat})$ through a reaction that results in ZrO that probably occurs between 91-105 days. The 225-day sample is located at the fourth transition but it is not possible to observe any fluctuations occurring between 105 and 225 days because no APT data was taken over this period.

In comparison with the 3-day annealed Zr-1Nb, the 3-day as-recrystallised Zr-1Nb sample has a thicker $Zr(O_{sat})$ layer with an average value of 21nm (more than twice that of the 3-day annealed Zr-1Nb) because as-recrystallised Zr-1Nb has a lower oxidation rate compared to the annealed Zr-1Nb. 3 out of 4 datasets from the 3-day as-recrystallised Zr-1Nb contain very thin $Zr(O_{sat})$ layers that are probably just signs of the onset of $Zr(O_{sat})$ formation (Figure 5.8a).

As the oxidation progresses through the transition point, at 210 days the $Zr(O_{sat})$ thickness increases to 69nm. The 210-day sample has the thickest $Zr(O_{sat})$ layer of all annealed and as-recrystallised Zr-1Nb samples. The one with the thickest $Zr(O_{sat})$ layer contains 101nm of this layer (Figure 5.8b). It is not clear if there is any thickness reduction shortly after the transition point, but because of the rather gradual transition in this sample (Section 4.3.2), there are presumably areas in this material that are still in pre transition, and therefore it is not possible to determine the O/M interface state of the analysed specimens right at transition. For this rather sparse data, the as-recrystallised sample also follows the trend of the pre-transition annealed sample; the $Zr(O_{sat})$ thickness increases over time and with decreasing oxidation rate.

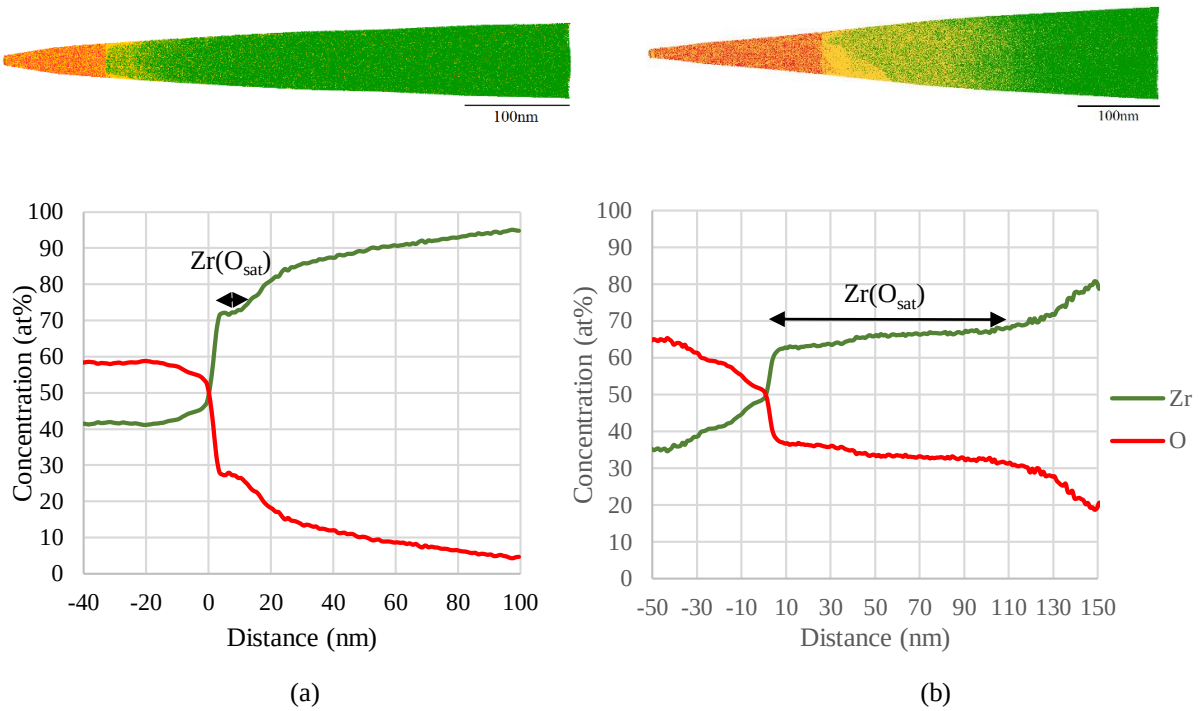
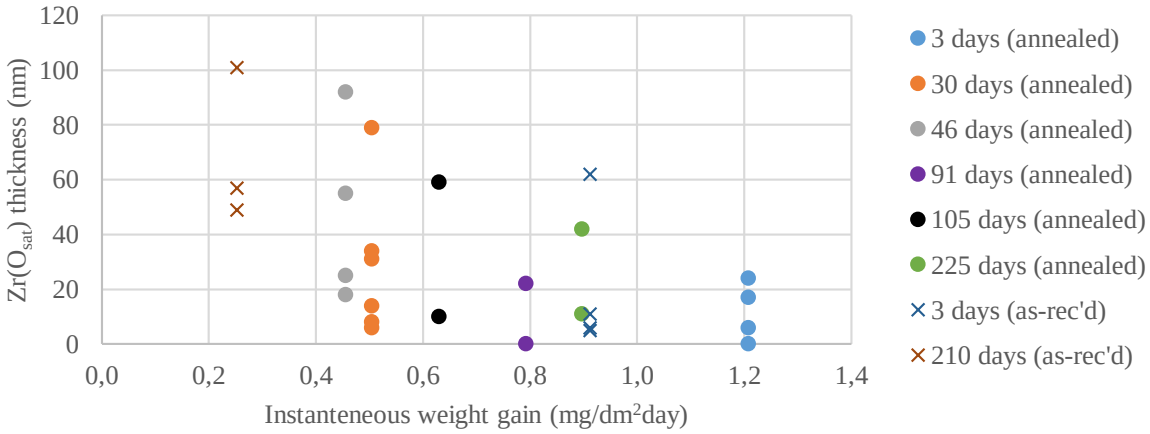
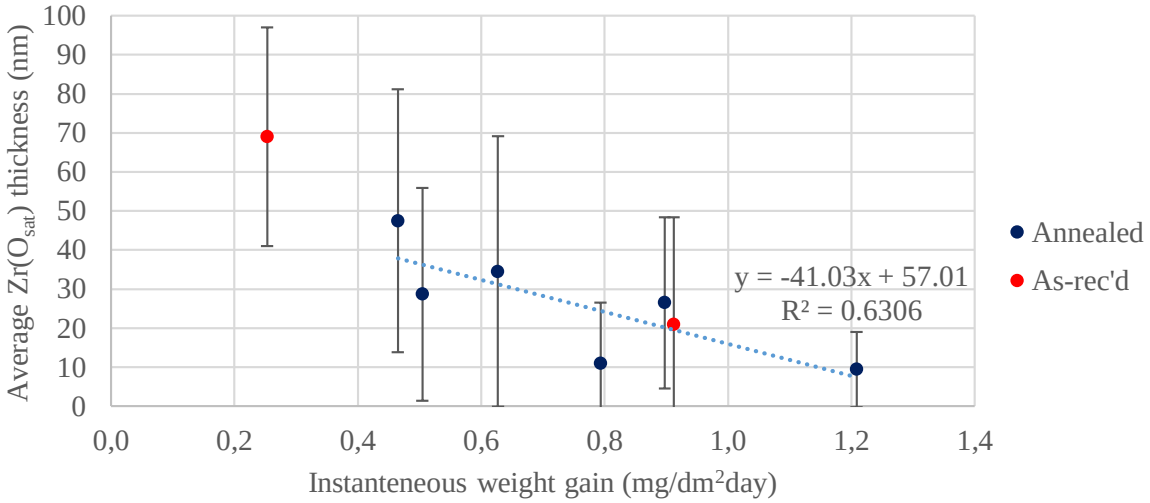


Figure 5.8: Atom maps and concentration profiles of Zr and O across the O/M interfaces of (a) 3-day and (b) 210-day as-recrystallised Zr-1Nb samples, both taken from proxigrams at 50 at% O isosurfaces. The red, yellow and green dots in the atom maps correspond to O_2^+, $ZrO^{1,2,3+}$ and $Zr^{1,2,3+}$ ions respectively.

If the Zr(O_{sat}) thickness for all the Zr-1Nb samples studied is plotted against instantaneous oxidation rate, a clear relationship can be observed (Figure 5.9a-b). It is important to reiterate that there are strong Zr(O_{sat}) thickness variations between samples of the same material, and there are a limited number of observations especially in the post transition regime. Nevertheless, results from the work reported here indicate that as the instantaneous oxidation rate increases, the Zr(O_{sat}) thickness decreases. This trend seems to be followed for all samples of both as-recrystallised and annealed materials regardless their states of transition.



(a)



(b)

Figure 5.9: (a) The Zr(O_{sat}) thickness data from annealed and as-recrystallised Zr-1Nb and (b) the averaged Zr(O_{sat}) thickness, both plotted against instantaneous oxidation rate.

5.4.4. Sawtooth-shaped interfaces

The non-uniformity of oxidation rate across a sample can not only result in local variations of suboxide and Zr(O_{sat}) thicknesses, but also the O(S)/M and O/S interface morphology. In an ideal case where the oxidation rate is relatively uniform across a sample, we might expect the O/M interface to be flat. However, this is not always the case (Section 4.3). In an extreme case, the interface between ZrO suboxide and the undulating metal can have a sawtooth

shape, containing needle-like segments that are sharp on the submicron scale. This is the so-called the sawtooth-shaped or Widmanstatten interface [99].

Sawtooth-shaped S/M interfaces have been observed previously [6,62,64,82,210], including protruding oxide segments into these suboxide or metal as well as protruding ZrO into the metal matrix. Because the sawtooth-shaped interfaces are extremely fine, they are hard to resolve in SEM images during specimen preparation. Therefore the images in Section 4.3 cannot be used to determine whether or not such interface exists in any particular sample. Using the precession diffraction TEM technique [213], it is possible to examine this interface (Figure 5.3a-b). APT can then be used to analyse these structures at higher resolution.

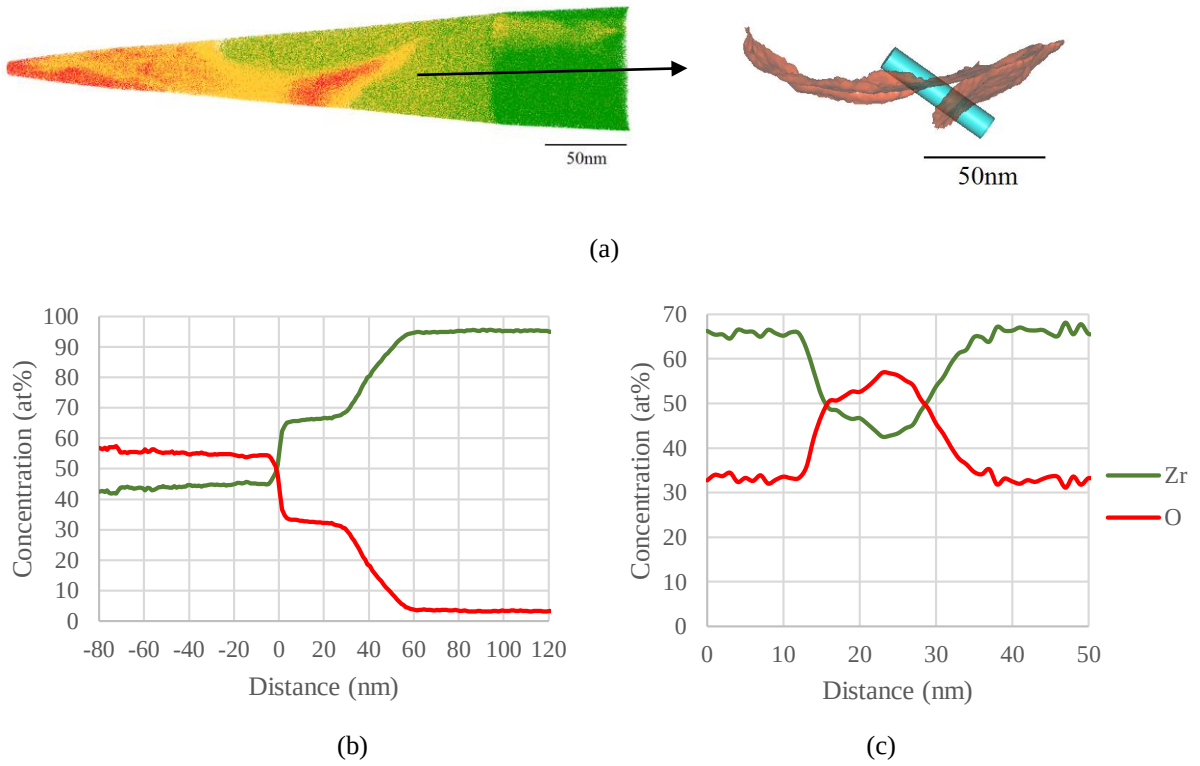
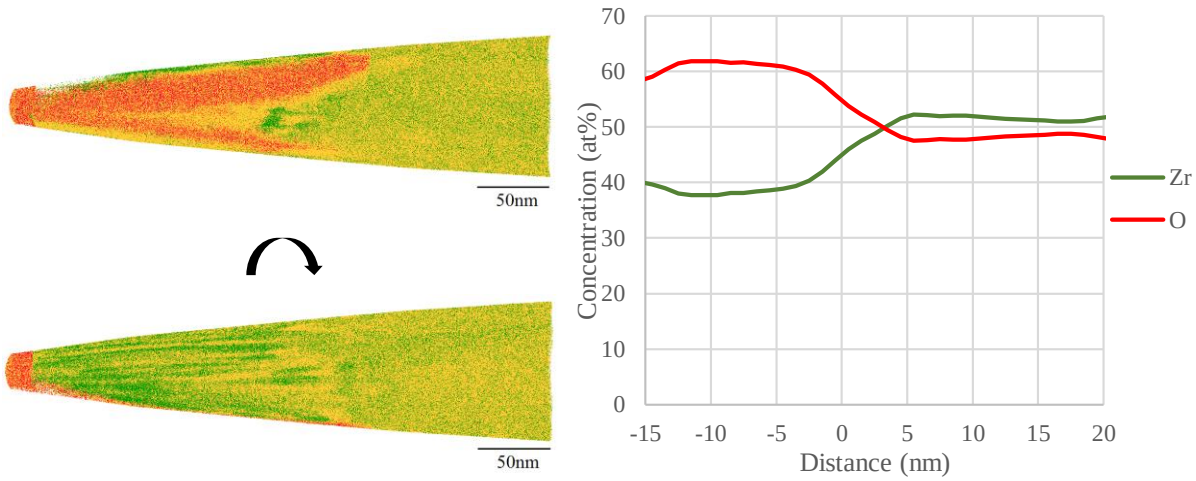


Figure 5.10: (a) Atom map of the sawtooth-shaped O/M interfaces of 46-day annealed Zr-1Nb, and a 45 at% O isosurface showing the location of a cylinder ROI penetrating through the isosurface. The red, yellow and green dots in the atom maps correspond to O_2^+, $ZrO^{1,2,3+}$ and $Zr^{1,2,3+}$ ions respectively. (b) is the concentration profile of Zr and O taken from a proxigram of the 45 at% O isosurface and (c) across the cylinder from (a).

This type of interface is not common in my samples. Among all datasets from annealed, as-recrystallised Zr-1Nb and X2, only 3 samples contained this type of interface; 46-day and 91-

day annealed Zr-1Nb (1 dataset each) and 585-day X2 (2 datasets). In the 46-day annealed Zr-1Nb, there is a sawtooth-shaped O/M interface characterised by the protrusion of suboxide into the Zr(O_{sat}) layer (Figure 5.10a), showing the locally uneven oxidation rate at the nanometre scale (Figure 5.10b-c). In the same dataset, there is also a region inside the Zr metal that is rich in $ZrO^{1,2,3+}$ ions, and can be interpreted as a local finger of Zr(O_{sat}). This also indicates locally accelerated oxide pickup in the metal region.

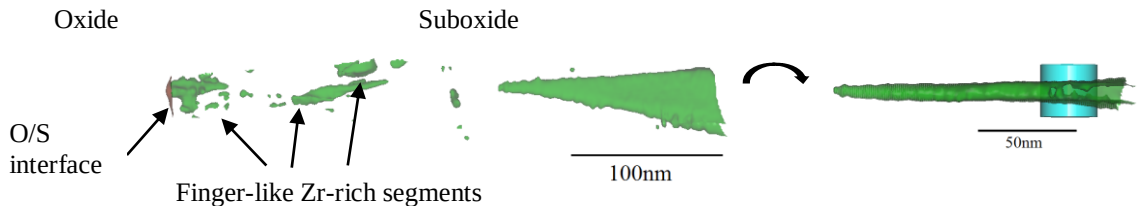
The oxidation rate of the 585-day X2 sample is probably very uneven as 2 out of 4 analyses contain sawtooth-shaped interfaces. The first dataset contains a sawtooth-shaped O/S interface with protruding oxide, corresponding to a region with a higher local oxidation rate (Figure 5.11a-b). In the region where the oxide is not protruding, there is another type of S/M interface in which there are finger-like Zr-rich segments penetrating into the suboxide matrix (lower image in Figure 5.11a). This region seems to be associated with a lower local oxidation rate.



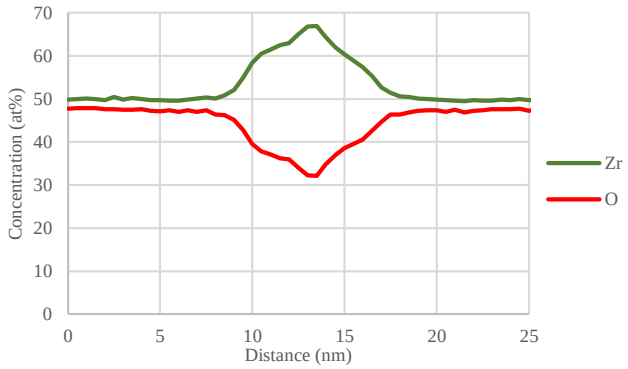
(a) (b)

Figure 5.11: (a) Atom maps showing two sides of the reconstruction of the sawtooth-shaped O/S interface of a 585-day X2 sample, and (b) the concentration profile of Zr and O across the interface taken from a proxigram of 55 at% O isosurface.

There is also a dataset with a protruding metal finger inside a suboxide matrix in the 585-day X2 material, similar to the lower oxidation rate region in the lower image of Figure 5.11a (Figure 5.12a-b). The metal contains a maximum of 30 at% O, corresponding to the Zr(O_{sat}) composition (Figure 5.12c). The presence of this layer supports a previous study that shows a sawtooth-shaped metal protrusion with similar composition [210].



(a)



(b)

Figure 5.12: (a) Isosurfaces of 52 at% O (red) and 55 at% Zr (green) near the O/S interface of a 585-day X2 sample, and a cylinder ROI penetrating the S/M sawtooth-shaped interface. (b) is the concentration profile of Zr and O across the cylinder in (a).

5.5. Discussion

As an α-stabiliser, the presence of O can alter the solubility limits of other elements such as Nb [214]. For example, ~0.27 wt% of O can reduce the Nb solubility limit by ~0.2 at% at ~900K (Figure 5.13). Nb concentration in the metal matrix are discussed in Chapter 8. In addition, O can also enhance the mechanical properties of Zr alloys [24,46].

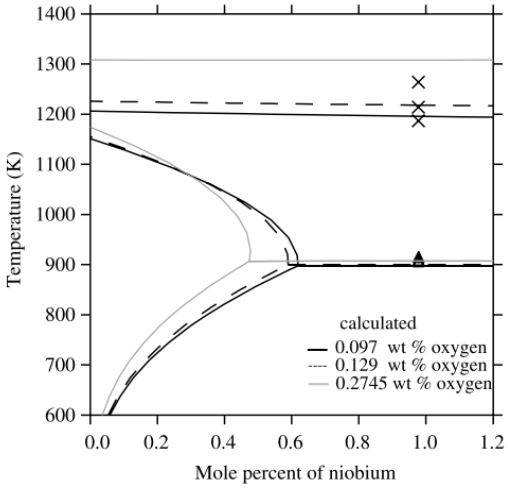


Figure 5.13: Calculated isoplethal section of the Zr-rich portion of the Zr–O–Nb system and measured data by Toffolon et al. [215]. The symbols denote measured data: Δ = α→(α+β) temperature; x =(α+β)→β temperature. The lines are calculated by Thermo-Calc: grey lines are for 0.2745wt% O, dashed lines for 0.129wt% O, black lines for 0.097wt% O [202,214].

Regarding the oxide growth, there are competing processes that occur in this multilayer oxide structure. Firstly, there is oxide formation from ZrO and $Zr(O_{sat})$ at the O/S and O/M interface respectively, with reactions:

$$ZrO + [O] \rightarrow ZrO_2 \quad (5.1a)$$

$$Zr(O_{sat}) + [O] \rightarrow ZrO_2 \quad (5.1b)$$

Secondly, at the S/M interface $Zr(O_{sat})$ can also be oxidised to form ZrO suboxide by the following reaction:

$$Zr(O_{sat}) + [O] \rightarrow ZrO \quad (5.2)$$

Thirdly, there is also the thickening of $Zr(O_{sat})$ in the metal adjacent to ZrO_2 or ZrO. These three processes all require an O supply, and the rates at which they occur depends on the arrival of O. Reactions 5.1a-b result in the advancement of O/S and O/M interfaces, and therefore can thin ZrO and $Zr(O_{sat})$ layers respectively. Reaction 5.2 favours the thickening of the ZrO layer and thinning of the $Zr(O_{sat})$ layer. Therefore, the thickness of the $Zr(O_{sat})$ layer is increased by the third process and decreased by the first and second.

Mathematically, this can be modelled using the theory of a double-layered scale on a pure metal [216]. This theory is based on the assumption that the rate of diffusion of metal cations outwards is much lower than O diffusion inwards, and therefore the growth rate of each layer is controlled by O transport. If the model is applied to this system, only ZrO_2 and ZrO are considered as the oxidised products, and not $Zr(O_{sat})$. The thickening rates of ZrO_2 ($\frac{dh_{ZrO_2}}{dt}$) and ZrO ($\frac{dh_{ZrO}}{dt}$) are given by:

$$\frac{dh_{ZrO_2}}{dt} = \frac{k'_p(ZrO_2)}{h_{ZrO_2}} \quad (5.3a)$$

$$\frac{dh_{ZrO}}{dt} = \frac{k'_p(ZrO)}{h_{ZrO}} \quad (5.3b)$$

$k'_p(ZrO_2)$ and $k'_p(ZrO)$ refer to the rate constants for parabolic growth when the ZrO_2 and ZrO form on the metal, respectively. h_{ZrO_2} and h_{ZrO} correspond to the thickness of ZrO_2 barrier layer and ZrO respectively. Because the oxidation rate is controlled by the protective layer in the innermost part of the oxide (the barrier layer), only this part of ZrO_2 is taken into account in this model [77,78,192]. These constants can be determined experimentally, but depend on the properties of all phases involved. By further modifications of Equation 5.3a-b, a relationship between h_{ZrO_2} and h_{ZrO} can be derived [217]:

$$\frac{h_{ZrO_2}}{h_{ZrO}} = \frac{V_{ZrO}k_p(ZrO_2)}{2V_{ZrO_2}k_p(ZrO)} \quad (5.4)$$

V_{ZrO_2} and V_{ZrO} are the average molar volume while $k_p(ZrO_2)$ and $k_p(ZrO)$ are the rate constants for parabolic growth of ZrO_2 and ZrO respectively. k_p is different to k'_p because k_p only depends on the properties of the respective phase and the O activity at its boundary.

The atomic densities of ZrO_2 and ZrO are 85.3 atoms/nm^3 and 68.0 atoms/nm^3 respectively, giving the V_{ZrO}:V_{ZrO_2} molar volume ratio of ~1.25 [54,67]. Thus, the contribution from the

molar volume ratio is insignificant. Meanwhile, k_p is proportional to the square of the oxide phase thickness. Barrier layer thickness measurements have been carried out using EIS, and many authors reported that this layer is of the order of μm in the mid-late pre transition regime and the evolution of the barrier layer thickness is similar to the overall oxide thickness [78,79,82]. This is much thicker than the ZrO layer thickness of the materials studied in this work, which has a maximum of 100-200 nm (Figure 5.15) [218]. Therefore, $k_p(ZrO_2)$ should be much higher than $k_p(ZrO)$.

Pre transition, the oxidation rate ($\frac{dh_{ZrO_2}}{dt}$) decreases and h_{ZrO_2} increases (Equation 5.3a). The increase of barrier layer thickness in pre transition has been reported (Section 2.3.3) [78,79,82]. During this period, $k_p(ZrO_2)$ decreases because the instantaneous oxidation rate decreases, and as a result $\frac{h_{ZrO_2}}{h_{ZrO}}$ decreases. Note that because $k_p(ZrO_2)>k_p(ZrO)$, growth at the ZrO-Zr(O_{sat}) interface is much slower than at the ZrO_2-ZrO interface. The thickening of Zr(O_{sat}) layer that is observed above occurs in this pre-transition regime, probably because the advance of ZrO_2-ZrO/Zr(O_{sat}) interface becomes slower as oxidation progresses.

Shortly after the transition, $\frac{dh_{ZrO_2}}{dt}$ increases and the opposite of what happens during pre transition occurs resulting in increasing $\frac{h_{ZrO_2}}{h_{ZrO}}$ as the ZrO_2-ZrO/Zr(O_{sat}) interface moves rapidly. However, in the rest of post-transition regime, the undulating oxidation rate implies that the growth of ZrO_2-ZrO/Zr(O_{sat}) interface depends on $k_p(ZrO_2)$.

The relationship between ZrO and Zr(O_{sat}) thicknesses cannot be explained using the model above because Zr(O_{sat}) is not considered as an equilibrium oxide phase. EELS low loss mapping demonstrates that while the ZrO-Zr(O_{sat}) interface is very uneven locally, at locations where ZrO is thin, Zr(O_{sat}) is thick (e.g. area 1 in Figure 5.14) and vice versa. This indicates that the growth of ZrO is very inhomogeneous and consumes Zr(O_{sat}).

However, the ZrO_2-ZrO interface and the boundary between $Zr(O_{sat})$ and Zr metal with <30 at% O are relatively flatter (areas 3 and 4 in Figure 5.14). This suggests that perhaps the combined ZrO+$Zr(O_{sat})$ thickness decreases with oxidation rate. This is the case for annealed Zr-1Nb but not for X2 (Figure 5.15). In the annealed Zr-1Nb, the fact that globally ZrO+$Zr(O_{sat})$ and $Zr(O_{sat})$ thicknesses both decrease with oxidation rate implies that probably the ZrO thickness increases as $Zr(O_{sat})$ thickness increases.

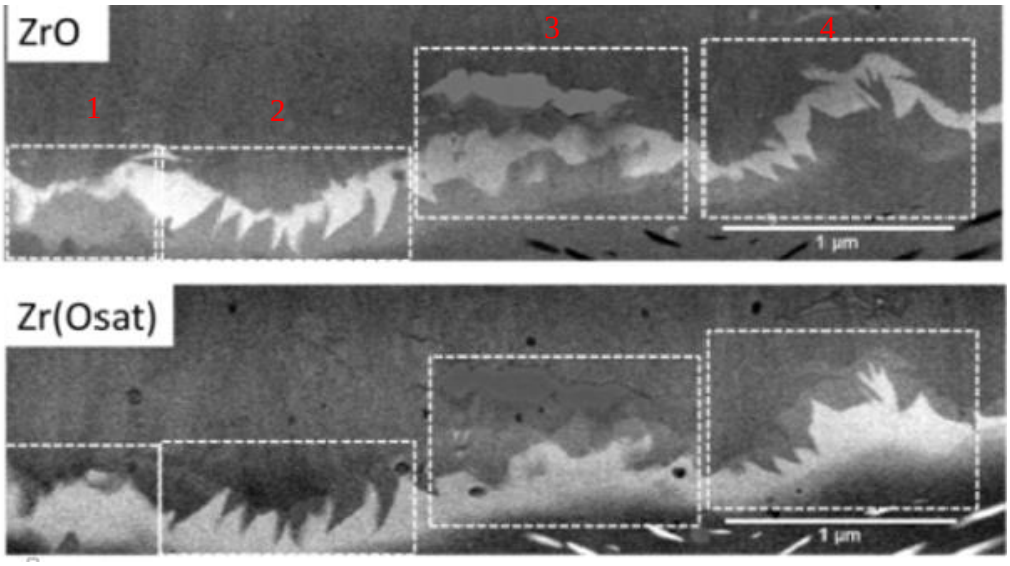


Figure 5.14: EELS low loss mapping for ZrO and $Zr(O_{sat})$ at the O/M interface of 360-day X2 [201].

In pre transition, the O picked up from instantaneous oxidation accumulates at the outer part of the oxide [83,217]. This has been proved by nanoSIMS experiments using pre-oxidised Zr that is further oxidised by water doped with ^{18}O, where there is no ^{18}O concentration near the O/M interface indicating that the evolution of barrier layer thickness is not related to the distribution of O from instantaneous oxidation (Figure 5.16a). However, this is not necessarily the case after transition (Figure 5.16b-c). This implies that the barrier layer is diminished, and at this stage the suboxide and/or $Zr(O_{sat})$ layer between ZrO_2 and Zr metal (with <30 at% O) are consumed by the newly-arrived O.

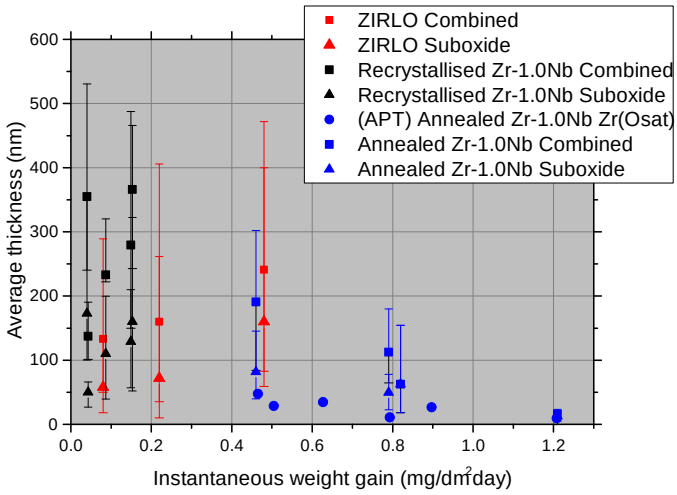


Figure 5.15: The ZrO suboxide and the combined ZrO+Zr(O_{sat}) average thickness from some of the materials studied in this thesis, including X2 and annealed Zr-1Nb. In this plot, X2 is referred to recrystallised Zr-1Nb [218].

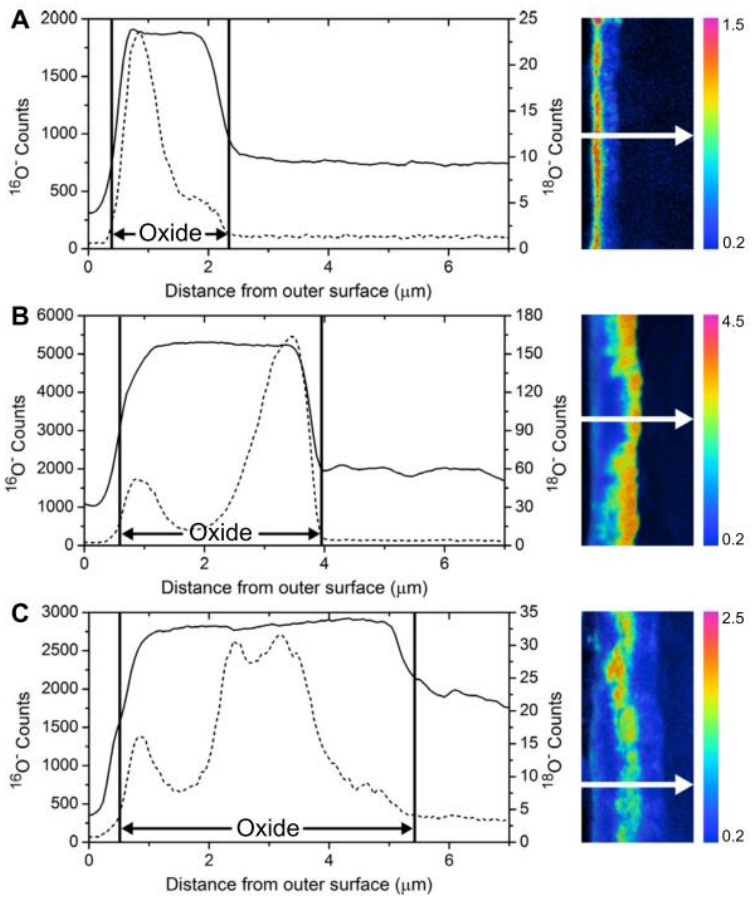


Figure 5.16: Typical line scans and HIS (Hue Saturation Intensity) images indicating the relative locations of the $^{16}O^-$ signal (solid lines) and $^{18}O^-$ peaks (dashed lines) and widths of oxides in low tin ZIRLO samples (A) 34+20 day sample (pre-transition), (B) 80+20 day sample (post-transition), (C) 160+20 day sample (post-transition) [83].

5.6. Summary

- The oxide and suboxide analyses in APT always result in a slight underestimate of the O stoichiometry due to the generation of O_2 neutral species.
- The layered oxide structure with decreasing O content is ZrO_2-ZrO-$Zr(O_{sat})$-Zr metal as previously analysed by many authors [10,64,205,210] has been observed. ZrO is a suboxide phase and $Zr(O_{sat})$ is Zr metal with ~30 at% O.
- $Zr(O_{sat})$ forms due to O deficiency when the oxidation rate is low and its thickness decreases systematically with increasing oxidation rate. The thickness evolution of this layer is closely related to how fast the ZrO_2-ZrO/$Zr(O_{sat})$ interface advances where with decreasing oxidation rate (e.g. pre transition) the ZrO_2-ZrO/$Zr(O_{sat})$ interface movement speed gradually decreases, resulting in the thickening of $Zr(O_{sat})$, and vice versa in increasing oxidation rate condition.
- The $Zr(O_{sat})$ layer evolution in the annealed and as-recrystallised Zr-1Nb samples is similar. In my samples, the X2 has a thicker suboxide than as-recrystallised Zr-1Nb, probably due to the difference in oxidation kinetics and oxidising water chemistry.
- Non-uniformity in oxidation rate causes local variations in $Zr(O_{sat})$ layer thickness and the shapes of interfaces between the different phases, with the most extreme cases showing the formation of sawtooth-shaped interfaces. Different sawtooth-shaped interface types have been observed, including the protrusion of oxide into a suboxide matrix, suboxide protrusion into the $Zr(O_{sat})$ matrix and $Zr(O_{sat})$ protrusion into the suboxide matrix.

6. HYDROGEN AND DEUTERIUM

6.1. Introduction

Hydrogen detection in APT is not straightforward. The origins of H detected in the analysis is ambiguous, in particular because H cannot be excluded from the LEAP analysis chamber and can be attracted to the surface of the specimen and field evaporated [219]. Hence, it is impossible to know if the H incorporated into the final reconstruction was a constituent of the original specimen or introduced by the experiment. Although researchers have attempted to measure these respective contribution of H to the analysis, it is not possible to separate real sample H from contamination [203].

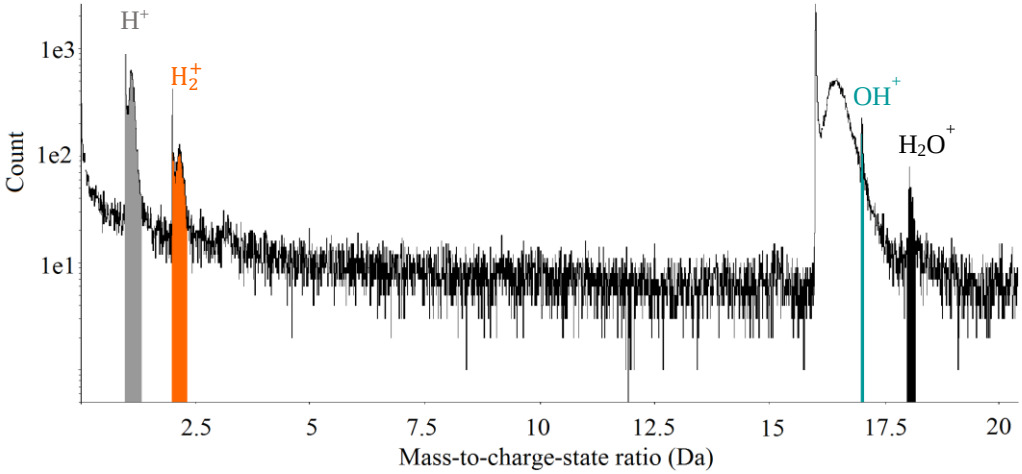
H can also be introduced during specimen preparation stage. During electropolishing, H from the polishing solution can diffuse into the specimen. Likewise, FIB milling can also result in additional H being introduced into the APT tip [220]. Another possible route for contamination is during the time when the tip is exposed to open air between transfer from specimen preparation to the atom probe vacuum chamber [6,205].

Because of these limitations with the reliable APT analysis of H, research has moved towards using deuterium (D/^{2}H) as an effective surrogate for the distribution of H within the microstructure. Although D occurs naturally, its isotopic abundance is low (~0.015%), so if it is deliberately introduced into the treated specimen in place of H then any D detected in the APT analysis can be interpreted with confidence as being a real signal originating from constituent atoms in the specimen, rather than being introduced by external sources [221]. Previous publications have shown that the introduction of D into APT samples can be carried out using various methods, e.g. by ion implantation (in Si) or D charging (in steels) during specimen preparation [222-225].

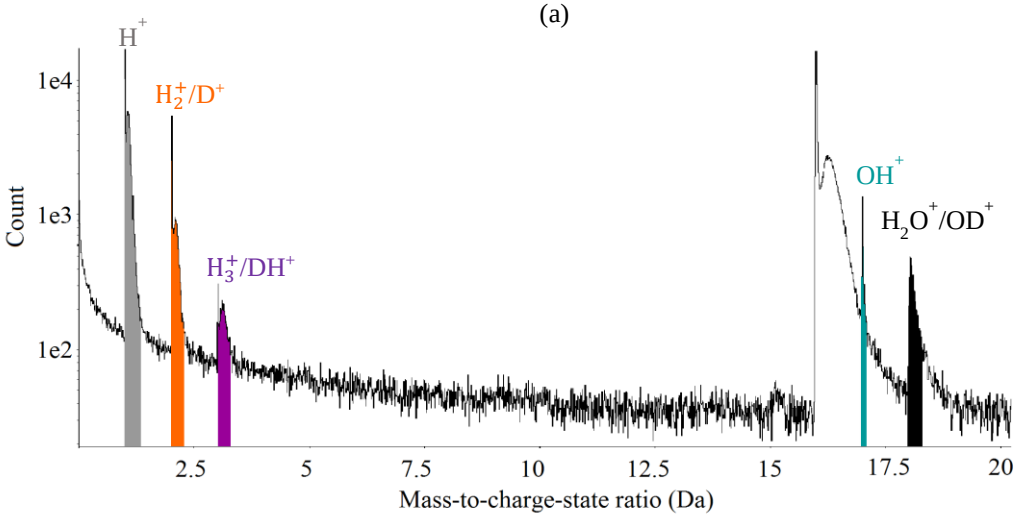
The objective of this work is to develop techniques for the APT characterisation of D and a better understanding how to interpret the resulting analyses. The motivation is to understand the route of H transport through the oxide layer that results in HPU in the underlying metal. The APT experiments for this analysis were mostly carried out in the oxide ~500-600nm from the O/M interface. While this chapter focuses on the fully-deuterated materials (Zr-2.5Nb), results from partially-deuterated (annealed Zr-1Nb and X2) and undeuterated samples are also displayed for the sake of comparison.

6.2. Detection of hydrogenic species

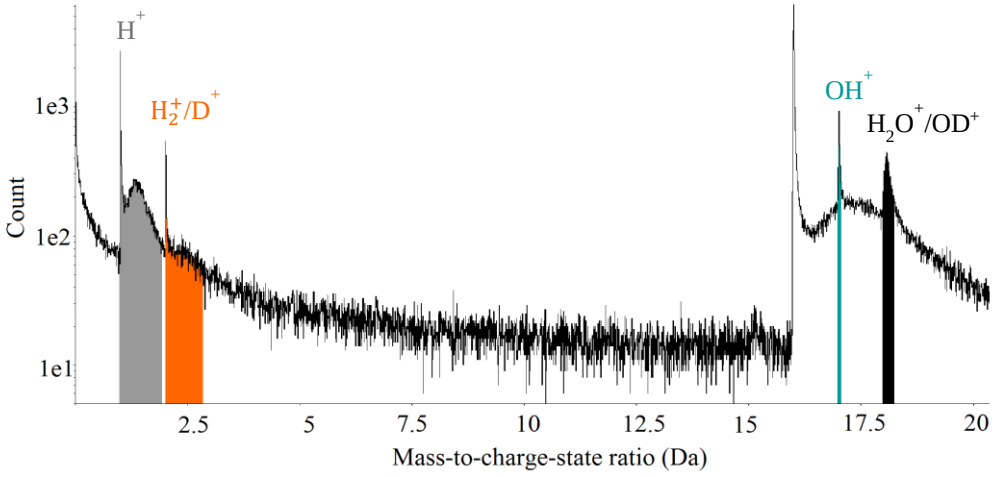
Hydrogenic species are detected in the APT mass spectra as peaks originating from three broad categories of ions; hydrogen, water and metal hydride, but the focus in this section is in the first two. Figure 6.1a-c illustrates typical mass spectra, from 0-20Da, of undeuterated, partially-deuterated and fully-deuterated samples. The detected hydrogenic peaks include 1Da, 2Da and 3Da peaks containing H^+, H_2^+ and H_3^+ respectively, and in D-containing specimens these also include D^+ (2Da) and DH^+ (3Da). The water peaks are those originating from the detection of ions from water molecules. These peaks include 17Da, 18Da and 19Da containing OH^+, H_2O^+ and H_3O^+ respectively [226]. For D-containing samples, these include OD^+ (18Da) and ODH^+ (19Da).



(a)



(b)



(c)

Figure 6.1: Typical oxide mass spectra between 1-20Da of (a) undeuterated, (b) partially-deuterated and (c) fully-deuterated samples showing all the hydrogen and water peaks.

The metal hydride peaks refer to the molecular ions incorporating both Zr and H, and in D-containing samples may also include D (deuterides). The hydride peaks in an undeuterated metal sample are visible in the metal mass spectrum but not in the oxide mass spectrum due to the overlapping thermal tails (Section 3.2.3.2). However, for deuterated samples, it is not possible to directly measure the H and D contents because all the peaks containing D also overlap with the corresponding species containing two H atoms. For example, peaks containing $ZrD^{1,2,3+}$ ions also contain $ZrH_2^{1,2,3+}$ signals that cannot be separated. The case for oxide analysis is more complex as the peaks in the oxide mass spectra exhibit large thermal tails and all hydride and deuteride (for D-containing specimens) peaks are located in these tails. Therefore, these peaks are not discussed in the oxide analysis.

There are two main differences in the current work reported below compared to typical H/D analyses conducted previously [221,223-225]. Firstly, these experiments used voltage-pulsing mode rather than laser-pulsing mode APT. The use of voltage-pulsing mode minimises the amount of hydrogen detected in the form of H_2^+, which otherwise overlaps with D^+. The use of voltage-pulsing mode is appropriate for steels and alloys, but is not viable for the analysis of ZrO_2. Haley et al. showed that by using the voltage-pulsing mode, their measured D:H ratio (2Da:1Da peak ratio) from a typical uncharged steel was ~0.008 but increased to ~0.16 after the sample was charged with D, indicating that the 2Da peak in voltage mode APT contained mostly D from the charging [223]. However, this is not the case in laser-pulsing mode APT which exhibits a much higher ratio for the undeuterated specimen. Furthermore, unlike in voltage-pulsing mode, the mass spectrum can also present a 3Da peak which is associated with H_3^+ and/or DH^+ in the case of deuterated samples (Figure 6.1b) due to an increased molecular ion formation in laser mode APT [227]. H_3^+ ions from transition metals may originate from H_3 produced by atomic mixing between H_2 molecules [227,228].

The second difference between the current study and previous work using the D as a surrogate for measuring the distribution of H is associated with the D incorporation mechanisms. Because the H to be analysed in this study originates from a water corrosion process, D has to be introduced into the corroding water instead of charged or implanted during the APT specimen preparation. In addition, if a sample has been oxidised in light water prior to deuteration, which is the case for both annealed Zr-1Nb and X2 materials, then the sample will contain a considerable amount of constituent H. As the aim of D incorporation is to maximise D-containing signals and minimise H-containing signals, this is not ideal for APT analysis.

6.3. Hydrogen in the metal

As Zr has a high affinity for H, it is expected that the as-manufactured Zr alloys will contain H [169]. The H concentration in bulk Zr-2.5Nb is reported to be between 4-45 ppm, and therefore for alloys studied in this thesis the content should not differ significantly from this range [133]. However, in this study the gross H content varies from 0.77-27.52 at% (corresponding to 85-4145 wtppm), which is much higher than the reported bulk values. The discrepancies arise because H can originate from several different external sources (Section 6).

6.4. Hydrogen and deuterium in the oxide

6.4.1. Ratio of hydrogenic peaks

The measured H concentration in the bulk oxide is similar to that in the metal. Because the quantification of H and D contents in the oxide was not possible in APT analyses, this was not attempted in this project, but I use differences in the ratios of hydrogenic peaks measured

in undeuterated, partially-deuterated and fully-deuterated samples respectively to provide evidence that D from the testing environment is being detected. To ensure the validity of this comparison, the selected samples were analysed using the same experimental conditions (50K temperature and 0.5nJ laser energy) and at least 2 million ions from the oxide were collected in each experiment. In addition, none of the selected samples for this analysis contain any hydrogenic species segregation because such segregation can alter the hydrogenic peak ratios significantly (Section 6.4.2.1)

The results of calculating 2Da:1Da peak ratios are shown in Table 6.1. Because the 3Da peak does not occur in all datasets, and contains only a very few ions (the highest 3Da:1Da ratio across all samples is only ~0.04), this peak is not taken into account in this analysis. There is an observable trend that the average 2Da:1Da ratio increases from 0.20 in the undeuterated samples to 0.32 in partially-deuterated and 0.37 in fully-deuterated samples. The spread of data is very small in undeuterated samples, but much higher in deuterated samples; the standard deviation of the deuterated samples is ~4.2x greater than that of the undeuterated ones.

Table 6.1: The 2Da:1Da peak ratio taken from 7 samples each of undeuterated, partially-deuterated and fully-deuterated materials.

Samples	Number of samples	Lowest 2Da:1Da ratio	Highest 2Da:1Da ratio	Average 2Da:1Da ratio	Standard deviation
Undeuterated (3-day, 30-day, 105-day and 225-day annealed Zr-1Nb)	7	0.14	0.29	0.20	0.05
Partially-deuterated (46-day and 91-day annealed Zr-1Nb)	7	0.17	0.44	0.32	0.12
Fully-deuterated (150-day and 1040-day Zr-2.5Nb)	7	0.13	0.77	0.37	0.23

A similar approach was carried out in the water peaks to calculate the 18Da:17Da ratios (Figure 6.2). Because both 17Da and 18Da peaks are located in the thermal tail of ^{16}O, in this

calculation the contribution from the thermal tail has to be excluded. This study makes two assumptions; firstly that the thermal tail background is approximately flat across the width of the peak and secondly, that the background contribution to the peak is equal to the background level just before the beginning of the peak. The 19Da peak is not included in the calculation because this peak only occurs in 5 samples analysed. In addition, the total ion count from this peak is very low compared to the 17Da and 18Da peaks.

Table 6.2: The 18Da:17Da peak ratio taken from the undeuterated, partially-deuterated and fully-deuterated materials.

Samples	Number of samples	Lowest 18Da:17Da ratio	Highest 18Da:17Da ratio	Average 18Da:17Da ratio	Standard deviation
Undeuterated (3-day, 30-day, 105-day and 225-day annealed Zr-1Nb)	13	0.07	2.80	1.19	0.88
Partially-deuterated (46-day and 91-day annealed Zr-1Nb)	7	0.58	3.13	1.50	0.85
Fully-deuterated (150-day and 1040-day Zr-2.5Nb)	8	1.21	3.27	2.21	0.77

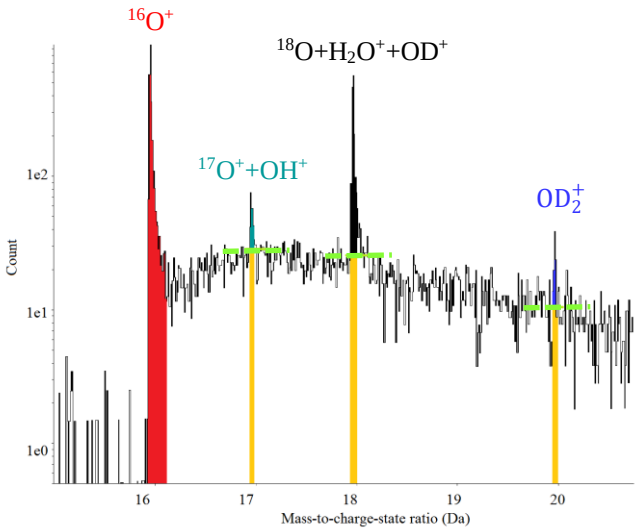


Figure 6.2: An example of calculation of the number of ions from the water peaks taken from a dataset containing D segregation. Although the mass spectra were ranged according to Figure 6.1a-c, when calculating the 18Da:17Da ratios only the ions above the background level (light green lines) are included. Ions below the background level (orange) are excluded from the calculation.

In Table 6.2, there is an indication that the 18Da:17Da ratio increases when the sample is deuterated. The 18Da:17Da ratio increases from 1.19 in undeuterated samples to 1.50 in partially-deuterated samples and finally to 2.21 in fully-deuterated samples. If we apply a 1σ confidence criterion, the upper limit of the 18Da:17Da ratio from undeuterated samples (2.07) is still lower than the average ratio from fully-deuterated samples (2.21). This is also true for 2Da:1Da ratios in Table 6.1 even with 3σ confidence (>99.7% probability).

The spread of data in Table 6.2 is large, as the standard deviations are 0.88, 0.85 and 0.77 for undeuterated, partially-deuterated and fully-deuterated samples respectively, much greater than those for the 2Da:1Da ratio. This is probably because the water content inside the LEAP analysis chamber varies more than the hydrogen gas content. Therefore, statistically, we have more confidence in detecting D as D^+ in the 2Da signal compared to OD^+ in the 18Da signal.

A significant limitation for this approach to interpret the potential D-containing signal is that for an individual analysis, undeuterated samples can have 2Da:1Da or 18Da:17Da ratios higher than measured in fully-deuterated samples, e.g. the highest measured 18Da:17Da ratio in an undeuterated sample is ~2.3x higher than the lowest ratio measured in a fully-deuterated sample. This indicates that apart from deuteration, there are other factors affecting this ratio depending on how many H_2O^+ species can be formed. Firstly, although the experiments were carried out in similar pressures (~10^{-11} torr), the H content from gaseous species (especially H_2 and H_2O) inside the analysis chamber may be different. Secondly, even if the H content in the chamber and specimens is constant across all experiments, because the individual tip shapes are not identical, there are different local field variations on the specimens. Adsorption of H from the gas molecules onto an APT specimen is thought to be due to dipole-dipole interactions and is influenced by the local field strengths [175,203,227]. This is supported by observations demonstrating that the amount of hydrogen and water ions detected changes with voltage in laser mode APT [203,227]. Because the specimen shape

affects the standing voltage required for field evaporation, and these values are different in different specimens, it can be assumed that the discrepancies of 2Da:1Da and 18Da:17Da ratios between samples can also be attributed to the specimen shape.

Deuteration of the specimen has similar effect in increasing both the 2Da:1Da and 18Da:17Da ratios. The 2Da:1Da ratio increases from ~0.20 to ~0.37 while 18Da:17Da ratio increases from ~1.19 to ~2.21. This means that the 2Da and 18Da peak from deuterated samples contain a significant amount of D^+ and OD^+ respectively, and therefore any segregation or localisation of ions from these peaks in atom maps can be regarded with some confidence as evidence for D segregation.

6.4.2. Hydrogen and deuterium segregation

6.4.2.1. Oxide grain boundaries

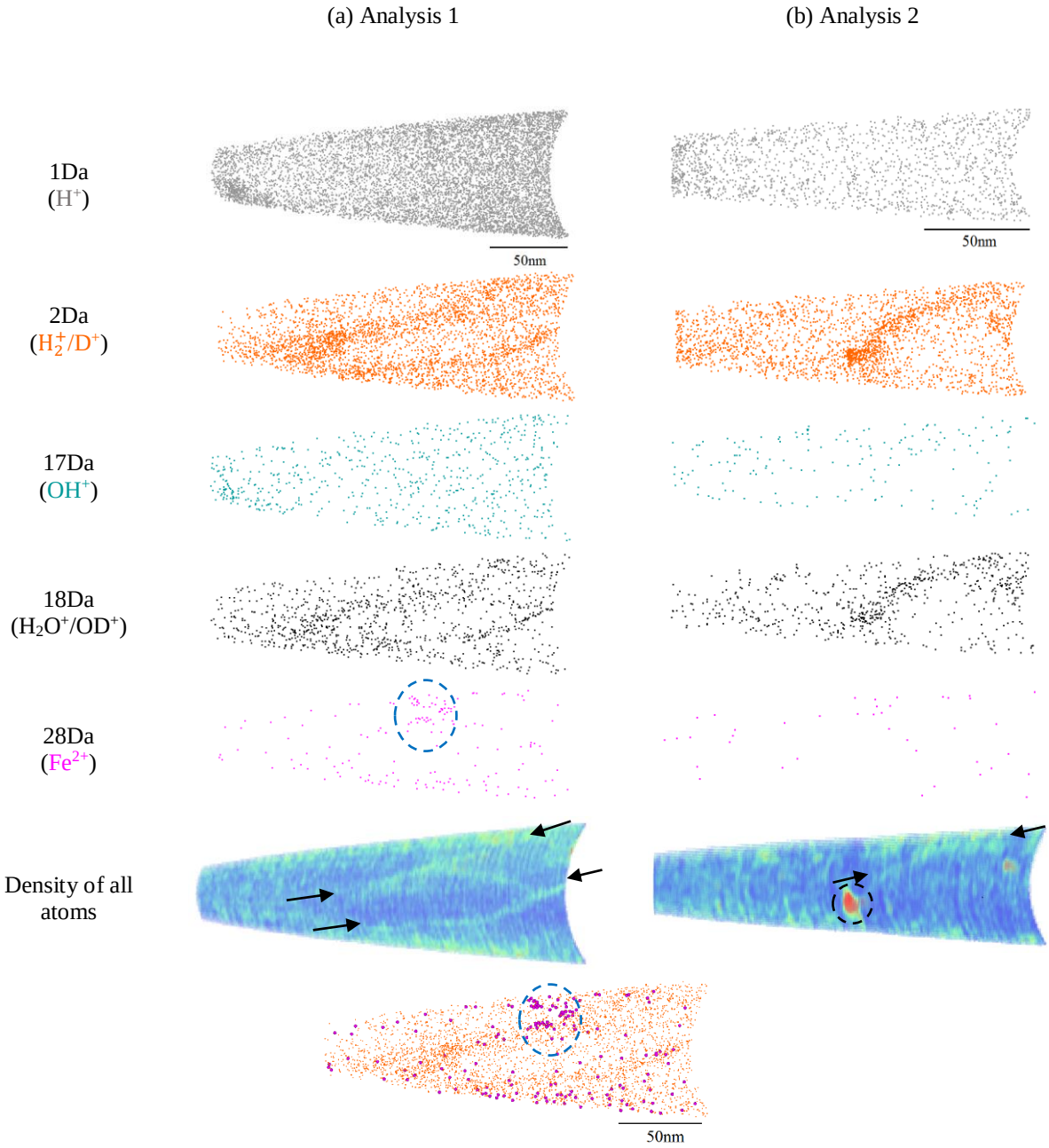
The spatial segregation of ions contributing to the hydrogen and/or water peaks can indicate the location of enhanced concentrations of H or D in the oxide that could identify preferred diffusion paths of H and/or D. However, any segregation observed using H peaks could also be artefacts (Section 6), and therefore all datasets with apparent H and/or D segregation must be interpreted carefully.

In this thesis, the only evidence for segregation that is considered to be reliable is D segregation to linear features that are most likely oxide grain boundaries. This segregation is observed only in fully-deuterated samples and only in 3 out of 23 datasets containing significant volumes of oxide, showing that only a few grain boundaries have this type of segregation. The results from 2 out of these 3 datasets are displayed in Figure 6.3a-b (Analyses 1 and 2). In both cases, only D-containing peaks (2Da and 18Da) apparently segregate to planar features. Because the 1Da and 17Da species show no localisation, these

signals are just from hydrogenic contamination, and are not actual constituent atoms of the specimen.

Fe atom maps are also presented because Fe can segregate to oxide grain boundaries (Section 7.3.3) and a similar examination carried out by Sundell et al. indicated that the segregation of D also correlates with that of Fe (Figure 6.4) [226]. In this previous study, Fe segregates to an oxide grain boundary to which the 18Da peak ions also segregates. However, this co-segregation of D and Fe was not observed for Analyses 1 and 2 (Figure 6.3a-b). In Analysis 1, 3 small Fe clusters are found on the linear feature to which the D segregates (Figure 6.3c). Because Fe clusters are mostly found on oxide grain boundaries (Section 7.3.3), the presence of these Fe clusters in may reinforce the suggestion that there is a grain boundary in this region of this analysis.

Because the Fe distribution cannot be used wholly to determine if the features to which D-containing ions are segregating are grain boundaries, the density maps of all atoms are used to identify these features. Grain boundaries can cause trajectory aberrations that result in atom maps with different local atomic density compared to the matrix (Section 3.1.5). This has been used to determine the position of grain boundaries with no elemental segregation [229]. For Analysis 1, it is clear that there are two lines with a localised, higher density of detected atoms than from the oxide matrix, and that these correspond to the locations of 2Da and 18Da peak segregation. In Analysis 2, this is not as clear, probably due to the existence of a localised “hot spot” in the density map (Section 6.4.2.2) but the high density line can still be observed at a similar location to the increase in D concentration.



(c)

Figure 6.3: 10nm thick slices of reconstructions taken from 2 Zr-2.5Nb oxide samples, named Analyses (a) 1 and (b) 2 both of which show D segregation. The atom maps show distributions of 1, 2, 17, 18, 28Da peaks and the density of all atoms. Black arrows and circles in the density maps correspond to the D-decorated oxide grain boundaries and a possible pore (discussed below). The blue circle in the Fe atom map of Analysis 1 highlights the locations of Fe clusters along a grain boundary. The location of these clusters relative to the boundary is shown in (c) where magnified Fe^{2+} ions (purple spheres) are displayed in the same atom map with 2Da ions (smaller orange dots).

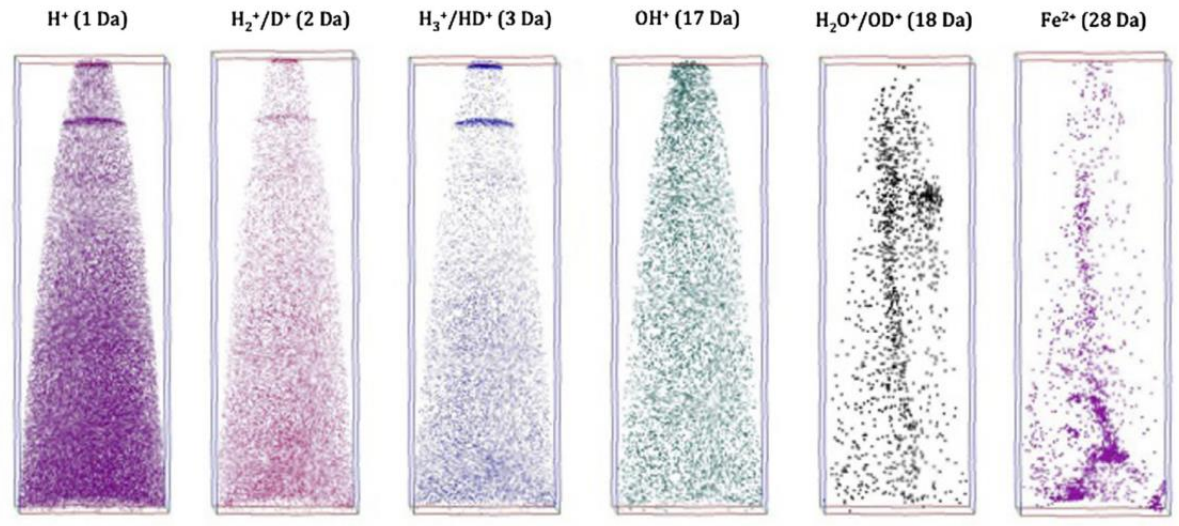


Figure 6.4: Atom maps of 1, 2, 3, 17, 18 and 28Da peaks from a Zr-2.5Nb oxide sample containing a segregation of 18Da and 28Da signals [226].

Only 1 out of 3 datasets contained the co-segregation of both Fe and D-containing ions (Analysis 3 in Figure 6.5). Analysis 3 is slightly different to Analyses 1 and 2 because the 2Da peak shows no sign of obvious segregation.

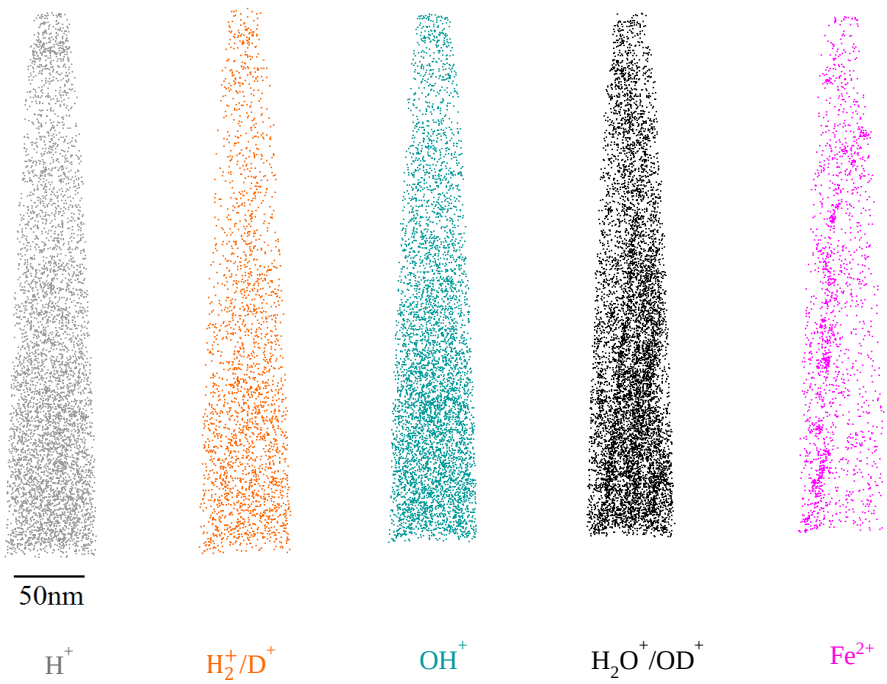


Figure 6.5: A dataset of Zr-2.5Nb oxide (analysis 3) containing D and Fe co-segregation, showing distributions of 1, 2, 17, 18 and 28Da peaks.

In Analysis 3, it appears that the 18Da and 28Da ions segregate to the same feature (Figure 6.5). To determine whether this is the case, the reconstruction is divided into four sections and the atom map projections of each section of the plane perpendicular to the specimen axis are examined, showing that the segregation of 18Da and 28Da ions are in different regions (Figure 6.6). It can be assumed that the segregation is to planar features, as can be confirmed in atom maps B, C and especially D where lines corresponding to the projections of the planes are observed. While the segregation of 18Da ions can be clearly seen, this is not the case for 28Da ions. The 28Da ions segregate to a plane that is close to the edge of the specimen, and its distribution is not as uniform as the OD^+ ions.

To confirm whether the segregation of 18Da and 28Da ions are to a grain boundary, the distribution of density of all atoms in the areas where ions from these mass spectrum peaks segregate is investigated in Figure 6.7. Both the planes to which 18Da and 28Da segregate have different ion densities than the matrix, and furthermore the area to the right and left hand sides of these planes show different density contrasts, suggesting that these planes are grain boundaries. Differential ion densities between two neighbouring grains has been observed previously using APT [229].

An examination of undeuterated Zr-0.5Nb-0.1Sb shows segregation of H^+ and OH^+ to an apparent oxide grain boundary (Figure 6.8). Such segregation is not observed in any of the Zr-2.5Nb samples. It is not possible to determine whether the segregated H originates from the actual sample, but this example shows that in an undeuterated sample the segregation of 1Da and 17Da is not correlated to the apparent segregation of 2Da and 18Da, i.e. H_2^+ and H_2O^+ do not segregate when H^+ and OH^+ segregate. Furthermore, the segregation of Fe to the planar feature with low atomic density demonstrates that this feature is also likely to be an oxide grain boundary.

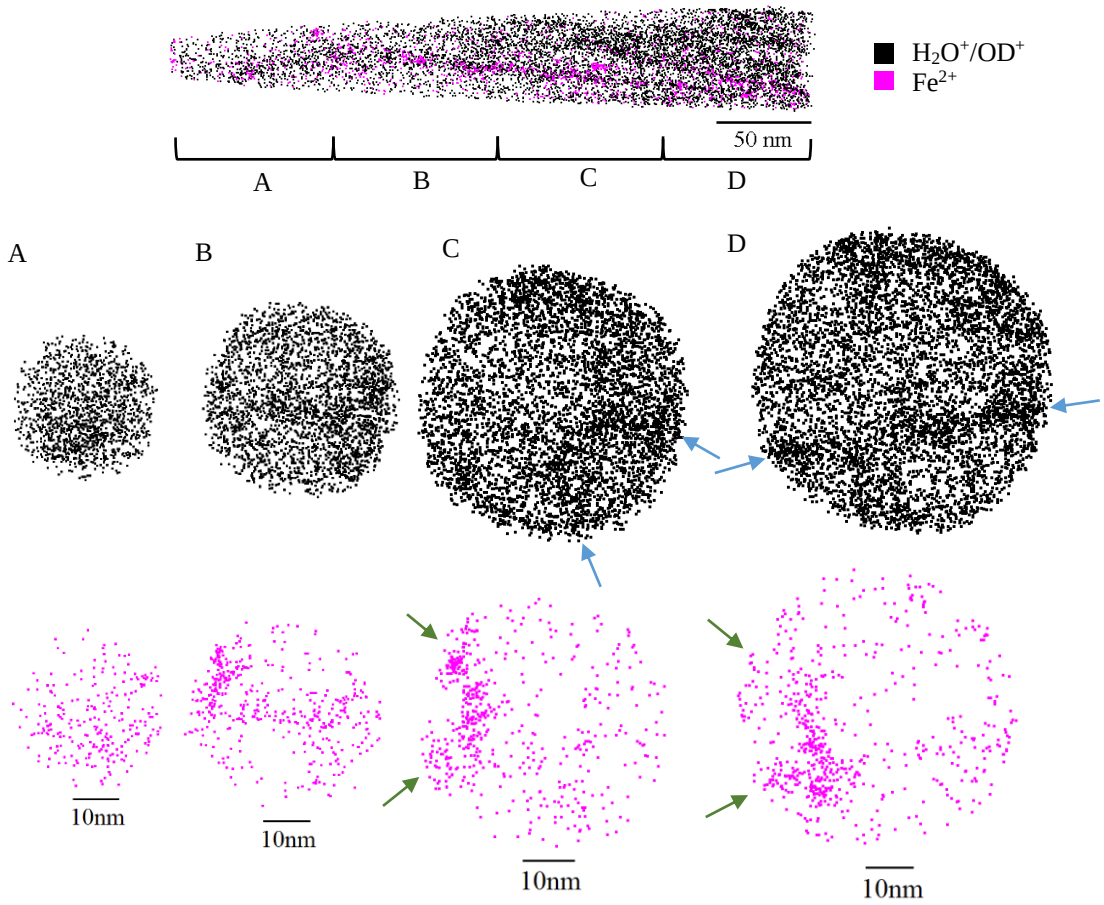


Figure 6.6: The thin slices of the reconstruction in the plane perpendicular to the depth direction of the analysis of four sections from Analysis 3 showing the distributions of 18Da (black;H_2O^+/OD^+) and 28Da (pink;Fe^{2+}) ions. For visual clarity ions are imaged twice as large in the lower images and the blue and green arrows indicate the positions to which the 18Da and 28Da ions segregate respectively.

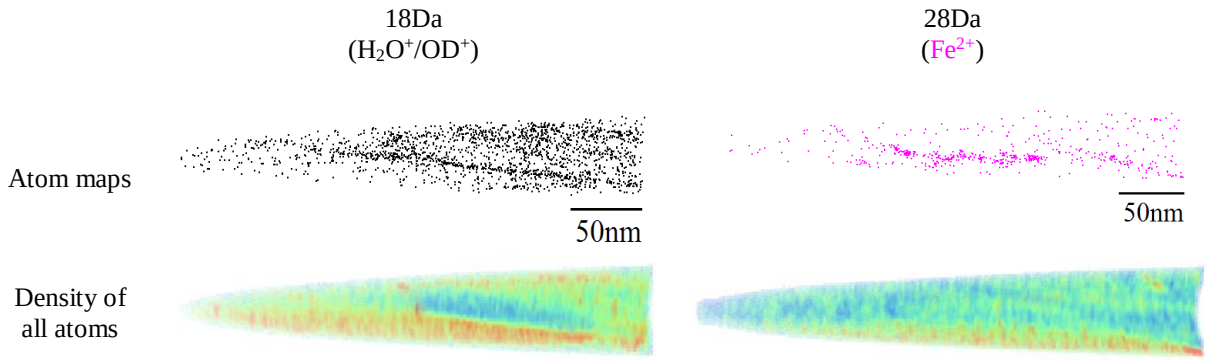


Figure 6.7: 10nm thick atom maps and density of all atoms distribution in Analysis 3 where the 18Da and 28Da peaks exhibit segregation.

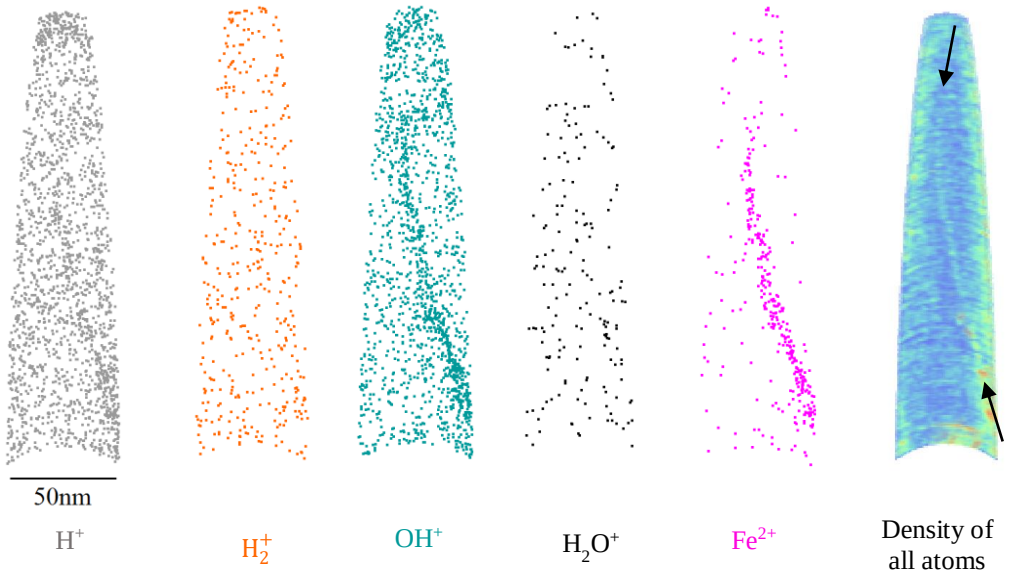


Figure 6.8: A 10 nm slice of a reconstruction of Zr-0.5Nb-0.1Sb oxide containing an oxide grain boundary with H^+, OH^+ and Fe^{2+} segregation, showing distributions of 1, 2, 17, 18 and 28Da peaks as well as the density of all atoms. The arrows near the atomic density map indicate the location of the grain boundary.

Although the density maps demonstrate density differences in the locations where D segregates, besides grain boundaries there are other linear features that can also result in a density contrast in the reconstruction. Hence, the suppostion that these features are grain boundaries is not completely certain [169]. Possible other features include crystallographic poles and zone line artefacts. However, these possibilities are discounted in this case because no crystallographic pole is observed in the oxide and furthermore the poles are characterised by straight lines running parallel to the direction of analysis, which is not the case in Analyses 1 and 2 [169,230,231]. Another possibility is the occurrence of microfractures that can develop during the experiments but once again there are some reasons that for disregarding this possibility.

Microfractures are characterised by a continuous, crescent-shaped planar feature in the atom maps and localised higher evaporation field (Figure 6.9). Clearly, they have different shapes compared to the features observed in Analyses 1-3 (Figure 6.3a-b and Figure 6.5). In most samples, H^+ ions are normally distributed uniformly across the samples but this is not the

case if the sample has had a microfracture (Figure 6.9). More importantly, because neither the 2Da nor 18Da ions displays any segregation to microfractures, the features in Analyses 1-3 (with 18Da and/or 2Da segregation) are unlikely to be microfractures, in agreement with Sundell et al. (Figure 6.4) where the microfracture is not segregated by 18Da ions [226].

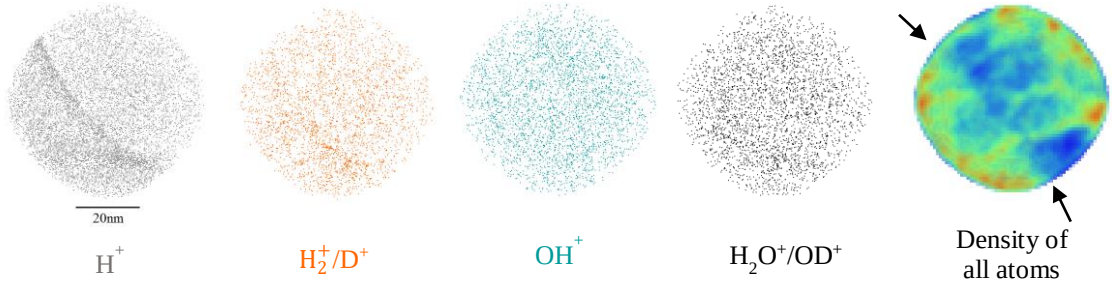


Figure 6.9: The distributions of hydrogen and water peaks and the density of all atoms in a typical deuterated oxide sample (Zr-2.5Nb) dataset containing a microfracture. The images are the projection of the sample perpendicular to the sample axis. The density map is only taken in the fractured volume for the sake of visual clarity where the fractured area of the sample (bottom left quadrant) has a slightly lighter contrast compared to the rest of the sample. The arrows indicates the microfracture location.

To compare the amount of D in the segregated regions in Analyses 1-3, cuboidal ROIs containing the segregated feature were created. In the same sample another ROI containing a volume with no 2Da and/or 18Da segregation was created. The 2Da:1Da ratios from these ROIs are compared in Table 6.3. In this calculation it is assumed that the H_2^+:H^+ ratio is equal to the average 2Da:1Da ratio of undeuterated samples (0.20) (Section 6.4.1) and the rest of 2Da peak is considered to be D^+. If D behaves in the same manner as H, then the D_2^+:D^+ ratio should be equal to the H_2^+:H^+ ratio and the expected number of D_2^+ ions (calculated using the D_2^+:D^+ ratio that is assumed to be equal to the H_2^+:H^+ ratio) should match the total counts of the 4Da peak in the mass spectra. However, in all datasets involved in this chapter, no 4Da peak was observed because the total D_2^+ count falls below the minimum detectable limit (Table 6.3).

In this calculation, it was assumed that the 4Da peak is rectangular and that the minimum detectable count is defined as 4x the standard deviation (4σ confidence) of background counts times the width of the 1Da peak. This is one way to estimate the minimum number of counts in a peak that can be detected in the mass spectrum, and this is a simplification of the concept in [232]. In all the analyses the number of D_2^+ ions is below the minimum detectable counts at 4Da. This is in a good agreement with the observation that no peak at 4Da is detected in any of these datasets. Therefore, this suggests that H_2^+:H^+ ratio appears to be at least as small as D_2^+:D^+ ratio.

Table 6.3: Isotopic examination of hydrogen peaks from analyses 1-3 showing the number of ion counts and 2Da:1Da ratios from ROIs with (inside) and without (outside) D segregation.

	Counts/ratios					
	Analysis 1		**Analysis 2**		**Analysis 3**	
	Inside	**Outside**	**Inside**	**Outside**	**Inside**	**Outside**
Total 1Da	2381	12900	395	571	1131	1069
Total 2Da	681	3793	532	313	697	405
Expected H_2^+ contribution to 2Da peak	483	2619	80	116	230	217
Expected D^+ contribution to 2Da peak	198	1174	452	197	467	188
Expected D_2^+	40	238	92	40	95	38
Minimum detectable counts at 4Da	44	539	109	58	141	93
2Da:1Da ratios	0.29	0.29	1.35	0.55	0.62	0.38

Although the 2Da peak apparently segregates in both Analyses 1 and 2, in Analysis 2 D forms the majority of the 2Da peak, resulting in a high 2Da:1Da ratio (1.35) but this is not the case in Analysis 1 (with a 2Da:1Da ratio of 0.29 assuming that the H_2^+:H^+ ratio is 0.20). Furthermore, the 2Da:1Da ratio inside the segregated region of Analysis 1 is slightly lower than the average 2Da:1Da ratio of fully-deuterated samples (0.37). In analysis 3, D is also the

majority species in the 2Da peak but no 2Da segregation is observed. Therefore, there is no strong correlation between the 2Da:1Da ratio and the observation of segregation of 2Da ions.

Comparing the 2Da:1Da ratios inside and outside the segregated regions, in all analyses the 2Da:1Da ratio inside the segregated region is always higher than outside the segregated region. Analysis 2 demonstrates the highest difference between the 2Da:1Da ratio inside (1.35) and outside (0.55) the segregated region. On the other hand, despite showing segregation of the 2Da peak, the 2Da:1Da ratio inside the segregated region of Analysis 1 (0.29) is approximately the same as outside the segregated region (0.29). This is perhaps because the 2Da segregation is stronger in Analysis 2 than in Analysis 1.

Similar analysis is also carried out on the water peaks (Table 6.4). The number of ions in 17Da, 18Da and 20Da peaks was measured by the same method described in Section 6.4.1 where the thermal tail contribution is excluded. I assume that if OD^+ behaves in the same manner as OH^+, the H_2O^+:OH^+ ratio should be equal to the OD_2^+:OD^+ ratio. It is also assumed that the H_2O^+:OH^+ ratio is equal to the average 18Da:17Da ratio of the undeuterated samples (1.19 from Section 6.4.1). By assuming that the OD_2^+:OD^+ ratio is equal to the H_2O^+:OH^+ ratio, the expected amount of OD_2^+ can be determined. Because OD_2^+ does not always appear in all datasets, the minimum detectable limit is only calculated in the case where the OD_2^+ is not present.

The expected OD^+ count in all regions is greater than H_2O^+, suggesting that the 18Da peak in each sample probably contains more OD^+ than H_2O^+ (Table 6.4). The segregated region exhibits higher 18Da:17Da ratios compared to the region with no segregation in the same dataset. The 18Da:17Da ratios inside the segregated region in Analyses 1 and 2 are 7.56 and 9.31 respectively, corresponding to ~2.8x and ~1.9x higher values than the ratios outside the segregated region. This implies that the number of OD^+ ions is much greater in the segregated

region than outside. In Analysis 3, the difference between the 18Da:17Da ratios inside and outside the segregated regions is not significant. There are two possible explanations for this. Firstly, the segregation is possibly very weak. Secondly, the 18Da:17Da ratio depends on the volume of the ROI covering the segregated feature. However, in this work, the ROIs were created as small as possible to be more representative to the segregated regions (~10^5nm^3), but covering as many segregated features as possible to be representative of the whole dataset.

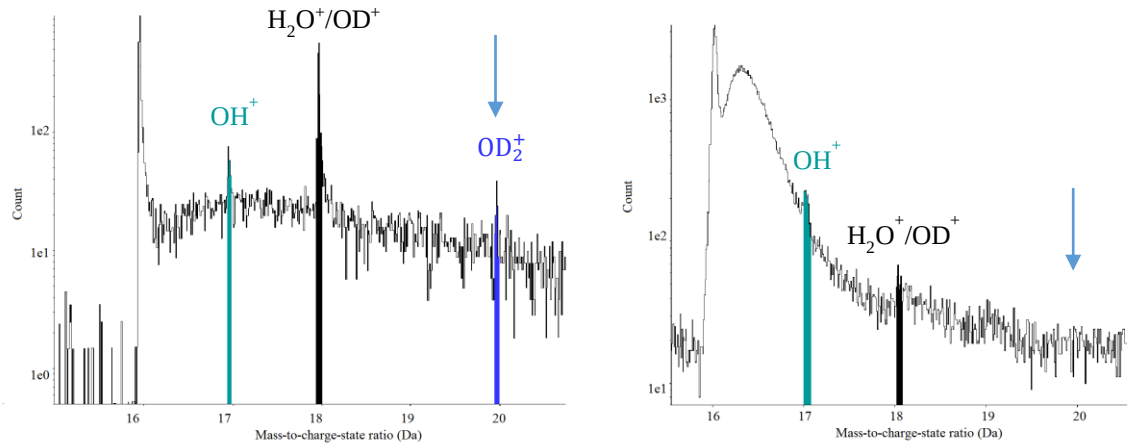
Table 6.4: Isotopic examination of hydrogen peaks from Analyses 1-3 showing the number of ion counts and 18Da:17Da ratios from ROIs with (inside) and without (outside) D segregation.

	Counts/ratios					
	Analysis 1		**Analysis 2**		**Analysis 3**	
	Inside	**Outside**	**Inside**	**Outside**	**Inside**	**Outside**
Total 17Da	116	355	305	111	888	696
Total 18Da	879	975	2836	538	3194	2207
Expected H_2O^+ contribution to 18Da peak	138	423	362	132	1056	829
Expected OD^+ contribution to 18Da peak	741	552	2474	406	2138	1378
Expected OD_2^+	882	657	2944	483	2544	1640
Minimum detectable counts at 20Da	-	72	-	76	-	136
Total 20Da	41	-	101	-	42	-
18Da:17Da ratios	7.56	2.74	9.31	4.85	3.60	3.17

Table 6.4 shows that there is no 20Da peak (OD_2^+) in the mass spectra outside the segregated region even though the expected number of OD_2^+ ions is higher than the minimum detectability limit in each dataset. Given that O-D and O-H bond energies are very similar, OD^+ and OH^+ are expected to behave in the same way [233]. The discrepancy might be attributed to the underestimation of the contribution from minor O isotopes (^{17}O and ^{18}O). The natural isotopic abundances of ^{17}O and ^{18}O are 0.038% and 0.20% respectively but in

this study only the peak of ^{16}O peak is ranged, and the contributions of ^{17}O and ^{18}O are considered to be insignificant. However, the thermal tail may have a non-negligible contribution to the total amount of ^{16}O. It is not possible to account for this contribution because the thermal tail also incorporates contributions from other ions. Therefore, the resulting measurements can underestimate minor O isotopes, especially ^{18}O, and this in turn can shift the 18Da:17Da ratio to a lower value, resulting in the decrease of the expected number of OD_2^+ ions.

Despite the discrepancy described above, OD_2^+ ions are detected in the segregated regions. The fact that the OD_2^+ ions are not present outside the segregated regions where the peak at 20Da is detected in the dataset containing D segregation (Figure 6.10a-b) implies that these ions are concentrated in areas with a high 18Da:17Da ratio. Although it is not possible to display the atom map containing only the OD_2^+ ions due to low signal-to-noise ratio at 20Da, the presence of OD_2^+ is a positive indication that the water peaks might have the same behaviour as the hydrogen peaks.



(a) (b)

Figure 6.10: The mass spectra 16-20Da of the water peaks from Zr-2.5Nb datasets (a) with and (b) without apparent segregation of D-containing species. The blue arrows point out the 20Da peak that is present in (a) but not in (b).

Outside the segregated region, the 18Da:17Da ratios in analyses 1, 2 and 3 are 2.74, 4.85 and 3.17 respectively, far higher than the average 18Da:17Da ratio in the fully-deuterated samples (2.21) (Section 6.4.1). This implies that the matrix surrounding the segregated region has higher OD^+ content, i.e. presumably more enriched in D. In other words, the D segregation to grain boundaries is more likely to occur in the regions with higher local D concentration. However, high D content does not necessarily correspond to D segregation as there are datasets with high 18Da:17Da ratio (e.g. 3.27) with no D segregation.

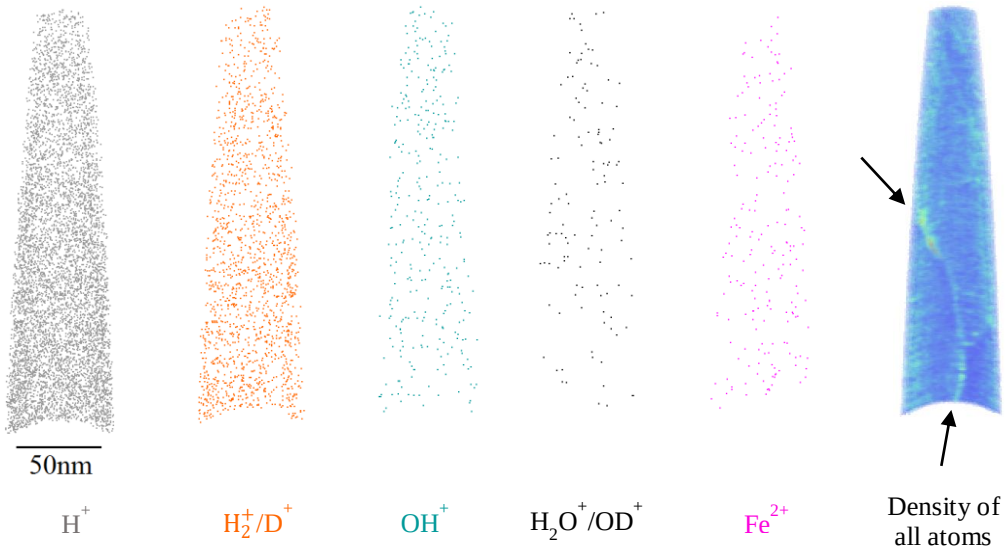


Figure 6.11: A 10 nm slice of a reconstruction of Zr-2.5Nb oxide containing an oxide grain boundary but with no D or Fe segregation, showing distributions of 1, 2, 17, 18 and 28Da peaks as well as the density of all atoms. The arrows near the atomic density map indicates the location of the grain boundary.

D segregation is only observed in 3 out of 23 datasets containing oxide, and the 20 datasets with no D segregation have a combined ~136 million ions that corresponds to a reasonably large volume of material (roughly estimated ~$6.5 \times 10^6 nm^3$). Considering that the oxide grain size is only ~5-90 nm in width and 100-500 nm in length (for columnar grains) and ~15-50 nm (for equiaxed grains) [10,77,88,167,234], it can be assumed that although not observable, there are a significant number of grain boundaries sampled within in these 20 datasets that are not enriched in D. The existence of grain boundaries can be confirmed in the datasets with no

observable segregation of D- and H-containing ions by the presence of a localised line of high density corresponding to a grain boundary (Figure 6.11).

In conclusion, while both the 2Da and 18Da peaks (containing D^+ and OD^+ respectively) can be used to detect D segregation, in the current study the 18Da segregation is more reliable for several reasons. Firstly, ions from 18Da peak segregate in Analyses 1-3, while ions from 2Da peak only segregate in Analyses 1 and 2. Another case where ions from 18Da peak appear segregated but not ions from the 2Da peak like in Analysis 3 has been reported previously (Figure 6.4) [226]. Secondly, based on examination of the water peaks in the segregated regions, the 18Da:17Da ratio is always higher than both the ratio outside the segregated region and the average 18Da:17Da ratio of fully-deuterated samples. Meanwhile, there is no apparent correlation between the D content at 2Da and the 2Da:1Da ratios inside and outside the segregated regions. However, it is also important to reiterate that these statistics have large standard deviations, and therefore should not be overinterpreted.

6.4.2.2. Porosity

In Analysis 2, there is a localised spot with high atomic density next to the high density line that has been interpreted as a grain boundary (Figure 6.3b), corresponding to the concentration of D-containing ions at 2Da and 18Da. This phenomenon occurs only in 2 datasets and hence is very uncommon. Because this spot gives a distinct contrast in the density map, it is probably a physical feature and because it is enriched in D close to a grain boundary, this is possibly a pore. Pores a few nm in size are known from TEM analysis to exist along oxide grain boundaries (Figure 6.12a-b) (Section 2.3.3) [10,71,235].

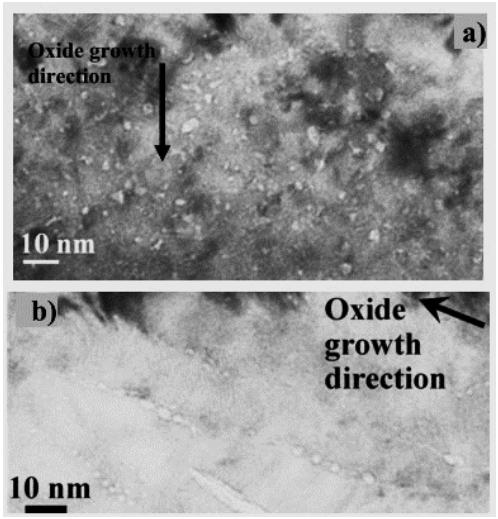


Figure 6.12: Examples of characteristic porosities observed in the oxide near the metal-oxide interface by imaging with under-focus Fresnel contrast. (a) shows fine isolated pores in Zircaloy-4 tube oxide; (b) shows disconnected pores along a boundary between columnar monoclinic grains near the oxide/metal interface in 60 days ZIRLO oxide [10].

Although very limited experimental data has been published about pores in APT, vacancies in irradiated W have been examined by FIM, characterised by missing atoms in the FIM image and a localised lower atomic concentration than the matrix [236-238]. A later study suggested that pores should also behave in the same way [239]. However, in contrast to [239], pores should display a high local atom density instead, due to a trajectory aberration focussing the ions inward when they reach the surfaces of the tip. Instead of using a concentration profile, the atomic density is used to identify the pores because the atomic density profile is more sensitive to microstructural features, and pores have been known to give an atomic density contrast as previously observed [240]. However, if the feature in Figure 6.3b is a pore, it is not possible to obtain correct information regarding its size and composition from an APT reconstruction because when a pore is exposed to the surface during experiment, it can attract H from the vacuum system, and during the reconstruction will be represented as a H-rich cluster rather than a void. As in this case the feature contains significant amount of D rather

than H, it is likely to contain D that is probably in gaseous form or D-containing species chemisorbed on the surfaces of the pore, consistent with other reports [80,139,241].

Similar segregation is also observed in a partially-deuterated sample (Figure 6.13), and the ions that segregate to this feature are H^+ and OH^+ but is similar in size and shape to the spot observed in Analysis 2 discussed above. It is not possible to determine whether the H inside the void originates from the vacuum or deposited in the actual sample as a corrosion product.

The concentration inside the feature (Table 6.5) shows that there is a small difference in terms of Zr and O contents with the surrounding matrix, suggesting two possibilities. Firstly, the field evaporation process inside the feature might be slightly different compared to the oxide matrix. Secondly, the feature might also be slightly enriched in O. The significant difference is that the feature contains almost twice the H concentration compared to the oxide matrix.

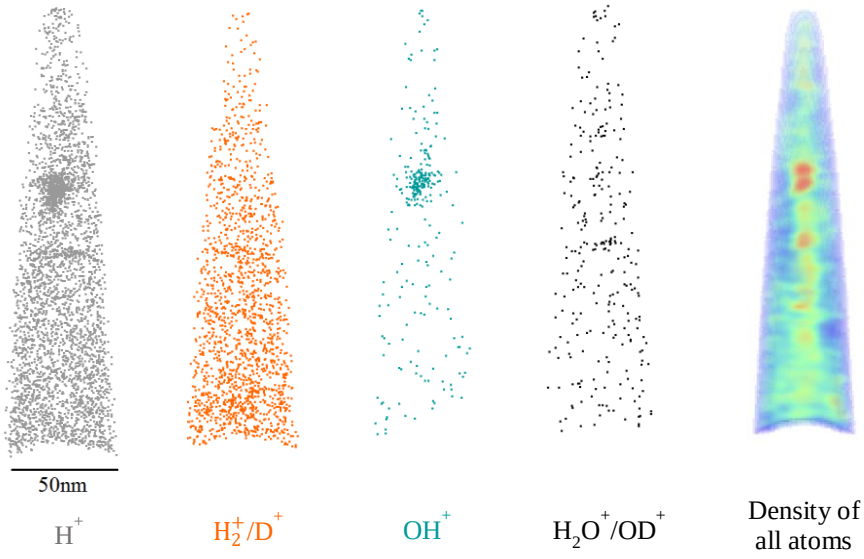


Figure 6.13: The distributions of hydrogen and water peaks and the density of all atoms in a 10nm thick slice of partially-deuterated oxide sample (46-day annealed Zr-1Nb) containing a concentration of H^+ and OH^+ ions.

Table 6.5: The compositions inside and outside the H-rich feature in Figure 6.13.

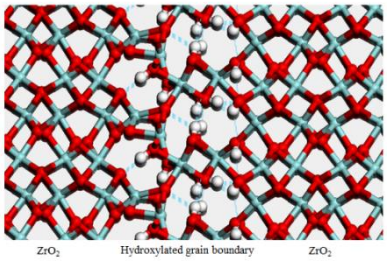
Locations	**Concentration (at%)**		
	Zr	**O**	**Gross H**
Inside	35.04	63.17	1.60
Outside (oxide matrix)	34.96	64.46	0.54

6.5. Discussion

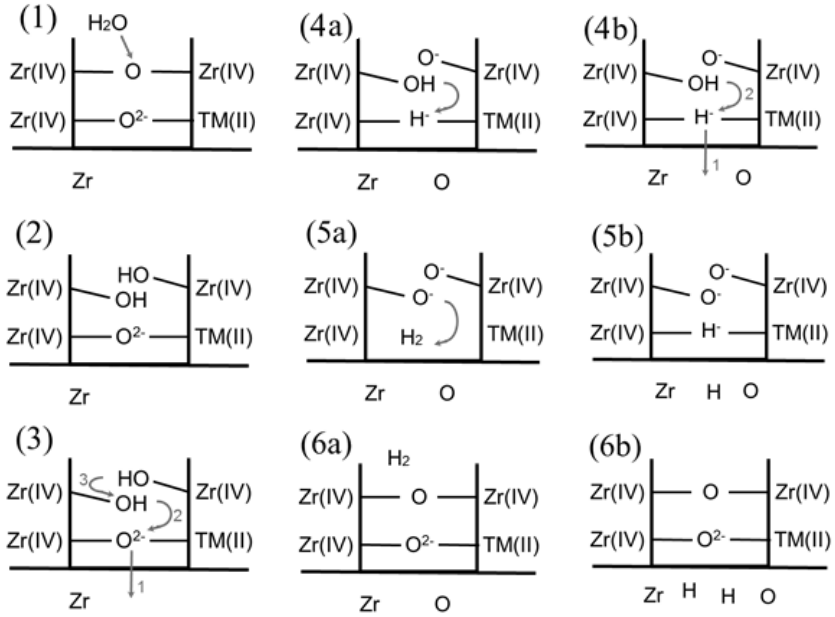
The observation of D segregation to oxide grain boundaries in this study agree with those previously reported [192,226]. The evidence for D segregation to grain boundaries reinforces the hypothesis by Lindgren et al. about hydroxylated oxide grain boundaries (Figure 6.14a) [42,124,192,226]. Hydroxylated grain boundaries are formed by the breaking of the oxygen bond at the grain boundaries and water molecule splitting, resulting in a H bridge (Figure 6.14b (1-3)). After that, two possible mechanisms can occur; one of them is H_2 gas evolution where H from hydroxyls and H bridging two grains recombine (Figure 6.14b (4a-6a)). Another possibility is HPU in the Zr metal where H bridging between the two grains diffuses to the Zr metal (Figure 6.14b (4b-6b)) [124].

Hydroxyl formation in the oxide is well-known (Section 2.4.2). There is a possibility that the local H distribution can be different in different locations in the oxide as the H ingress is a stochastic process [80,82]. The fact that the oxide matrix surrounding the D-rich grain boundaries contains a much higher 18Da:17Da ratio than samples with no D segregation indicates that the D segregation to grain boundaries (i.e. hydroxylation) occurs after the surrounding matrix is rich in hydrogenic species and possibly hydroxylated. As this hydroxylation process occurs at grain boundaries, the hydroxyl pathways can become interconnected [80].

In my work, no sign of H or D segregation is found in the oxide layer adjacent to the O/M interface as all the datasets containing D segregation are taken between 500-600nm from the O/M interface. This suggests that H trapping at hydroxylated grain boundaries only occurs at the outer part of the oxide. In the innermost part of the oxide, H atoms enter the metal by a rapid diffusion mechanism that is probably electrochemically-assisted process rather than directly via grain boundaries as described in Figure 6.14b (4b-6b) [80].



(a)



(b)

Figure 6.14: (a) A model of a hydroxylated grain boundary in a ZrO_2 matrix where O, Zr and H atoms are in red, light blue and white respectively. (b) is the HPU mechanism via a grain boundary decorated with a transition metal, proposed by Lindgren et al. where stages (1-2) is the hydrolysis of the grain boundary, (3) is O uptake in Zr metal, (4a-6a) is the hydrogen gas evolution and (4b-6b) is HPU [124].

The details of H behaviour in this region and how it can penetrate the O/M interface are not well-understood because the barrier layer is highly resistive, impervious to electrolyte and contains almost no H [78,82,83] (Section 2.3.3). The barrier layer grows at pre transition but is short circuited during transition, possibly due to the generation of cracks near the O/M interface [79,82]. The cracks associated with transition are normally lateral cracks but vertical cracks have been observed as well, and proven to assist O transport [83]. It is possible that H can also be transported via this type of vertical crack (Figure 6.15), but the appearance of vertical cracks is extremely rare. Another suggested route for H transport is along dislocation

lines [139], but no D/H segregation to linear features in the oxide or metal is observed in this work.

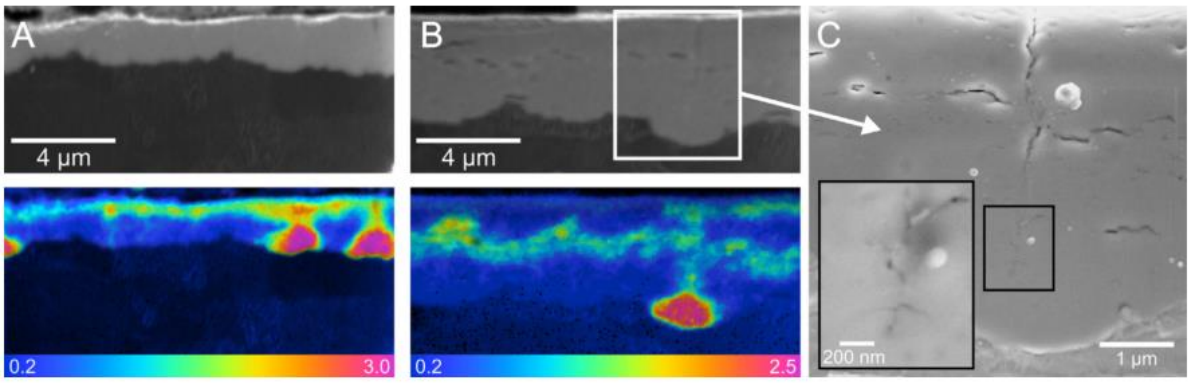


Figure 6.15: Secondary electron (top) and corresponding HSI (bottom) images of regions from (A) 34 + 20 day low tin ZIRLO and (B) 160 + 20 day low tin ZIRLO showing local variations in thickness associated with regions of significantly higher $^{18}O^{-}/^{16}O^{-}$ ratios at the O/M interface [83]. (C) Secondary electron images taken from the area marked in (B) with a higher magnification image from the crack tip [83].

In the innermost part of the oxide, the compressive stress is much higher than in the non-protective oxide layer [92,141,242]. The compressive stress can influence the H diffusion in this region, as the relationship between H diffusion and the stress is [141,242]:

$$D = D_0 \exp\left(\frac{-V_H \sigma_h}{RT}\right) \tag{6.1}$$

with D and D_0 are H diffusion coefficients with and with no applied stress respectively, V_H is the activation volume of H, σ_h is the hydrostatic stress, R is the gas constant and T is temperature. In monoclinic oxide grains, the H diffusion coefficient at 600K is 10^{-25}-10^{-24} m^2/s and can be reduced by ~40%/GPa in the presence of compressive stress [125,242], implying that H is immobile in the innermost part of the oxide. Therefore, the transport via vertical cracks is much more favourable than bulk diffusion.

Hydroxylation can also occur on pores [136]. Pores can also trap the hydrogen gas produced by the evolution process described in Figure 6.14b (4a-6a) [135,137]. If the interconnected pores observed in the post-transition regime [235] contain hydroxyls, especially if the pores

are adjacent to grain boundaries, they might also be a pathway for H transport [138,139]. This is probably the case in Analysis 2 where a D-rich pore is observed adjacent to a grain boundary [226].

6.6. Summary

- Interpretation of H distribution from APT analysis is ambiguous because H detected in the mass spectrum can originate from various external sources and therefore, D is incorporated into the samples as a surrogate for H. Deuteration of the samples can result in signals with D-containing ions (D^+ and OD^+) as the majority species.
- Considerable care needs to be taken to extract meaningful H/D data from APT experiments, especially in the oxide matrix.
- D segregation has been observed; this is evidenced by the segregations of 2Da and/or 18Da peaks, but the segregations of 18Da peak were found to provide a more reliable interpretation. Generally, the regions containing D segregation contain higher D content than outside the segregated regions. The features to which D segregates are likely to be oxide grain boundaries even though there is no Fe segregation.
- The results from this work agree with the mechanism involving hydroxylated oxide grain boundaries where H is transported via grain boundaries. However, this mechanism is perhaps only valid at the outer part of the oxide and does not occur in all oxide grain boundaries. At the O/M interface, H transport probably occurs by a different mechanism.
- Occasional evidence of porosity has been observed, with trapped D and H. The pores, if interconnected could be an alternative pathway for H transport.

7. IRON

7.1. Introduction

From Section 2.2.2.1, we know that iron is one of the most common impurities found in Zr-Nb alloys [18,19,23,30,49]. Although Fe-rich features in Zr-Nb have been observed by different authors, but very little is understood regarding its role in oxidation and HPU [6,31-33,192]. Fe tends to be located in the SPPs that may act as a local expressway for H transport [9,127,129]. These SPPs can also be cathodic sites for HPU reaction (Sections 2.3.4 and 2.4.3) [108,243].

To investigate this, the Fe distributions in the metal, oxide and at O/M interface were analysed. Fe ions in the mass spectra are mainly detected in the 28Da peak as $^{56}Fe^{2+}$. The $^{56}Fe^{2+}$ signal at 28Da peak overlaps with CO^{+}, causing a difficulty in ranging (Section 3.2.3.2.2).

Fe segregation was observed in all materials, and therefore the results in this chapter come from all materials studied in this thesis. The overall Fe contents in the as-recrystallised and annealed Zr-1Nb materials measured by Westinghouse using ICPMS were 753 and 596 wtppm, corresponding to 0.12 at% and 0.10 at%, respectively [198]. In the Zr-2.5Nb sample the Fe content is slightly lower (440 wtppm or 0.07 at%), within the range of those normally reported in the literature (100-1000 wtppm in Zr-1Nb and Zr-2.5Nb taken from various authors) [18,19,31,244].

7.2. Iron in the metal

7.2.1. Metal matrix

The matrix composition measurement results from the successful analyses of 4 as-recrystallised and 5 annealed Zr-1Nb APT samples (Section 4.2). The Fe contents in as-recrystallised and annealed Zr-1Nb matrices are both 0.01±0.007 at%, corresponding to Fe/Zr ratios of $(1.4\pm0.8)\times10^{-4}$ and $(1.3\pm0.9)\times10^{-4}$. These values are very close to the Fe maximum solubility in α-Zr between 800-850°C (~0.01 wt% or ~0.02 at%) (Figure 7.1) [20,39]. This implies that only approximately ~11-12% of the overall Fe stays in solution in the matrix for both samples. Therefore, most Fe segregates to other features in the materials.

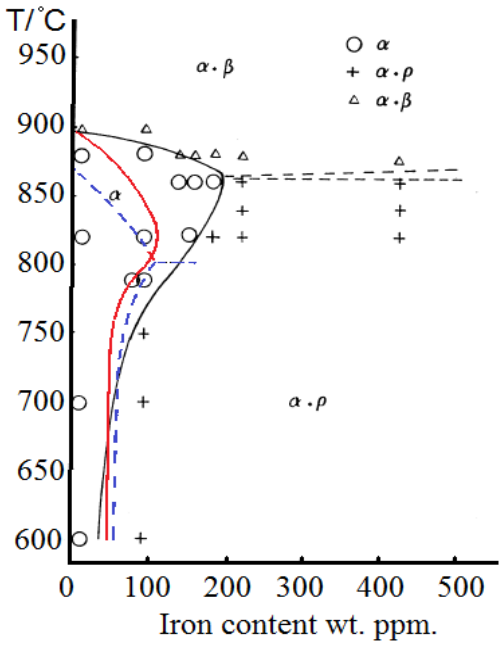
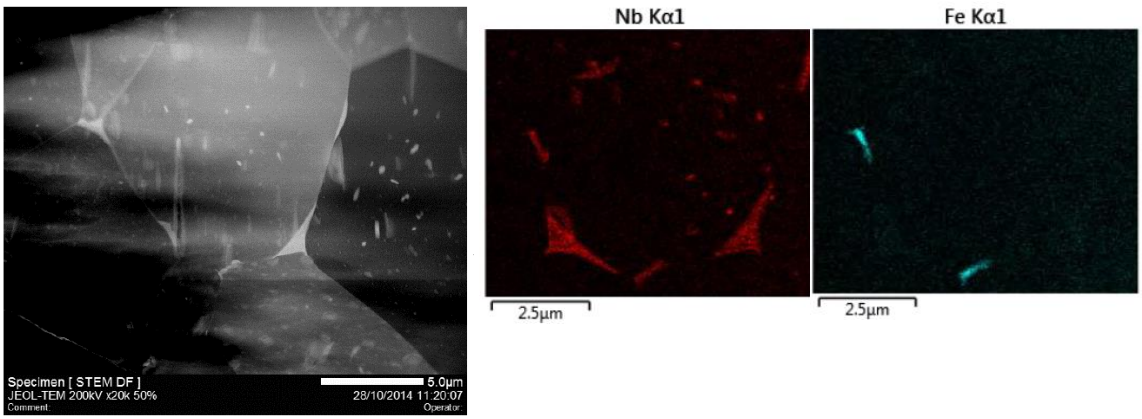


Figure 7.1: Zr-rich region of the Zr-Fe phase diagram for Zr-Fe (blue dashed line), Zr-1.4Sn-0.1O-Fe (red line) and Zr-1.4Sn-0.0036Fe-Cr (black line) systems [6,39,245]. The black line is obtained from experiments, where circles indicate the points where Fe is fully soluble in the α-Zr matrix, plus symbols representing the two-phase region where α-Zr(Fe) coexists with Fe-containing intermetallics and triangles where β-Zr(Fe) coexists with Fe-containing intermetallics.

7.2.2. Metallic β-Nb particles

One possible segregation site for Fe is into SPPs (Section 2.2.2.1). However, β-Nb is the only type of precipitate analysed in detail in my work. The alloys in this work could also contain $Zr(Nb,Fe)_2$ and β-Zr in the annealed Zr-1Nb material but they are too far apart to be found in the very small volumes analysed by APT (Figure 7.2a-c). β-Zr (concentrated in Nb in Figure 7.2b) and $Zr(Nb,Fe)_2$ (concentrated in Fe in Figure 7.2c) SPPs at grain boundaries are located at least ~1μm apart [201], very large compared to the dimension of a typical APT specimen. Therefore, the probability of capturing these precipitates in an APT specimen is low.



(a) (b) (c)

Figure 7.2: (a) SPPs in 225-day annealed Zr-1Nb sample observed using TEM and EDX elemental mapping of (b) Nb and (c) Fe taken in the grain at the centre of (a) [201].

A total of 10 metallic β-Nb particles in the metal were captured in my APT data; 4 particles from Zr-2.5Nb, 2 particles from as-recrystallised Zr-1Nb and 4 particles from X2. The O content in these particles ranges from 0-7.6 at%, and the particles with the highest O content are located in the $Zr(O_{sat})$ region described in Section 5.4.3. Fe profiles of these particles were taken using proxigrams that mimic the particle/metal (P/M) interface (Section 3.2.3.3) because the overall number of Fe atoms in and around the particles is very low, and therefore all the detected Fe atoms must be included in the datasets to give statistically significant

analysis. Typical Fe profiles across the P/M interface from as-recrystallised Zr-1Nb, X2, and Zr-2.5Nb are given in Figure 7.3.

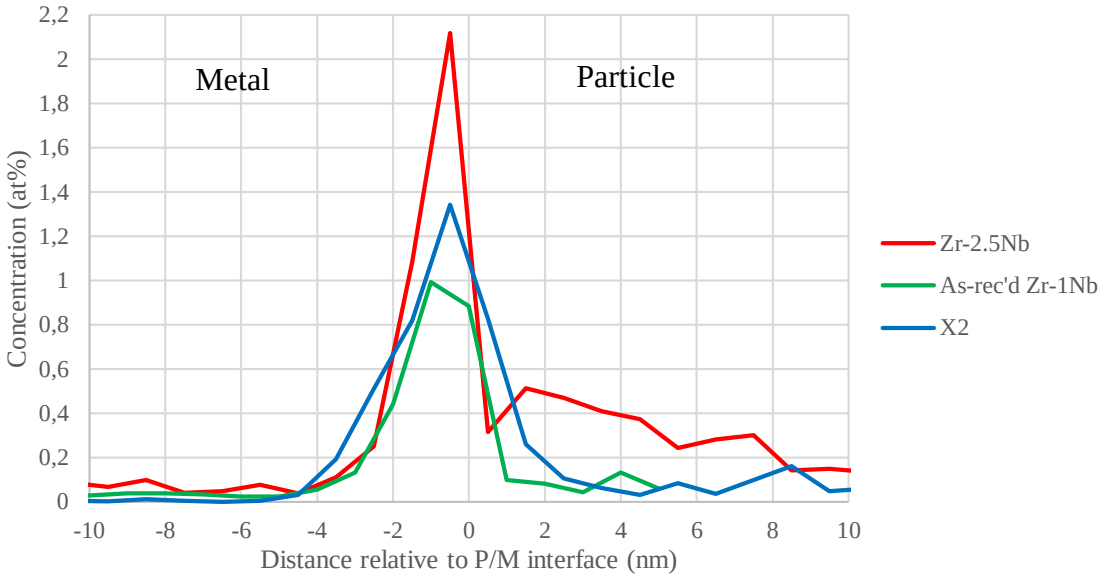


Figure 7.3: A comparison of Fe concentration profiles across the P/M interface taken by proxigrams from 3 different alloys; Zr-2.5Nb, as-recrystallised Zr-1Nb and X2.

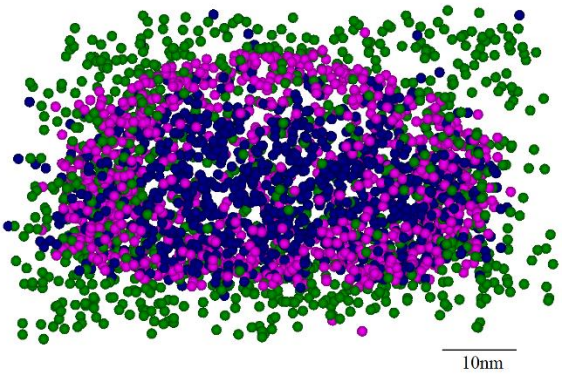


Figure 7.4: An atom map of a metallic β-Nb SPP in the X2 metal matrix showing the distribution of $Zr^{1,2,3+}$ (green), $Nb^{1,3+}$ (blue) and Fe^{2+} (pink) ions.

In Figure 7.3, the Fe content inside the particle is slightly higher than in the metal matrix, but more obviously, there is also Fe decorating the outer part of the particle corresponding to the peak at the interface (Figure 7.4). The comparison between different alloys is detailed in Table 7.1. In general, β-Nb particles in Zr-2.5Nb contains more Fe than in as-recrystallised Zr-1Nb and X2. Although the Fe content in X2 is unknown, this alloy is metallurgically similar to as-recrystallised Zr-1Nb and is expected to contain a similar amount of Fe.

Table 7.1: Comparison of Fe concentration profiles across the P/M interfaces in Zr-2.5Nb, as-recrystallised Zr-1Nb and X2.

	Zr-2.5Nb	**As-recrystallised Zr-1Nb**	**X2**
Number of particles	4	2	4
Average maximum Fe concentration at P/M interface (at%)	1.82	1.58	1.26
Average peak width (nm)	3	6	9
Average interfacial excess (atoms/nm^2)*	2.0	1.3	1.5
Average Fe concentration inside the particle (at%)	0.30	0.11	0.12

*The interfacial excess is measured relative to the Fe content in the metal matrix.

β-Nb particles in as-recrystallised Zr-1Nb and X2 have similar Fe profiles across the P/M interface, but in general they contain less Fe compared to particles in Zr-2.5Nb. To quantify Fe decorating the P/M interface, I have used interfacial excess (Section 3.2.3.3). The Fe interfacial excess at the P/M interface in Zr-2.5Nb is 2.0±0.5 atoms/nm^2, higher than in as-recrystallised Zr-1Nb (1.3±0.2 atoms/nm^2) and X2 (1.5±0.4 atoms/nm^2). With 1σ criterion, the average interfacial excess in Zr-2.5Nb is still outside the statistical error of the results from as-recrystallised Zr-1Nb and X2. The β-Nb particles in the Zr-2.5Nb also contain more Fe; the average Fe content inside these particles is 0.30±0.07 at%, much higher than in either as-recrystallised Zr-1Nb (0.11±0.03 at%) or X2 (0.12±0.03 at%). However, the measured Fe content in β-Nb in Zr-2.5Nb is much lower than the reported values measured by XRD (1.4 at%) [31]. This could be because the ranging method that I use underestimates the amount of Fe, and because the measured concentration approaches the lower limits of what can be measured by both APT and XRD, and hence the standard deviations in both cases are high.

7.2.3. Metal grain boundaries

Apart from the particles, Fe also segregates to metal grain boundaries in α-Zr because the Fe solubility in bulk α-Zr is very low (Section 7.2.1). This has been evidenced by several authors

using APT and STEM [6,31,33,34]. The Fe distribution across the grain boundary area is rather homogeneous (Figure 7.5a-b). The Fe concentration (Figure 7.5c) is a few nm in apparent width, but this is considered an artefact due to trajectory aberrations [169,190].

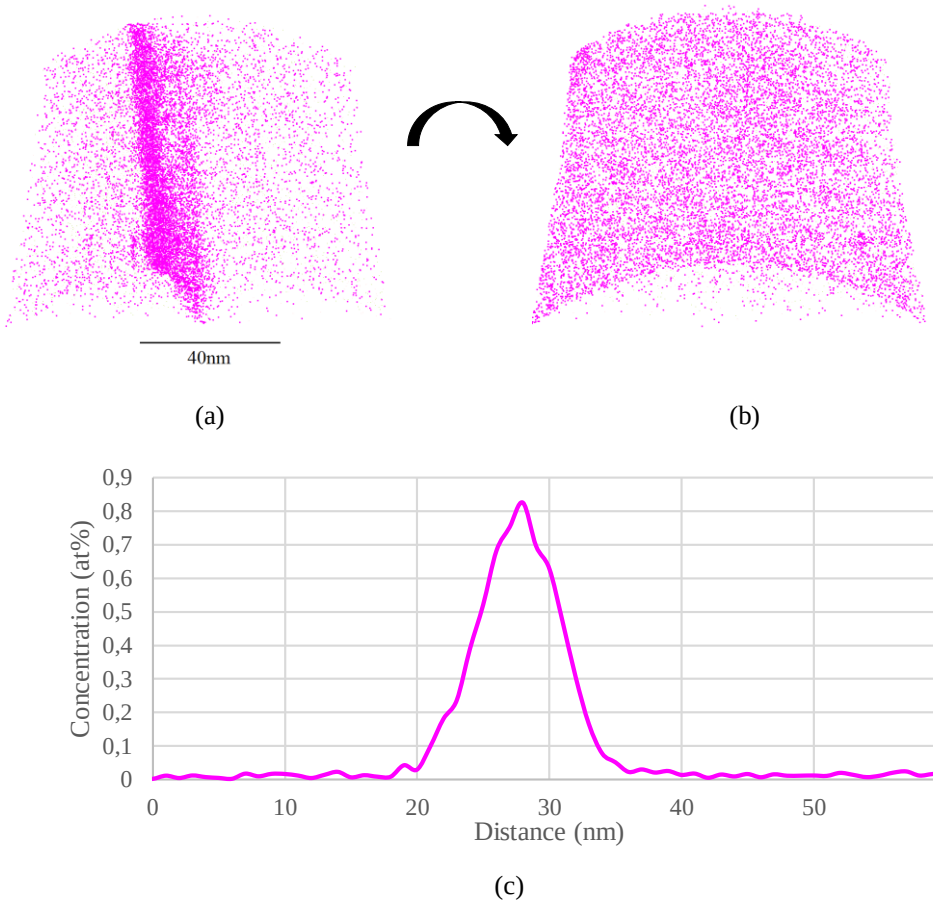


Figure 7.5: (a) A typical Fe-rich metal grain boundary in as-recrystallised Zr-1Nb, (b) image (a) rotated 90° showing the grain boundary cross section and (c) the Fe concentration profile across the boundary.

Examinations of 7 metal grain boundaries (3 from as-recrystallised Zr-1Nb, 1 from Zr-2.5Nb and 3 from Zr-0.5Nb-0.1Sb) demonstrate that the width of segregation and maximum concentration range from 9-21 nm and 0.34-1.13 at% respectively. The average interfacial excess is 1.9±0.7 atoms/nm^2 and the average Gibbsian excess is 13.4±5.2% monolayers of α-Zr basal plane, indicating that on average at least ~13% of the grain boundary area is covered with excess Fe atoms. This value is lower than the reported values (~30%) in Zircaloy-2 and ZIRLO [33,34]. The fact that all the grain boundaries detected in this work have Gibbsian excess values below 30% (the highest is ~22.1%) could be due to lower overall Fe content in

Zr-Nb system where, unlike in the Zircaloys and ZIRLO, Fe is not deliberately added to the alloys. However, a grain boundary with much lower Gibbsian excess (~3% monolayers of α-Zr basal plane) has also been reported in ZIRLO [6], suggesting that there is also a large variations in segregation between grain boundaries.

7.3. Iron in the oxide

7.3.1. Oxide and suboxide matrices

Examinations from 7 as-recrystallised and 29 annealed samples demonstrate that the average Fe content in the bulk oxide is 0.01±0.002 at% in as-recrystallised and 0.01±0.004 at% in annealed Zr-1Nb, corresponding to Fe/Zr ratio of $(3.5\pm0.5)\times10^{-4}$ and $(3.3\pm1.2)\times10^{-4}$ in as-recrystallised and annealed samples respectively. The comparison between Fe content in the metal and oxide matrices is displayed in Table 7.2.

Table 7.2: Comparison between Fe content in the metal and oxide matrices in as-recrystallised and annealed Zr-1Nb

	As-recrystallised Zr-1Nb		**Annealed Zr-1Nb**	
	Metal	**Oxide**	**Metal**	**Oxide**
Number of samples	4	7	5	29
Average Fe content (at%)	0.01*	0.01	0.01*	0.01
Standard deviation of Fe content (at%)	0.007	0.002	0.007	0.004
Average Fe/Zr ratio ($x10^4$)	1.4	3.5	1.2	3.3
Standard deviation of Fe/Zr ratio ($x10^4$)	0.7	0.5	0.8	1.2

*Fe concentration in the metal is taken from the percentage of all atoms from all metal datasets rather than averaging between samples.

According to Table 7.2, the Fe concentration varies considerably between samples as the standard deviations are high in both as-recrystallised and annealed Zr-1Nb. This could be due to real sample-to-sample microscopic variations and/or the uncertainty in separating the $^{56}Fe^{2+}$ and CO^{+} signals in the 28Da peak (Section 3.2.3.2.2). However, using a 1σ criterion,

the Fe/Zr ratio in the oxide is still higher compared to that measured in the metal, suggesting that the bulk oxide is more enriched in Fe than the metal.

In terms of Fe in the ZrO suboxide region, 3 datasets from X2 containing at least 200nm of ZrO were analysed. The average Fe concentration in these ZrO regions is 0.01±0.007 at%, giving a Fe/Zr ratio of $(1.9\pm1.3)\times10^{-4}$. Therefore, the Fe/Zr ratio in the ZrO suboxide is apparently between the Fe/Zr ratio in the metal and oxide matrices. However, the standard deviation is high, and thus it is difficult to be sure of the significance of these measurements.

7.3.2. Oxidised β-Nb particles

The Fe profile from a total of 6 oxidised β-Nb particles in the oxide of Zr-2.5Nb were examined. Oxidised β-Nb particles in the oxide have different Fe profiles compared to the metallic (unoxidised) β-Nb particles in the metal (Figure 7.6). It is clear that unlike the metallic particle, there is no Fe decorating the P/O interface in the oxidised particle, indicating a redistribution of Fe decoration around the particle during oxidation. The dissolution of Fe decorating the P/M interface occurs immediately after the particle is exposed to the oxide rather than slowly.

The Fe and O contents inside 4 metallic β-Nb particles in the metal (Section 7.2.2) and 6 oxidised β-Nb particles in the oxide of Zr-2.5Nb are plotted in Figure 7.7a. The O content in the oxidised particles varies from 18.8-27.3 at% and these particles are all located in the oxide. I detected no particles with O content between 7.6-18.8 at%, suggesting that there is probably a high influx of O into β-Nb once the particle starts to oxidise. The average concentration of Fe inside the oxidised particles is 0.30±0.12 at%, very similar to the content inside the metallic particles (0.30±0.07 at% from Section 7.2.2).

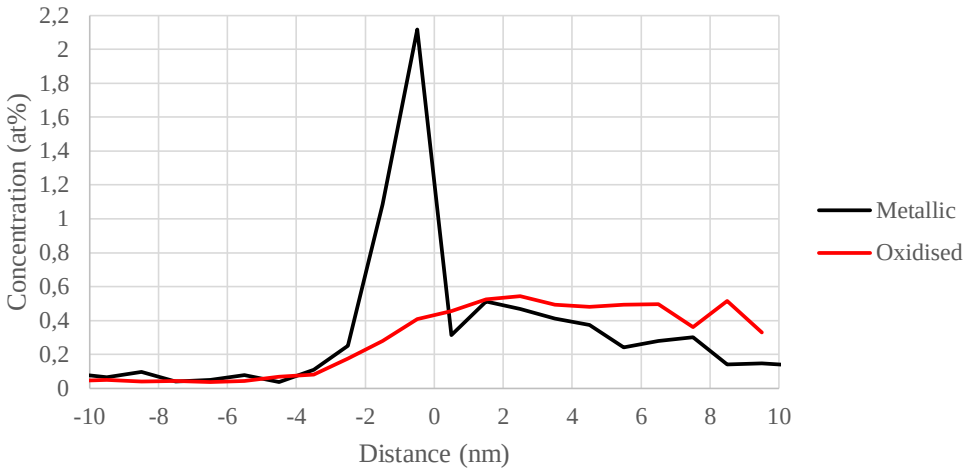
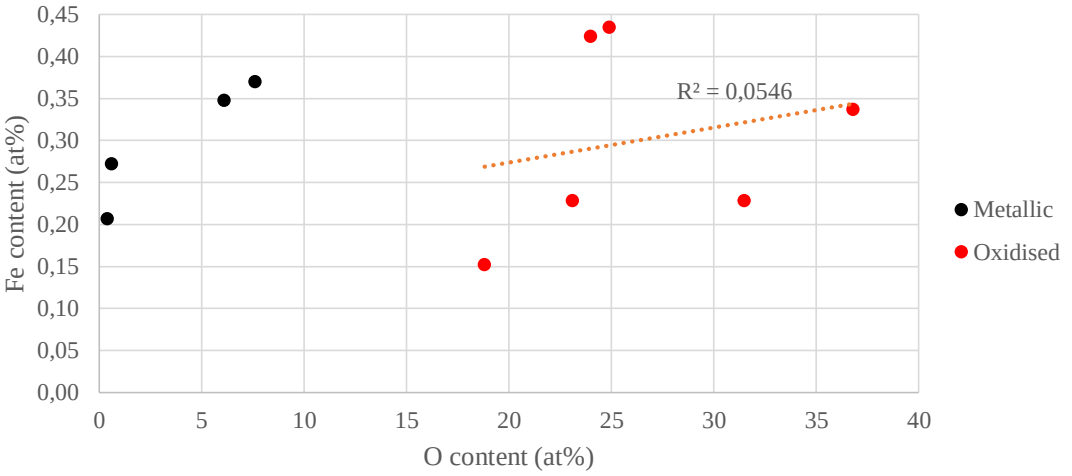


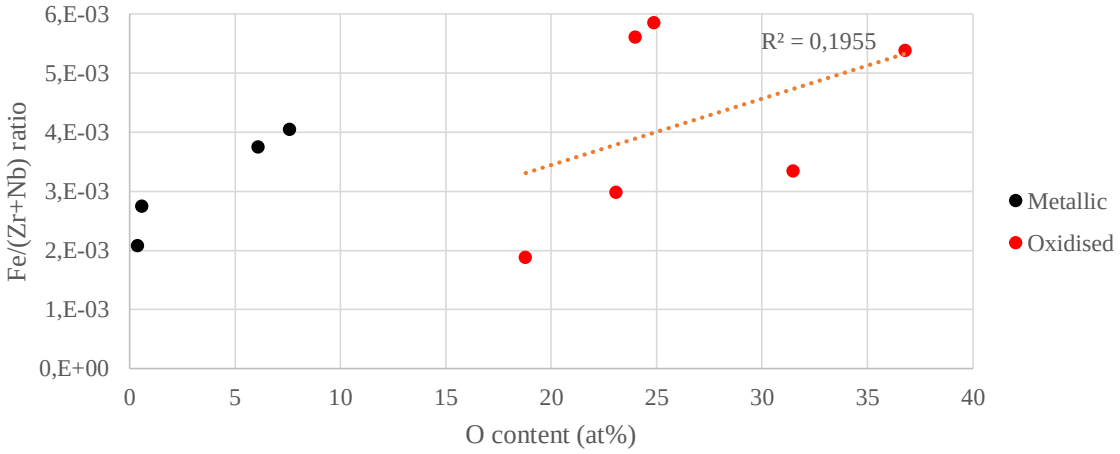
Figure 7.6: A comparison of Fe profile across the particle/matrix interface from a metallic and oxidised β-Nb particles.

The average Fe/(Zr+Nb) ratio in the metallic particles is $(3.2\pm0.9)x10^{-3}$ and in the oxidised particles is $(4.2\pm1.7)x10^{-3}$, indicating that the Fe content inside the metallic particles remains almost constant after oxidation (Figure 7.7b). Both Fe content and Fe/(Zr+Nb) ratio of the oxidised particles might show an apparently weak increasing trend as the O content increases (Figure 7.7a-b), suggesting that Zr diffuses out from the particle faster than Fe at a later stage of oxidation.

Based on the above observations, and using Zr-2.5Nb as an example, the Fe redistribution during β-Nb oxidation can be modelled (Figure 7.8). Consider a metallic β-Nb in the metal containing ~0.30 at% Fe of and the P/M interface is occupied by Fe with average interfacial excess of ~2.0 atoms/nm^2. After oxidation, the Fe inside the particle is not redistributed as the average Fe concentration remains constant (~0.30 at%) but the Fe that formerly decorates the P/M interface is redistributed into the oxide matrix. This can be seen by the disappearance of Fe decoration at the outer part of the particle. The net effect of this process is to increase the Fe content in the bulk oxide by a factor of 2.5-3 (Table 7.2).



(a)



(b)

Figure 7.7: (a) O vs Fe content and (b) O content vs Fe/(Zr+Nb) ratio from 4 metallic and 6 oxidised β-Nb in Zr-2.5Nb.

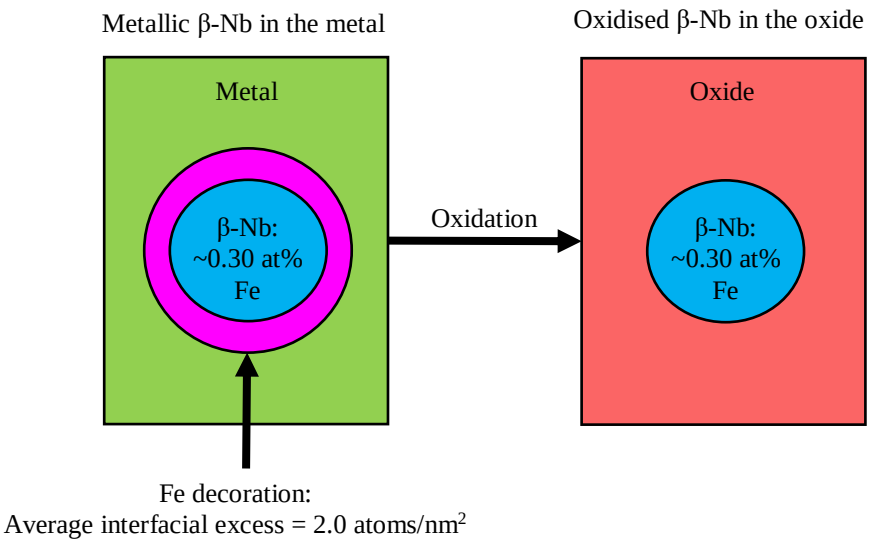


Figure 7.8: A model of Fe redistribution during the β-Nb oxidation.

7.3.3. Oxide grain boundaries

The oxide grain size (e.g. 5-90 nm in width and 100-500 nm in length for columnar grains [10,77,88,167,234]) is much smaller than the metal grain size (several μm), and hence there are a lot more grain boundaries in the oxide than in the metal. However, because the overall Fe content is very low, it is insufficient to decorate all the oxide grain boundaries. Most oxide grain boundaries are not decorated with Fe, e.g. in Figure 6.11 (Section 6.4.2.1) where an oxide grain boundary with no Fe segregation is identified from the atomic density map.

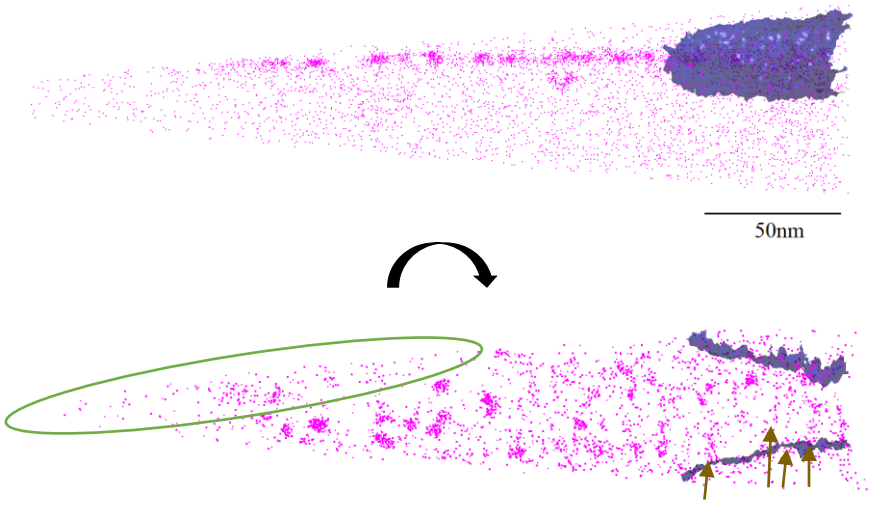
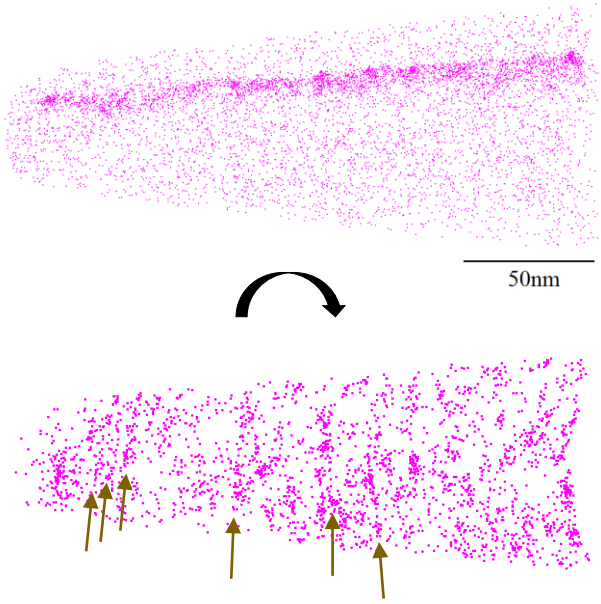


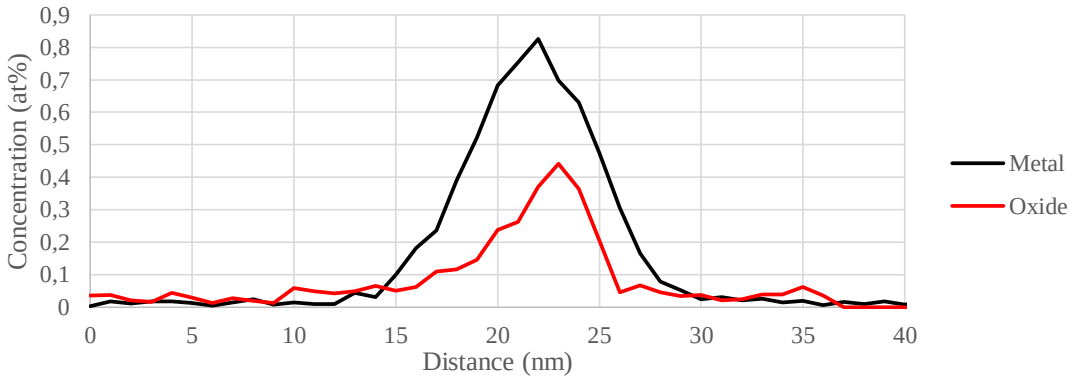
Figure 7.9: An Fe-rich oxide grain boundary (top) and a 10 nm slice of its cross section (bottom). There are two β-Nb particles on the grain boundary, represented by two 5 at% Nb isosurfaces (blue). Note that Fe dots in the bottom image are magnified 1.5x for clarity. The green ellipse indicates a localised Fe-depleted region on the grain boundary and the brown arrows point out apparent dislocation lines. This dataset is from the oxide on Zr-2.5Nb.

However, there are also Fe-decorated oxide grain boundaries. The Fe distribution on these grain boundaries is different compared to the metal grain boundaries (Section 7.2.3). An Fe-rich grain boundary consists of Fe clusters and apparent decoration of dislocation lines, e.g. in Figure 7.9. Fe decoration on this grain boundary is also inhomogeneous, as there is an Fe-depleted region in the grain boundary cross section. In this particular example, the grain boundary is pinned by two β-Nb particles and the area between the two particles is apparently

strained as it contains a few dislocation lines. It is not possible to determine whether Fe atoms decorating the oxide grain boundaries are metallic or oxidised using APT, but the fact that most of these atoms are evaporated in the form of metallic Fe^{2+} indicates that they are likely to be metallic.



(a)



(b)

Figure 7.10: (a) An oxide grain boundary in Zr-2.5Nb with a relatively homogeneous Fe distribution and its cross section containing Fe clusters and parallel dislocation lines (brown arrows). (b) is a comparison of Fe profiles across the oxide grain boundary in (a) and a metal grain boundary from Figure 7.5.

Because the Fe distribution on Fe-rich oxide grain boundaries is inhomogeneous, the Fe-depleted region is not included when calculating the degree of Fe segregation. This kind of Fe-depleted region is not always present as there are grain boundaries showing fairly

homogeneous Fe distribution (Figure 7.10a). Although the dataset in Figure 7.10a does not contain any particles pinning the grain boundary, decorated dislocation lines parallel to each other can still be seen. A comparison of an Fe profile across a typical Fe-rich grain boundary in the oxide and the metal is displayed in Figure 7.10b. It is clear that the oxide grain boundary contains much less Fe than the metal grain boundary.

Examination of 6 Fe-rich oxide grain boundaries (1 from as-recrystallised Zr-1Nb, 3 from Zr-2.5Nb and 2 from Zr-0.5Nb-0.1Sb) show that the width and maximum Fe concentration at these grain boundaries range from 9-18 nm and 0.09-0.53 at% respectively. The average interfacial excess is 0.4±0.2 atoms/nm^2 and Gibbsian excess is 0.8±0.3% monolayers of the m-ZrO_2 close-packed plane. Note that the ZrO_2 P-B ratio has been taken into account in these calculations (Section 3.2.3.3). The comparison between metal and Fe-rich oxide grain boundaries is shown in Table 7.3.

Table 7.3: Comparison of Fe distribution between metal and Fe-rich oxide grain boundaries.

	Metal grain boundaries	**Fe-rich oxide grain boundaries**
Fe distribution description	Homogeneous distribution	Inhomogeneous distribution; consist of Fe clusters and decorated dislocation lines
Number of grain boundaries analysed	7	6
Average width (nm)	12±5	12±4
Average maximum concentration (at%)	0.76±0.26	0.24±0.20
Average interfacial excess (atoms/nm^2)	1.9±0.7	0.4±0.2
Average Gibbsian excess (% monolayers of α-Zr or m-ZrO_2 close-packed plane)	13.4±5.2	0.8±0.3

It is obvious that the metal grain boundaries contain more Fe than the Fe-rich oxide grain boundaries (Table 7.3). There is a high confidence in this observation; if we apply a 2σ criterion, the average interfacial excess of Fe-rich oxide grain boundaries (0.4 atoms/nm^2) is

outside the lower limit of metal grain boundaries (0.5 atoms/nm^2). The Gibbsian excess is not a good parameter for comparing the amount of Fe in the metal and oxide grain boundaries because this parameter measures the amount of Fe on grain boundaries relative to the respective matrices. If the same amount of Fe atoms is present in a metal and oxide grain boundaries, the Gibbsian excess of the oxide grain boundary is lower than the metal one because the oxide has a greater atomic density. However, it provides information regarding how strong Fe segregates relative to the grain boundaries' respective matrices. It is clear that in the metal the Fe segregation to grain boundaries is much stronger than in the oxide.

7.4. Iron at the O/M interface

In this section, examples from as-recrystallised and annealed Zr-1Nb are used to demonstrate the Fe distribution in the metal adjacent to the O/M interface. The Fe behaviour in this particular area is related to the oxidation kinetics (Sections 4.3.1 and 4.3.2). In addition, the oxidation of metal grain boundaries is also discussed to explain the redistribution of Fe as they are consumed by the O/M interface.

7.4.1. Metal adjacent to the O/M interface

The average overall Fe content in this region taken from 7 as-recrystallised and 27 annealed Zr-1Nb samples is 0.03±0.01 at% and 0.03±0.03 at% respectively, corresponding to Fe/Zr ratios of $(4.1\pm1.8)\times10^{-4}$ and $(5.3\pm4.7)\times10^{-4}$ in as-recrystallised and annealed samples respectively. These values are higher than the Fe/Zr ratios in the oxide and metal matrices, especially for the annealed samples, indicating that this region is usually more enriched in Fe.

Fe rejection is commonly found at the beginning of oxidation, and the degree of rejection is described in terms of Fe interfacial enrichment in atoms/nm^2. The interfacial enrichment is

calculated using the same method as interfacial excess but refers to the amount of rejected Fe per unit area of O/M interface. Note that this parameter describes the excess of Fe atoms that are distributed within the matrices adjacent to the O/M interface rather than on the interface. As Fe segregates to dislocation lines, the Fe distribution in the metal changes throughout the course of oxidation (Table 7.4).

Table 7.4: Information on rejected Fe and Fe-rich features in the metal adjacent to the O/M interface.

Materials	**Annealed Zr-1Nb**						**As-recrystallised Zr-1Nb**	
State	Pre-transition			Post-transition			Pre-transition	Post-transition
Oxidation duration (days)	3	30	46	91	105	225	3	210
Instantaneous oxidation rate (mg/dm^2day)	1.21	0.51	0.47	0.79	0.63	0.90	0.91	0.25
Number of analyses	6	6	4	4	4	3	4	3
Average Fe interfacial enrichment ($atoms/nm^2$)	1.3	0.4	0.6	0.2	0.3	0.04	0.8	0.1
Standard deviation of Fe interfacial enrichment ($atoms/nm^2$)	0.7	0.3	0.1	0.1	0.2	0.04	0.3	0.2
Fe clusters	Very few	√	√	Very few	Very few	√	Very few	√
Dislocation lines	Very few	√	√	Very few	Very few	√	Very few	√
Sub grain boundaries	x	√	√	x	Very few	√	Very few	√
Strain-induced c-loops	x	x	x	x	x	√	x	x

At the beginning of oxidation, Fe is rejected from the oxide into the metal and this can be seen from the 3-day annealed Zr-1Nb sample (Figure 7.11). The dataset in Figure 7.11 contains the largest amount of rejected Fe compared to other 3-day annealed samples, and the Fe interfacial enrichment in this particular dataset is 2.0 $atoms/nm^2$. The rejected Fe

concentration fluctuates over a distance below the O/M interface of ~120nm. The average Fe interfacial enrichment of the 3-day annealed Zr-1Nb samples is 1.3±0.7 atoms/nm^2. The rate of Fe rejection is inhomogeneous throughout the same sample and this results in a high standard deviation between analyses. Apart from a few Fe clusters, there is no apparent Fe segregation in the metal. Similar rejection of Fe has been observed by previous APT studies where Fe segregates to the O/S (oxide/suboxide) interface in 7-day oxidised crystal bar Zr [210].

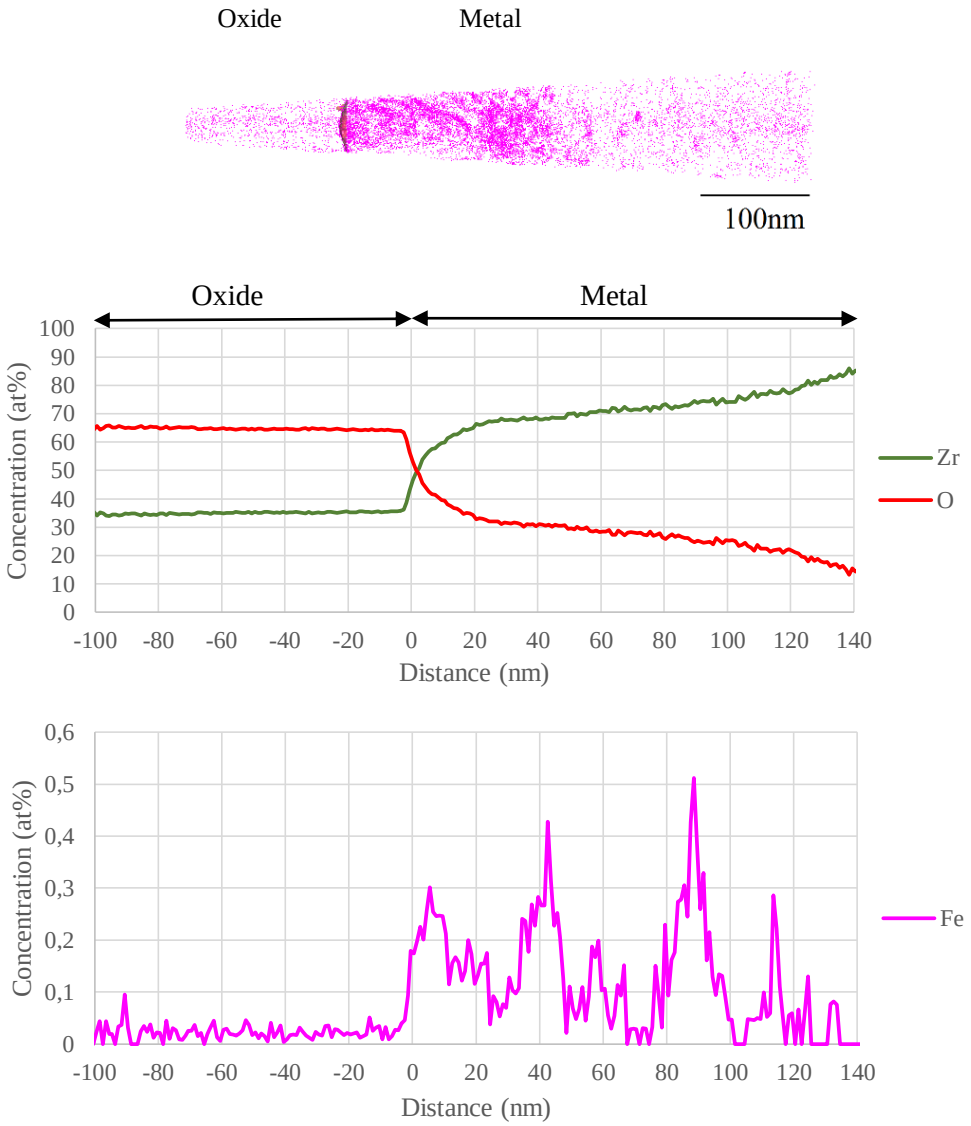


Figure 7.11: The Fe atom map and Zr, O and Fe concentration profiles across the O/M interface of a 3-day annealed Zr-1Nb sample showing rejected Fe.

Later in the pre-transition regime, at 30 days, Fe-rich dislocation lines start to build up in the metal region (Figure 7.12). The number of dislocation lines varies as in some 30-day samples, very few dislocation lines are found. The dislocation lines can be located very close to the O/M interface, and it is difficult to determine whether the Fe decorating the dislocation lines originates from pre segregation in the metal matrix or rejected Fe subsequently segregated to the dislocation lines. In this case, I make an assumption that the peak in the concentration profile corresponds to the rejected Fe. With this assumption, the average Fe interfacial enrichment drops from 1.3 atoms/nm^2 (3 days) to 0.4 atoms/nm^2.

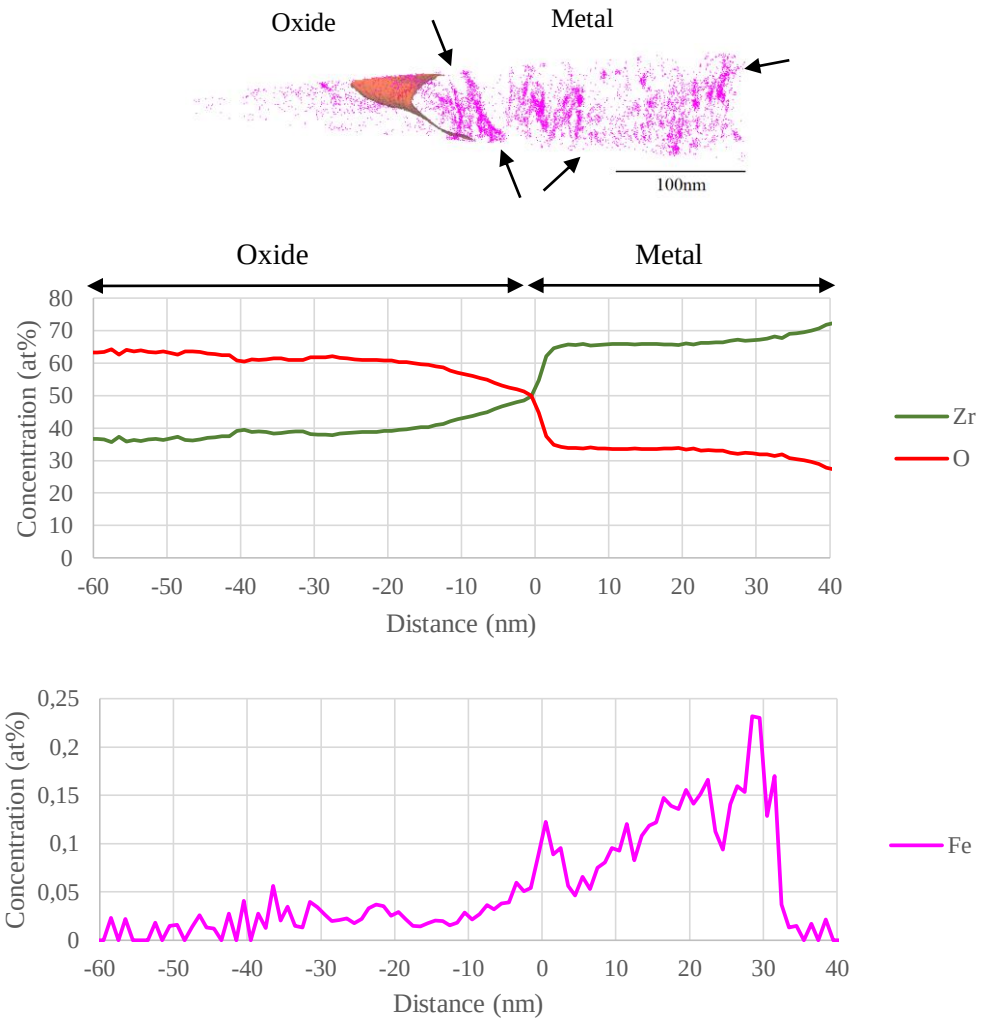


Figure 7.12: The Fe atom map and Zr, O and Fe concentration profiles across the O/M interface of a 30-day annealed Zr-1Nb sample. The black arrows on the atom map show the location of sub grain boundaries containing decorated dislocation lines lying on the same plane.

At 46 days, the annealed sample is still in the pre-transition regime but has the lowest instantaneous oxidation rate (Section 4.3.2). Fe rejection can occur at the S/M interface as well as the O/M interface (Figure 7.13). The 46-day sample is very similar to the 30-day sample in that they both contain a moderate amount of rejected Fe (similar average interfacial enrichment; 0.4 atoms/nm^2 for 30-day samples and 0.6 atoms/nm^2 for the 46-day samples) as well as decorated dislocation lines and sub grain boundaries (Section 7.4.2). After transition, the oxidation rate increases and reaches the maximum at 91 days. There is no detectable Fe segregation to the metal (Figure 7.14) nor dislocation lines.

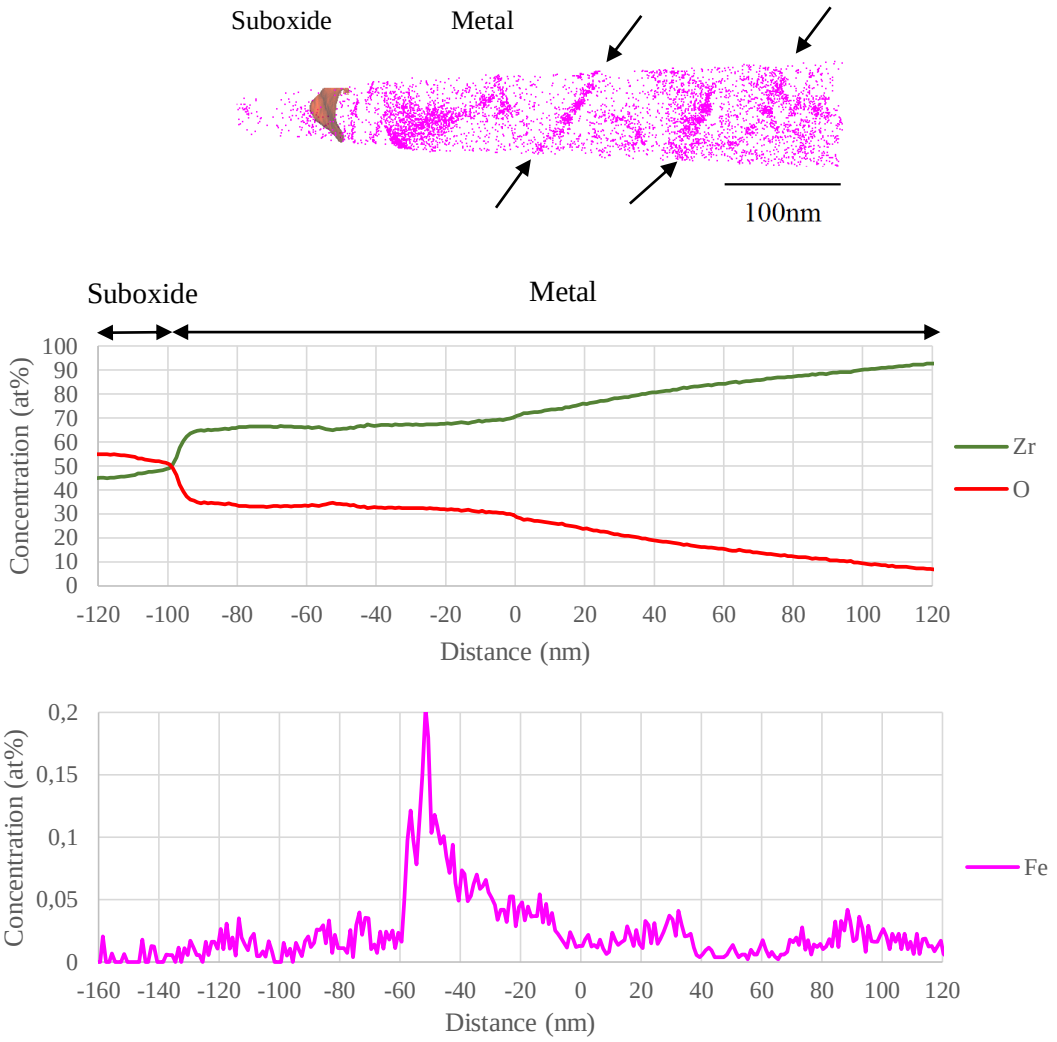


Figure 7.13: The Fe atom map and Zr, O and Fe concentration profiles across the S/M interface of a 46-day annealed Zr-1Nb sample. The black arrows on the atom map show the location of sub grain boundaries containing decorated dislocation lines lying on the same plane.

14 days later at 105 days, the oxidation rate has decreased slightly from 0.79 mg/dm^{2}day (91 days) to 0.63 mg/dm^{2}day (105 days). The amount of Fe rejection is still very small, but decorated dislocation lines start to form due to increasing stress in the metal as the distance between the O/M interface to the nearest cracks in the oxide increases (Figure 7.15).

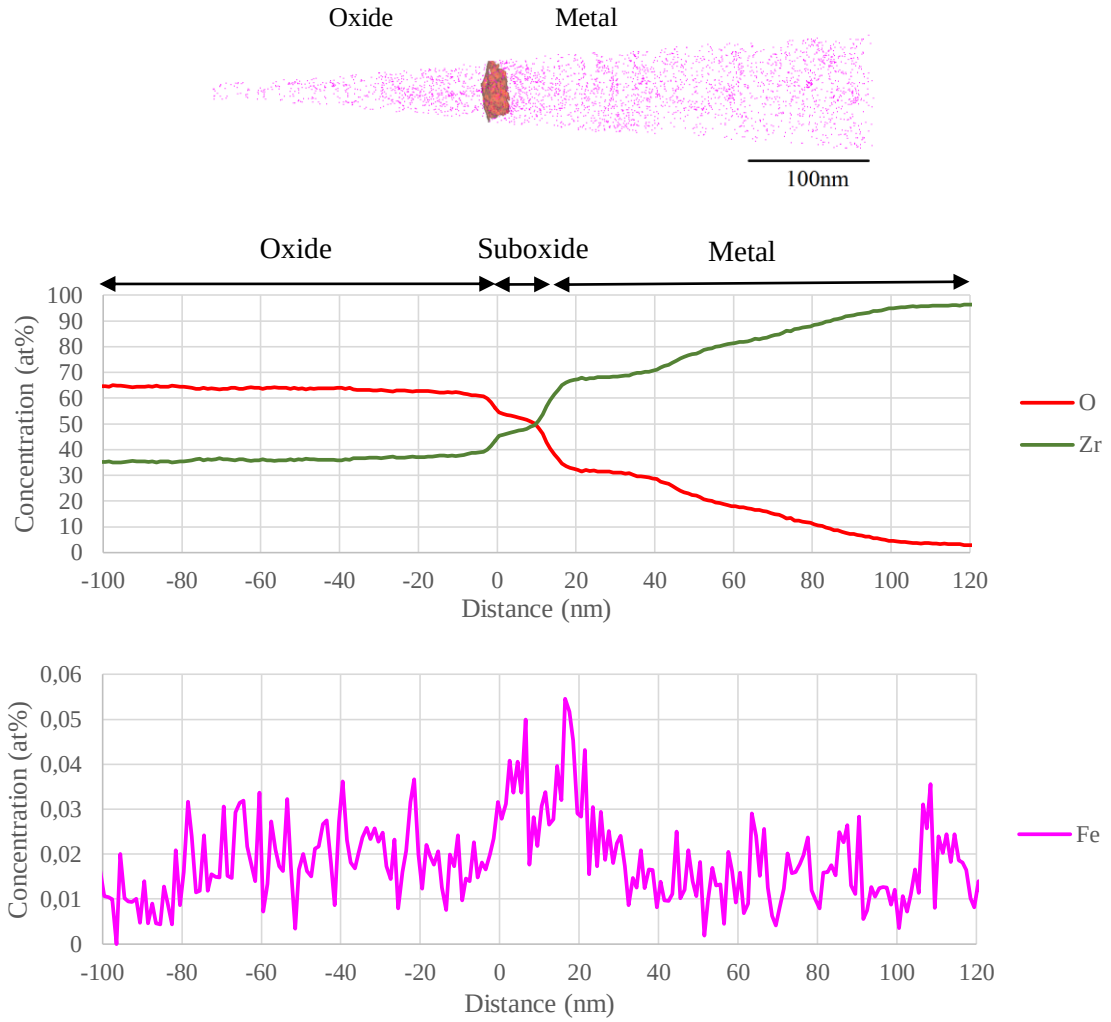


Figure 7.14: The Fe atom map and Zr, O and Fe concentration profiles across the S/M interface of a 91-day annealed Zr-1Nb sample. Note the low values on the Fe concentration axis.

The 225-day sample has a high instantaneous oxidation rate (0.90 mg/dm^{2}day) but there is almost no Fe rejection as the average Fe interfacial enrichment is only 0.04 atoms/nm^2. The example from Figure 7.16 contains ZrO suboxide that is sometimes associated with a low local oxidation rate [64] even though the overall 225-day sample has a high instantaneous

oxidation rate. There are dislocation lines and strain-induced c-loops (Section 7.4.2) in the metal region corresponding to the peaks in Fe profile.

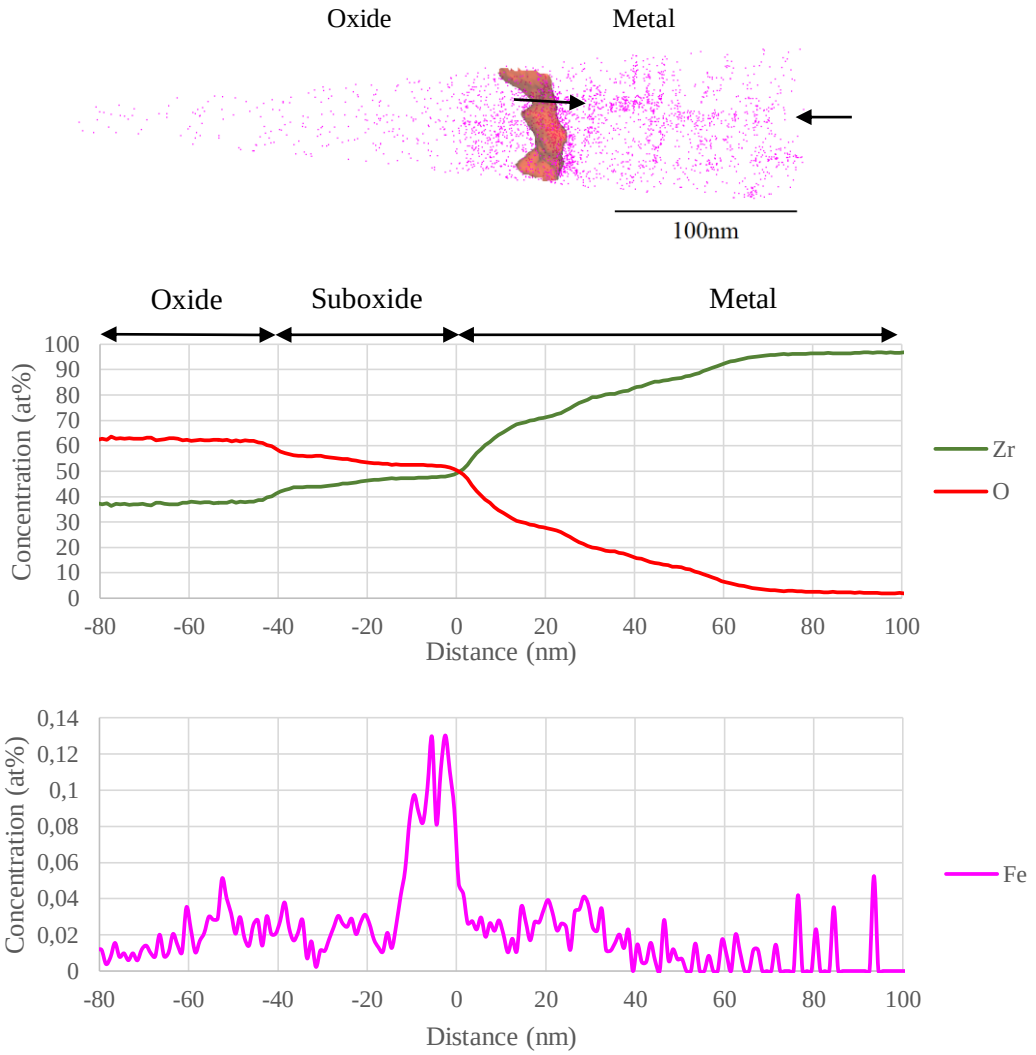


Figure 7.15: The Fe atom map and Zr, O and Fe concentration profiles across the S/M interface of a 105-day annealed Zr-1Nb sample taken from a 50 at% O proxigram. The black arrows on the atom map show the location of a sub grain boundary containing decorated dislocation lines lying on the same plane.

Results from as-recrystallised Zr-1Nb were then used to determine whether the same trends in Fe segregation were also observed in a different starting alloy. Like in the 3-day annealed sample, strong Fe rejection is also observed in the 3-day as-recrystallised sample (Figure 7.17). In this particular example, the rejected Fe is located in the suboxide rather than the metal.

The 3-day as-recrystallised sample has an average Fe interfacial enrichment of 0.8±0.3 atoms/nm^2, which is lower than the 3-day annealed sample (1.3±0.7 atoms/nm^2) but significantly higher than the rest of the samples analysed. This could be attributed to the oxidation rate where the instantaneous oxidation rate of the 3-day as-recrystallised sample (0.91 mg/dm^{2}day) is slightly lower than the 3-day annealed sample (1.21 mg/dm^{2}day). Similar to the 3-day annealed sample, the metal adjacent to the O/M interface in the 3-day as-recrystallised sample is generally free from decorated dislocation lines.

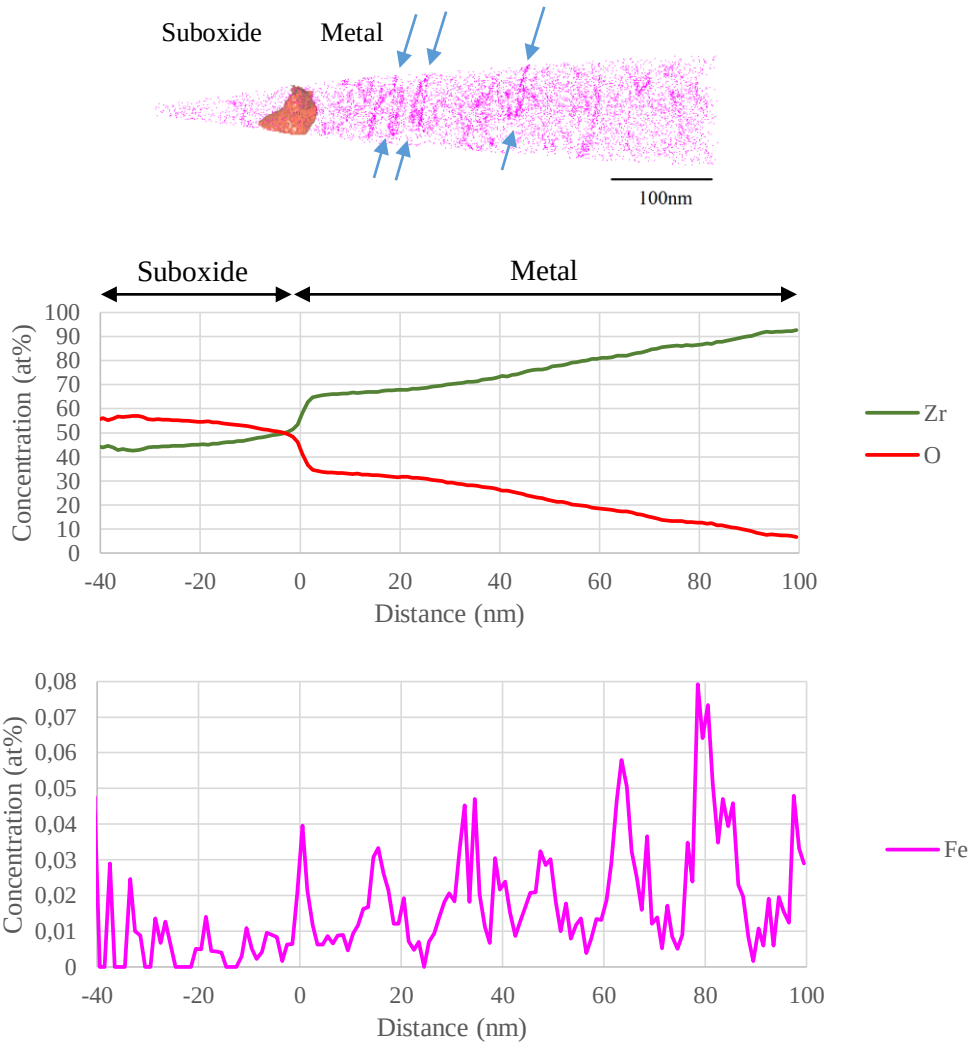


Figure 7.16: The Fe atom map and Zr, O and Fe concentration profiles across the S/M interface of a 225-day annealed Zr-1Nb sample taken from a 41 at% O proxigram. The blue arrows on the atom map show the locations of 4 strain-induced c-loops analysed in Section 7.4.2.

Another extreme in the as-recrystallised data is the 210-day sample where the instantaneous oxidation rate is the lowest among all as-recrystallised and annealed samples studied (0.25 mg/dm^{2}day). An example is shown in Figure 7.18 where there is a small amount of rejected Fe and two sub grain boundaries corresponding to the Fe peaks in the metal region. This dataset contains 0.4 atoms/nm^2 of Fe interfacial enrichment, the highest measured for 210-day as-recrystallised Zr-1Nb samples. No such Fe rejection was observed in the other two datasets, resulting in high standard deviation (0.2 atoms/nm^2) for this material (Table 7.4).

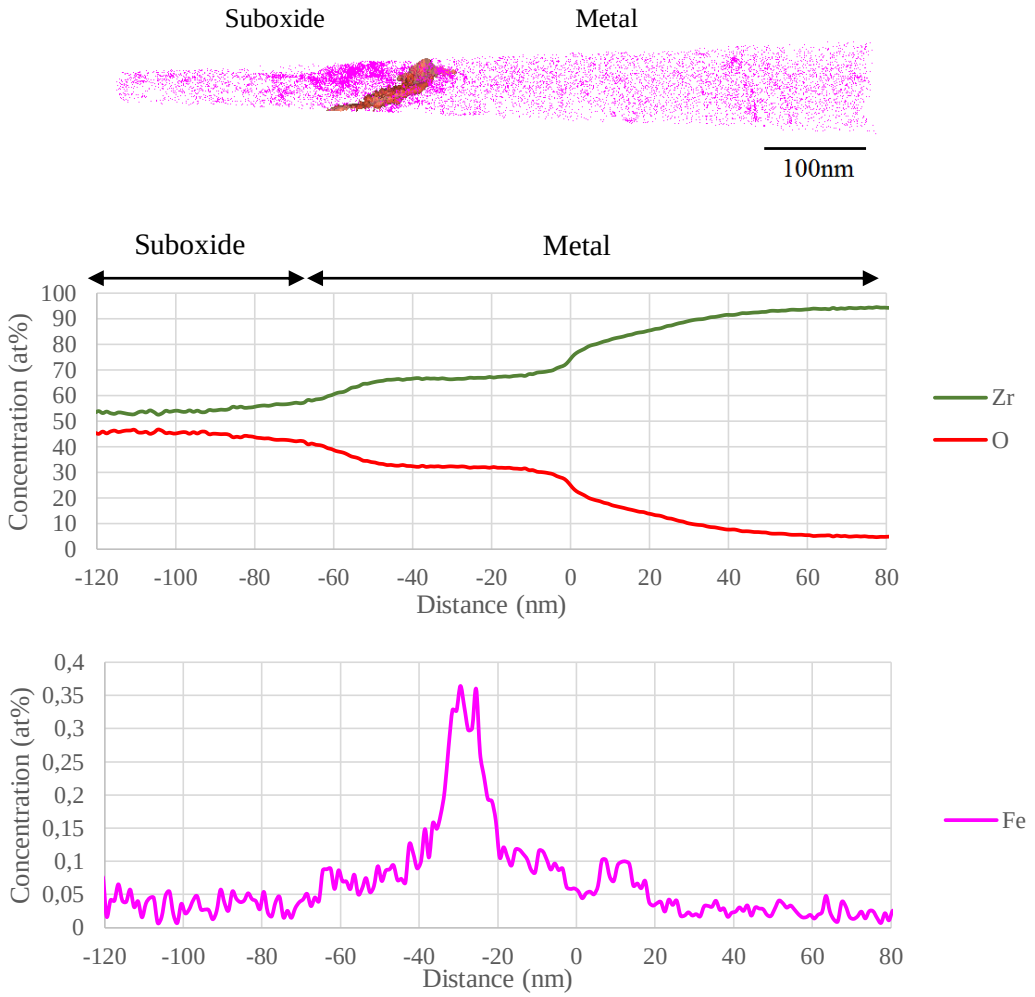


Figure 7.17: The Fe atom map and Zr, O and Fe concentration profiles across the S/M interface of a 3-day as-recrystallised Zr-1Nb sample.

To understand the extent of Fe rejection throughout the course of oxidation, the samples are grouped according to their positions relative to the first transition point, and Fe interfacial

enrichment is plotted against instantaneous oxidation rate (Figure 7.19). Even though the number of samples is rather limited, in pre transition the Fe interfacial enrichment increases of both annealed and as-recrystallised materials generally increases with oxidation rate. However, in post transition less correlation is observed because generally Fe rejection in this regime is almost negligible, although the single as-recrystallised point (210-day/yellow dot) does follow the trend. Therefore, we can conclude that Fe rejection tends to occur at the beginning of oxidation and gradually decreases over time in pre transition, but does not occur to a significant extent after transition, irrespective of the oxidation rate.

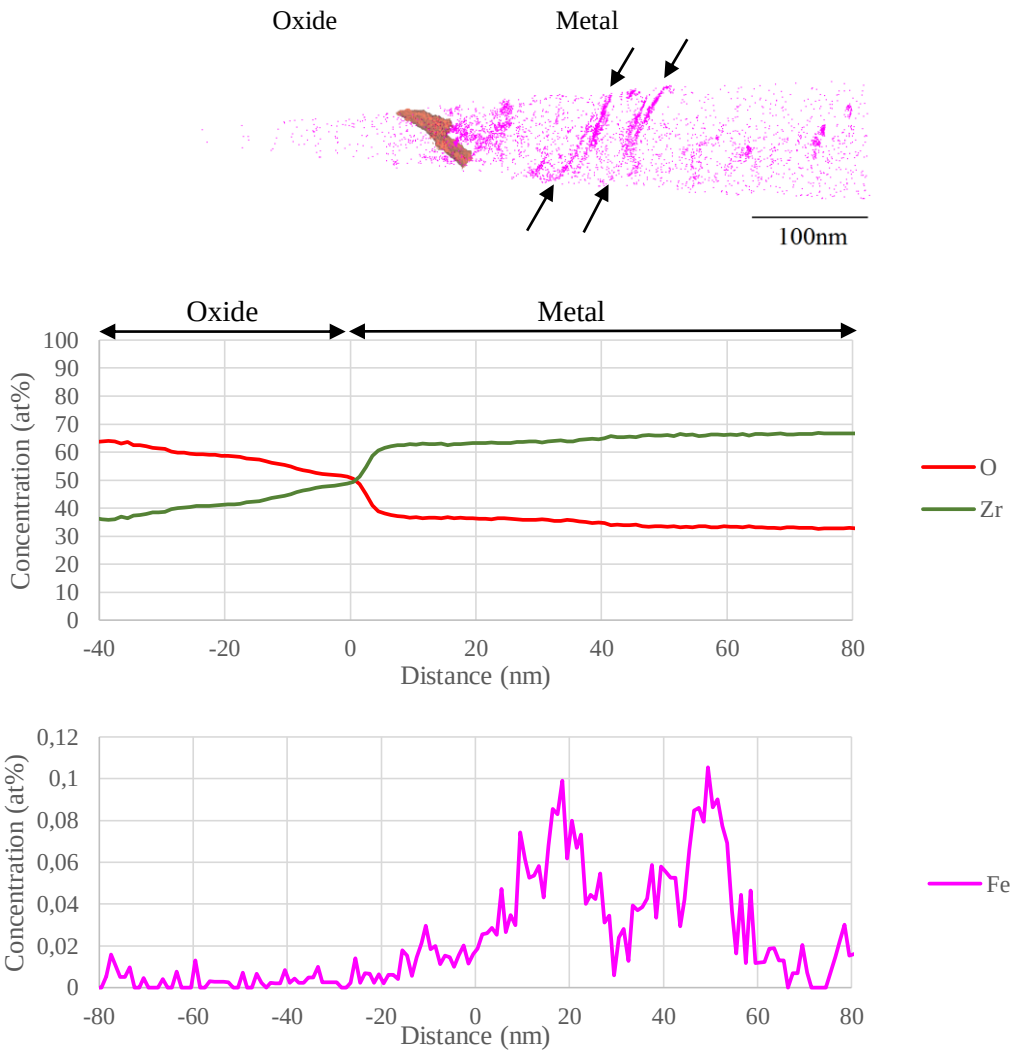


Figure 7.18: The Fe atom map and Zr, O and Fe concentration profiles across the O/M interface of a 210-day as-recrystallised Zr-1Nb sample. The black arrows on the atom map show the location of sub grain boundaries containing decorated dislocation lines lying on the same plane.

The analysis in Figure 7.19 is only valid to describe Fe rejection. To obtain a more complete picture of Fe behaviour at the metal near the O/M interface, the average Fe concentrations in the metal and oxide are plotted against instantaneous oxidation rate (Figure 7.20a-b). There is no apparent change of Fe concentration both in the metal adjacent to O/M interface and the bulk oxide throughout the course of oxidation. The standard deviations are large in pre transition due to inhomogeneity of Fe rejection in different locations. The Fe content in the metal adjacent to the O/M interface is apparently higher at pre transition than post transition for the annealed samples (Figure 7.20a) but the values in the post-transition regime are all within the experimental error. The average Fe content in the bulk oxide of annealed and as-recrystallised samples are all between 0.1-0.2 at%, suggesting that the variation is negligible (Figure 7.20b).

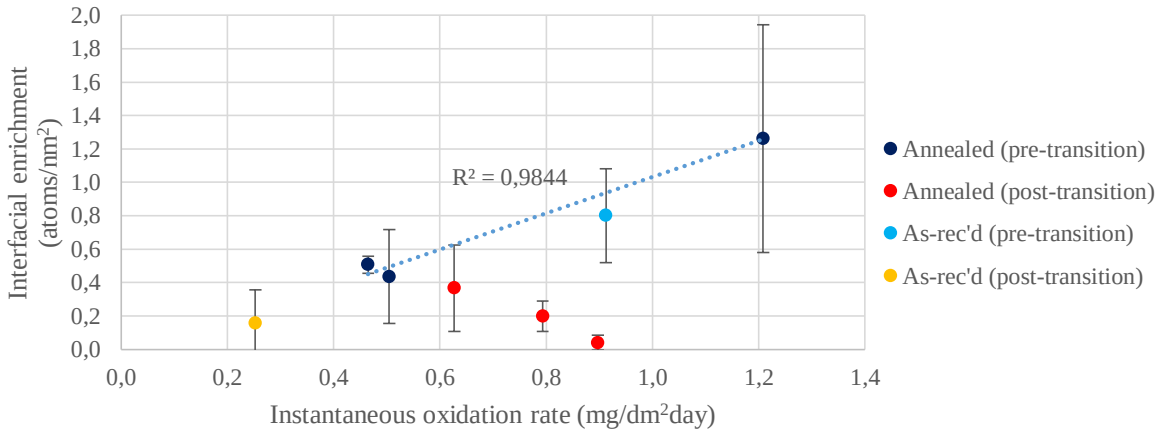
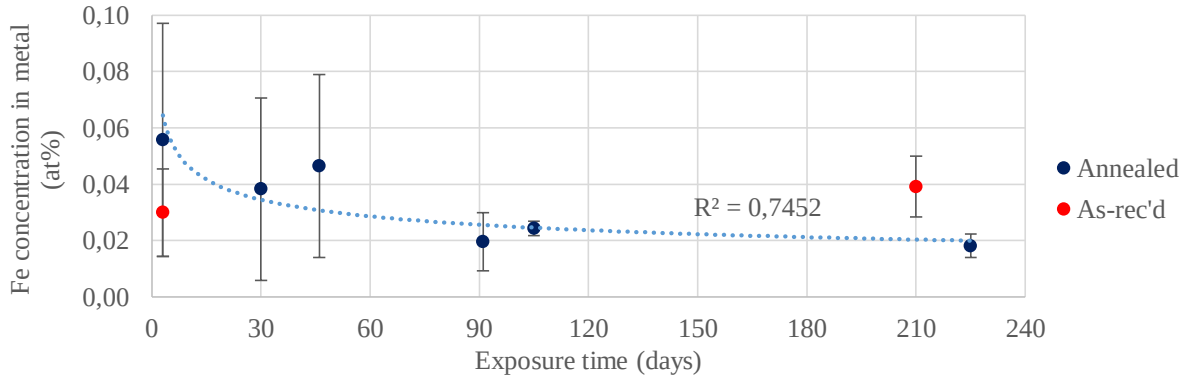


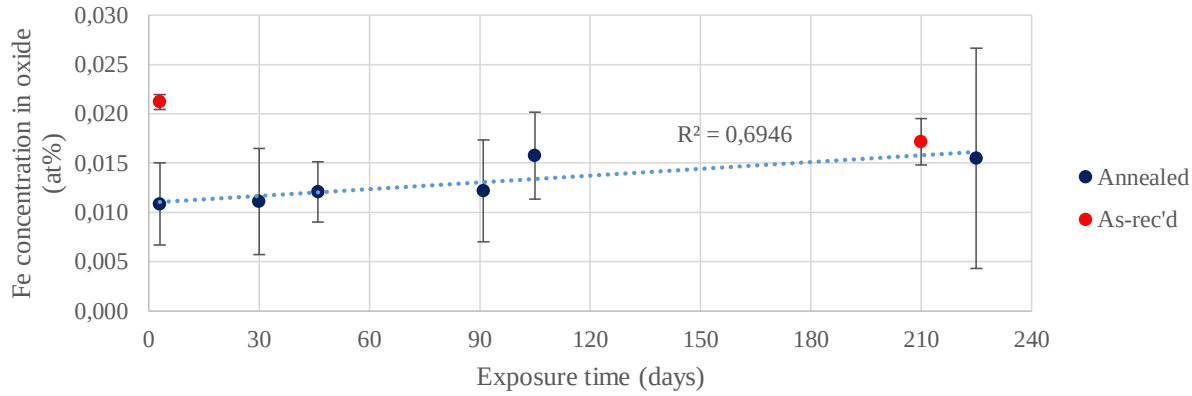
Figure 7.19: The Fe interfacial enrichment plotted against instantaneous oxidation rate.

If the Fe concentration is plotted against instantaneous HPUF rate, an apparent relationship is observed in annealed Zr-1Nb, where the Fe concentration in the metal adjacent to O/M interface increases with instantaneous HPUF rate (Figure 7.21).The 3-day as-recrystallised sample with a very high instantaneous HPUF value does not follow this trend, probably because in the samples where Fe is rejected, the rejected Fe is concentrated in the oxide/suboxide rather than in the metal. This is not accounted for when measuring the Fe in the metal adjacent to the O/M interface.

In this work, Fe rejection at the O/S interface has not been analysed in detail, especially for annealed and as-recrystallised Zr-1Nb because of the lack of available datasets, and hence it is not possible to compare the rejection at O/S and O(S)/M interfaces. However, there is neither significant Fe rejection nor evidence for decorated dislocation lines in the suboxide adjacent to the O/S interface (Figure 7.22a-b). As for sawtooth-shaped interfaces (Figure 7.22c), there is a very small amount of Fe rejected at the S/M interface, with an interfacial enrichment of 0.02 atoms/nm^2 (Figure 7.22d).



(a)



(b)

Figure 7.20: Average Fe concentration in (a) the metal adjacent to O/M interface and (b) the bulk oxide vs exposure time.

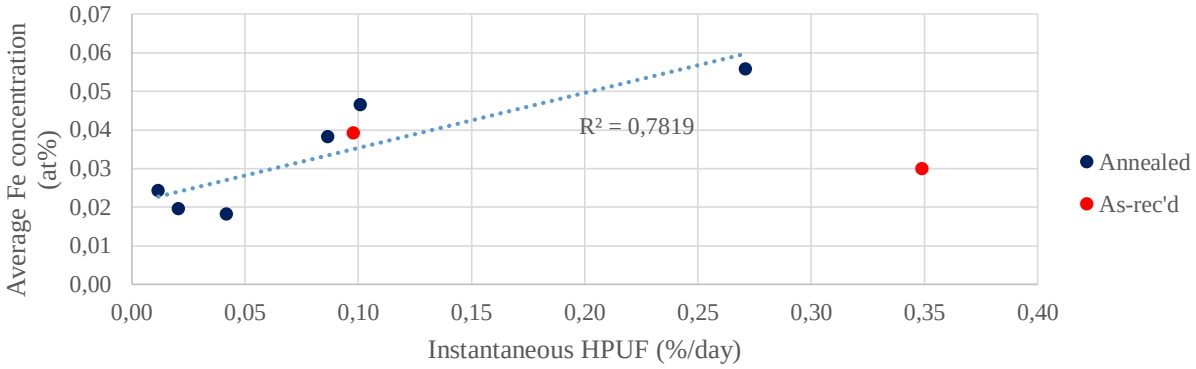


Figure 7.21: Average Fe concentration in the metal adjacent to O/M interface vs instantaneous HPUF rate.

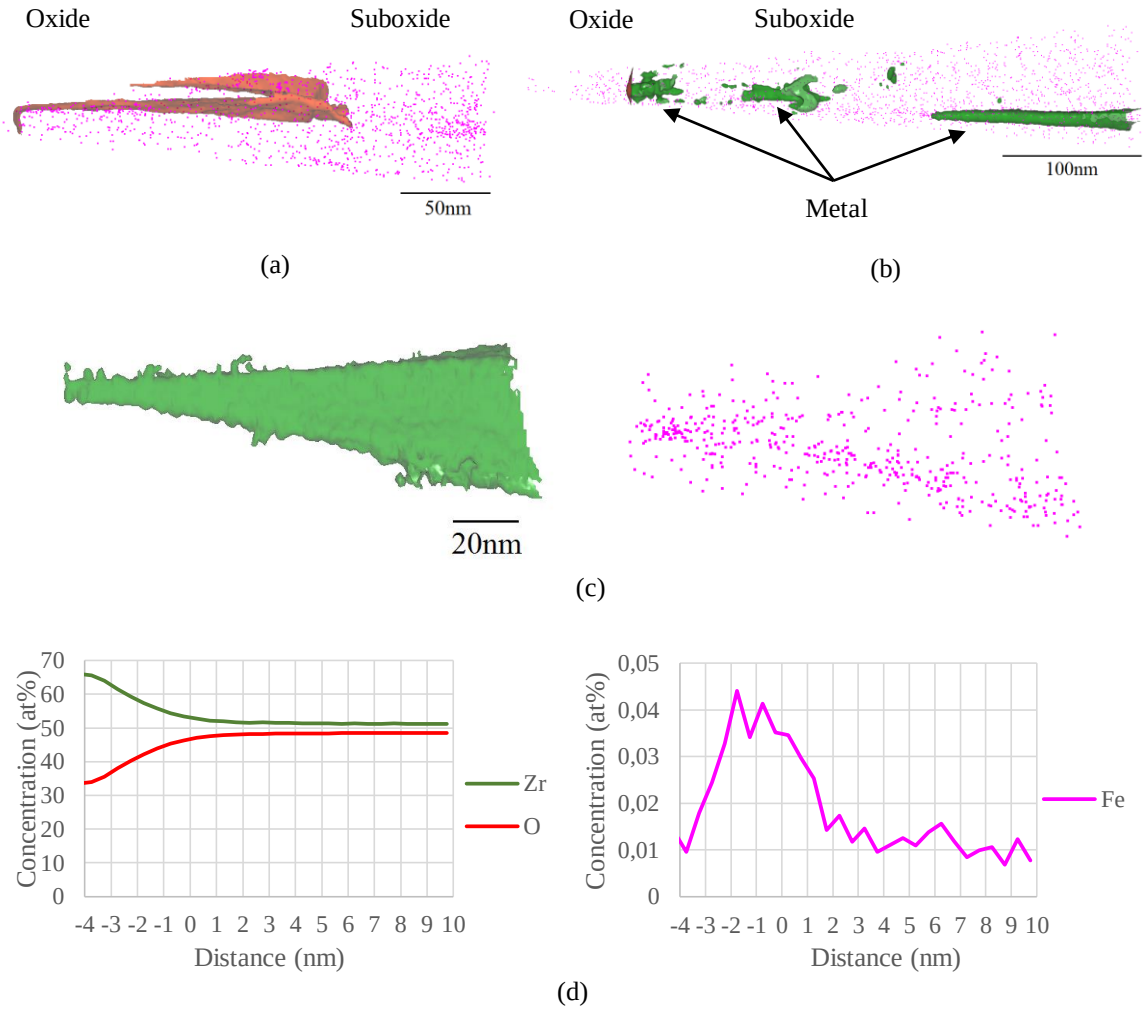


Figure 7.22: (a) and (b) are the O/S interface of the 585-day X2 samples. (c) is the sawtooth-shaped S/M interface from (b) and the Fe distribution (magnified 2x) distribution near the interface. (d) is the Zr, O and Fe profiles across the S/M interface in (c).

7.4.2. Iron-containing features

This section details the Fe-containing microstructural features observed in the metal adjacent to the O/M interface, including sub grain boundaries and strain-induced c-loops. Sub grain boundaries are dislocation lines arranged in the same plane, and can be formed during creep as the strain builds up in the metal adjacent to O/M interface during oxidation [91,246].

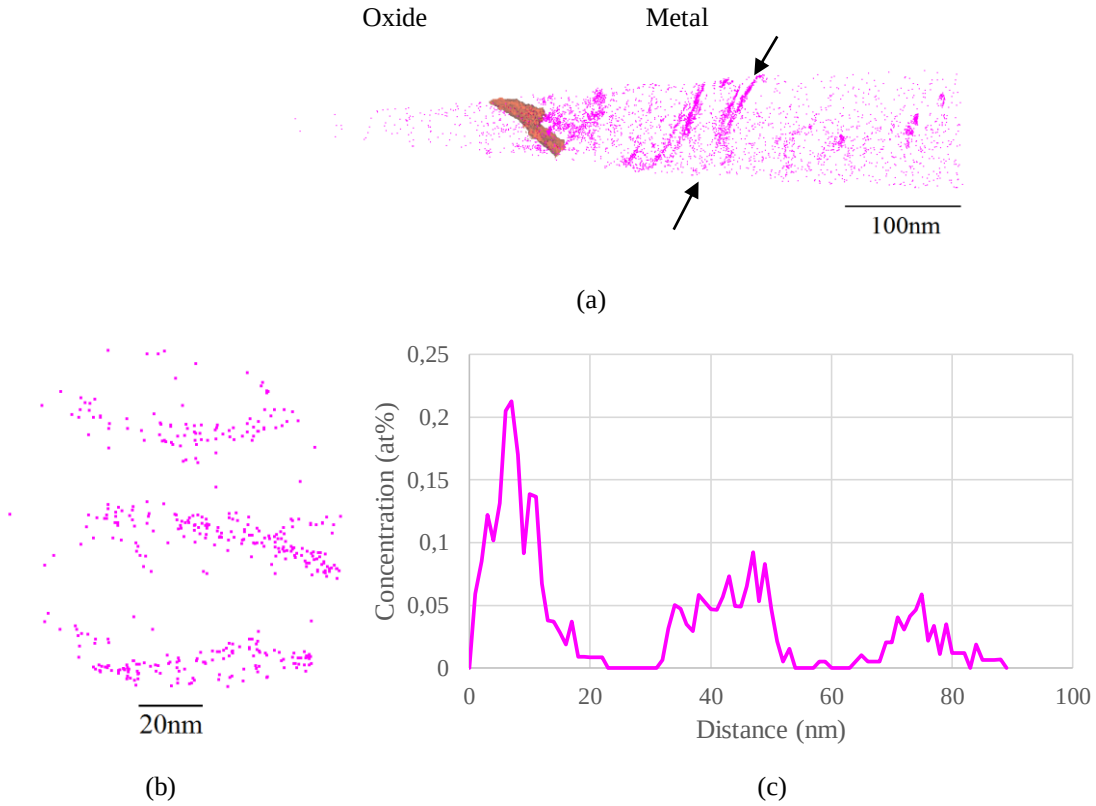


Figure 7.23: (a) Fe segregation to a sub grain boundary (indicated by black arrows) in the metal adjacent to the O/M interface of 210-day as-recrystallised Zr-1Nb and (b) its cross section. (c) is the Fe concentration profile along the vertical direction in the atom map in (b).

In the lowest energy state, the dislocation lines are separated by an approximately equal distance, e.g. in Figure 7.23a-b where 3 dislocation lines are aligned parallel to the O/M interface. The distance between the centre points of the first and second and the second and the third peaks of Fe concentration are both 33nm (Figure 7.23c), suggesting that the distances between the neighbouring dislocation lines are probably the same. When the dislocation rearrangement is not complete, they are tangled and not oriented in the same

direction, e.g. in Figure 7.24Figure 7.25 where in the bottom image 4 dislocation lines on the left hand side are parallel to each other, but not to the dislocation lines on the right hand side.

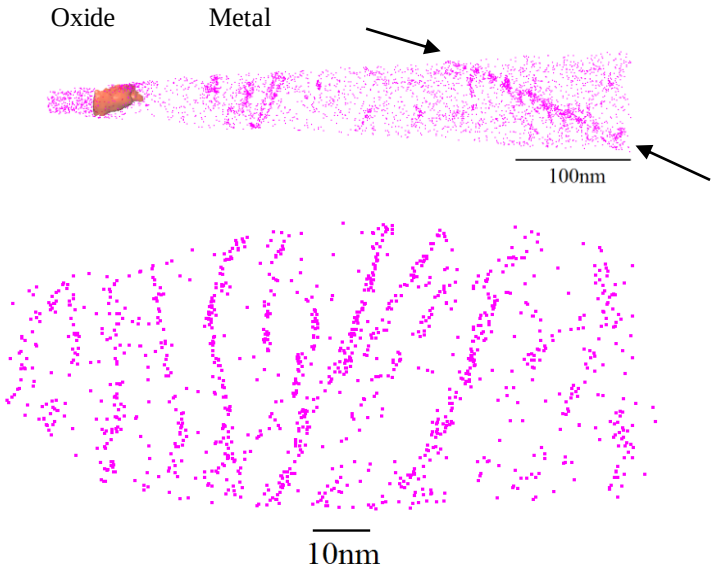


Figure 7.24: Fe segregation to a dislocation tangle (indicated by black arrows) in the metal adjacent to the O/M interface of a 30-day annealed Zr-1Nb (top) and its cross section (bottom).

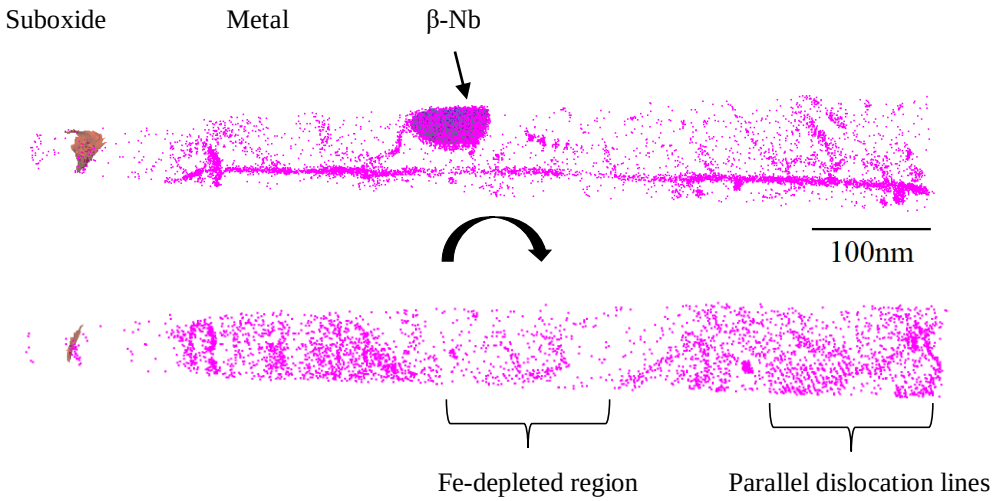


Figure 7.25: A sub grain boundary in the metal adjacent to S/M interface in an 585-day X2 sample (top) and its cross section (bottom) where an Fe-depleted region and parallel dislocation lines are observed.

The Fe decoration on sub grain boundaries can be very inhomogeneous, e.g. the sub grain boundary in Figure 7.25 shows parallel decorated dislocation lines but there is also another part depleted in Fe. In this particular example, the Fe-depleted region is located adjacent to a

β-Nb particle, but it is not possible to determine whether there is any correlation between the particle and the adjacent Fe-depleted region.

The only sample containing strain-induced c-loops is the 225-day annealed Zr-1Nb (Figure 7.26). Although APT cannot be used to determine the direction of these loops, c-loops with similar size have been observed in unirradiated samples [158], indicating that the loops in Figure 7.26 are c-loops. There are 4 loops in this dataset (Loops 1-4) located in planes parallel to each other as well as to the S/M interface. Loop 1 is ellipsoidal, approximately ~80nm in length and ~20nm in width and not entirely captured in the dataset as it is larger than the diameter of the specimen. Loops 2 and 3 are both ~40nm in length and ~20nm and ~15nm in width respectively. Loop 4 is in the same plane as loop 2, but is circular with diameter 5-10 nm.

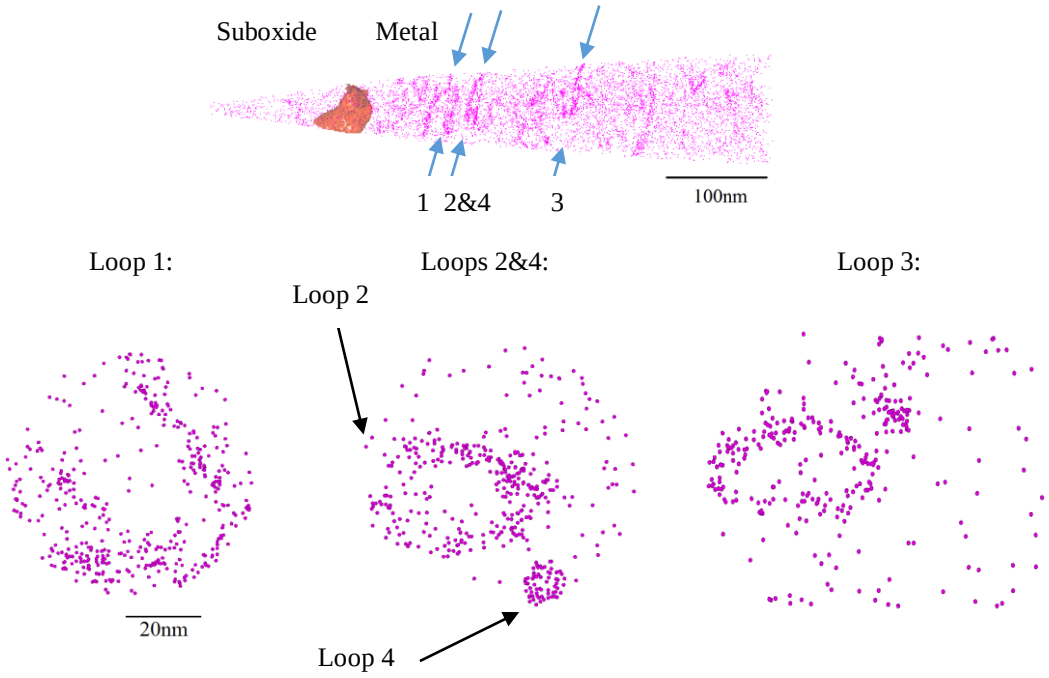


Figure 7.26: 4 strain-induced c-loops (indicated by blue arrows in the top atom map) decorated with Fe (pink dots in the top atom map and spheres in the bottom maps).

7.4.3. Grain boundary oxidation

From Sections 7.2.3 and 7.3.3, we learn that the metal grain boundaries contain much more Fe than the Fe-rich oxide grain boundaries. It is important to determine whether there is any relationship between the metal and Fe-rich oxide grain boundaries to obtain information on the redistribution of Fe decorating the metal grain boundaries and the origin of Fe on the oxide grain boundaries. Therefore, this section discusses the metal grain boundary oxidation process.

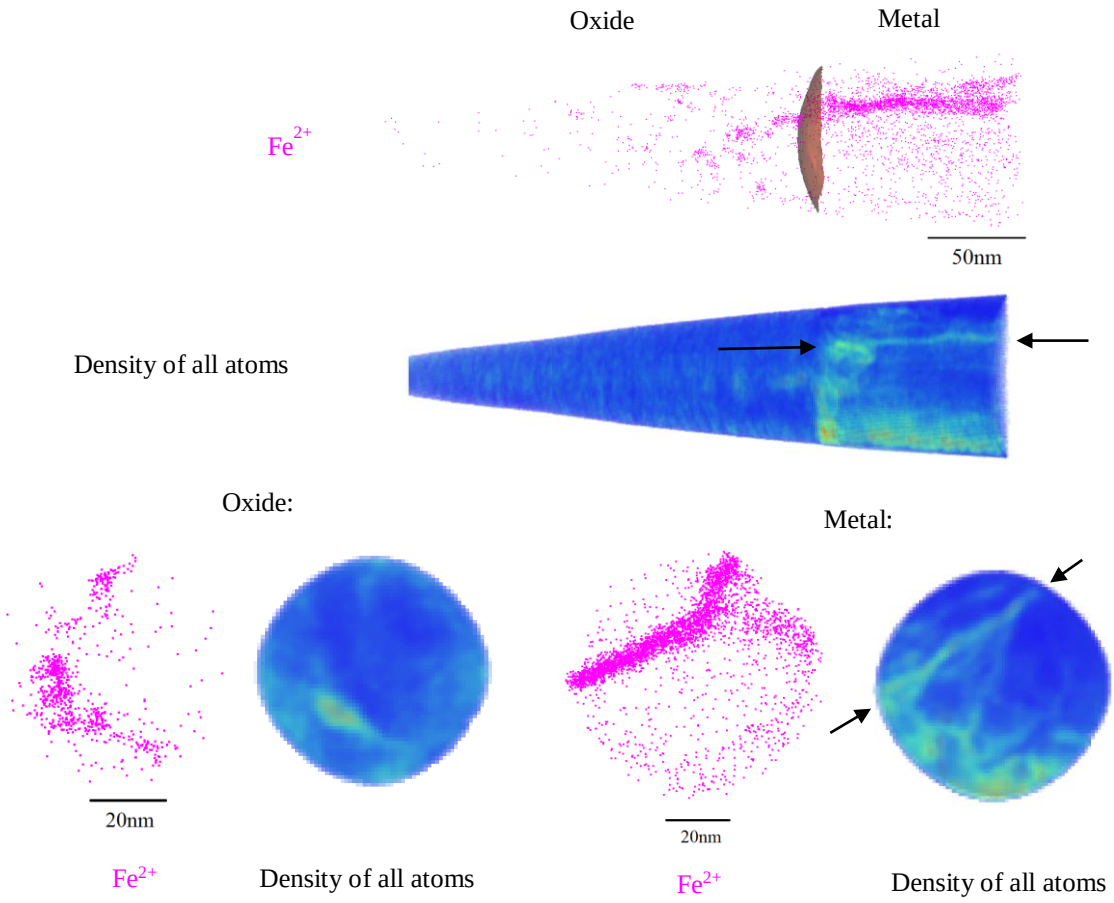


Figure 7.27: A discontinuity of Fe decoration of a metal grain boundary at the O/M interface in Zr-2.5Nb. The maps in the top show the Fe atom map and the density of all atoms in the whole dataset, with black arrows indicating the position of the metal grain boundary. The maps in the bottom show the distribution of Fe (magnified 2x) and density of all atoms in both oxide and metal regions projected normal to the specimen axis.

There are two possibilities that can occur as a metal grain boundary is oxidised. The first possibility (Figure 7.27) is where there is a discontinuity of Fe decoration on a metal grain

boundary at the O/M interface. In the metal, there is an obvious grain boundary, probably a triple junction corresponding to the localised high atom density line in the atomic density map. The grain boundary itself apparently does not carry on into the oxide as the localised high density line is discontinuous at the O/M interface.

In the oxide, there are several Fe clusters that appear to be located on a planar feature (corresponding to a line in the bottom image). The planar feature is probably an oxide grain boundary. There is no corresponding planar density contrast in the location where Fe clusters are concentrated, but not all oxide grain boundaries give an atomic density contrast. Although it is not clear whether these Fe clusters in the oxide segregate to an oxide grain boundary, we can be certain that there is redistribution of the Fe segregated to the metal grain boundary upon oxidation where in this particular example the Fe/Zr ratio drops from ~$3.4x10^{-4}$ in the metal to ~$3.2x10^{-4}$ in the oxide. This is not expected in the metal matrix where the overall Fe/Zr ratio increases when the matrix is oxidised (Section 7.3.1).

The Fe decoration on a metal grain boundary can be continuous through the O/M interface (Figure 7.28a). Looking at the cross section of this grain boundary (Figure 7.28b), the Fe decoration in the metal side is homogeneous, similar to the metal grain boundary (Section 7.2.3). In the oxide part, there are Fe clusters characteristic of the Fe-rich oxide grain boundaries (Section 7.3.3). In both metal and oxide parts, the boundary gives an atomic density contrast (Figure 7.28c), suggesting that the grain boundary is structurally continuous through the O/M interface. The redistributed Fe atoms are probably dispersed in the oxide matrix because there is no sign of Fe rejection near the O/M interface. The Fe content in the matrix adjacent to the boundary is higher in the oxide part (0.02 at%) than in the metal part (0.004 at%).

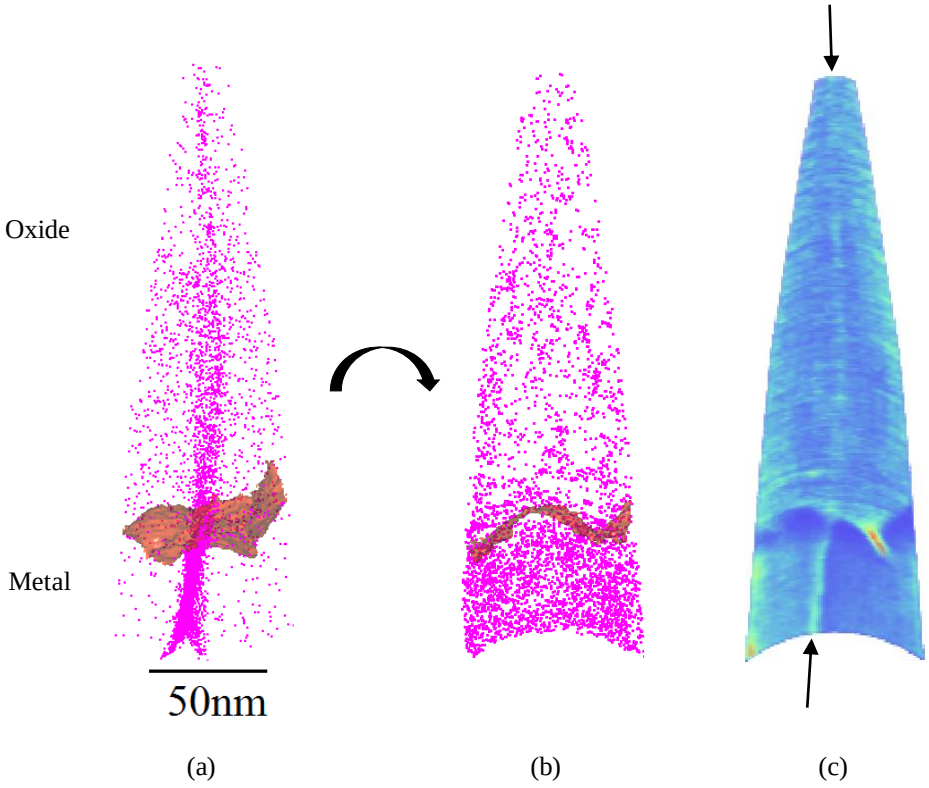


Figure 7.28: (a) A metal grain boundary penetrating through the O/M interface, and thin slices of the reconstruction showing (b) its cross section (where the pink dots are magnified 1.5x) and (c) the density of all atoms with black arrows indicating the position of the grain boundary.

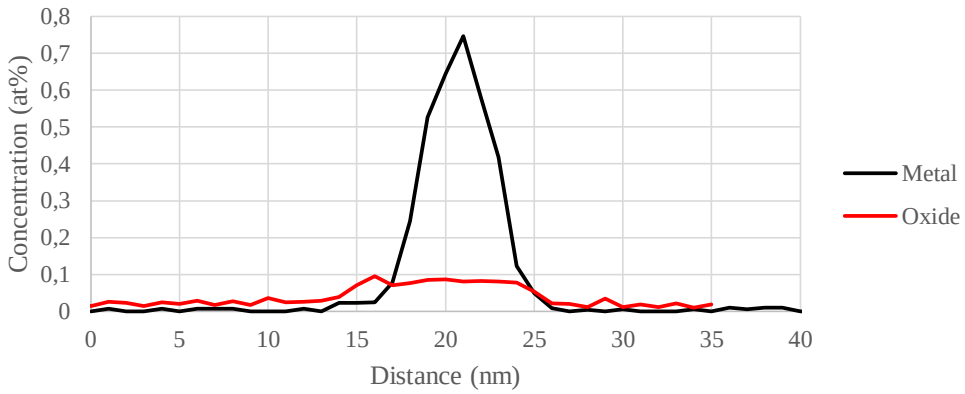


Figure 7.29: Fe concentration profiles across the boundary in the metal and oxide regions from Figure 7.28.

Although the Fe distribution is different in these 2 cases (Figure 7.27 and Figure 7.28a-c), there is a similarity about how Fe on the metal grain boundary is redistributed. In the first possibility where the metal grain boundary is discontinuous, almost all the Fe atoms on the original boundary are redistributed into the oxide matrix, leaving only Fe clusters in the vicinity of the projected trace of the grain boundary. Regarding the second possibility where

the grain boundary is continuous, in the particular dataset from Figure 7.28 the Fe interfacial excess drops from 1.7 atoms/nm^2 in the metal to 0.2 atoms/nm^2 in the oxide (Figure 7.29). This means that the boundary loses 1.5 Fe atoms/nm^2 during oxidation. It is important to note that when a metal grain boundary is oxidised, the interfacial excess is expected to decrease as the material is being diluted with ~67 at% O.

7.5. Irradiation effects

The only dataset obtained on the irradiated X2 samples described in Section 4.3.3 with the O/M interface does not contain a lot of metal (Figure 7.30). However, it appears that there is an Fe rejection from the oxide to metal. The maximum concentration of Fe in the metal is ~0.3 at%, corresponding to interfacial excess of 0.4 atoms/nm^2.

In another dataset, an Fe-rich oxide grain boundary in the irradiated sample has a very different profile compared to the unirradiated ones discussed in Section 7.3.3. The irradiated Fe-rich oxide grain boundaries in this sample are more diffuse and contain Fe with a more homogeneous distribution. In Figure 7.31, there are two grain boundaries in one oxide dataset of irradiated X2 (GB 1 and GB 2). The widths of apparent Fe concentration across these boundaries are 50nm (GB 1) and 34nm (GB 2), much wider than the average width in unirradiated oxide grain boundaries (12nm). The interfacial excess values are 6.5 atoms/nm^2 in GB 1 and 3.4 atoms/nm^2 in GB 2, corresponding to the Gibbsian excess of 14.7% and 7.7% monolayers of m-ZrO_2 close-packed plane for GB 1 and GB 2 respectively. Note that the Gibbsian excess may not be the most appropriate parameter to describe Fe segregation to these grain boundaries because the Fe profile is so diffuse and much wider than any imaging artefact normally observed in APT, and interfacial excess is used instead. Although the interfacial excess value of GB 1 is almost 2x GB 2, the interfacial excess at GB 2 is still

~8.5x the average value of unirradiated Fe-rich grain boundaries (0.4 atoms/nm^2). Therefore, these irradiated oxide grain boundaries are much more enriched in Fe than the unirradiated ones.

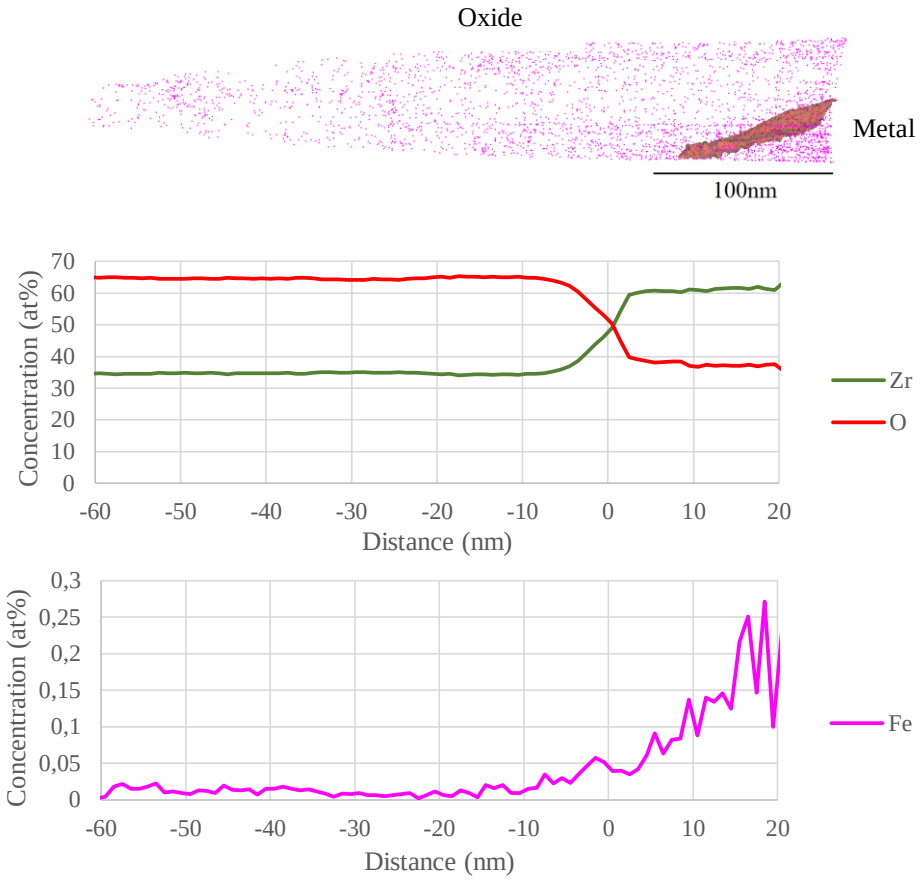


Figure 7.30: The Fe atom map and Zr, O and Fe concentration profiles across the O/M interface of a 1-cycle irradiated X2 sample.

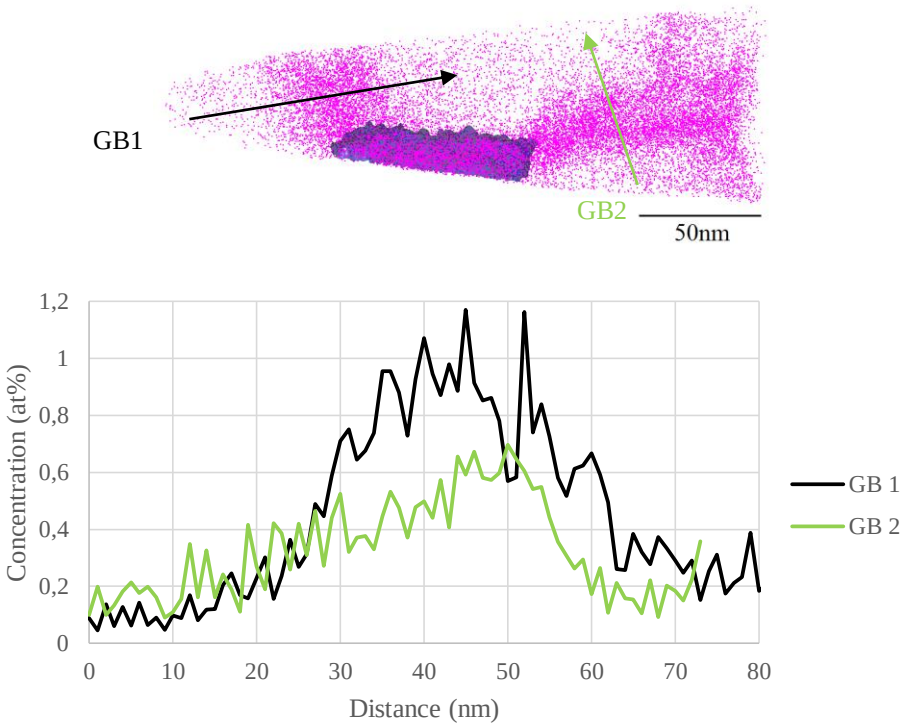


Figure 7.31: Two Fe-rich oxide grain boundaries in the irradiated X2 sample; GB 1 and GB 2, and the Fe concentration profiles across both. The blue isosurface in the atom map corresponds to a Nb-rich particle.

7.6. Discussion

The overall Fe distribution map explained in this section is summarised in Figure 7.32. The information here is obtained from all the materials studied in this thesis (Chapter 4). The oxide Fe/Zr ratios are $(3.5\pm0.5)\times10^{-4}$ and $(3.3\pm1.2)\times10^{-4}$, ~2.6x and ~2.7x higher than these ratios in the metal matrix of as-recrystallised and annealed samples respectively (Section 7.3.1). This suggests that the oxide matrix is more enriched in Fe than the metal. To understand why this could be the case, a more complete picture of Fe redistribution during oxidation must be assessed. This redistribution process is divided into three parts; oxidation of SPPs, oxidation of decorated grain boundaries and redistribution at the O/M interface.

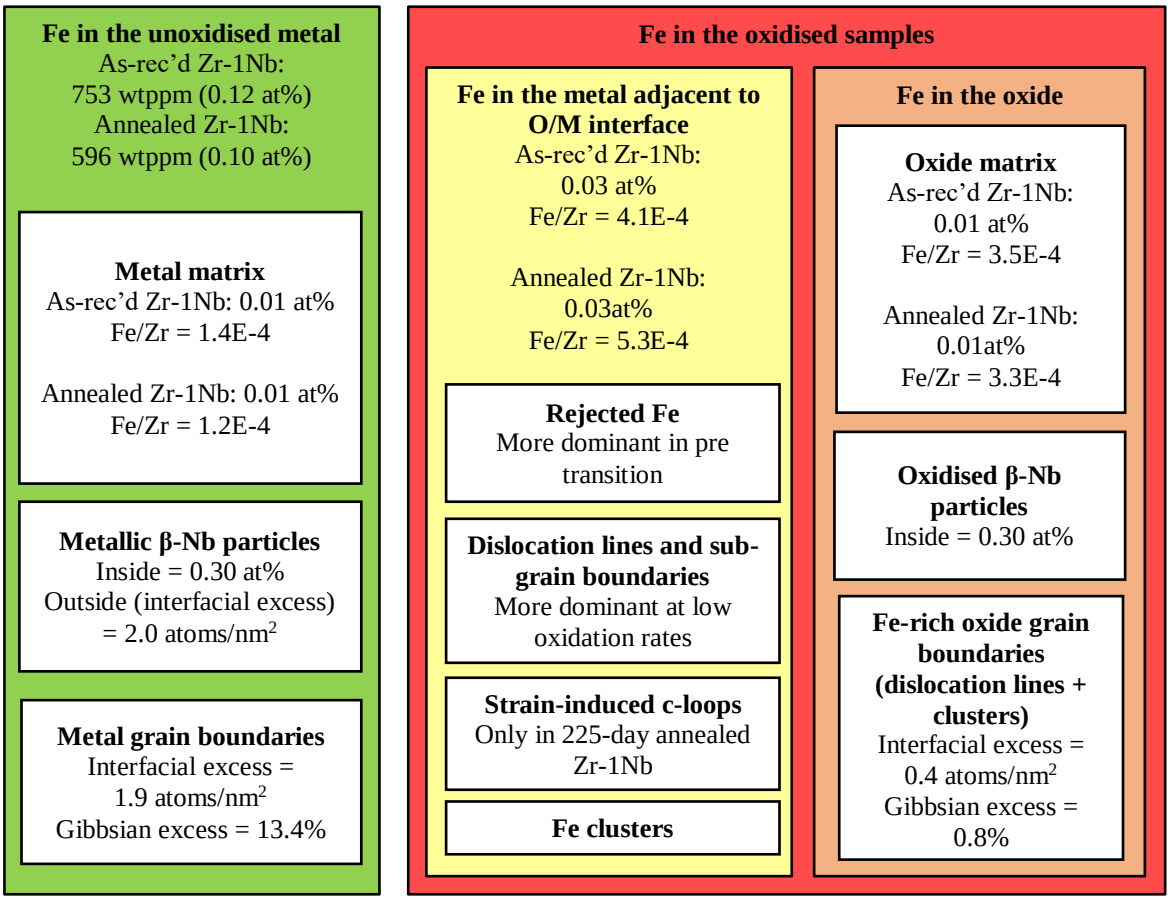


Figure 7.32: Summary of Fe distribution in Chapter 7.

Overall, β-Nb oxidation can only increase the Fe concentration in the oxide matrix. However, because Fe content and Fe/(Zr+Nb) ratio might even increase at higher O content as the more reactive Zr preferentially oxidises (Section 7.3.2), the Fe inside the particle is even less likely to leach out at later stages of oxidation. Fe diffusion in ZrO_2 at 400°C is in the order of ~10^{-19} m^2/s [112,165], suggesting that Fe is mobile in the oxide matrix. This is the reason why no Fe-enriched layer is observed around the oxidised particles.

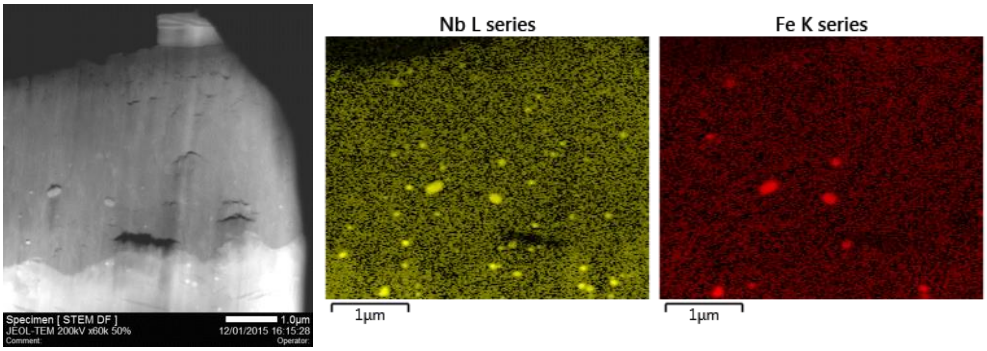
It has been shown that the Fe-rich oxide grain boundaries can be inherited from the metal grain boundaries (Section 7.4.3). When a metal grain boundary is oxidised, it could either disappear or continue across the O/M interface. In both cases, there is a redistribution of Fe decorating the original metal grain boundaries during oxidation as oxide grain boundaries in general have much lower interfacial excess than metal grain boundaries.

Regarding the irradiation effects, there are more Fe atoms segregating to oxide grain boundaries in comparison with unirradiated samples (Section 7.5). These extra Fe atoms could originate from the dissolution of $Zr(Nb,Fe)_2$ particles. It has been reported that $Zr(Nb,Fe)_2$ particles can transform to β-Nb under irradiation [162]. TEM results suggest that under irradiation Fe in the $Zr(Nb,Fe)_2$ particles is dissolved when they are oxidised as there are no Fe-rich particles found in either oxide or metal (Figure 7.33a-b) [201]. This is the evidence that Fe is not located in the SPPs under irradiation.

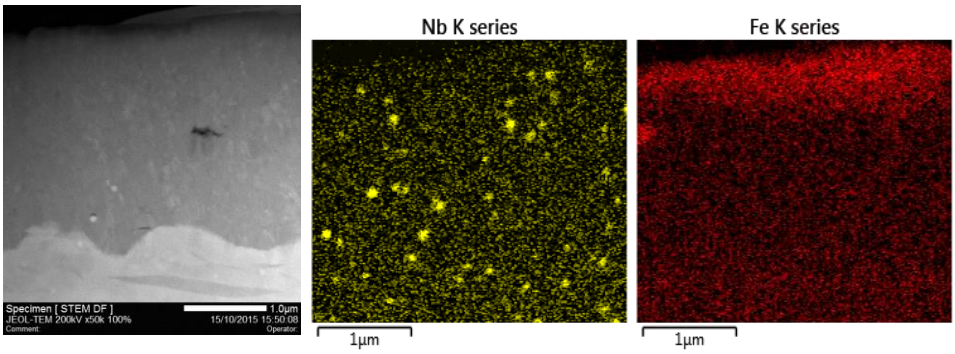
There is also an observation on irradiated Zircaloy-2 that excess Fe forms clusters or segregates to c-loops (Figure 7.34) [164]. This could also be a source of the excess Fe atoms at the irradiated oxide grain boundaries. Irradiation induces oxygen vacancies in the oxide [165]. Fe acting like a self-interstitial atoms (SIAs) can recombine with oxygen vacancies and ultimately this can enhance Fe diffusion in the oxide such that the probability of Fe arriving at grain boundaries is increased under irradiation [165].

In the 2 alloys studied, the Fe/Zr ratios in the metal adjacent to the O/M interface are higher than the Fe/Zr ratios in either metal or oxide matrix because there is an Fe rejection from the oxide to metal during oxidation (Section 7.4.1). The Fe behaviour in this region also depends on the oxidation kinetics and oxidation rate.

Regardless of the stage of transition, dislocation lines are developed when the oxidation rate is low, probably due to stress accumulation in the metal near the O/M interface. These dislocation lines can also be found to form sub grain boundaries with different levels of Fe decoration. However, the concentration of dislocation lines does not seem to alter the overall Fe content significantly, they just act as preferential segregation sites for free Fe.



(a)



(b)

Figure 7.33: TEM and EDX images showing the Nb and Fe distributions near the O/M interface of (a) unirradiated and (b) irradiated X2 samples [201].

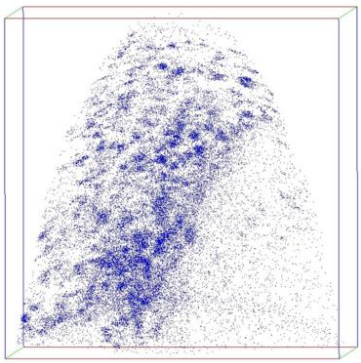
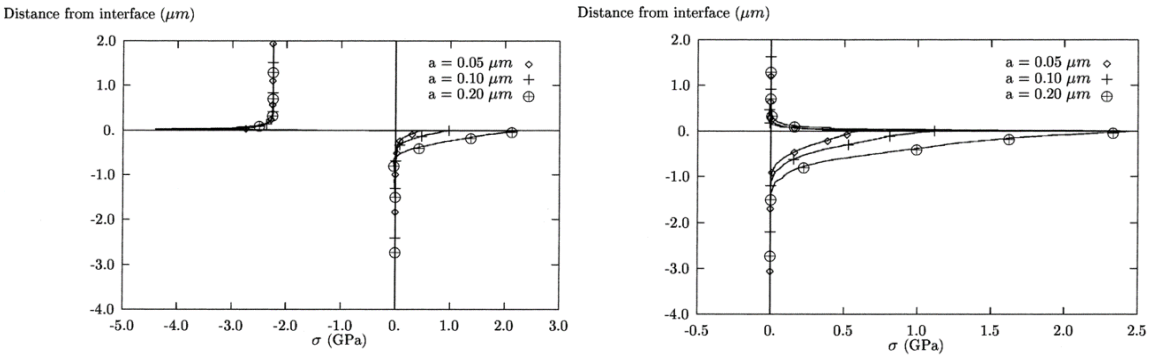


Figure 7.34: Distribution of Fe atoms (blue) in 9-cycle irradiated Zircaloy-2 adjacent to a grain boundary [164]. The box is 140nm x 140nm x 140nm.

From Section 2.3.3, we know that there is a significant amount of compressive stress in the oxide. For Zr alloys oxidised in pressurised water, the stress could be as high as 1-2 GPa [73,93,96,97,247] and the stress in both the metal and oxide increases sharply towards the O/M interface (Figure 7.35a-b) [92]. The metal region of interest in Section 7.4.1 is within ~500nm of the O/M interface, which according to Figure 7.35a-b can experience a few GPa

of tensile stress (greater than the Zr-1Nb yield stress which is 214-230 MPa [248]) sufficient to cause the plastic deformation that is seen in the metal adjacent to the O/M interface. Note that the yield strengths of the as-recrystallised and annealed Zr-1Nb in this work might deviate from the values reported in the literature, but will be far below the stress in the metal near the O/M interface.



(a) (b)

Figure 7.35: A model of the (a) hoop and (b) radial stress distributions across the O/M interface with 0.05μm, 0.10μm and 0.20μm undulation amplitude for a 2μm thick oxide layer [92].

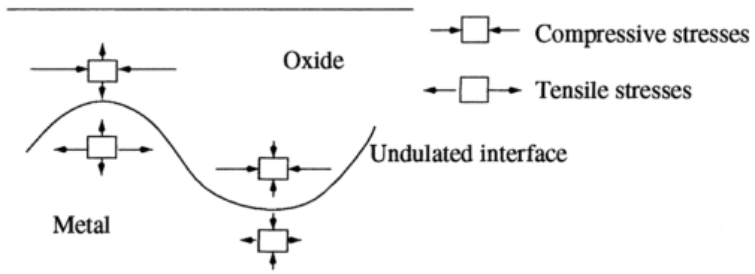
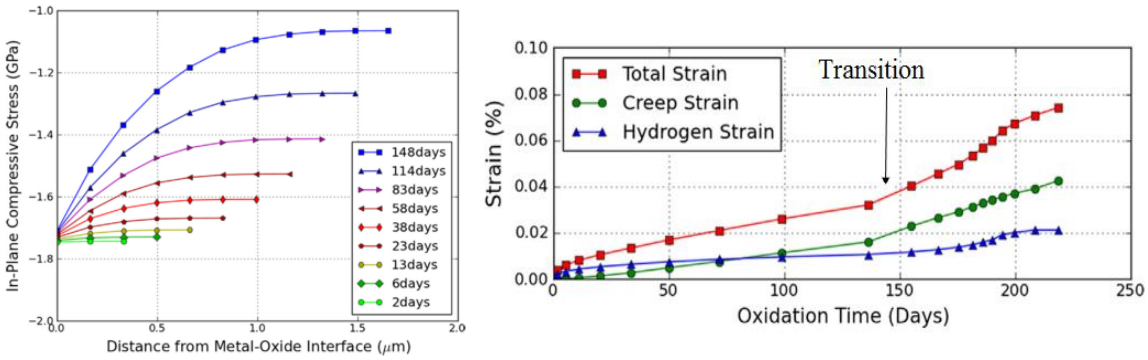


Figure 7.36: Schematic diagram of the relative stress magnitudes near an undulated O/M interface [92].

The shape of the O/M interface can significantly alter the stress generated in the metal, e.g. interfacial roughness from 0.05-0.20 μm causes the maximum tensile stress (hoop and radial) in the metal to increase by a factor of 5-6 [92]. In the materials studied in this work (Section 4.3), the undulation amplitude is much greater than this, which ultimately can result in a very inhomogeneous stress profile in the metal (Figure 7.36).

During oxidation, the metal is strained and undergoes creep [97,246,249,250]. Creep is thought to occur to relax the oxidation-induced stress in the oxide [93,246]. Oxide stress

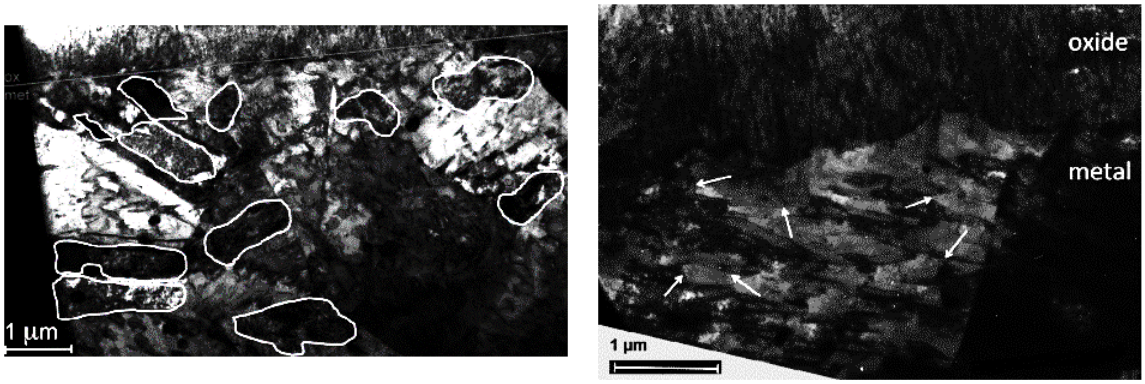
relaxation in pre transition has been observed, indicating that straining and creep occur continuously in the metal (Figure 7.37a). As the metal strain increases over time during oxidation (Figure 7.37b), it is not surprising to have an absence of deformation in 3-day samples because the strain developed is very small. At the other extreme, in the 225-day sample, the metal is heavily strained and this is probably why c-loops are found only in this sample. After the transition, there is a stress relaxation in the oxide that reduces the strain rate in the metal (Figure 7.37b) [91,97]. This could be why there are very few decorated dislocation lines in the 91-day and 105-day annealed samples.



(a) (b)

Figure 7.37: (a) Stress distribution profile along the thickness of the oxide in pre transition and (b) metal creep strain evolution during oxidation of Zircaloy-4 at 360°C [91].

In terms of the deformation mechanisms occurring during creep, three types have been reported; dislocation patches, dislocation tangles and sub grain boundaries (Figure 7.38a-b) [250]. Dislocation patches are areas with high dislocation density like those observed in 30-day and 46-day annealed and 210-day as-recrystallised Zr-1Nb samples. Dislocation tangles and sub grain boundaries are also observed and discussed in Section 7.4.2.



(a) (b)

Figure 7.38: TEM images of (a) Dislocation patches (marked in white) in metal underneath a 1µm thick oxide (removed during specimen preparation) and (b) sub grain boundaries (white arrows) in the metal adjacent to a 2µm thick oxide [250]. Both samples are Zircaloy-2.

The Fe rejection is much more significant at pre transition than in post transition samples and especially noticeable in early pre transition. However, it is important to reiterate that the local Fe rejection varies a lot within the same sample, probably due to inhomogeneous local oxidation rates. Fe rejection is the only mechanism that can reduce the Fe concentration in the oxide but I have observed that the Fe content in the oxide does not vary significantly in samples with different oxidation durations. The fact that a significant amount of rejection only occurs in the pre-transition stage also implies that this mechanism is not as significant in determining the Fe content in the oxide as SPP or grain boundary oxidation.

Fe partitioning at the O/M interface is a thermodynamic process where Fe atoms can end up in either the oxide or metal. The driving force of this rejection is thought to originate from the difference between the free energies of Zr and Fe oxidation. Per one mole of oxygen, the free energies of FeO and Fe_3O_4 formations are both -444 kJ, much higher than ZrO_2 (-965 kJ) [112]. This process obviously requires a time to reach the equilibrium condition and this is not the case in the samples where the oxidation rate is high e.g. the 3-day annealed and as-recrystallised Zr-1Nb samples, resulting in Fe rejection.

As the oxidation rate decreases further in the pre-transition regime, the rejected Fe can then be trapped into dislocation lines. Extrapolating from the data produced by Hood and Schultz, the diffusion coefficient of Fe in Zr-2.5Nb at 360°C is roughly ~10^{-17} m^2/s, corresponding to ~2.3μm diffusion length in 3 days [251]. However, at 3 days, there are very few dislocation lines in the metal and hence Fe tends to accumulate near O/M interface. At a later stage in the pre-transition regime, the diffusion length is greater than this. Although this suggests that rejected Fe can decorate dislocation lines, it is difficult to determine whether the observed Fe decorating dislocation lines and in the clusters originates from rejected Fe from the oxide or from the metal matrix. In addition, it is not clear why post transition the Fe rejection is much less pronounced even at high oxidation rates. A possible explanation is that the local Fe rejection is inhomogeneous and not captured in the samples examined in this work.

The entire Fe redistribution from this chapter is summarised in Figure 7.39. The most important point here is that there is an enrichment of Fe in the oxide matrix from the oxidation of β-Nb particles and metal grain boundaries. Although there is a possible mechanism of bulk oxide Fe content reduction via Fe rejection, this effect is much less significant than Fe release from β-Nb particles and metal grain boundaries.

The information that is not covered in this chapter includes the oxidation of β-Zr and $Zr(Nb,Fe)_2$. It has been proposed that the Fe/(Zr+Nb) ratio in $Zr(Nb,Fe)_2$ decreases upon oxidation [37] but there is little information available regarding the behaviour of Fe in β-Zr. This suggests that the oxidation of $Zr(Nb,Fe)_2$ can result in the increase of Fe content in the bulk oxide. In addition, the total Fe content in the samples after oxidation might be higher than before oxidation due to Fe contamination from the autoclave [115]. This has been seen in 1040-day Zr-2.5Nb studied in this thesis (Chapter 4) but it is not possible to account for this contribution.

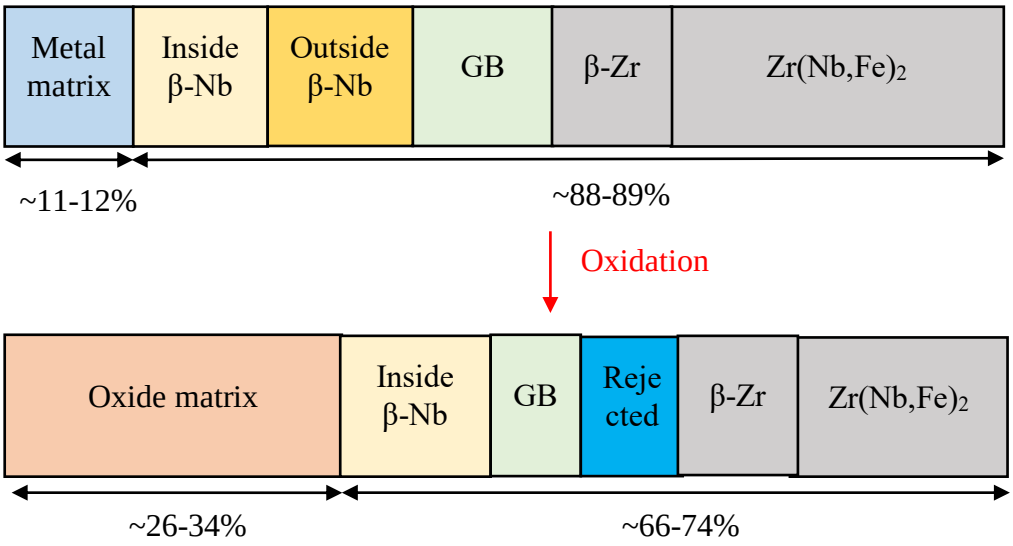


Figure 7.39: Schematic diagram of Fe redistribution map during oxidation of as-recrystallised and annealed Zr-1Nb. Note that the lengths of β-Nb/β-Zr, grain boundary (GB), rejected Fe and $Zr(Nb,Fe)_2$ rectangles do not represent the ratio between the amount of Nb in these regions.

Now the question that should be addressed is how Fe can influence the oxidation and HPU behaviour in Zr-Nb alloys. An obvious possibility is the substitution of $Fe^{2,3+}$ at Zr^{4+} sites in the ZrO_2 matrix that results in a p-type semiconductor as proposed by several authors [252,253]. This argument is supported by the fact that the sizes of Fe^{2+} and Fe^{3+} with radii of 78pm and 65pm respectively are comparable to Zr^{4+}, with 72pm radius [254]. However, this is not the case if we consider the Fe deep states in ZrO_2 [255]. The Fe^{3+} state is located ~3.0eV below the conduction band of ZrO_2 (Figure 7.40), suggesting that this state will not be filled to create a free hole.

Although $Fe^{2,3+}$ ions are unlikely to dope Zr^{4+}, their presence in the oxide can compensate for the space charge (Section 2.4.3). Regarding the extent of Fe contribution to space charge compensation, it is important to note that not all the Fe is immediately oxidised when the matrix is oxidised because there is experimental evidence for metallic Fe in the innermost part of the oxide (e.g. in Figure 7.41) [256], indicating that Fe exhibits a delayed oxidation behaviour. The evidence refers to the Fe inside oxidised β-Nb discussed above (Section

7.3.2). The width of the protective layer increases during pre transition but drops to zero around the transition point [256]. From Section 7.3.2, the Fe/(Zr+Nb) ratio in β-Nb appears to be either constant or increasing upon oxidation. This implies that it is difficult to oxidise and redistribute the Fe from the particles.

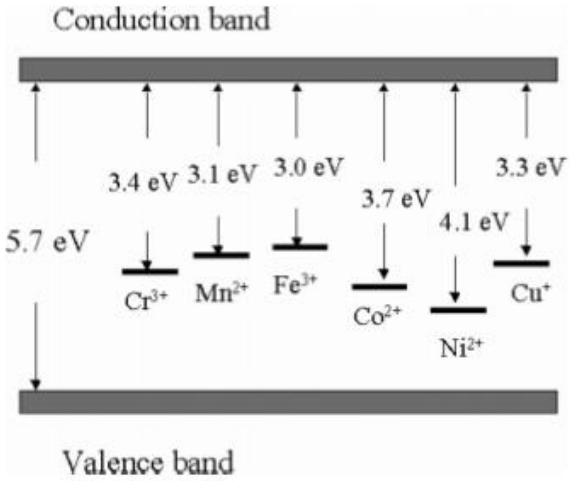


Figure 7.40: Schematic impurity levels of the transition-metal ions in the ZrO_2 thin films [255].

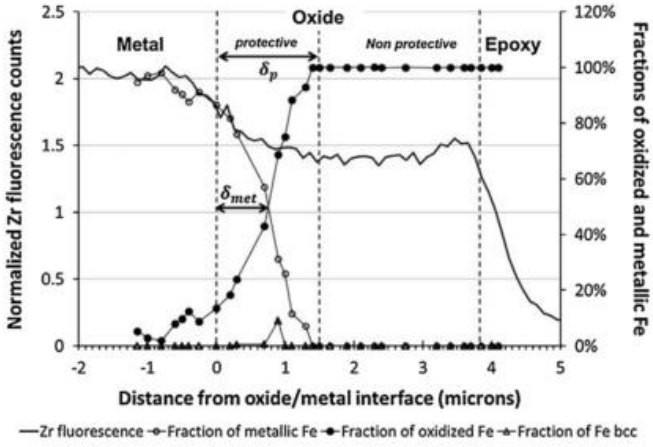


Figure 7.41: The fraction of metallic and oxidised Fe in Zircaloy-4 oxide as a function of the distance to the O/M interface [256]. δ_{met} and δ_p are the thickness where the fraction of metallic Fe is 50% and 0% respectively.

The amount of required Fe to fully compensate the space charge is shown in Figure 7.42. In my samples, the concentration of Fe in the oxide matrix is ~0.01 at% for annealed Zr-1Nb and ~0.01 at% for as-recrystallised Zr-1Nb samples, both slightly lower than measured in Figure 7.42, meaning that Γ_{Fe} is still very large and Fe can only compensate for a small

fraction of the space charge. This implies that the role of Fe in controlling oxidation and HPU by space charge compensation mechanism is not significant.

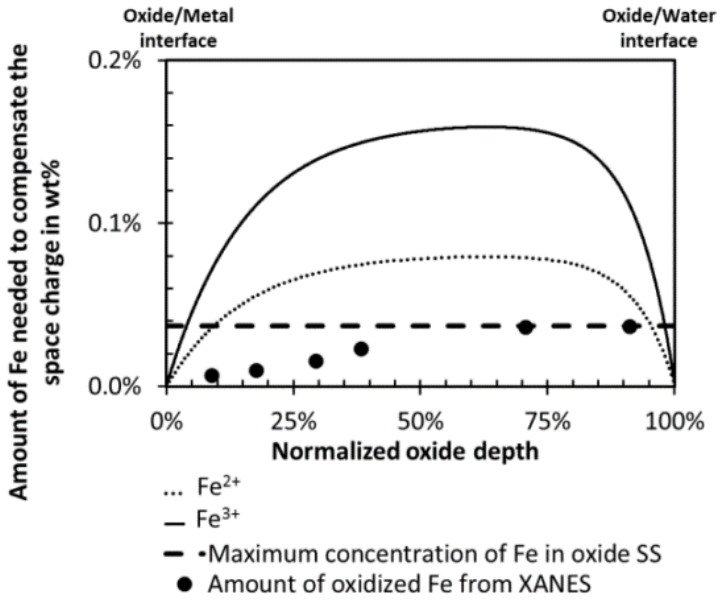


Figure 7.42: The theoretical amount of Fe in the oxide to compensate the space charge (Γ=0) in Zr-2.5Nb [143]. The dashed line is the predicted maximum concentration of Fe in the oxide and the XANES results are the black points.

Apart from the space charge compensation, there is another mechanism by which Fe can control HPU. Although Fe also decorates oxide grain boundaries, in most cases no correlation is found between Fe and D/H segregation to oxide grain boundaries (Chapter 6). If we consider that there is a competition between HPU and H_2 gas evolution, if an element promotes H_2 gas evolution it will prevent HPU [42,144]. If the hydroxylation occurs by "hydride" bridge formation [42], the energy to break this bridge to form H_2 gas (Reaction (4-6)a in Figure 6.14) should be investigated. Fe^{2+} gives a negative energy of H_2 gas formation, suggesting that the reaction is favoured (Figure 7.43). Hence, Fe is beneficial for HPU behaviour because it encourages H_2 gas formation, and I have clear evidence for the presence of Fe in the oxides of my samples.

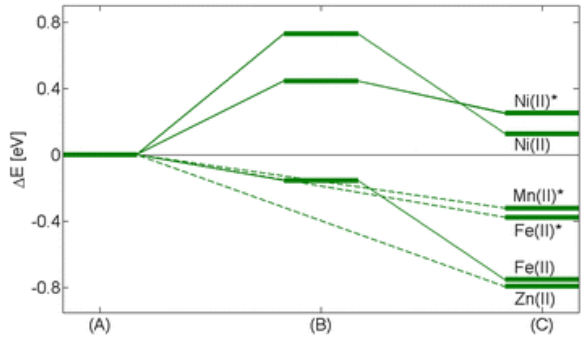


Figure 7.43: Energy changes for (B) the intermediate TM–H_2 structure and (C) the structure where H_2 is formed relative to (A) the hydride structure for transition metals are all in oxidation state II [42]. The asterisk indicates a high-spin state and no asterisk is a low-spin state. No stable TM–H_2 structures were found for MnII*, FeII* and ZnII.

All these observations from the literature suggest that Fe in the oxide may affect the HPU. However, the data from annealed Zr-1Nb shows that there is an apparent relationship between the average Fe concentration in the metal adjacent to O/M interface and instantaneous HPUF rate (Figure 7.21). The 3-day as-recrystallised sample does not seem to follow the same trend, but this is probably because the Fe rejection that is supposed to increase the Fe content in the metal is at this early stage of oxidation accumulated in the rapidly growing oxide or suboxide instead of metal. It is not clear if there is any correlation between Fe in the metal and HPU.

7.7. Summary

- Fe solubility in the metal matrix is very low as it segregates to β-Nb, where Fe is found both inside and at the periphery of the particles, as well as to metal grain boundaries.
- Fe content in the oxide matrix is also very low, but the Fe/Zr ratio is higher than the metal due to the oxidation of β-Nb, metal grain boundaries and probably also $Zr(Nb,Fe)_2$ [37].

- Upon oxidation of β-Nb, Fe originally in the particle is not redistributed, but the Fe decorating P/M interface is redistributed.
- Upon oxidation of metal grain boundaries, Fe decorating the boundaries can either be partially or fully redistributed depending on the alignment between the adjacent metal and oxide grains.
- Fe content in the metal adjacent to O/M interface is higher than the metal and oxide matrices, mainly due to the Fe rejection. Fe rejection is the only mechanism that decreases Fe content in the oxide matrix but is only significant in pre transition. Overall, the effect of Fe rejection on the Fe content in the oxide matrix is negligible.
- Fe-rich dislocation lines and sub grain boundaries have been observed in the metal adjacent to the O/M interface, demonstrating creep of the metal. These features, however, do not appear when the instantaneous oxidation rate is high because in pre transition the strain in metal is still low, and in post transition the appearance of cracks near the O/M interface can reduce the local strain.
- I have considered if Fe in the oxide can control the oxidation and HPU by space charge compensation. Fe can also encourage the H_2 gas evolution that can suppress HPU. The extent by which Fe can affect corrosion and HPU is not clear but because the amount of Fe in the oxide is much smaller than that required to fully compensate the space charge, Fe probably does not influence the oxidation and HPU significantly. In addition, there is a sign that Fe in the metal adjacent to O/M interface can promote HPUF.
- Fe is dissolved under irradiation and in the oxide the Fe segregation to grain boundaries is more diffuse compared to in the unirradiated samples. Furthermore, there is also an apparent Fe rejection at O/M interface in the irradiated X2.

8. NIOBIUM

8.1. Introduction

The incorporation of Nb into Zr has been proved to be beneficial for both corrosion and HPU reductions (Sections 2.3.4 and 2.4.3) [9,17,88,257,258]. There are several possible intermetallics and phases in Zr-Nb alloys but only β-Nb is discussed in detail here because I have collected little experiment data on β-Zr and $Zr(Nb,Fe)_2$. Most of β-Nb examined in this work comes from the decomposition of the β-phase in Zr-2.5Nb during a stress relief treatment at 400°C (Section 4.3.4). This is probably because the probability to capture a particle in Zr-2.5Nb is greater compared to the other alloys, primarily due to the higher Nb content. For analysis of the O/M interface, examples from as-recrystallised and annealed Zr-1Nb are discussed. Similar to Chapter 7, this chapter discusses the Nb distribution in the metal and oxide in order to study how this element is redistributed during oxidation.

The particles and grain boundaries examined for the analysis of Nb content are the same features used for Fe analysis in Chapter 7. Although Nb segregation was detected in the metal grain boundaries, no Nb segregation to oxide grain boundaries ~500-600 μm from the O/M interface was observed. However, near the O/M interface Nb can segregate to the oxide grain boundaries (Section 8.4.2).

8.2. Niobium in the metal

8.2.1. Metal matrix

According to the results in Section 4.2, the Nb contents in the metal matrix of as-recrystallised and annealed Zr-1Nb are 0.41±0.01 at% and 0.41±0.04 at% respectively, corresponding to Nb/Zr ratio of $(4.2\pm0.4)\times10^{-3}$ and $(4.2\pm0.3)\times10^{-3}$ for as-recrystallised and

annealed Zr-1Nb respectively. The standard deviations (relative to the average values) are much smaller compared to Fe concentration in metal (Section 7.2.1), because the average concentration is higher and secondly, overlaps between Nb-containing and other signals are more straightforward to solve while this is not the case with the overlap between Fe^{2+} and CO^{+} (Section 3.2.3.2.2). The Nb solubility in the metal can be altered by the presence of O (Section 5.2). With ~1 at% (0.18 wt%) O content in the bulk metal, Nb solubility limits at recrystallisation (580°C) and annealed (720°C) temperatures are very similar and close to the dashed line in Figure 5.13, ~0.4 at% in a good agreement with my results [214,215]. With ~0.41% Nb in the metal matrix, most of the Nb in as-recrystallised and annealed Zr-1Nb (as well as X2 and Zr-2.5Nb) must be located in particles and grain boundaries.

8.2.2. Metallic β-Nb particles

Typical concentration profiles across the P/M interface in these alloys are illustrated in Figure 8.1a-c. There is a variation in Nb/Zr ratios in different alloys; β-Nb particles in Zr-2.5Nb have a significantly lower Nb/Zr ratio (2.9±0.9) compared to those in both as-recrystallised Zr-1Nb (8.5±1.4) and X2 (6.4±1.4) (Table 8.1). The average lengths of apparent Nb diffusion into the Zr matrix are 5±2nm, 8±1nm and 8±4nm for β-Nb particles in Zr-2.5Nb, as-recrystallised Zr-1Nb and X2 respectively, suggesting that the Nb concentration profile is more diffuse in as-recrystallised Zr-1Nb and X2 compared to in Zr-2.5Nb. The Nb profile discrepancies in different alloys might be attributable to different processing routes where β-Nb particles in as-recrystallised Zr-1Nb and X2 grew during the heat treatment in the α+β-Nb phase region while β-Nb in Zr-2.5Nb originates from decomposition of β-Zr after a heat treatment in the β-phase region (Figure 2.6).

Table 8.1: Average composition of analysed metallic β-Nb particles in Zr-2.5Nb, as-recrystallised Zr-1Nb and X2.

	Zr-2.5Nb	As-recrystallised Zr-1Nb	X2
Number of particles	4	2	4
Average Nb content (at%)	70.25	86.25	85.13
Average Zr content (at%)	25.28	10.35	13.65
Average O content (at%)	3.68	3.10	0.93
Average Nb/Zr ratio	2.9	8.5	6.4
Average Nb diffusion length (nm)	5	8	8

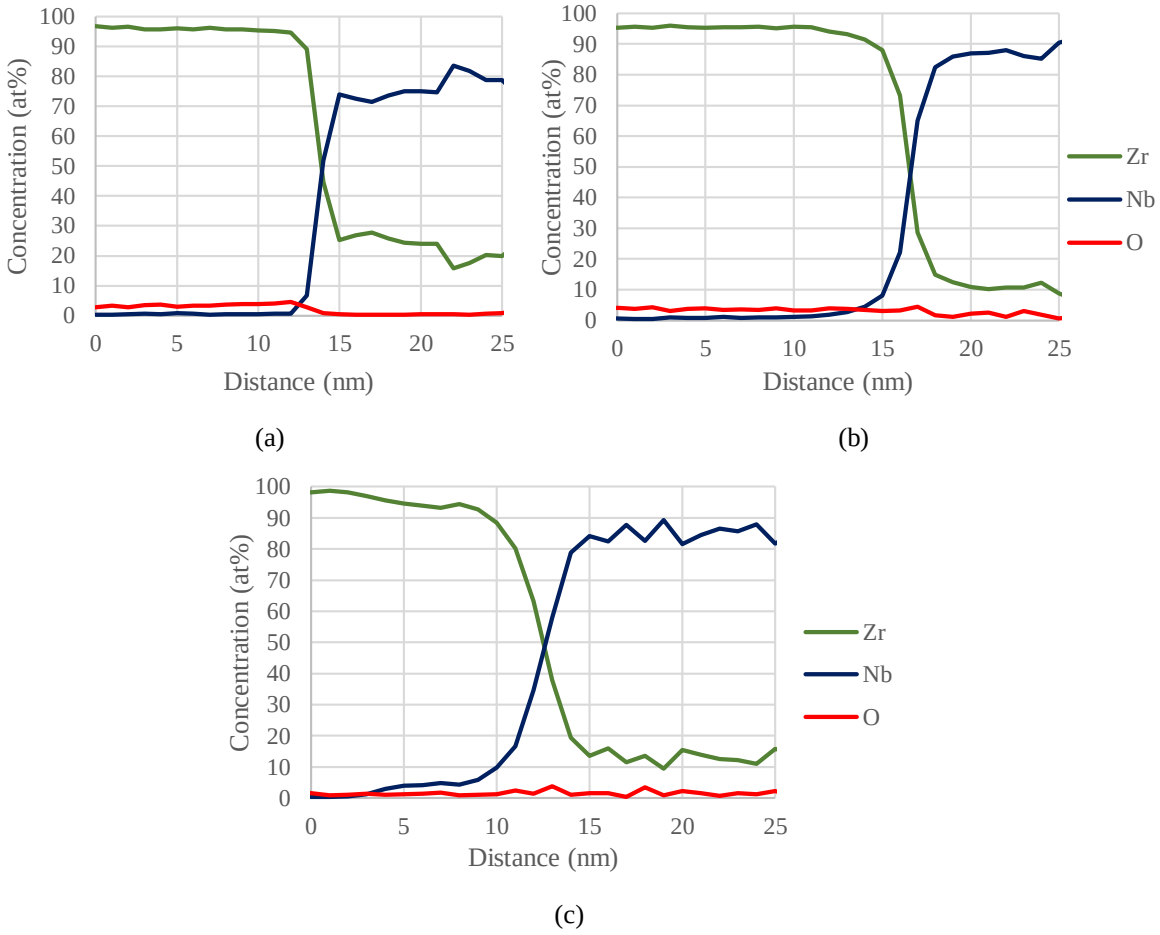


Figure 8.1: Typical Zr, Nb and O concentration profiles across P/M interfaces in (a) Zr-2.5Nb, (b) as-recrystallised Zr-1Nb and (c) X2.

8.2.3. Metal grain boundaries

It is not possible to precisely calculate the extent of segregation of Nb to metal grain boundaries because while it is possible to calculate the number of $Nb^{1,2,3+}$ ions and deconvolute the overlaps with metal hydride peaks (Section 3.2.3.2.2), separating them in the

atom maps is not possible. Because the ROI method using to calculate the 1D concentration profile only accounts for the atoms displayed in the atom map, only ions originate from the peak ranged as Nb ($Nb^{1,3+}$ only) are taken into account while Nb^{2+} disregarded. As a result, the overall Nb content is underestimated due to the exclusion of Nb^{2+}.

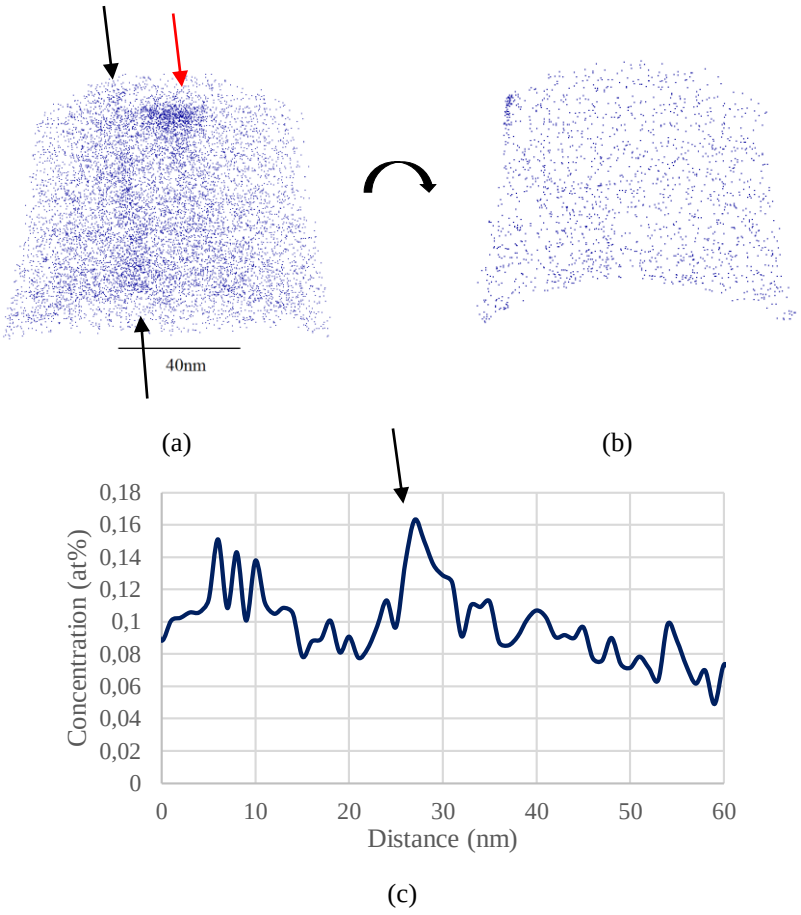


Figure 8.2: (a) A metal grain boundary (black arrows) containing Nb segregation and (b) its cross section. The red arrow points out the location of a Nb-rich particle. (c) is the Nb concentration profile across the boundary (marked with the black arrow).

The Nb segregation to metal grain boundaries is homogeneous (Figure 8.2a-b). Examination of 7 metal grain boundaries show that only 1 grain boundary does not contain detectable Nb segregation. The average interfacial excess and Gibbsian excess values from these 7 metal grain boundaries are 0.5±0.3 atoms/nm^2 and 3.6±2.3% of a monolayer of α-Zr basal plane, much lower than the reported value in the literature (~15% of a monolayers of α-Zr basal

plane) [33]. This segregation is also much weaker than Fe segregation, with only ~28% average interfacial excess/Gibbsian excess value of Fe segregation (Section 7.2.3).

8.3. Niobium in the oxide

8.3.1. Oxide matrix

In the oxide matrix the Nb content is 0.13±0.03 at% and 0.13±0.05 at% for as-recrystallised and annealed Zr-1Nb respectively. The corresponding Nb/Zr ratio is $(3.7\pm1.0)\times10^{-3}$ in as-recrystallised Zr-1Nb and $(3.7\pm1.4)\times10^{-3}$ in annealed samples. The comparison between the measured Nb content in the oxide and metal is given in Table 8.2. The metal and oxide of as-recrystallised and annealed Zr-1Nb are very similar in terms of Nb content once the O atoms are ignored. Comparing the Nb/Zr ratio in the oxide and metal, although on average the oxide contains a slightly lower Nb/Zr ($\sim3.7\times10^{-3}$), it is not clear whether the value is higher than the metal Nb/Zr ratio ($\sim4.2\times10^{-3}$) if we apply a 1σ criterion.

Table 8.2: Comparison of Nb content in the metal and oxide matrices for as-recrystallised and annealed Zr-1Nb

	As-recrystallised Zr-1Nb		Annealed Zr-1Nb	
	Metal	Oxide	Metal	Oxide
Number of samples	4	7	5	29
Average Nb content (at%)	0.41*	0.13	0.41*	0.13
Standard deviation of Nb content (at%)	0.01	0.03	0.04	0.05
Average Nb/Zr ratio ($\times10^{3}$)	4.2	3.7	4.2	3.7
Standard deviation of Nb/Zr ratio ($\times10^{3}$)	0.3	1.0	0.4	1.4

*Nb concentration in the metal is taken from the percentage of sum of all atoms from all metal datasets rather than averaging between samples.

According to the data taken from 3 X2 samples, the Nb content in ZrO suboxide is 0.34±0.04 at%, giving a Nb/Zr ratio of $(6.7\pm0.7)\times10^{-3}$. This seems to be higher than Nb/Zr in either metal or oxide.

8.3.2. Oxidised β-Nb particles

10 oxidised β-Nb particles from Zr-2.5Nb were examined. Most of these particles are located on original grain boundaries in the metal. This is not surprising because they originate from the decomposition of β-Zr precipitated on grain boundaries (Figure 8.4).

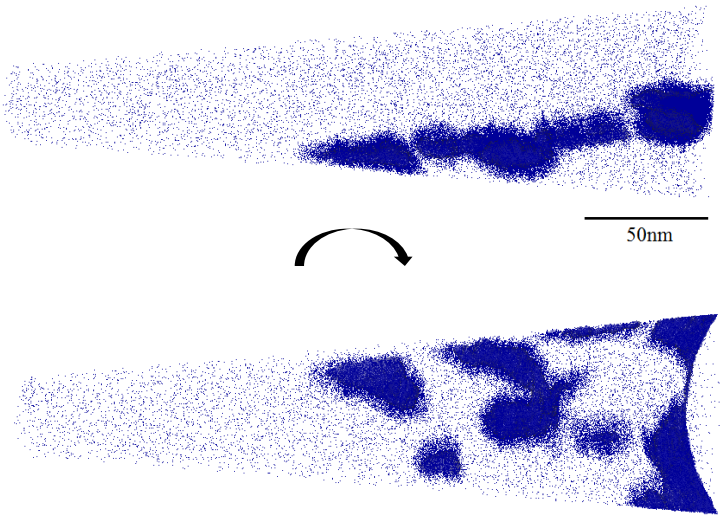
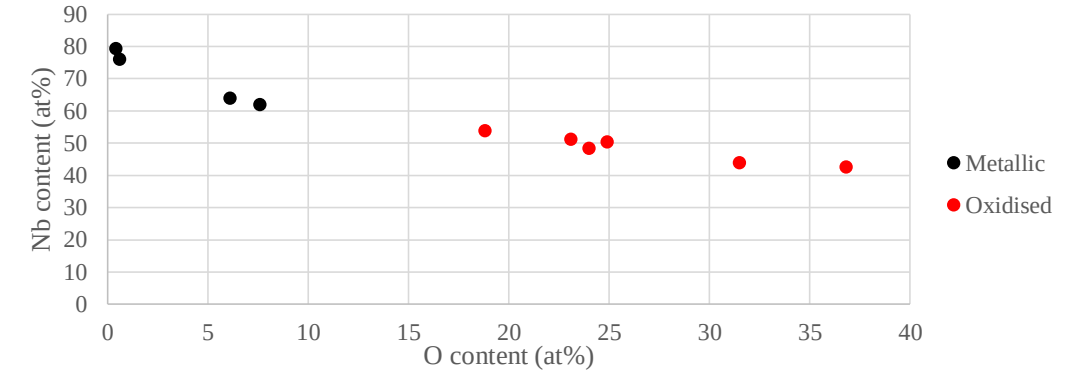


Figure 8.3: Oxidised β-Nb particles in the oxide on the original metal grain boundaries.

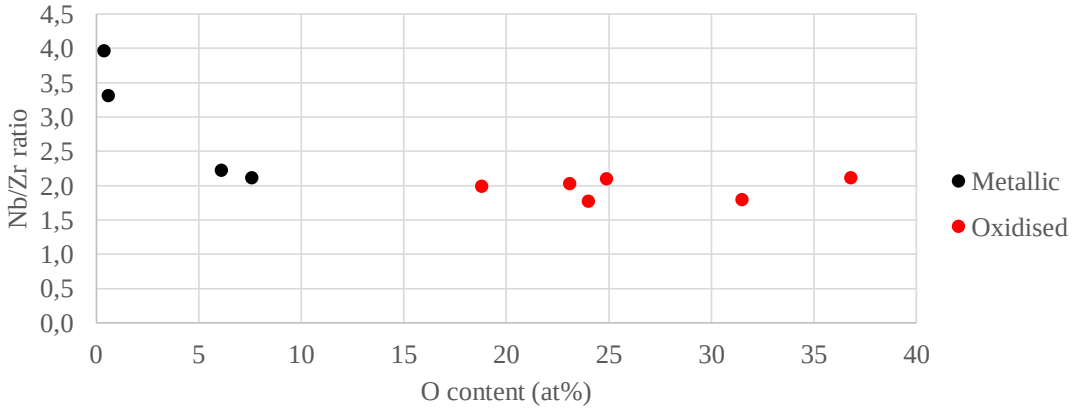
There is a trend for the Nb content and Nb/Zr ratio to decrease as the O content in the particle increases (Figure 8.4a-b). Note that the Nb/Zr ratio decreases much more slowly at higher O contents and is almost constant for the oxidised particles. This proves that Nb in these β-Nb particles diffuses out at a faster rate than Zr during the early stages of oxidation, but the out diffusion flux might decrease at higher O contents where an apparent stable compound of Nb_2ZrO_x is observed.

To demonstrate the Nb out diffusion, the Nb diffusion length at the P/O interface is plotted against O content (Figure 8.5). The diffusion length tends to increase as the O content increases. There is a significant difference of Nb diffusion length between the metallic and oxidised particles, suggesting that the diffusion takes place once the particles are oxidised.

Based on this observation, the β-Nb oxidation can be modelled in terms of Nb distribution (Figure 8.6). As a β-Nb particle is oxidised, O atoms enter the particle and at the same time, Nb leaches out from the particle. Zr probably also diffuses out from the particle, but if this is the case, the Zr diffusion rate should be slower than Nb as the Nb/Zr ratio decreases during oxidation. This agrees with a previous study where oxidised β-Nb particles containing 10-60 at% Nb were observed [110].



(a)



(b)

Figure 8.4: The relationships between O content in the β-Nb particles and (a) Nb content and (b) Nb/Zr ratio.

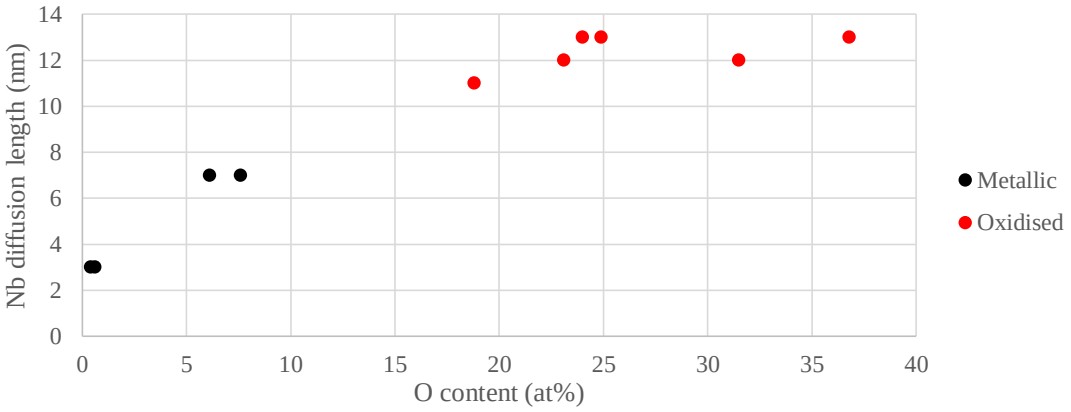


Figure 8.5: Nb diffusion length vs O content.

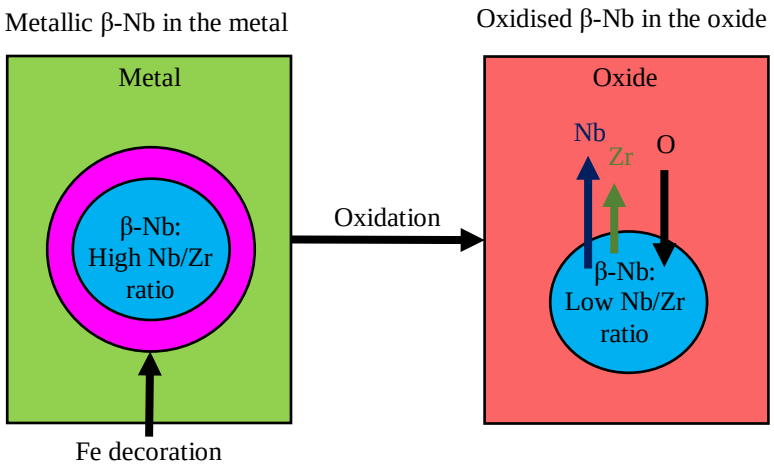


Figure 8.6: Elemental diffusion during β-Nb oxidation. The arrows at right hand side correspond to the diffusion directions of Nb, Zr and O.

8.4. Niobium at the O/M interface

8.4.1. Metal adjacent to the O/M interface

Nb in the metal adjacent to the O/M interface can exhibit clustering. However, this clustering seems to occur when the instantaneous oxidation rate is low and the metal near the O/M interface is deformed. Creep deformation of the metal occurs when the instantaneous oxidation is low (Section 7.4.1). For annealed Zr-1Nb, there is no clustering in any of the 3-day samples (Figure 8.7a), but at 30 days there are samples with (Figure 8.7b) and without Nb clusters in the metal underneath the oxide. At 46 days, all APT samples capturing the

O/M interface contain Nb clusters, even though the size could be smaller than some of the 30-day samples (Figure 8.7c).

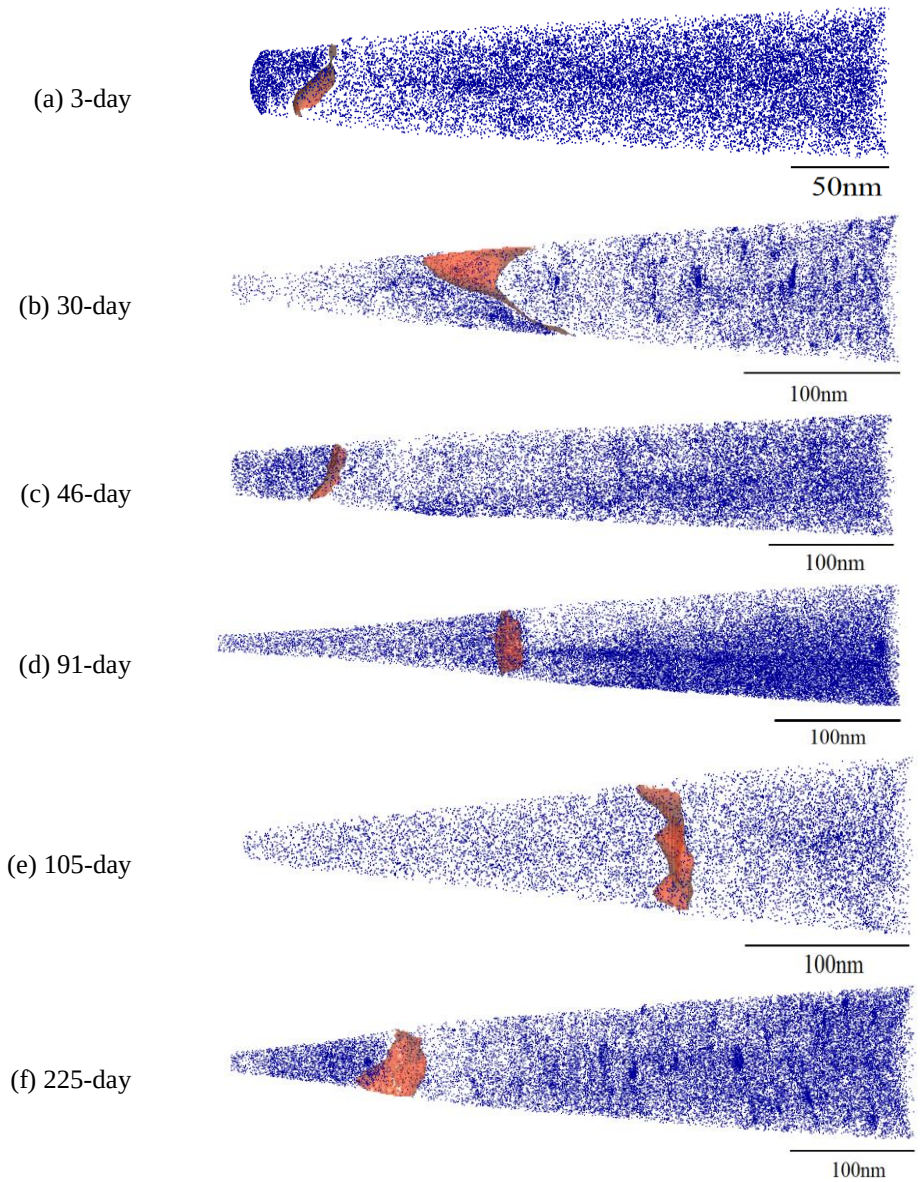


Figure 8.7: Nb distribution near the O/M interface of (a) 3-day, (b) 30-day, (c) 46-day, (d) 91-day, (e) 105-day and (f) 225-day annealed Zr-1Nb. Note the different scale bar in each image. The red isosurfaces correspond to the O(S)/M interface where the oxide/suboxide regions are on the left hand side and metal regions are on the right hand side of the isosurfaces.

Post transition, as the oxidation rate increases and reaches the local maximum at 91 days, there is no clustering (Figure 8.7d) even after the oxidation rate decreases at 105 days (Figure 8.7e). Although the 225-day sample has a high instantaneous oxidation rate overall (0.90 mg/dm^{2}day). The local instantaneous oxidation rate in the sample in Figure 8.7f (the same as

in Figure 7.16) seems to be low as there are a lot dislocation lines found in the metal as well as Nb clusters.

As-recrystallised Zr-1Nb also follows a similar trend. Like the annealed Zr-1Nb, the 3-day samples with high instantaneous oxidation rate do not exhibit clustering (Figure 8.8a). On the other hand, the 210-day sample with much lower instantaneous oxidation rate contains Nb clusters in the metal adjacent to O/M interface (Figure 8.8b).

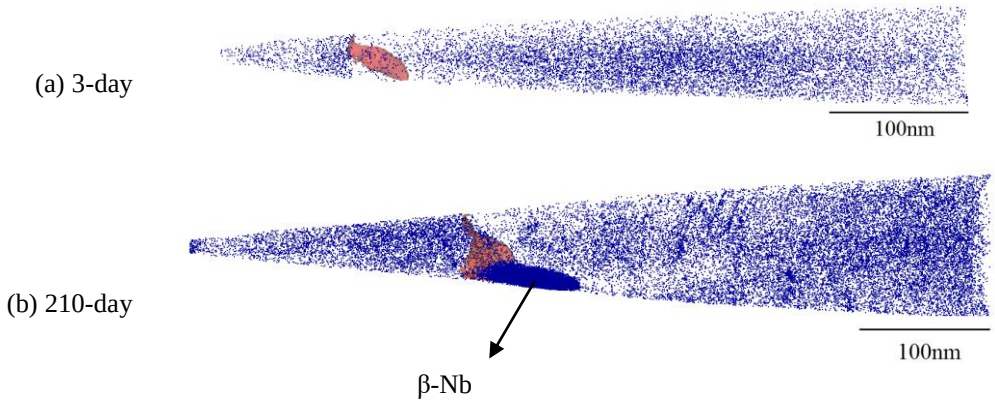


Figure 8.8: Nb distribution near the O/M interface of (a) 3-day, (b) 210-day as-recrystallised Zr-1Nb. The red isosurfaces correspond to the O/M interface where the oxide regions are on the left hand side and metal regions are on the right hand side of the isosurfaces.

There are no Nb clusters detected in the oxide (Figure 8.7a-f and Figure 8.8a-b). Because this is the case for most samples, it is thought that the clusters are dissolved upon oxidation. However, occasionally Nb clusters can be found in the oxide adjacent to O/M interface (Figure 8.9) where a few Nb clusters are found roughly ~50nm from the O/M interface. If we assume that the local instantaneous oxidation rate of the sample in Figure 8.9 is equal to the overall sample (0.79 mg/dm^{2}day or 53nm/day), the duration for which the clusters are exposed to the oxide is approximately 1 day. Therefore, the Nb clusters may not be dissolved immediately after being oxidised.

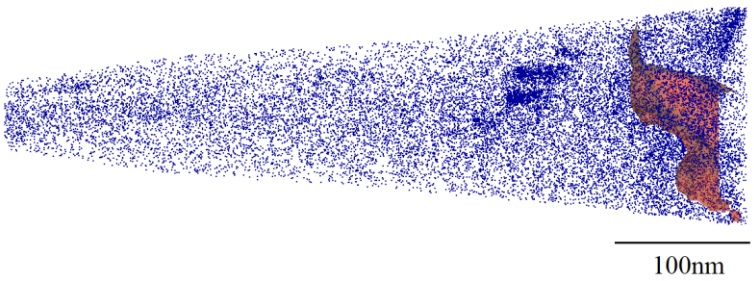


Figure 8.9: Nb clusters in the oxide adjacent to O/M interface of 91-day annealed Zr-1Nb. The red isosurfaces correspond to the S/M interface where the suboxide region is on the left hand side and metal region is on the right hand side of the isosurfaces.

8.4.2. Grain boundary oxidation

Like Fe, Nb decoration to a metal grain boundary could be either discontinuous or continuous at the O/M interface, depending whether the grain boundary itself is continuous (Section 7.4.3). Unfortunately, in the dataset where Fe segregates to a grain boundary that is discontinuous at the O/M interface (Figure 7.27), Nb does not exhibit segregation. The only Nb segregation to an oxide grain boundary is observed from the dataset where a metal grain boundary penetrates through the O/M interface (Figure 8.10).

The Nb decoration on the metal part is homogeneous while on the oxide there are several Nb clusters (lower image in Figure 8.10). The Nb interfacial excess drops from 1.1 atoms/nm^2 in the metal to 0.5 atoms/nm^2 in the oxide, corresponding to a 0.6 atoms/nm^2 or ~55% decrease. Compared to Fe segregation to the same boundary where the Fe interfacial excess decreases from 1.6 atoms/nm^2 in the metal to 0.3 atoms/nm^2 in the oxide (1.3 atoms/nm^2 or ~84% decrease), the Nb interfacial excess decrease is lower, implying that the metal grain boundary loses more Fe than Nb when oxidised.

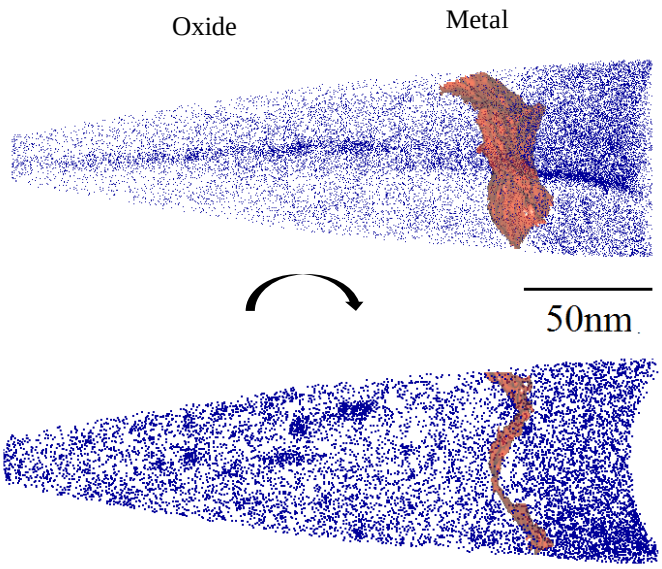


Figure 8.10: An oxidised metal grain boundary where the Nb decoration on the metal grain boundary is continuous across O/M interface. The lower image shows the cross section of the grain boundary.

8.5. Irradiation effects

The Nb distribution at the O/M interface of 1-cycle irradiated X2 is illustrated in Figure 8.11. In this dataset, there are a lot of Nb clusters in both oxide and metal that seems to agree with the Nb clusters in the metal that have been observed previously (Figure 8.12b). In the oxide, it is not clear whether the clusters originate from the metal or form in the oxide matrix after oxidation.

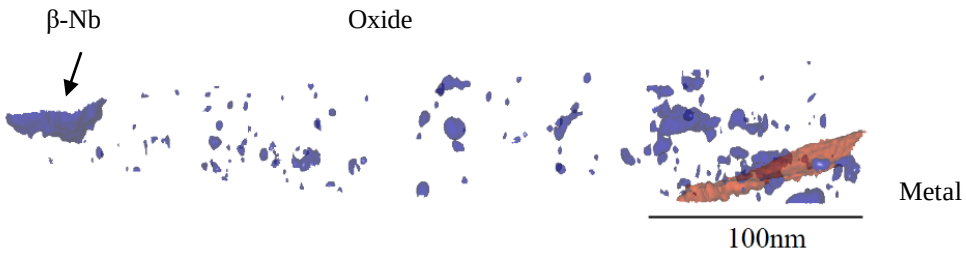


Figure 8.11: Nb isosurfaces (blue) representing Nb clusters and a β-Nb particle near O/M interface of a 1-cycle irradiated X2 sample. The red isosurface represents the O/M interface.

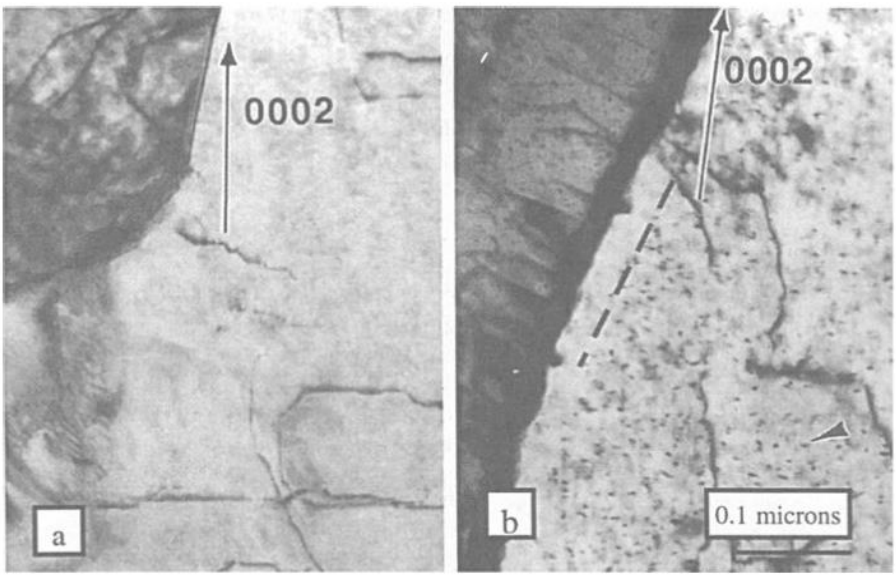


Figure 8.12: The microstructures of Zr-2.5Nb (a) unirradiated and (b) irradiated at 546 K to a fluence of 6.2×10^{25} n/m^{-2} plus 1h at 773 K [163]. The dashed line in (b) separates the regions with and without Nb-rich precipitates.

There is also an oxidised β-Nb particle in the oxide (Figure 8.11). The concentration profile across the P/O interface is displayed in Figure 8.13. This particle is similar in size to what reported previously (Figure 8.14) [104]. This particle contains ~25.5 at% Zr, ~24.7 at% Nb and ~47.4 at% O with a Nb/Zr ratio of ~0.97, about half the average Nb/Zr ratio of oxidised particles in Section 8.3.2 (~1.96).

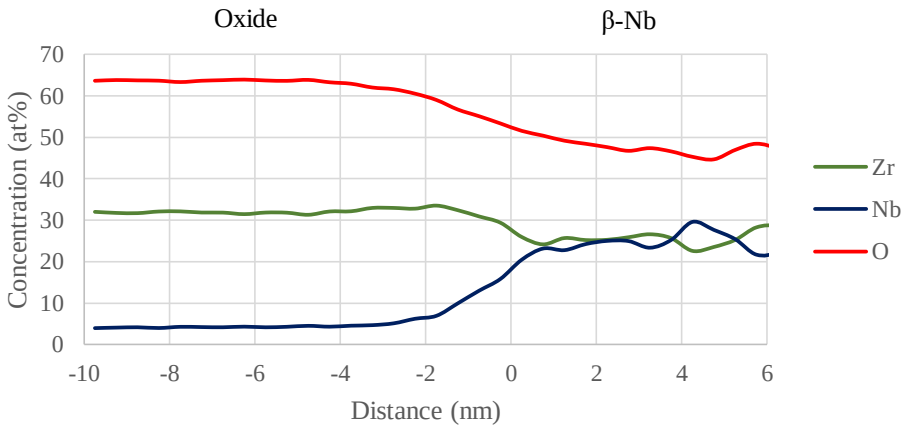


Figure 8.13: The Zr, Nb and O concentration profiles across the P/O interface of β-Nb particle from Figure 8.11.

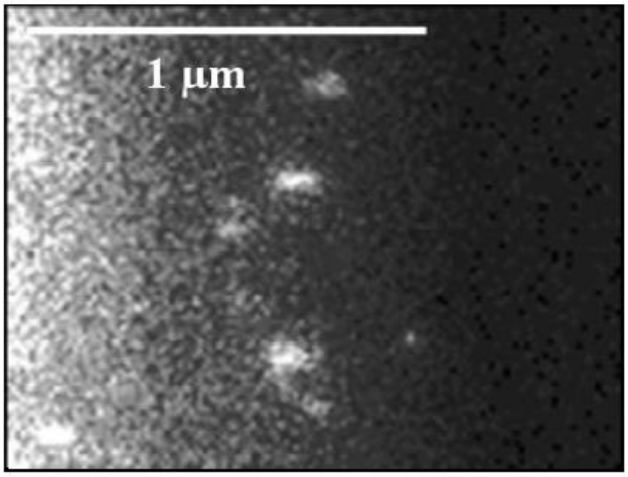


Figure 8.14: EDS mapping of Nb in the oxide of M5 alloy ~3μm from the O/M interface [104].

8.6. Discussion

The overall Nb distribution data from this chapter is summarised in Figure 8.15. The redistribution of Nb in Zr-1Nb during oxidation based on the observations and data reported in this chapter can be seen in Figure 8.16. In this work, the missing information is regarding the oxidation of β-Zr and $Zr(Nb,Fe)_2$. It has been reported that Nb/Zr ratio in β-Zr is between 0.20-0.39 when the O content inside the SPP is ~68at%, indicating that Nb may not leach out from the SPP upon oxidation [27]. However, Nb/Zr ratio decreases upon oxidation when both $Zr(Nb,Fe)_2$ is oxidised (Figure 2.37 in Section 2.3.4) [37].

The β-Nb oxidation data is obtained from Zr-2.5Nb instead of Zr-1Nb. However, a previous report about Zr-1Nb heat treated in αZr+βNb also showed the leaching of Nb from β-Nb particles [110]. Although the Nb/Zr values should be different in Zr-2.5Nb and as-recrystallised Zr-1Nb due to different Nb content in β-Nb (Section 8.2.2) but the β-Nb particles in as-recrystallised Zr-1Nb is expected to display a similar behaviour to those in Zr-2.5Nb.

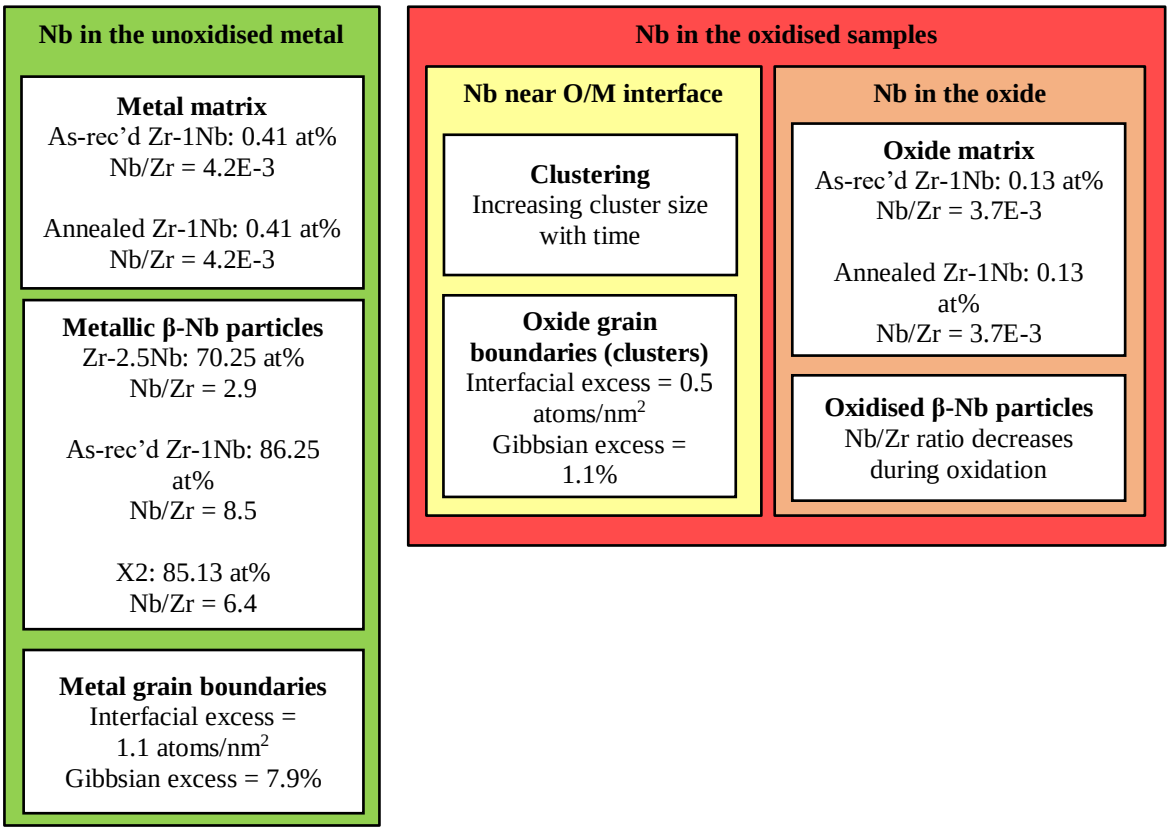


Figure 8.15: Summary of Nb distribution from data in Chapter 8.

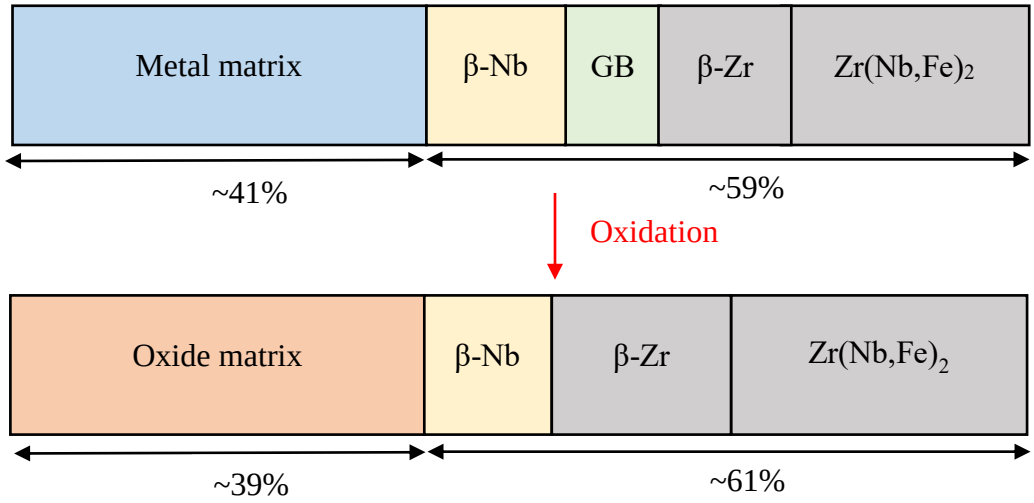


Figure 8.16: Schematic diagram of Nb redistribution map during oxidation of as-recrystallised and annealed Zr-1Nb. Note that the lengths of β-Nb/ β-Zr, grain boundary (GB) and $Zr(Nb,Fe)_2$ rectangles do not represent the ratio between the amount of Nb in these regions.

ZrO_2 is thermodynamically very stable as the free energy of ZrO_2 formation (per mole of O_2) is -965 kJ, much lower compared to β-Nb oxidation to Nb_2O_5 (-727 kJ) [112]. This indicates that β-Nb is more noble compared to Zr and explains why the β-Nb particles in the oxide

layer are only oxidised slowly. The Nb content in the metal (~0.41 at%) is higher than the oxide (~0.13 at%) in both as-recrystallised and annealed Zr-1Nb (Sections 8.2.1 and 8.3.1). However, the Nb/Zr ratio in the metal ($4.2x10^{-3}$) is very close to the one in the oxide ($\sim 3.7x10^{-3}$).

The observations in this chapter do not support the possibility that the Nb content in the metal is higher than in the oxide, mainly due to two reasons. Firstly, most Nb is located in the SPPs, especially β-Nb but the Nb/Zr ratio decreases upon oxidation (Section 7.3.2), indicating that Nb leaches out from the SPPs into the oxide matrix. This clearly suggests that the oxide should be more enriched in Nb than the metal and not the opposite.

Secondly, the Nb segregation to metal grain boundaries is weak (Section 8.2.3). No oxide grain boundaries located ~500-600 nm from the O/M interface contain any Nb segregation, suggesting that the excess Nb on metal grain boundaries is dissolved upon oxidation. The dissolution occurs gradually in the case where the grain boundary is continuous, leaving only Nb clusters in the oxide part of the grain boundary (Section 8.4.2). From this process, we can conclude that the Nb content on grain boundaries is much less compared to in β-Nb and therefore perhaps cannot play a significant role in controlling oxidation and HPU and the dissolution of excess Nb atoms on metal grain boundaries can only result in the increase of Nb content in the oxide matrix.

The explanation for why the Nb content in both metal and oxide matrices is more less the same is probably because there is a sizeable proportion of unoxidised Nb in the inner part of the oxide where APT analysis was carried out in this work (Figure 8.17) [5,256]. For alloys containing β-Nb, the unoxidised Nb in the innermost part of oxide layer is likely to originate from partially-oxidised β-Nb.

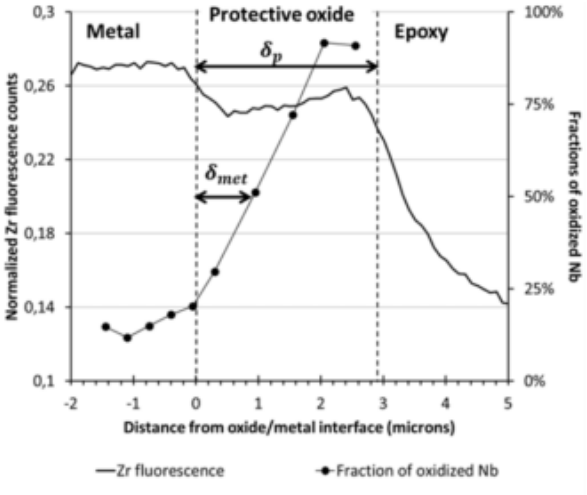


Figure 8.17: XANES results on a Zr-2.5Nb specimen showing the fraction of oxidised Nb as a function of oxide depth [5].

Nb exhibits a delayed oxidation because oxidised Nb can have multiple charge states from +2 to +5 (Figure 8.18a-b) [122,123]. The oxidised Nb ions can dope Zr^{4+} in the oxide [124,259]. Considering that the radii of Nb^{2+}, Nb^{3+}, Nb^{4+} and Nb^{5+} are 71pm, 70pm, 69pm and 64pm respectively which all are comparable to Zr^{4+} (72pm), it is possible that all these Nb ions can substitute for Zr^{4+} in the oxide [254,259]. As illustrated in Figure 8.19, they create electronic levels located not far (~1eV) from the edge of the ZrO_2 conduction band, supporting the possibility of doping [260].

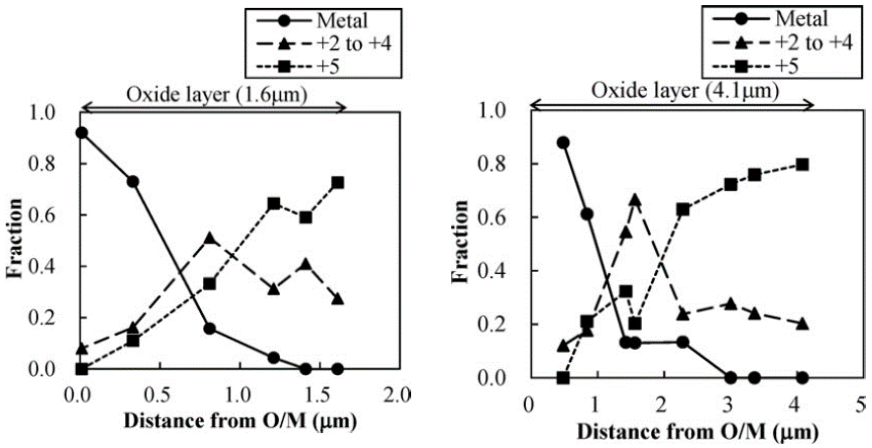


Figure 8.18: The fractions of metallic Nb and Nb ions from +2 to +5 across the oxide layer of Zr-2.5Nb oxidised at 360°C for (a) 40 and (b) 220 days, containing 1.6μm and 4.1μm oxides respectively [122].

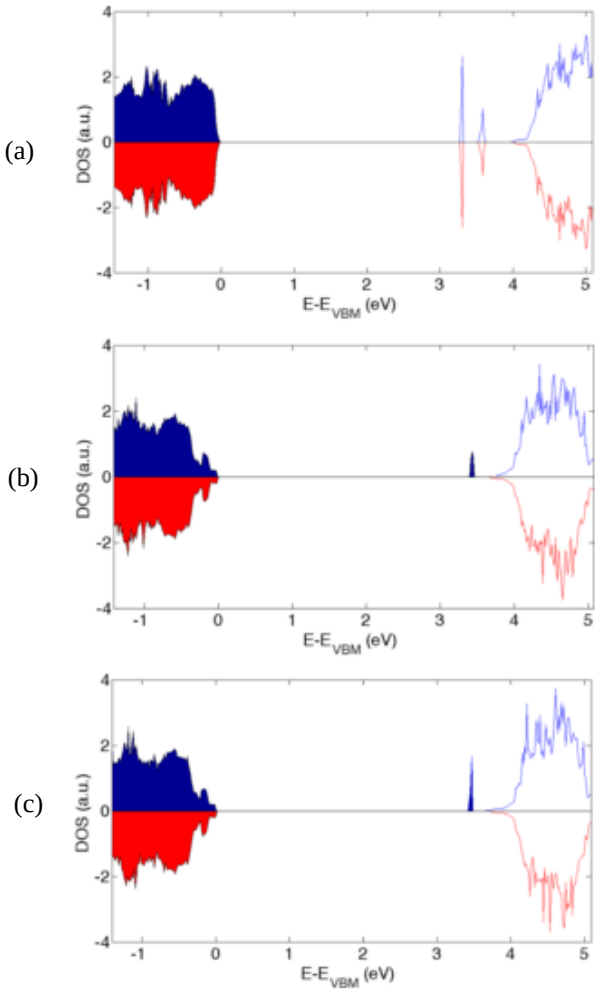


Figure 8.19: Calculated electronic density of states of (a) Nb^{5+}, (b) Nb^{4+} and (c) Nb^{3+} in ZrO_2 [260]. Filling corresponds to the occupied states.

If we argue that the electrochemical barrier layer (typically hundreds of nm thick) is responsible for controlling the oxidation and HPU rates, then it is the Nb with +4 state or lower that plays a more important role as their concentration in this region of the oxide is higher than Nb^{5+} (Figure 8.18a-b). While according to Figure 8.19c, Nb^{3+} can n-type dope Zr^{4+}, resulting in extra electrons in the conduction band, there is very limited information about Nb^{2+} deep level in the literature and it is not clear whether this ion can have the same effect as Nb^{3+}.

However, this should not be a problem in terms of space charge compensation because doping is not required for a species to contribute to space charge. Nb^{5+} can also contribute to

space charge, but unlike $Nb^{2,3+}$ (Nb ions with lower valence than Zr^{4+}) which are beneficial for HPU (similar to Fe, where the effect is explained in Section 7.6), Nb^{5+} has the opposite effect where it can increase the space charge instead [5,143]. However, Bossis et al. speculated that Nb^{5+} near the W/O interface has a beneficial effect for HPU as it can provide extra electrons to close in the HPU cathodic reaction in this location [104].

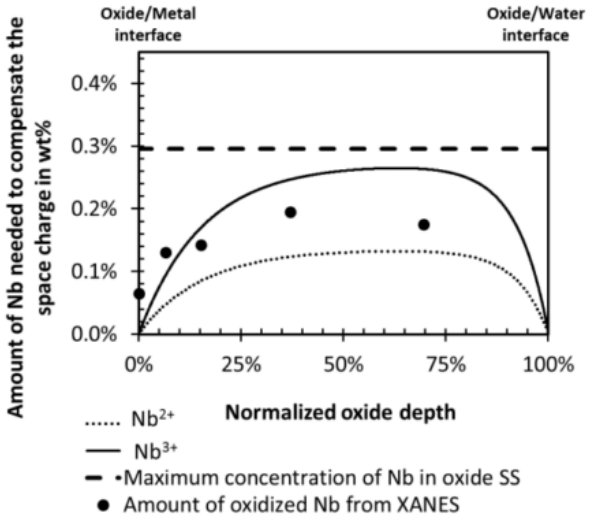


Figure 8.20: The theoretical amount of Nb in the oxide to compensate the space charge (Γ=0) in Zr-2.5Nb [143]. The dashed line is the predicted amount of Nb in the oxide and the XANES results are the black points.

Couet et al. calculated the amount of required Nb to fully compensate for the space charge (Figure 8.20) [143]. With ~0.13 at% Nb content in the ZrO_2 matrix (Section 8.3.1), there is a sufficient amount of $Nb^{2,3+}$ to fully compensate for the space charge, especially in the innermost part of the oxide. This implies that Nb plays a significant role on corrosion and HPU.

Because most Nb clusters are dissolved upon oxidation, clustering in the metal near O/M interface (Section 8.4.1) probably does not have a significant influence in controlling the oxidation and HPU. The clustering is apparently induced by strain because it only appears in the samples containing dislocation lines due to plastic deformation. However, irradiation can also lead to the formation of fine β-Nb precipitates (<10nm) in the metal (Figure 8.12) by depleting the Nb content in the original, larger β-Nb and this can lower the Nb content in the

metal matrix (Section 2.5) [162,163,261]. It is also plausible that the fine β-Nb SPPs are the clusters observed in the irradiated oxide (Section 8.5) as they are similar in size. Under irradiation, the original β-Nb precipitates that usually contain 85-90 at% Nb become more depleted in Nb, such that the Nb content reduces to 50-70 at% [161]. This could be the reason why the Nb/Zr ratio of the oxidised β-Nb (Section 8.5) is much lower compared to the average value from the unirradiated particles.

It has been proposed that probably the in-pile β-Nb oxidation is similar to out-of-pile behaviour [261]. Because β-Nb oxidises slowly (Section 8.3.2) [261], Nb/Zr ratio in the SPPs is still high when the particles are not heavily oxidised. In fact, the β-Nb particles in the innermost part of the oxide (<500nm) are still unoxidised [261]. The implication of these observations is the lower Nb content in the oxide matrix available to compensate for the space charge under irradiation than out-of-pile. Although this should increase the corrosion rate, recent results suggest that Zr-Nb alloys show a reduction of oxidation weight gain under irradiation [262]. Therefore, further work is required to examine the Nb effect under irradiation.

8.7. Summary

- Most Nb is located in the SPPs and I have only been able to study β-Nb. Upon oxidation, the Nb/Zr ratio decreases and remains almost constant at the later stage of oxidation, suggesting that Nb diffuses out from the particles at a higher rate than Zr. Although the effect in increasing Nb content in the oxide is not significant in the innermost part of the oxide but this could be more pronounced in the outer part of the oxide.

- Nb can segregate to metal grain boundaries but the segregation is weak. Upon oxidation, the grain boundaries gradually lose Nb but this process does not appear to affect the Nb content in the local oxide matrix.
- Nb contents in both metal and oxide matrices are very similar, probably because most Nb is still inside the SPPs and remains metallic when the SPPs are incorporated to the oxide 500-600 nm from the O/M interface.
- Nb tends to exhibit clustering under straining in the metal adjacent to the O/M interface. Upon oxidation, Nb clusters are mostly dissolved even though the dissolution does not occur immediately after the clusters are exposed to the oxide.
- Because Nb displays a delayed oxidation and can form $Nb^{2,3+}$, it influences the oxidation and HPU by space charge compensation. It is likely that there is a sufficient amount of Nb to fully compensate the space charge in the oxide barrier layer.
- Under irradiation, the density of Nb clusters (probably β-Nb) increases and hence it is not surprising to observe some of these clusters in the oxide near the O/M interface. The Nb forming these clusters come from the original β-Nb as evidenced by low Nb/Zr ratio in the oxidised β-Nb. This in turn can decrease the Nb content in the oxide matrix and reduce the space charge compensation.

9. ANTIMONY

9.1. Introduction

Early literature suggests that antimony is beneficial for HPU [142] (Section 2.4.3) but very little work has been done on Zr-Sb alloys. This chapter discusses the results from Zr-0.5Nb-0.1Sb with the emphasis on Sb and comparison with Fe and Nb. The Sb maximum solubility limit in α-Zr (at ~875°C) is ~1.9 at%, but significantly lower at 580°C (below 0.2 at%) [263]. Although various intermetallics have been predicted [263,264] (Figure 9.1), no Sb-containing SPP was detected in any dataset.

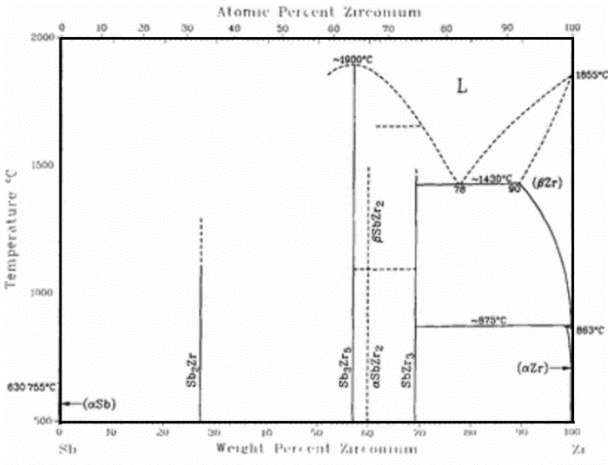
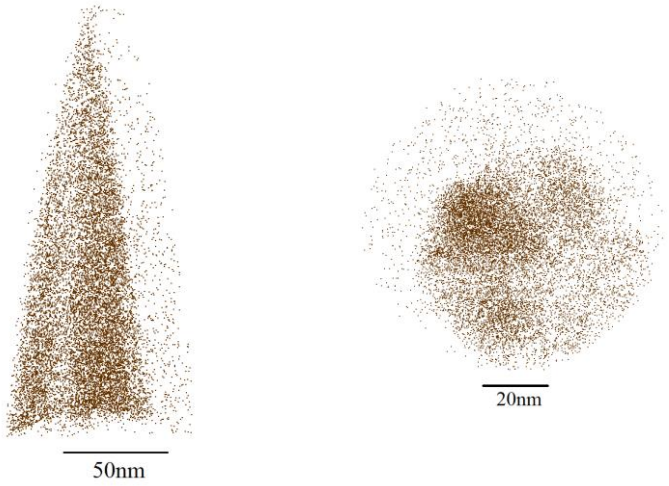


Figure 9.1: Sb-Zr phase diagram [263].

9.2. Antimony in the metal

9.2.1. Metal matrix

Despite having a similar evaporation field to Zr (30 V/nm for Sb and 28 V/nm for Zr), characterising Sb in the metal is difficult because Sb atoms segregate to crystallographic poles (Figure 9.2a-b).



(a) (b)

Figure 9.2: (a) The Sb distribution in Zr-0.5-0.1Sb alloy and (b) the view parallel to the needle axis, showing the segregation to a crystallographic pole.

The Sb concentration difference between two areas in the dataset can be significant, e.g. in the dataset from Figure 9.2a-b the Sb concentrations outside (pink ROI in Figure 9.3) and inside (blue ROI in Figure 9.3) the apparently segregated region are 0.01 at% and 0.21 at% respectively. Therefore, the distribution of Sb atoms depends on the relative position of detected crystallographic poles and it is not clear if the measured Sb concentration corresponds to the actual Sb contained in the sample. In addition, Sb clusters are occasionally observed (Figure 9.4).

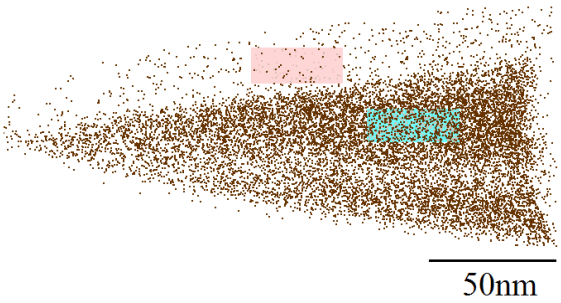


Figure 9.3: 2 cuboidal ROIs inside and outside the segregated region from the dataset in Figure 9.2a-b.

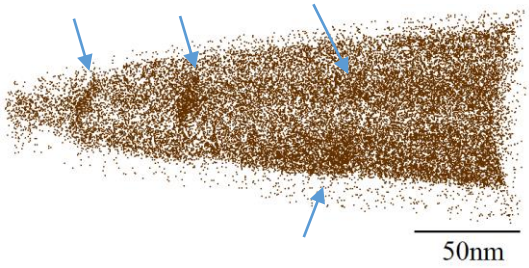


Figure 9.4: Sb clusters (blue arrows) in the metal.

From the examination of 6 samples containing metal, the average concentration of Sb is 0.08±0.04 at%, corresponding to a Sb/Zr ratio of $(8.3\pm3.7)\times10^{-4}$. This means that almost all Sb is in the solid solution. In the same alloy, Nb average concentration and Nb/Zr ratio are 0.34±0.05 at% and $(3.6\pm0.5)\times10^{-3}$ respectively, while the values for Fe are 0.006±0.004 at% and $(6.5\pm4.5)\times10^{-5}$.

9.2.2. Metal grain boundaries

Sb can segregate to metal grain boundaries, but the segregation is very weak. In Figure 9.5a-b, the Sb concentration in either side of the grain boundary is not the same due to the pole segregation effect. Compared with Fe and Nb segregation to the same feature, Sb segregation is weaker; the interfacial excess values of Fe (1.9 atoms/nm^2) and Nb (0.5 atoms/nm^2) are greater than Sb (0.3 atoms/nm^2). Consequently, the Gibbsian excess (relative to α-Zr basal plane) of Fe (13.5%) and Nb (3.3%) is also greater than Sb (1.9%). In a grain boundary with a weaker Fe segregation (interfacial excess of 0.7 atoms/nm^2 and Gibbsian excess of 5.2% monolayers of α-Zr basal plane), there is no detectable Sb segregation (Figure 9.6a-b). This indicates that the Sb segregation to metal grain boundaries might be correlated with Fe.

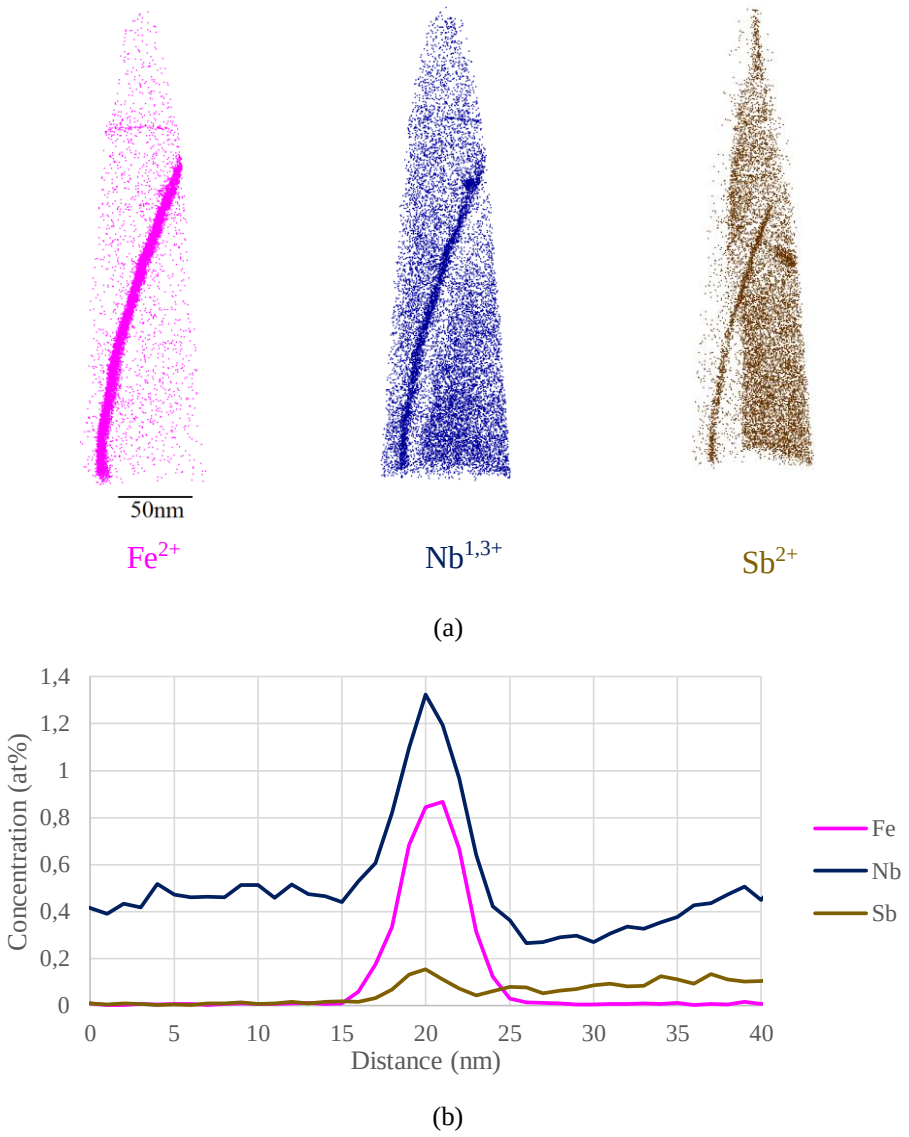
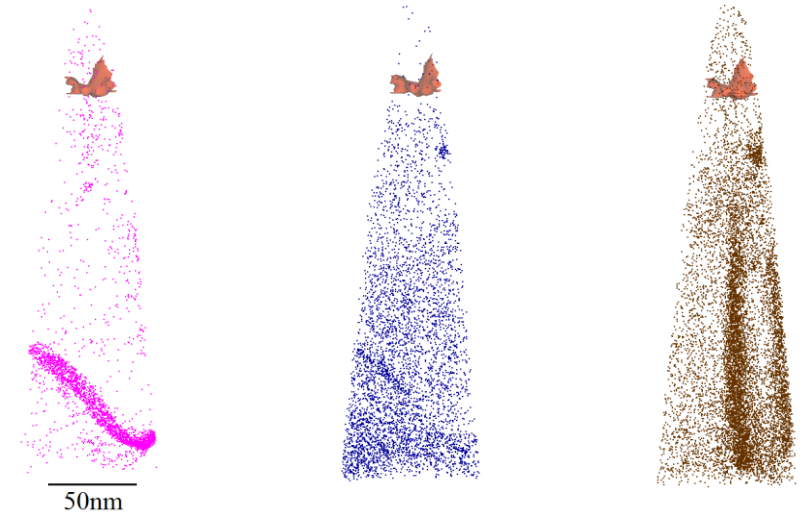
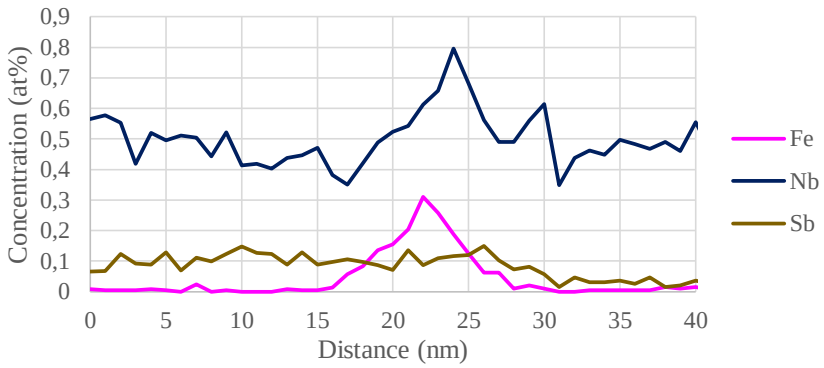


Figure 9.5: (a) The atom maps of Fe, Nb and Sb showing the segregation of these elements to a metal grain boundary and (b) the corresponding concentration profile across the boundary. Note that Nb^{2+} is not included in the atom map in (a) for visual clarity, but is included in the concentration profile in (b).

In the case where the grain boundary is continuous at the O/M interface (the dataset in Figure 7.28 and Figure 8.10), Sb decorating the metal grain boundary is redistributed in the oxide part (Figure 9.7). This is probably because Sb segregation to metal grain boundaries is not as strong as Fe and Nb. In this particular example, the Sb interfacial and Gibbsian excess values are 0.1 atoms/nm^2 and 1.0% monolayers of α-Zr basal plane respectively, only ~9% and ~14% of the corresponding values in Fe and Nb respectively.



(a)



(b)

Figure 9.6: (a) The atom maps of Fe, Nb and Sb showing the segregation of these elements to a metal grain boundary and (b) the corresponding concentration profile across the boundary. Note that Nb^{2+} is not included in the atom map in (a) for visual clarity but included in the concentration profile in (b). The red isosurface in (a) corresponds to the O/M interface where oxide is in the top and metal is in the bottom of the atom maps.

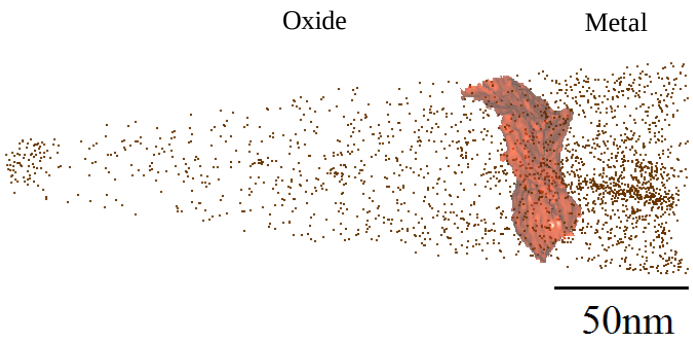


Figure 9.7: A continuous metal grain boundary at the O/M interface where Sb in the metal grain boundary is redistributed when the grain boundary is oxidised. The red isosurface mimics the O/M interface.

9.3. Antimony in the oxide

No Sb segregation was observed in the oxide. Although one oxide sample contains a grain boundary decorated with Fe (Figure 6.8), Sb does not segregate to that grain boundary. The average Sb content in the oxide taken from 11 samples is $(5.4\pm2.5)x10^{-3}$ at%, giving Sb/Zr ratio of $(1.5\pm0.7)x10^{-4}$. Although this indicates that Sb is probably more enriched in the metal, the average concentration in the metal should be interpreted carefully due to the pole segregation.

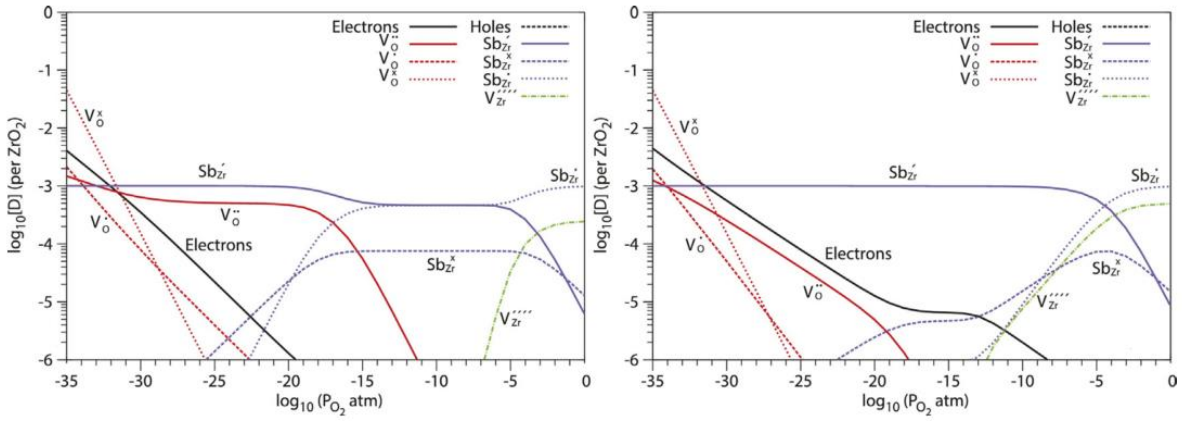
9.4. Discussion

In Zr-0.5Nb-0.1Sb, results from this study suggest that most Sb is located in the metal matrix and there is a sign of both clustering and weak Sb segregation to metal grain boundaries. It is apparent that the Sb content in the metal is higher than in the oxide but because Sb exhibits a pole segregation, it is not possible to measure the Sb concentration in the metal accurately.

Sb has several oxidation states; +3 and +5 [265] and hence, Sb^{3+} can compensate for the space charge while Sb^{5+} increases the space charge. The information about the distribution of these species in the oxide layer is still lacking but given that Sb has a beneficial effect on HPU, a significant amount of Sb^{3+} is expected in the innermost part of the oxide to compensate for the space charge.

Sb^{3+} and Sb^{5+} are 76pm and 60pm in radius respectively [254], suggesting that substitutional doping is possible, especially for Sb^{3+} as it has comparable size to Zr^{4+} (with radius of 72pm). The Brouwer diagrams show that across the oxide layer (with O partial pressure from $\sim10^{-75}$ atm near the O/M interface to $\sim10^{-10}$ atm near the W/O interface [109]) Sb^{3+} is the dominant species in the inner part of the oxide, while Sb^{3+} and Sb^{5+} co-exist at near the W/O interface (Figure 9.8a). However, with applied space charge Sb^{5+} is expected to disappear completely

up to ~10^{-10} atm (Figure 9.8b) [265]. This implies that Sb in the oxide matrix observed in this chapter is probably beneficial for HPU due to its contribution in space charge compensation. This might be the reason why an addition of 0.1 wt% Sb to Zr-0.5Nb is beneficial for HPU.



(a) (b)

Figure 9.8: Brouwer diagram showing the concentrations of point defects in t-ZrO_2 containing Sb at a concentration of 1x10^{-3} (per ZrO_2) as a function of oxygen partial pressure at 1500 K, (a) with no additional charge and (b) applied space charge at a concentration of 1x10^{-3} (e^- per ZrO_2) [265].

9.5. Summary

- Sb exhibits a pole segregation in the metal and hence it is not possible to accurately measure the Sb content in the metal.
- Sb segregates to metal grain boundaries to a lesser extent than Fe and Nb. The degree of Sb segregation tends to increase with Fe and Nb segregation. Sb on metal grain boundaries is redistributed as the boundary is oxidised.
- Sb is beneficial in reducing HPU due to its contribution to space charge compensation.

10. CONCLUSIONS

10.1. Conclusions

10.1.1. Oxidation mechanisms

The layered oxide structure of ZrO_2-ZrO-Zr(O_{sat})-Zr metal has been observed at the O/M interface. As the oxide layer grows inwards in the pre-transition regime, the oxidation rate decreases over time (Section 4.3), demonstrating a restriction of O supply. This in turn results in a decrease in the rate at which the ZrO_2-ZrO/Zr(O_{sat}) interface advances and consequently the ZrO or Zr(O_{sat}) layer thicknesses increase. In the case where both ZrO and Zr(O_{sat}) are present, the Zr(O_{sat}) layer thickness decreases as ZrO layer thickens. At early post transition, the opposite of this occurs, resulting in the decrease of ZrO and/or Zr(O_{sat}) thicknesses (Section 5.4.3). Therefore, the growth of Zr(O_{sat}) layer depends on the growth of the phase above it, i.e. the oxidation rate.

Across the same sample, the oxidation rate is very inhomogeneous (Sections 4.3 and 5.4.35.4) as has been observed by many previous authors [8,64,99,217,218,266]. In my observations, the oxide layer thickness variation increases with oxide thickness (Section 4.3). In samples near the transition point, cracks associated with transition can develop even though the whole sample is still pre transition (Section 4.3.2). The inhomogeneous oxidation rate leads to uneven O/M interface, in the most extreme cases forming a sawtooth-shaped O/M interface (Section 5.4.4). This includes the protrusions of oxide into a suboxide layer, suboxide into Zr(O_{sat}) layer and Zr(O_{sat}) into suboxide layer. Similar observations on these alloys have also been reported [64,99].

10.1.2. HPU mechanism

Signs of hydroxylation in the oxide layer have been observed (Section 6.4.2.1) and this is more likely to occur in regions containing a higher local H content. Although Fe can also segregate to oxide grain boundaries this segregation does not seem to be correlated to H segregation. In addition, porosity in the oxide has been observed (Section 6.4.2.2). APT is not a reliable technique to characterise H, but there is an apparent accumulation of H inside isolated pores. If the observed H originates from the corrosion process, the observations agree with the theory of H filling pores [135,137]. Interconnected porosity and grain boundaries can be pathways for H transport in the oxide layer as previously proposed [80,124,139].

However, it is not clear how H can travel through the barrier layer, as examinations at the O/M interface do not show any sign of H segregation. H diffusion is slow in the oxide but likely to be even slower in the barrier layer due to high compressive stress. Therefore, another pathway might be required to transport H across the barrier layer. One possible route is via vertical cracks, but this possibility has not been experimentally studied here.

10.1.3. Effect of alloying elements

10.1.3.1. Iron

Fe contents in both metal and oxide matrices are very low, but there is an indication that the oxide is more enriched in Fe (Sections 7.2.1 and 7.3.1). Upon oxidation of β-Nb, Fe originally in the particle is not lost, but the Fe decorating the P/M interface is redistributed to the surrounding oxide (Section 7.3.2). Upon oxidation of metal grain boundaries, Fe decorating the boundaries can either be partially or fully redistributed depending on the alignment between the adjacent metal and oxide grains (Sections 7.2.3, 7.3.3 and 7.4.3).

These two mechanisms responsible for the enrichment of Fe in the oxide have been directly observed in this thesis.

The implication of this Fe enrichment is on space charge compensation. $Fe^{2,3+}$ does not substitutionally dope Zr^{4+} [255] but can compensate for the space charge [143,145,146]. However, in the alloys studied in this thesis, the Fe content is probably too low to significantly compensate for the space charge. Although Fe segregates to oxide grain boundaries, there seems to be little correlation between Fe and H segregation to the boundaries. However, Fe can reduce HPU by promoting the H_2 gas evolution [42,144]. There is a sign that Fe in the metal adjacent to O/M interface can promote HPUF but it is not clear if and how Fe in this area can influence HPU.

10.1.3.2. Niobium

There is no significant difference between Nb contents in the metal and oxide matrices (Sections 8.2.1 and 8.3.1). Most Nb is located in the SPPs and in this thesis only β-Nb has been studied in detail. Upon oxidation of β-Nb, the Nb/Zr ratio decreases and remains almost constant at the later stage of oxidation, suggesting that Nb diffuses out from the particles at a higher rate than Zr. Thus, the effect of increasing Nb content in the oxide is not expected to be significant in the innermost part of the oxide but this could be more pronounced in the outer part of the oxide.

Nb displays a delayed oxidation and can form ions with intermediate oxidation states ($Nb^{2,3+}$) before reaches the most stable form of Nb^{5+}. $Nb^{2,3+}$ ions are able to compensate for the space charge in the innermost part of the oxide, and given the high Nb content in the oxide matrix it is likely that there is a sufficient amount of Nb to fully compensate the space charge in the oxide barrier layer. Although Nb^{5+} increases the space charge, its accumulation near the W/O

interface is thought to be beneficial for HPU because Nb^{5+} substitutional doping into Zr^{4+} can result in free electrons required for forming H_2 gas.

10.1.3.3. Antimony

Because Sb exhibits pole segregation, it was difficult to determine the original positions of Sb atoms in the metal, i.e. the concentration in the metal matrix (Section 9.2.1). Sb segregates to metal grain boundaries to a lesser extent than Fe and Nb, and the degree of Sb segregation tends to increase with Fe and Nb segregation. Sb on metal grain boundaries is redistributed if the boundary is oxidised. However, no information about any Sb-containing SPP was obtained. Sb is beneficial in reducing HPU due to its contribution to space charge compensation. Although Sb can be oxidised into Sb^{3+} and Sb^{5+}, Sb^{3+} is predicted to be dominant and hence Sb can compensate for the space charge and reduce HPU [265].

10.1.3.4. Comparison between alloying elements

The overall distributions of Fe, Nb and Sb are summarised in Table 10.1. In general, the Fe content in the metal matrix is lower than Nb and Sb and thus, the space charge compensation from Fe is less significant. However, there is Fe enrichment in the oxide from the redistribution of Fe originally decorating the β-Nb particles and grain boundaries. This is an indication of how Fe additions are effective to suppress HPU [5,143,150,165,253,256].

Table 10.1: Summary of comparison between alloying elements.

	Fe	Nb	Sb
Difficulties in data analysis			
Metal	Separation with CO^+ signal	Deconvolution with $Zr^{1,2+}$ and metal hydride peaks	Pole segregation
Oxide		Deconvolution with thermal tails	-
In the metal			
Content in the metal matrix	~0.01 at% Fe/Zr = ~$1x10^{-4}$	~0.4 at% Nb/Zr = ~$4x10^{-3}$	~0.1 at% Sb/Zr = ~$8x10^{-4}$
Metal grain boundary segregation	• Strong • Homogeneous • Large standard deviation	• Weak • Homogeneous • Does not segregate to all boundaries	• Very weak • Correlated with Fe and Nb segregation
Average interfacial excess to metal GBs (atoms/nm^2)	~1.7	~0.5	~0.1
Content in/on β-Nb	• Inside the particle = ~0.3 at% • Decoration at the P/M interface = ~1.8 atoms/nm^2	• ~70 at% in β-Nb from decomposed β-Zr • ~85 at% for alloys heat treated in αZr+βNb region	Unknown
Clustering	Only in the metal adjacent to the O/M interface	• Only in the metal adjacent to the O/M interface • Correlated with strain	Occasional clustering is observed
Distribution in the metal adjacent to the O/M interface	• Rejected from the oxide in pre transition • Segregates to dislocation lines at low oxidation rates	Clustering at low oxidation rates	No notable segregation
In the oxide			
Content in the oxide matrix (at%)	~0.01 at% Fe/Zr = ~$3x10^{-4}$	~0.1 at% Nb/Zr = ~$3.6x10^{-3}$	~0.5 at% Sb/Zr = ~$1.5x10^{-4}$
Oxide grain boundary segregation	• Weak • Consists of clusters and dislocation lines • Average interfacial excess = ~0.5 atoms/nm^2	• Consists of clusters and dislocation lines near the O/M interface • No segregation 500-600nm from the O/M interface	No observed segregation
Content in β-Nb	~0.28 at%	Decreases with O content	Unknown

Nb, on the other hand is the most dominant alloying element due to its relatively higher content. There is no apparent Nb enrichment in the oxide matrix, but the Nb beneficial for HPU is not only in the innermost part of the oxide ($Nb^{2,3+}$) but also Nb^{5+} near the W/O interface as Nb^{5+} can substitutionally dope Zr^{4+} and produce more free electrons for a cathodic reaction to occur near the W/O interface [104]. As Nb leaches out from the β-Nb particles, the enrichment of Nb in the oxide matrix can occur predominantly in the outer part of the oxide.

Sb is beneficial for both corrosion and HPU, and modelling suggests that Sb^{3+} is more likely than Sb^{5+} [265]. It is not clear whether there is an Sb enrichment in the oxide because of the uncertainty in determining the Sb content in the metal. Furthermore, the extent to which Sb^{3+} compensates for the space charge in the Zr-0.5Nb-0.1Sb alloy is not known, but because the Sb content in the oxide is likely to be higher than Fe, the Sb effect should be more prominent.

The trace element content in the oxide matrix might not the only important parameter in determining how the alloying elements influence the space charge. The type of SPP is also important as different SPPs have different behaviour during oxidation as they determine how fast the constituting elements are released to the oxide. In addition, the size and conductivity of SPPs once they are incorporated to the oxide can be important if we regard them as pathways for electronic conduction in the oxide barrier layer. Therefore, these results can be different in alloys with different heat treatment methods.

10.1.4. Irradiation effects

In this thesis, the irradiated X2 exhibits a remarkably better corrosion performance than unirradiated X2 oxidised in the same duration (~1.5 years) (Section 4.3.3) even though irradiation has been known to accelerate corrosion [39,104,117,165,166]. This is probably

attributed to the difference between autoclave (360°C) and reactor (~300°C) temperatures that could be even more pronounced under irradiation [267]. However, a recent study suggests that while irradiation can accelerate corrosion in Sn-containing alloys but the opposite effect was observed in Zr-Nb [262]. Therefore, the irradiation effect on Zr-Nb is still not well-understood. Although a direct comparison between irradiated and unirradiated X2 cannot easily be drawn, different element distributions associated with irradiation have been observed in this thesis (Table 10.2).

Table 10.2: Summary of irradiation effects.

	Unirradiated	**Irradiated**
Decorated oxide grain boundaries	• Consists of Fe clusters and apparent dislocation lines. • Contains less Fe.	Homogeneous and diffuse with much more Fe.
Nb clusters	• In the metal adjacent to the O/M interface. • Dissolved upon oxidation.	• Not dissolved during oxidation. • Probably originate from the β-Nb particles.
β-Nb particles	Contains higher Nb/Zr ratio.	Contains lower Nb/Zr ratio.

Under irradiation, Fe segregates to oxide grain boundaries but the Fe profile is more diffuse in this case. Moreover, more Fe atoms are found in the vicinity of the grain boundaries (Section 7.5), supporting the possibility that Fe from SPPs is redistributed into the matrix [162,201]. In the oxide, the density of Nb clusters increases (Section 8.5). These clusters are probably the small β-Nb particles with a few nm in size that originate from the pre-existing larger β-Nb [104,162]. The larger β-Nb particles have lower Nb/Zr ratio, as seen in the oxidised β-Nb. Although the dissolution of Fe results in the increase of $Fe^{2,3+}$ beneficial for space charge compensation (i.e. reducing HPU), the precipitation of small Nb clusters can decrease the Nb content in the oxide matrix available to compensate for space charge. The net effect of this should be the increase of HPU and oxidation because the Fe content is much lower than Nb.

10.2. Overall contribution of this thesis

This thesis examined the Zr-Nb oxidation process on the atomic scale. The oxidation mechanisms involving the thickening of the $Zr(O_{sat})$ layer has been studied, reinforcing the hypothesis from previous studies that the growth of this layer is related to the instantaneous oxidation rate [64,217]. In addition, the non-uniformity of oxidation rate has been demonstrated using FIB/SEM and APT, with the most extreme case being the sawtooth-shaped O(S)/M interface.

Another important point discussed in this thesis is the mechanistic understanding of HPU. The effect of D as a surrogate for H has been demonstrated. Although D segregation to the oxide grain boundaries has been previously observed [192,226], this thesis provides a deeper analysis on the isotopic ratio study and how D segregation is more favoured in the local areas with higher D content. Furthermore, porosity in the oxide has been identified.

The effect of alloying elements, including Fe, Nb and Sb has been analysed in detail. The study of Sb-containing alloys is relatively new. The approach is to examine the distributions of these elements in the metal, oxide and at the O/M interface. Phenomena such as the oxidation of β-Nb and grain boundaries have been studied. Fe and Nb have been observed using APT [6,33,34,64,124,164,192,210] but the understanding of the redistribution of these elements during oxidation is still lacking. The data from this thesis can support the hypothesis on how these elements can influence corrosion and HPU [143,145,256].

Irradiated samples have been studied to a lesser extent. The redistribution of Fe and Nb in the oxide under irradiation has been observed. These include the dissolution of Fe into the oxide matrix and the change of Nb content in β-Nb.

10.3. Future directions

Oxidation mechanism has been studied in a lesser extent in this thesis. However, given the limited number of samples analysed, examinations on more samples will be beneficial especially for post-transition samples. In addition, it is still not clear whether the thickness evolution Zr(O_{sat}) is the cause or consequence of the change in instantaneous oxidation rate.

H segregation to oxide grain boundaries has been observed as a possible pathway for H transport but no evidence of H transport across the oxide barrier layer has been shown. NanoSIMS analysis has demonstrated that vertical cracks can be a pathway for O transport [83]. Obviously, H transport via this type of cracks is also a possibility, but there is no supporting evidence to date. Examination of vertical crack tips in a deuterated specimen will be beneficial in understanding the segregation of H/D to this feature and assessing this possibility.

Studies regarding the oxidation of SPPs are still important. While the β-Nb oxidation has been studied extensively, the examinations of the behaviour of β-Zr and the Fe-containing SPPs upon oxidation are required to obtain a more complete picture of corrosion and HPU in Zr-Nb alloys and their relationships to heat treatments. Although the analysis of Sb is not straightforward due to its tendency to segregate to crystallographic poles, Zr-Nb-Sb alloys containing different Sb contents have not been studied in depth to study the beneficial effect of Sb on HPU.

Irradiation effects require in-depth examination. Irradiated Zr alloys have been studied using APT [164], but little is understood about how the alloying elements are redistributed during in-reactor oxidation. Examinations on samples corroded in heavy water reactors can also be carried out to study the HPU behaviour under irradiation. This will probably be the most important step in understanding in-reactor Zr corrosion and HPU mechanisms using APT.

REFERENCES

[1]Azevedo, C. R. F. (2011) Selection of fuel cladding material for nuclear fission reactors. *Engineering Failure Analysis* 18(8):1943-1962.

[2]IAEA (2007) Development of radiation resistant reactor core structural materials.

[3]IAEA (1998) Waterside corrosion of zirconium alloys in nuclear power plants.

[4]Ashby, M. F., Smidman, M. (2010) Materials for nuclear power systems. *Granta Design White Paper*.

[5]Couet, A. (2014) Hydrogen pickup mechanism of zirconium alloys. PhD thesis. Pennsylvania State University.

[6]Hudson, D. (2011) Zirconium oxidation on the atomic scale. DPhil thesis. University of Oxford.

[7]Bowman, F. E. (1956) Use of zirconium in liquid-sodium systems. *American Institute of Chemical Engineers Journal* 2(2):173-176.

[8]Grovenor, C. R. M., Ni, N., Hudson, D., Yardley, S. S., Moore, K. L., Smith, G. D. W., Lozano-Perez, S., Sykes, J. M. (2012) Mechanisms of oxidation of fuel cladding alloys revealed by high resolution APT, TEM and SIMS analysis. *Materials Research Society Symposium Proceedings* 1383:101-112.

[9]Garzarolli, F., Cox, B. (2012) Corrosion and hydriding. *ANT International*.

[10]Ni, N. (2011) Study of oxidation mechanisms of zirconium alloys by electron microscopy. DPhil thesis. University of Oxford.

[11]da Silva, M. J. G. (2006) Influence of oxide microstructure on corrosion behavior of zirconium-based model alloys. PhD thesis. Pennsylvania State University.

[12]IAEA. (2010) Delayed hydride cracking of zirconium alloy fuel cladding.

[13]Kubo, T., Kobayashi, Y. (2013) Effects of ð-hydride precipitation at a crack tip on crack propagation in delayed hydride cracking of Zircaloy-2. *Journal of Nuclear Materials* 439:202-211.

[14]Domizzi, G. and Ovejero-Garcia, J. (2005) Embrittlement of ZIrcaloy-4 by hydride precipitation. Proceedings of Behaviour of High Corrosion Resistance Zr-based Alloys. IAEA.

[15]Murty, K. L., Charit, I. (2008) Structural materials for Gen-IV nuclear reactors: Challenges and opportunities. *Journal of Nuclear Materials* 383:189-195.

[16]Northwood, D. O. (1985) The development and applications of zirconium alloys. *Materials Design* 6(2):58-70.

[17]Sabol, G. P. (2004) ZIRLO™ - an alloy development success. Zirconium in the Nuclear Industry: Fourteenth International Symposium. American Society for Testing and Materials.

[18]Cox, B., Garzarolli, F., Rudling, P. (2004) ZIRAT-9 Special Topics Report: Corrosion of Zr-Nb alloys. *ANT International*.

[19]Nikulina, A., Shishov, S., Cox, B., Garzarolli, F., Rudling, P. (2006) ZIRAT-11 Special Topic Report: Manufacturing of Zr-Nb alloys. *ANT International*.

[20]Olander, D., Motta, A. (2005) A New Book: Light Water Reactor Materials. *Nuclear Engineering and Technology* 37:309-3316.

[21]Douglass, D. L. (1971) Metallurgy of zirconium. Atomic Energy Review. IAEA.

[22]Tenckhoff, E. (2004) Review of deformation mechanisms, texture, and mechanical anisotropy in zirconium and zirconium base alloys. Zirconium in the Nuclear Industry: Fourteenth International Symposium. American Society for Testing and Materials.

[23]Kim, H. G., Park, S. Y., Lee, M. H., Jeong, Y. H., Kim, S. D. (2008) Corrosion and microstructural characteristics of Zr-Nb alloys with different Nb contents. *Journal of Nuclear Materials* 373:429-432.

[24]Adamson, R., Cox, B., Garzarolli, F., Strasser, A., Rudling, P., Wikmark, G. (2002) ZIRAT-7 Special Topics Report: Corrosion of zirconium alloys. *ANT International*.

[25]Zaimovskii, A. S. (1978) Zirconium alloys in nuclear power. *Atomic Energy* 45(6):1165-1168.

[26]Aldridge, S. A., Cheadle, B. A. (1972) Age hardening of Zr-2.5wt%Nb slowly cooled from the (α+β) phase field. *Journal of Nuclear Materials* 42:32-42.

[27]Lin, Y. P., Woo, O. T. (2000) Oxidation of β-Zr and related phases in Zr-Nb alloys: An electron microscopy investigation. *Journal of Nuclear Materials* 277:11-27.

[28]Bychkov, Y. F., Rozanov, A. N., Skorov, D. M. (1957) Some properties of alloys of zirconium with niobium. *The Soviet Journal of Atomic Energy* 2(2):165-170.

[29]Barberis, P., Charquet, D., Rebeyrolle, V. (2004) Ternary Zr-Nb-Fe(O) system: Phase diagram at 853K and corrosion behaviour in the domain Nb *Journal of Nuclear Materials* 326(2-3):163-174.

[30]Nikulina, A. V., Malgin, A. G. (2009) Impurities and their effect on the structure and properties of zirconium parts in nuclear reactors. *Atomic Energy* 105(5):328-339.

[31]Perovic, A., Perovic, V., Weatherly, G. G., Purdy, G. R., Fleck, R. G. (1993) A study of the distribution of Nb and Fe in two-phase Zr-2.5 wt% Nb alloys. *Journal of Nuclear Materials* 199(2):102-111.

[32]Perovic, V., Perovic, A., Weatherly, G. C., Brown, L. M., Purdy, G. R., Fleck, R. G., Holt, R. A. (1993) Microstructural and microchemical studies of Zr-2.5Nb pressure tube alloy. *Journal of Nuclear Materials* 205:251-257.

[33]Hudson, D., Smith, G. D. W. (2009) Initial observation of grain boundary solute segregation in a zirconium alloy (ZIRLO) by three-dimensional atom probe. *Scripta Materialia* 61(4):411-414.

[34]Sundell, G., Thuvander, M., Andrén, H. (2012) Enrichment of Fe and Ni at metal and oxide grain boundaries in corroded Zircaloy-2. *Corrosion Science* 65:10-12.

[35]Jeong, Y. H., Kim, H. G., Kim, T. H. (2003) Effect of β phase, precipitate and Nb-concentration in matrix on corrosion and oxide characteristics of Zr-xNb alloys. *Journal of Nuclear Materials* 317(1):1-12.

[36]Liu, Y. Z., Zhao, W. J., Peng, Q., Jiang, H. M., Zu, X. T. (2008) Study of microstructure of Zr-Sn-Nb-Fe-Cr alloy in the temperature range of 750-820°C. *Materials Chemistry and Physics* 107:534-540.

[37]Kim, H., Park, J., Jeong, Y. (2005) Ex-reactor corrosion and oxide characteristics of Zr–Nb–Fe alloys with the Nb/Fe ratio. *Journal of Nuclear Materials* 345(1):1-10.

[38]Sell, H., Trapp-Pritsching, S. and Garzarolli, F. (2004) Effects of alloying elements and impurities on in-BWR corrosion of zirconium alloys. Zirconium in the Nuclear Industry: Fourteenth International Symposium. American Society for Testing and Materials.

[39]Cox, B. (2005) Some thoughts on the mechanisms of in-reactor corrosion of zirconium alloys. *Journal of Nuclear Materials* 336(2-3):331-368.

[40]Barberis, P., Dupin, N., Lemaignan, C., Pasturel, A. and Grange, J. M. (2004) Microstructure and phase control in Zr-Fe-Cr-Ni alloys: thermodynamic and kinetic aspects. Zirconium in the Nuclear Industry: Fourteenth International Symposium. American Society for Testing and Materials.

[41]Isobe, T. and Matsuo, Y. (1991) Development of highly corrosion resistant zirconium-base alloys. Zirconium in the Nuclear Industry: Ninth International Symposium. American Society for Testing and Materials.

[42]Lindgren, M., Panas, I. (2013) Impact of additives on zirconium oxidation by water: mechanistic insights from first principles. *RSC Advances* 3(44):21613-21619.

[43]Hillner, E. (1977) Corrosion of zirconium based alloys. Zirconium in the Nuclear Industry: Third International Symposium. American Society for Testing Materials.

[44]Northwood, D. O., Meng-Burany, X. and Warr, B. D. (1991) Microstructure of Zr-2.5Nb alloy pressure tubing. Zirconium in the Nuclear Industry: Ninth International Symposium. American Society for Testing Materials.

[45]Woo, O. T., Carpenter, G. J. C., Sawicki, J. A., MacEwen, S. R. (1990) Zr-Fe intermetallic precipitates and Fe partitioning in Zr-2.5 at% Nb. *Journal of Nuclear Materials* 172(1):71-76.

[46]Gupta, P. D., Arunachalam, V. (1968) Thermally activated deformation in dilute zirconium/oxygen alloys. *Journal of Materials Science* 3(3):271-281.

[47]Yau, T. (2001) Effects of tin content in zirconium. Corrosion Solutions Conference Proceedings.

[48]Ploc, R. A. (2002) The effect of minor alloying elements on oxidation and hydrogen pickup in Zr-2.5Nb. Zirconium in the Nuclear Industry: Thirteenth International Symposium. American Society for Testing and Materials.

[49]Kim, H. G., Jeong, Y. H., Kim, T. H. (2004) Effect of isothermal annealing on the corrosion behavior of Zr-xNb alloys. *Journal of Nuclear Materials* 326(2-3):125-131.

[50]Liu, W., Li, Q., Zhou, B., Yan, Q., Yao, M. (2005) Effect of heat treatment on the microstructure and corrosion resistance of a Zr-Sn-Nb-Fe-Cr alloy. *Journal of Nuclear Materials* 341:97-102.

[51]Choubey, R., Aldridge, S., Theaker, J., Cann, C. and Coleman, C. (1996) Effects of extrusion-billet preheating on the microstructure and properties of Zr-2.5Nb pressure tube materials. Zirconium in the Nuclear Industry: Eleventh International Symposium. American Society for Testing and Materials.

[52]Holt, R. A. (1970) The beta to alpha phase transformation in Zircaloy-4. *Journal of Nuclear Materials* 35:322-334.

[53]Adamson, R., Garzarolli, F., Cox, B., Strasser, A., Rudling, P. (2007) ZIRAT-12 Special Topic Report: Corrosion mechanisms in zirconium alloys. *ANT International*.

[54]Oskarsson, M. (2000) Study on the mechanisms for corrosion and hydriding of zircaloy. PhD thesis. Royal Institute of Technology.

[55]Claussen, N., Ruhle, M., Heuer, A. (1984) Advances in Ceramics, vol. 12. *Science and technology of zirconia II*.

[56]Tapping, R. (1982) X-ray photoelectron and ultraviolet photoelectron studies of the oxidation and hydriding of zirconium. *Journal of Nuclear Materials* 107(2-3):151-158.

[57]Abriata, J., Garces, J., Versaci, R. (1986) The O-Zr (oxygen-zirconium) system. *Bulletin of Alloy Phase Diagrams* 7(2):116-124.

[58]Ni, N., Lozano-Perez, S., Sykes, J., Grovenor, C. (2011) Quantitative EELS analysis of zirconium alloy metal/oxide interfaces. *Ultramicroscopy* 111:123-130.

[59]Nishino, Y., Krauss, A. R., Lin, Y., Gruen, D. M. (1996) Initial oxidation of zirconium and Zircaloy-2 with oxygen and water vapor at room temperature. *Journal of Nuclear Materials* 228:346-353.

[60]Bisor-Melloul, C., Tupin, M., Bossis, P., Chene, J., Bechade, J. L., Motta, A. (2011) Understanding of hydriding mechanisms of Zircaloy-4 alloy during corrosion in PWR simulated conditions and influence of zirconium hydrides on Zircaloy-4 corrosion. *RGN-Revue Generale Nucleaire* 2:1-9.

[61]Motta, A. T., Yilmazbayhan, A., Comstock, R. J., Partezana, J., Sabol, G. P., Lai, B. and Cai, Z. (2008) Microstructure and growth mechanism of oxide layers formed on Zr alloys studied with micro-beam synchrotron radiation. Zirconium in the Nuclear Industry: Fourteenth International Symposium. American Society for Testing and Materials.

[62]Foord, D., Newcomb, S. (1996) The microstructural characterisation of factors which determine the degradation behaviour of Zircaloy-4. *Microscopy of Oxidation 3* :488-499.

[63]Hu, J., Garner, A., Ni, N., Gholinia, A., Nicholls, R. J., Lozano-Perez, S., Frankel, P., Preuss, M., Grovenor, C. R. M. (2015) Identifying suboxide grains at the metal-oxide interface of a corroded Zr-1.0%Nb alloy using (S)TEM, transmission-EBSD and EELS. *Micron* 69:35-42.

[64]de Gabory, B., Dong, Y., Motta, A. T., Marquis, E. A. (2015) EELS and atom probe tomography study of the evolution of the metal/oxide interface during zirconium alloy oxidation. *Journal of Nuclear Materials* 462:304-309.

[65]Puchala, B., Van Der Ven A. (2013) Thermodynamics of the Zr-O system from first-principles calculations. *Physical Review B - Condensed Matter and Materials Physics* 88(9):1-15.

[66]Zhang, J., Oganov, A. R., Li, X., Dong, H., Zeng, Q. (2015) Novel compounds in the Zr–O system, their crystal structures and mechanical properties. *Physical Chemistry Chemical Physics* 17(26):17301-17310.

[67]Nicholls, R. J., Ni, N., Lozano-Perez, S., London, A., Mccomb, D. W., Nellist, P. D., Grovenor, C. R. M., Pickard, C. J., Yates, J. R. (2014) Crystal structure of the ZrO phase at zirconium/zirconium oxide interfaces. *Advanced Engineering Materials* (2):211-215.

[68]Furuta, T., Motohashi, H. (1980) Products at the surface of zircaloy cladding under loca conditions. *Journal of Nuclear Materials* 95(3):303-306.

[69]Couet, A., Motta, A. T., Comstock, R. J. (2014) Hydrogen pickup measurements in zirconium alloys: Relation to oxidation kinetics. *Journal of Nuclear Materials* 451(1-3):1-13.

[70]Cox, B. (1987) Pore structure in oxide films on irradiated and unirradiated zirconium alloys. *Journal of Nuclear Materials* 148(3):332-343.

[71]Cox, B. (1969) Processes occuring during the breakdown of oxide films on zirconium alloys. *Journal of Nuclear Materials* 29:50-66.

[72]Ahmed, T., Keys, L. (1975) The breakaway oxidation of zirconium and its alloys: a review. *Journal of the Less Common Metals* 39(1):99-107.

[73]Godlewski, J., Gros, J., Lambertin, M., Wadier, J. and Weidinger, H. (1991) Raman spectroscopy study of the tetragonal-to-monoclinic transition in zirconium oxide scales and determination of overall oxygen diffusion by nuclear microanalysis of O^{18}. Zirconium in the Nuclear Industry: Ninth International Symposium. American Society for Testing Materials.

[74]Cox, B., Pemsler, J. P. (1968) Diffusion of oxygen in growing zirconia films. *Journal of Nuclear Materials* 28:73-78.

[75]Allen, T. R. (2012) Comprehensive Nuclear Materials. pp. 49-68.Comprehensive Nuclear Materials. vol.5. Elsevier.

[76]Howlader, M. M. R., Shiiyama, K., Kinoshita, C., Kutsuwada, M., Inagaki, M. (1998) The electrical conductivity of zircaloy oxide films. *Journal of Nuclear Materials* 253:149-155.

[77]Beie, H., Mitwalsky, A., Garzarolli, F., Ruhmann, H. and Sell, H. (1994) Examinations of the corrosion mechanism of zirconium alloys. Zirconium in the nuclear industry: Tenth International Symposium. American Society for Testing and Materials.

[78]Maroto, A. J. G., Bordoni, R., Villegas, M., Olmedo, A. M., Blesa, M. A., Iglesias, A., Koenig, P. (1996) Growth and characterization of oxide layers on zirconium alloys. *Journal of Nuclear Materials* 229:79-92.

[79]Göhr, H., Schaller, J., Ruhmann, H. and Garzarolli, F. (1996) Long-term in situ corrosion investigation of Zr alloys in simulated PWR environment by electrochemical measurements. Zirconium in the Nuclear Industry: Eleventh International Symposium. American Society for Testing and Materials.

[80]Ramasubramanian, N., Perovic, V. and Leger, M. (2000) Hydrogen transport in the oxide and hydrogen pickup by the metal during out-and in-reactor corrosion of Zr-2.5Nb pressure tube material. Zirconium in the Nuclear Industry: Twelfth International Symposium. American Society for Testing and Materials.

[81]Bojinov, M., Karastoyanov, V., Kinnunen, P., Saario, T. (2010) Influence of water chemistry on the corrosion mechanism of a zirconium–niobium alloy in simulated light water reactor coolant conditions. *Corrosion Science* 52(1):54-67.

[82]Bossis, P., Lelievre, G., Barberis, P., Iltis, X. and Lefebvre, F. (2000) Multi-scale characterization of the metal-oxide interface of zirconium alloys. Zirconium in the Nuclear Industry: Twelfth International Symposium. American Society for Testing and Materials.

[83]Yardley, S. S., Moore, K. L., Ni, N., Wei, J. F., Lyon, S., Preuss, M., Lozano-Perez, S., Grovenor, C. R. M. (2013) An investigation of the oxidation behaviour of zirconium alloys using isotopic tracers and high resolution SIMS. *Journal of Nuclear Materials* 443(1-3):436-443.

[84]Godlewski, J. (1994) How the tetragonal zirconia is stabilized in the oxide scale that is formed on a zirconium alloy corroded at 400°C in steam. Zirconium in the nuclear industry: Tenth international symposium. American Society for Testing Materials.

[85]Barberis, P. (1995) Zirconia powders and Zircaloy oxide films: tetragonal phase evolution during 400°C autoclave tests. *Journal of Nuclear Materials* 226(1-2):34-43.

[86]Petigny, N., Barberis, P., Lemaignan, C., Valot, C., Lallemant, M. (2000) In situ XRD analysis of the oxide layers formed by oxidation at 743 K on Zircaloy 4 and Zr–1NbO. *Journal of Nuclear Materials* 280(3):318-330.

[87]Garner, A., Gholinia, A., Frankel, P., Gass, M., MacLaren, I., Preuss, M. (2014) The microstructure and microtexture of zirconium oxide films studied by transmission electron backscatter diffraction and automated crystal orientation mapping with transmission electron microscopy. *Acta Materialia* 80:159-171.

[88]Yilmazbayhan, A., Breval, E., Motta, A. T., Comstock, R. J. (2006) Transmission electron microscopy examination of oxide layers formed on Zr alloys. *Journal of Nuclear Materials* 349:265-281.

[89]Hsieh, W., Kai, J., Tsai, C., Guo, X. (1997) The kinetics of uniform oxide formation and its relationship to radiation effects on Zircaloy-2. *Materials Chemistry and Physics* 50(1):37-44.

[90]Bedworth, R., Pilling, N. (1923) The oxidation of metals at high temperatures. *Journal of the Institute of Metals* 29(3):529-582.

[91]Platt, P., Polatidis, E., Frankel, P., Klaus, M., Gass, M., Howells, R., Preuss, M. (2015) A study into stress relaxation in oxides formed on zirconium alloys. *Journal of Nuclear Materials* 456:415-425.

[92]Parise, M., Sicardy, O., Cailletaud, G. (1998) Modelling of the mechanical behavior of the metal–oxide system during Zr alloy oxidation. *Journal of Nuclear Materials* 256(1):35-46.

[93]Guerain, M., Duriez, C., Grosseau-Poussard, J. L., Mermoux, M. (2015) Review of stress fields in Zirconium alloys corrosion scales. *Corrosion Science* 95:11-21.

[94]Lin, J., Li, H., Nam, C., Szpunar, J. A. (2004) Analysis on volume fraction and crystal orientation relationship of monoclinic and tetragonal oxide grown on Zr–2.5 Nb alloy. *Journal of Nuclear Materials* 334(2):200-206.

[95]Zhang, H., Fruchart, D., Hlil, E., Ortega, L., Li, Z., Zhang, J., Sun, J., Zhou, L. (2010) Crystal structure, corrosion kinetics of new zirconium alloys and residual stress analysis of oxide films. *Journal of Nuclear Materials* 396(1):65-70.

[96]Polatidis, E., Frankel, P., Wei, J., Klaus, M., Comstock, R. J., Ambard, A., Lyon, S., Cottis, R. A., Preuss, M. (2013) Residual stresses and tetragonal phase fraction characterisation of corrosion tested Zircaloy-4 using energy dispersive synchrotron X-ray diffraction. *Journal of Nuclear Materials* 432(1–3):102-112.

[97]Preuss, M., Frankel, P., Lozano-Perez, S., Hudson, D., Polatidis, E., Ni, N., Wei, J., English, C., Storer, S. and Chong, K. (2012) Studies regarding corrosion mechanisms in

zirconium alloys. Zirconium in the Nuclear Industry: Sixteenth International Symposium. American Society for Testing and Materials.

[98]Ni, N., Lozano-Perez, S., Sykes, J., Smith, G., Grovenor, C. (2011) Focussed ion beam sectioning for the 3D characterisation of cracking in oxide scales formed on commercial ZIRLO™ alloys during corrosion in high temperature pressurised water. *Corrosion Science* 53(12):4073-4083.

[99]Hu, J., Setiadinata, B., Aarholt, T., Bagot, P., Moody, M., Grovenor, C., Garner, A., Harte, A., Moore, K., Frankel, P., Preuss, M. and Ni, N. (2015) High-resolution characterization of corrosion and hydrogen pickup of Zr cladding alloys. Proceedings of TopFuel.

[100]Tupin, M., Pijolat, M., Valdivieso, F., Soustelle, M., Frichet, A., Barberis, P. (2003) Differences in reactivity of oxide growth during the oxidation of Zircaloy-4 in water vapour before and after the kinetic transition. *Journal of Nuclear Materials* 317(2):130-144.

[101]Tupin, M., Pijolat, M., Valdivieso, F., Soustelle, M. (2005) Oxidation kinetics of ZrNbO in steam: Differences between the pre-and post-transition stages. *Journal of Nuclear Materials* 342(1):108-118.

[102]Wadman, B., Lai, Z., Andren, H., Nyström, A., Rudling, P. and Pettersson, H. (1994) Microstructure of oxide layers formed during autoclave testing of zirconium alloys. Zirconium in the nuclear industry: Tenth International Symposium. American Society of Testing Materials.

[103]Evans, A., Hutchinson, J. (1984) On the mechanics of delamination and spalling in compressed films. *International Journal of Solids and Structures* 20(5):455-466.

[104]Bossis, P., Pecheur, D., Hanifi, K., Thomazet, J. and Blat, M. (2006) Comparison of the high burn-up corrosion on M5 and low tin Zircaloy-4. Zirconium in the Nuclear Industry: Fourteenth International Symposium. American Society of Testing Materials.

[105]Ni, N., Lozano-Perez, S., Jenkins, M., English, C., Smith, G., Sykes, J., Grovenor, C. (2010) Porosity in oxides on zirconium fuel cladding alloys, and its importance in controlling oxidation rates. *Scripta Materialia* 62(8):564-567.

[106]Park, D. J., Park, J. Y., Jeong, Y. H., Lee, J. Y. (2010) Microstructural characterization of ZrO_2 layers formed during the transition to breakaway oxidation. *Journal of Nuclear Materials* 399(2):208-211.

[107]Kumar, A., Nasrallah, M., Douglass, D. L. (1974) The effect of yttrium and thorium on the oxidation behavior of Ni-Cr-Al alloys. *Oxidation of Metals* 8(4):227-263.

[108]Weidinger, H., Ruhmann, H., Cheliotis, G., Maguire, M. and Yau, T. (1991) Corrosion-electrochemical properties of zirconium intermetallics. Zirconium in the Nuclear Industry: Ninth International Symposium. American Society of Testing Materials.

[109]Pêcheur, D., Lefebvre, F., Motta, A., Lemaignan, C. and Charquet, D. (1994) Oxidation of intermetallic precipitates in Zircaloy-4: Impact of irradiation. Zirconium in the Nuclear Industry: Tenth International Symposium. American Society for Testing Materials.

[110]Pêcheur, D. (2000) Oxidation of β-Nb and Zr(Fe, V)2 precipitates in oxide films formed on advanced Zr-based alloys. *Journal of Nuclear Materials* 278(2–3):195-201.

[111]Cox, B., Sheikh, H. (1997) Redistribution of the alloying elements during Zircaloy-2 oxidation. *Journal of Nuclear Materials* 249(1):17-32.

[112]Proff, C., Abolhassani, S., Lemaignan, C. (2013) Oxidation behaviour of zirconium alloys and their precipitates â€“ A mechanistic study. *Journal of Nuclear Materials* 432:222-238.

[113]Anada, H., Herb, B. J., Nomoto, K., Hagi, S., Graham, R. A. and Kuroda, T. (1996) Effect of annealing temperature on corrosion behavior and ZrO_2 microstructure of Zircaloy-4 cladding tube. Zirconium in the nuclear industry: Eleventh international symposium. American Society for Testing and Materials.

[114]Kubo, T. and Uno, M. (1991) Precipitate behavior in Zircaloy-2 oxide films and its relevance to corrosion resistance. Zirconium in the Nuclear Industry: Ninth International Symposium. American Society for Testing and Materials.

[115]Pêcheur, D., Lefebvre, F., Motta, A. T., Lemaignan, C., Wadier, J. F. (1992) Precipitate evolution in the Zircaloy-4 oxide layer. *Journal of Nuclear Materials* 189(3):318-332.

[116]Barberis, P., Ahlberg, E., Simic, N., Charquet, D., Lemaignan, C., Wikmark, G., Dahlbäck, M., Limbäck, M., Tägtström, P. and Lehtinen, B. (2002) Role of the second-phase particles in zirconium binary alloys. Zirconium in the Nuclear Industry: Thirteenth International Symposium. American Society for Testing and Materials.

[117]Garzarolli, F., Stehle, H. and Steinberg, E. (1996) Behaviour and properties of zircaloys in power reactors: a short review of pertinent aspects in LWR fuel. Zirconium in the Nuclear Industry: Eleventh International Symposium. American Society for Testing and Materials.

[118]Toffolon-Masclet, C., Brachet, J., Jago, G. (2002) Studies of second phase particles in different zirconium alloys using extractive carbon replica and an electrolytic anodic dissolution procedure. *Journal of Nuclear Materials* 305(2):224-231.

[119]Proff, C., Abolhassani, S., Lemaignan, C. (2011) Oxidation behaviour of binary zirconium alloys containing intermetallic precipitates. *Journal of Nuclear Materials* 416(1):125-134.

[120]Park, J., Yoo, S. J., Choi, B., Jeong, Y. H. (2007) Oxide microstructures of advanced Zr alloys corroded in 360°C water loop. *Journal of Alloys and Compounds* 437(1):274-279.

[121]Urbanic, V. F., Chan, P. K., Khatamian, D. and Woo, O. (1994) Growth and characterization of oxide films on zirconium-niobium alloys. Zirconium in the Nuclear Industry: Tenth International Symposium. American Society for Testing and Materials.

[122]Sakamoto, K., Une, K., Aomi, M., Otsuka, T., Hashizume, K. (2015) Change of chemical states of niobium in the oxide layer of zirconium-niobium alloys with oxide growth. *Journal of Nuclear Science and Technology* 52(10):1259-1264.

[123]Sakamoto, K., Une, K. and Hashizume, K. (2012) Oxidation behavior of niobium in oxide layer of zirconium-niobium alloys. Proceedings of TopFuel.

[124]Lindgren, M., Sundell, G., Panas, I., Hallstadius, L., Thuvander, M. and Andrén, H. (2015) Toward a comprehensive mechanistic understanding of hydrogen uptake in zirconium alloys by combining atom probe analysis with electronic structure calculations. Zirconium in the Nuclear Industry: Seventeenth International Symposium. American Society for Testing and Materials.

[125]Muta, H., Etoh, Y., Ohishi, Y., Kurosaki, K., Yamanaka, S. (2012) Ab initio study of hydrogen diffusion in zirconium oxide. *Journal of Nuclear Science and Technology* 49(5):544-550.

[126]Smith, T. (1966) Kinetics and mechanism of hydrogen permeation of oxide films on zirconium. *Journal of Nuclear Materials* 18:323-336.

[127]Hatano, Y., Hitaka, R., Sugisaki, M., Hayashi, M. (1997) Influence of size distribution of $Zr(Fe,Cr)_2$ precipitates on hydrogen transport through oxide film of Zircaloy-4. *Journal of Nuclear Materials* 248:311-314.

[128]Hatano, Y., Sugisaki, M. (1996) Oxidation behavior of iron and nickel in Zr_2(Fe, Ni) precipitates in Zircaloy-2. *Journal of Nuclear Science and Technology* 33(11):829-833.

[129]Hatano, Y., Isobe, K., Hitaka, R., Sugisaki, M. (1996) Role of intermetallic precipitates in hydrogen uptake of Zircaloy-2. *Journal of Nuclear Science and Technology* 33(12):944-949.

[130]Baur, K., Garzarolli, F., Ruhmann, H. and Sell, H. (2000) Electrochemical examinations in 350°C water with respect to the mechanism of corrosion-hydrogen pickup. Zirconium in the Nuclear Industry: Twelfth International Symposium. American Society for Testing and Materials.

[131]Isobe, K., Hatano, Y., Sugisaki, M. (1997) Observation of the spatial distribution of hydrogen in Zircaloy-2 oxidized in H_2O steam at 723 K by a technique of tritium microautoradiography. *Journal of Nuclear Materials* 248:315-318.

[132]Van Essen, R., Buschow, K. (1979) Hydrogen absorption in various zirconium-and hafnium-based intermetallic compounds. *Journal of the Less Common Metals* 64(2):277-284.

[133]Cox, B., Wong, Y. -. (1999) A hydrogen uptake micro-mechanism for Zr alloys. *Journal of Nuclear Materials* 270:134-146.

[134]Takagi, I., Hattori, T., Hashizumi, M., Higashi, K. (1996) Deuterium radial redistribution in Zr-liner cladding tubes. *Nuclear Instruments and Methods in Physics Research Section B: Beam Interactions with Materials and Atoms* 118(1):238-241.

[135]Cox, B. (1999) A mechanism for the hydrogen uptake process in zirconium alloys. *Journal of Nuclear Materials* 264(3):283-294.

[136]Nishino, Y., Endo, M., Ibe, E., Yasuda, T. (1997) Formation and dissolution of oxide film on zirconium alloys in 288°C pure water under γ-ray irradiation. *Journal of Nuclear Materials* 248:292-298.

[137]Cox, B. (1985) Mechanisms of hydrogen absorption by zirconium alloys. Chalk River Nuclear Laboratories.

[138]Lim, B. H., Hong, H. S., Lee, K. S. (2003) Measurements of hydrogen permeation and absorption in zirconium oxide scales. *Journal of Nuclear Materials* 312(2):134-140.

[139]Elmoselhi, M. B., Warr, B. D. and McIntyre, S. (1994) A study of the hydrogen uptake mechanism in zirconium alloys. Zirconium in the Nuclear Industry: Tenth International Symposium. American Society for Testing and Materials.

[140]Ramasubramanian, N. and Balakrishnan, P. V. (1994) Aqueous chemistry of lithium hydroxide and boric acid and corrosion of Zircaloy-4 and Zr-2.5Nb alloys. Zirconium in the Nuclear Industry: Tenth International Symposium. American Society for Testing Materials.

[141]Une, K., Sakamoto, K., Matsunaga, J., Etoh, Y., Aomi, M., Takagi, I., Sawada, K. and Watanabe, H. (2012) Controlling factors of hydrogen absorption of zirconium alloys. Proceedings of TopFuel.

[142]Berry, W. E., Vaughan, D. A., White, E. L. (1961) Hydrogen pickup during aqueous corrosion of zirconium alloys. *Corrosion* 17(3):109-117.

[143]Couet, A., Motta, A. T., Ambard, A. and Comstock, R. J. (2016) Hydrogen pick-up mechanism in zirconium alloys. Zirconium in the Nuclear Industry: Eighteenth International Symposium. American Society for Testing and Materials (unpublished).

[144]Youssef, M. Y. M. (2014) Predicting the equilibria of point defects in zirconium oxide: A route to understand the corrosion and hydrogen pickup of zirconium alloys. PhD thesis. Massachusetts Institute of Technology.

[145]Couet, A., Motta, A. T., Ambard, A. (2015) The coupled current charge compensation model for zirconium alloy fuel cladding oxidation: I. Parabolic oxidation of zirconium alloys. *Corrosion Science* 100:73-84.

[146]Couet, A. (2014) Oxide electronic conductivity and hydrogen pickup fraction in Zr alloys. Annual Meeting on Transactions of the American Nuclear Society and Embedded Topical Meeting: Nuclear Fuels and Structural Materials for the Next Generation Nuclear Reactors.

[147]Eloff, G., Greyling, C., Viljoen, P. (1993) The role of space charge in the oxidation of Zircaloy-4 between 350 and 450° C in air. *Journal of Nuclear Materials* 199(3):285-288.

[148]Fromhold, A. (1980) Theory of metal oxidation vol. 2. ed.1. North Holland.

[149]Fromhold, A. (1995) Space-charge modification of the ionic currents for oxide growth. *Solid State Ionics* 75:229-239.

[150]Kakiuchi, K., Itagaki, N., Furuya, T., Miyazaki, A., Ishii, Y., Suzuki, S., Terai, T., Yamawaki, M. (2005) Effect of iron on hydrogen absorption properties of zirconium alloys. *Journal of Physics and Chemistry of Solids* 66(2-4):308-311.

[151]Choudhuri, G., Jagannath, Kiran Kumar, M., Kain, V., Srivastava, D., Basu, S., Shah, B. K., Saibaba, N., Dey, G. K. (2013) Influence of Fe content on corrosion and hydrogen pick up behavior of Zr–2.5Nb pressure tube material. *Journal of Nuclear Materials* 441(1-3):178-189.

[152]Gale, W. F., Totemeier, T. C. (2003) Smithells metals reference book. ed.1. Butterworth-Heinemann.

[153]Bryner, J. (1979) The cyclic nature of corrosion of Zircaloy-4 in 633 K water. *Journal of Nuclear Materials* 82(1):84-101.

[154]Zielinski, A., Sobieszczyk, S. (2011) Hydrogen-enhanced degradation and oxide effects in zirconium alloys for nuclear applications. *International Journal of Hydrogen Energy* 36(14):8619-8629.

[155]Viswanathan, U., Singh, R., Basak, C., Anantharaman, S., Sahoo, K. (2006) Evaluation of effect of hydrogen on toughness of Zircaloy-2 by instrumented drop weight impact testing. *Journal of Nuclear Materials* 350(3):310-319.

[156]Namburi, H. K., Valance, S. and Bertsch, J. (2012) Delayed hydride cracking in Zircaloy-2 fuel cladding tubes. Proceedings of TopFuel.

[157]Griffiths, M., Mecke, J. and Winegar, J. (1996) Evolution of microstructure in zirconium alloys during irradiation. Zirconium in the Nuclear Industry: Eleventh International Symposium. American Society for Testing and Materials.

[158]Griffiths, M., Holt, R., Rogerson, A. (1995) Microstructural aspects of accelerated deformation of Zircaloy nuclear reactor components during service. *Journal of Nuclear Materials* 225:245-258.

[159]Griffiths, M. (2009) Microstructure evolution in Zr alloys during irradiation: Dose, dose rate, and impurity dependence. Zirconium in the Nuclear Industry: Fifteenth International Symposium. American Society for Testing and Materials.

[160]Shishov, V., Nikulina, A. V., Markelov, V. A., Peregud, M. M., Kozlov, A. V., Averin, S. A., Kolbenkov, S. A. and Novoselov, A. E. (1996) Influence of neutron irradiation on dislocation structure and phase composition of Zr-base alloys. Zirconium in the Nuclear Industry: Eleventh International Symposium. American Society for Testing and Materials.

[161]Shishov, V., Peregud, M., Nikulina, A., Pimenov, Y. V., Kobylyansky, G., Novoselov, A., Ostrovsky, Z. and Obukhov, A. (2005) Influence of structure-phase state of Nb containing Zr alloys on irradiation-induced growth. Zirconium in the Nuclear Industry: Fourteenth International Symposium. American Society for Testing and Materials.

[162]Shishov, V., Peregud, M., Nikulina, A., Kon'kov, V., Novikov, V., Markelov, V., Khokhunova, T., Kobylyansky, G., Novoselov, A. and Ostrovsky, Z. (2009) Structure-phase state, corrosion and irradiation properties of Zr-Nb-Fe-Sn system alloys. Zirconium in the Nuclear Industry: Fifteenth International Symposium. American Society for Testing and Materials.

[163]Urbanic, V. and Griffiths, M. (2000) Microstructural aspects of corrosion and hydrogen ingress in Zr-2.5 Nb. Zirconium in the Nuclear Industry: Twelfth International Symposium. American Society for Testing and Materials.

[164]Sundell, G., Thuvander, M., Tejland, P., Dahlback, M., Hallstadius, L., Andrén, H. (2014) Redistribution of alloying elements in Zircaloy-2 after in-reactor exposure. *Journal of Nuclear Materials* 454(1-3):178-185.

[165]Iltis, X., Lefebvre, F., Lemaignan, C. (1995) Microstructural study of oxide layers formed on Zircaloy-4 in autoclave and in reactor part II: Impact of the chemical evolution of intermetallic precipitates on their zirconia environment. *Journal of Nuclear Materials* 224(2):121-130.

[166]Lemaignan, C. (2002) Physical phenomena concerning corrosion under irradiation of Zr alloys. Zirconium in the Nuclear Industry: Thirteenth International Symposium. American Society for Testing and Materials.

[167]Abolhassani, S., Restani, R., Rebac, T., Groeschel, F., Hoffelner, W., Bart, G., Goll, W. and Aeschbach, F. (2005) TEM examinations of the metal-oxide interface of zirconium based alloys irradiated in a pressurized water reactor. Zirconium in the Nuclear Industry: Fourteenth International Symposium. American Society for Testing and Materials.

[168]Urbanic, V. F., Warr, B. D. and Manolescu, A. (1989) Oxidation and deuterium uptake of Zr-2.5Nb pressure tubes in CANDU-PHW reactors. Zirconium in the Nuclear Industry: Eighth International Symposium. American Society for Testing and Materials.

[169]Gault, B., Moody, M.P., Cairney, J.M.,Ringer S.P. (2012) Atom Probe Microscopy. ed.1. Springer.

[170]Kelly, T. F., Larson, D. J. (2012) Atom probe tomography 2012. *Annual Review of Materials Research* 42(1):1-31.

[171]Kelly, T. F., Miller, M. K. (2007) Invited review article: Atom probe tomography. *The Review of Scientific Instruments* 78(031101).

[172]Muller, E. W. (1956) Resolution of the Atomic Structure of a Metal Surface by the Field Ion Microscope. *Journal of Applied Physics* 27(5):474.

[173]Muller, E. W. (1968) The atom-probe field ion microscope. *Review of Scientific Instruments* 39(1):83.

[174]Cerezo, A., Godfrey, T. J., Smith, G. D. W. (1988) Application of a position-sensitive detector to atom probe microanalysis. *Review of Scientific Instruments* 59(6):862.

[175]Kellogg, G. L., Tsong, T. T. (1980) Pulsed-laser atom-probe field-ion microscopy. *Journal of Applied Physics* 51(2):1184.

[176]Miller, M. K., Forbes, R. G. (2009) Atom probe tomography. *Materials Characterization* 60(6):461-469.

[177]Muller, E. W. (1956) Field Desorption. *Physical Review* 102(3):618-624.

[178]Gomer, R. (1959) Field desorption. *The Journal of Chemical Physics* 31(2):341-345.

[179]Bunton, J. H., Olson, J. D., Lenz, D. R., Kelly, T. F. (2007) Advances in pulsed-laser atom probe: Instrument and specimen design for optimum performance. *Microscopy and Microanalysis* 13:418-427.

[180]Haydock, R., Kingham, D. R. (1980) Post-ionization of field-evaporated ions. *Physical Review Letters* 44(23):1521-1523.

[181]Kingham, D. R. (1982) The post-ionization of field evaporated ions: A theoretical explanation of multiple charge states. *Surface Science Letters* 116(2):273-301.

[182]Birdseye, P. J., Smith, D. A. (1970) The electric field and the stress on a field-ion specimen. *Surface Science* 23(1):198-210.

[183]Mikhailovskij, I. M., Wanderka, N., Storizhko, V. E., Ksenofontov, V. A., Mazilova, T. I. (2009) A new approach for explanation of specimen rupture under high electric field. *Ultramicroscopy* 109(5):480-485.

[184]Bemont, E., Bostel, A., Bouet, M., Da Costa G., Chambreland, S., Deconihout, B., Hono, K. (2003) Effects of incidence angles of ions on the mass resolution of an energy compensated 3D atom probe. *Ultramicroscopy* 95:231-238.

[185]Kelly, T. F. (2011) Kinetic-energy discrimination for atom probe tomography. *Microscopy and Microanalysis* 17(01):1-14.

[186]Walls, J., Southworth, H. (1979) Magnification in the field-ion microscope. *Journal of Physics D: Applied Physics* 12(5):657.

[187]Brandon, D. (1964) The accurate determination of crystal orientation from field ion micrographs. *Journal of Scientific Instruments* 41(6):373.

[188]Gault, B., Haley, D., de Geuser, F., Moody, M. P., Marquis, E. A., Larson, D. J., Geiser, B. P. (2011) Advances in the reconstruction of atom probe tomography data. *Ultramicroscopy* 111(6):448-457.

[189]Waugh, A., Boyes, E., Southon, M. (1976) Investigations of field evaporation with a field-desorption microscope. *Surface Science* 61(1):109-142.

[190]Felfer, P. J., Gault, B., Sha, G., Stephenson, L., Ringer, S. P., Cairney, J. M. (2012) A new approach to the determination of concentration profiles in atom probe tomography. *Microscopy and Microanalysis* 18(2):359-364.

[191]Thompson, K., Lawrence, D., Larson, D. J., Olson, J. D., Kelly, T. F., Gorman, B. (2007) In situ site-specific specimen preparation for atom probe tomography. *Ultramicroscopy* 107(2-3):131-139.

[192]Sundell, G., Thuvander, M., Andrén, H. (2016) Barrier oxide chemistry and hydrogen pick-up mechanisms in zirconium alloys. *Corrosion Science* 102:490-502.

[193]Thuvander, M., Andrén, H. (2011) Methods of quantitative matrix analysis of Zircaloy-2. *Ultramicroscopy* 111(6):711-714.

[194]Schemel, J. (1977) ASTM manual on zirconium and hafnium. American Society for Materials Testing.

[195]Kreyszig, E. (2010) Advanced engineering mathematics. John Wiley & Sons.

[196]Nordin, H. (2015) Personal communication.

[197]Nordin, H., Elliot, A. and Bergin, S. (2012) High temperature aqueous corrosion and deuterium uptake of coupons prepared from the front and back ends of Zr-2.5Nb pressure tubes. Zirconium in the Nuclear Industry: SIxteenth International Symposium. American Society for Testing and Materials.

[198]Partezana, J. (2014) Personal communication.

[199]Wei, J., Frankel, P., Blat, M., Ambard, A., Comstock, R. J., Hallstadius, L., Lyon, S., Cottis, R. A., Preuss, M. (2012) Autoclave study of zirconium alloys with and without hydride rim. *Corrosion Engineering, Science and Technology* 47(7):516-528.

[200]Ly, A., Ambard, A., Blat-Yrieix, M., Legras, L., Frankel, P., Preuss, M., Curfs, C., Parry, G. and Bréchet, Y. (2012) Understanding crack formation at the metal/oxide interface during corrosion of Zircaloy-4 using a simple mechanical model. Zirconium in the Nuclear Industry: Sixteenth International Symposium. American Society for Testing and Materials.

[201]Hu, J. (2015) Personal communication.

[202]Arroyave, R., Kaufman, L., Eagar, T. W. (2002) Thermodynamic modeling of the Zr-O system. *Calphad* 26(1):95-118.

[203]Sundell, G., Thuvander, M., Andrén, H. (2013) Hydrogen analysis in APT: Methods to control adsorption and dissociation of H_2. *Ultramicroscopy* 132:285-289.

[204]Wadman, B., Andrén, H., Falk, L. (1989) Atom probe analysis of thin oxide layers on zircaloy needles. *Le Journal de Physique Colloques* 50(C8):C8-303-C8-308.

[205]Hudson, D., Cerezo, A., Smith, G. D. W. (2009) Zirconium oxidation on the atomic scale. *Ultramicroscopy* 109(5):667-671.

[206]Brian, J., Mitchell, A. (1990) The dissociative recombination of molecular ions. *Physics Reports* 186(5):215-248.

[207]Saxey, D. W. (2011) Correlated ion analysis and the interpretation of atom probe mass spectra. *Ultramicroscopy* 111(6):473-479.

[208]Gault, B., Saxey, D. W., Ashton, M. V., Sinnott, S. B., Chiaramonti, A. N., Moody, M. P. and Schreiber, D. K. (2015) Behavior of molecules and molecular ions near a field emitter. arXiv preprint arXiv:1511.09029.

[209]Stiller, K., Viskari, L., Sundell, G., Liu, F., Thuvander, M., Andrén, H., Larson, D. J., Prosa, T., Reinhard, D. (2012) Atom probe tomography of oxide scales. *Oxidation of Metals* 79(3-4):227-238.

[210]Dong, Y., Motta, A. T., Marquis, E. A. (2013) Atom probe tomography study of alloying element distributions in Zr alloys and their oxides. *Journal of Nuclear Materials* 442(1-3):270-281.

[211]Kirchhofer, R., Teague, M. C., Gorman, B. P. (2013) Thermal effects on mass and spatial resolution during laser pulse atom probe tomography of cerium oxide. *Journal of Nuclear Materials* 436(1-3):23-28.

[212]Ni, N., Lozano-Perez, S., Sykes, J., Grovenor, C. (2010) Transmission EELS Quantification Study of Oxygen Content at Zirconium Alloy Metal/Oxide Interface. *Microscopy and Microanalysis* 16(S2):1614-1615.

[213]Portillo, J., Rauch, E. F., Nicolopoulos, S., Gemmi, M. and Bultreys, D. (2010) Precession electron diffraction assisted orientation mapping in the transmission electron microscope. Materials Science Forum. Trans Tech Publications.

[214]Jerlerud Perez, R., Massih, A. R. (2007) Thermodynamic evaluation of the Nb-O-Zr system. *Journal of Nuclear Materials* 360:242-254.

[215]Toffolon, C., Brachet, J., Servant, C., Legras, L., Charquet, D., Barberis, P. and Mardon, J. (2002) Experimental study and preliminary thermodynamic calculations of the pseudo-ternary Zr-Nb-Fe-(O,Sn) system. Zirconium in the Nuclear Industry: Thirteenth International Symposium. American Society for Testing and Materials.

[216]Yurek, G. J., Hirth, J. P., Rapp, R. A. (1974) The formation of two-phase layered scales on pure metals. *Oxidation of Metals* 8(5):265-281.

[217]Ni, N., Hudson, D., Wei, J., Wang, P., Lozano-Perez, S., Smith, G. D. W., Sykes, J. M., Yardley, S. S., Moore, K. L., Lyon, S., Cottis, R., Preuss, M., Grovenor, C. R. M. (2012) How the crystallography and nanoscale chemistry of the metal/oxide interface develops during the aqueous oxidation of zirconium cladding alloys. *Acta Materialia* 60(20):7132-7149.

[218]Hu, J., Setiadinata, B., Aarholt, T., Garner, A., Partezana, J., Bagot, P., Lozano-Perez, S., Preuss, M., Moody, M. and Grovenor, C. (2016) High-resolution characterization of Zr nuclear fuel cladding alloys. Zirconium in the nuclear industry: Eighteenth international symposium. American Society of Testing Materials (unpublished).

[219]Sundell, G. (2012) Atom probe tomography of hydrogen and of grain boundaries in corroded Zircaloy-2. Licentiate of Engineering thesis. Chalmers University of Technology.

[220]Carpenter, G. J. C., Jackman, J. A., McCaffrey, J. P., Alani, R. (2003) In situ hydride formation in zirconium and titanium during ion milling. *Microscopy and Microanalysis* 1(04):175-184.

[221]Karnesky Jr, R. A., Bartelt, N. C., Huang, D., Teslich, N., Kumar, M. (2012) Imaging and quantification of hydrogen isotope trapping. *Sandia National Laboratories*.

[222]Takamizawa, H., Hoshi, K., Shimizu, Y., Yano, F., Inoue, K., Nagata, S., Shikama, T., Nagai, Y. (2013) Three-dimensional characterization of deuterium implanted in silicon using atom probe tomography. *Applied Physics Express* 6(6):066602.

[223]Haley, D., Merzlikin, S. V., Choi, P., Raabe, D. (2014) Atom probe tomography observation of hydrogen in high-Mn steel and silver charged via an electrolytic route. *International Journal of Hydrogen Energy* 39(23):12221-12229.

[224]Takahashi, J., Kawakami, K., Tarui, T. (2012) Direct observation of hydrogen-trapping sites in vanadium carbide precipitation steel by atom probe tomography. *Scripta Materialia* 67(2):213-216.

[225]Takahashi, J., Kawakami, K., Kobayashi, Y., Tarui, T. (2010) The first direct observation of hydrogen trapping sites in TiC precipitation-hardening steel through atom probe tomography. *Scripta Materialia* 63(3):261-264.

[226]Sundell, G., Thuvander, M., Yatim, A. K., Nordin, H., Andrén, H. (2015) Direct observation of hydrogen and deuterium in oxide grain boundaries in corroded Zirconium alloys. *Corrosion Science* 90:1-4.

[227]Kellogg, G. (1987) Pulsed-laser atom probe mass spectroscopy. *Journal of Physics E: Scientific Instruments* 20(2):125.

[228]Ai, C., Tsong, T. (1984) Field promoted and surface catalyzed formation of H 3 and NH 3 on transition metal surfaces: A pulsed-laser imaging atom-probe study. *Surface Science* 138(2):339-360.

[229]Herbig, M., Kuzmina, M., Haase, C., Marceau, R. K., Gutiérrez-Urrutia, I., Haley, D., Molodov, D. A., Choi, P., Raabe, D. (2015) Grain boundary segregation in Fe–Mn–C twinning-induced plasticity steels studied by correlative electron backscatter diffraction and atom probe tomography. *Acta Materialia* 83:37-47.

[230]Gault, B., Danoix, F., Hoummada, K., Mangelinck, D., Leitner, H. (2012) Impact of directional walk on atom probe microanalysis. *Ultramicroscopy* 113:182-191.

[231]Yao, L., Moody, M., Cairney, J., Haley, D., Ceguerra, A., Zhu, C., Ringer, S. (2011) Crystallographic structural analysis in atom probe microscopy via 3D Hough transformation. *Ultramicroscopy* 111(6):458-463.

[232]Larson, D. J., Prosa, T. J., Ulfig, R. M., Geiser, B. P., Kelly, T. F. (2013) Local electrode atom probe tomography. Springer.

[233]Boyarkin, O. V., Koshelev, M. A., Aseev, O., Maksyutenko, P., Rizzo, T. R., Zobov, N. F., Lodi, L., Tennyson, J., Polyansky, O. L. (2013) Accurate bond dissociation energy of water determined by triple-resonance vibrational spectroscopy and ab initio calculations. *Chemical Physics Letters* 568:14-20.

[234]Yilmazbayhan, A., Motta, A. T., Comstock, R. J., Sabol, G. P., Lai, B., Cai, Z. (2004) Structure of zirconium alloy oxides formed in pure water studied with synchrotron radiation and optical microscopy: Relation to corrosion rate. *Journal of Nuclear Materials* 324:6-22.

[235]Ni, N., Lozano-Perez, S., Jenkins, M. L., English, C., Smith, G. D. W., Sykes, J. M., Grovenor, C. R. M. (2010) Porosity in oxides on zirconium fuel cladding alloys, and its importance in controlling oxidation rates. *Scripta Materialia* 62(8):564-567.

[236]Stiller, K. (1987) Field ion microscopy of 180-230 keV Xe ion damage in tungsten. *Radiation Effects* 105(1-2):53-71.

[237]Seidman, D. (1973) The direct observation of point defects in irradiated or quenched metals by quantitative field ion microscopy. *Journal of Physics F: Metal Physics* 3(2):393.

[238]Scanlan, R., Styris, D., Seidman, D. (1971) An in situ field ion microscope study of irradiated tungsten: I. Experimental results. *Philosophical Magazine* 23(186):1439-1457.

[239]Miller, M. K., Longstreth-Spoor, L., Kelton, K. (2011) Detecting density variations and nanovoids. *Ultramicroscopy* 111(6):469-472.

[240]Godfrey, T. J., Lewis, R. J., Smith, D. A., Smith, G. D. W. (1976) On the nature and distribution of defects in tungsten lamp wire. *Journal of the Less Common Metals* 44:319-326.

[241]Lemaignan, C. (1992) Impact of β− radiolysis and transient products on irradiation-enhanced corrosion of zirconium alloys. *Journal of Nuclear Materials* 187(2):122-130.

[242]Une, K., Sakamoto, K., Takagi, I., Sawada, K., Watanabe, H., Aomi, M. (2013) Deuterium diffusion in oxide layers of Zr–2.5Nb alloy. *Journal of Nuclear Materials* 439(1–3):84-92.

[243]Garzarolli, F., Cox, B. and Rudling, P. (2012) Optimization of Zry-2 for high burnups. Zirconium in the Nuclear Industry: Sixteenth International Symposium. American Society for Testing and Materials.

[244]Mihalache, M., Radu, V., Ohai, D. (2010) Study on the microstructural changes in Zr-2.5Nb due to the LOCA thermal transients. *University POLITEHNICA of Bucharest Scientific Bulletin, Series B* 72(4):185-196.

[245]Charquet, D., Hahn, R., Ortlieb, E., Gros, J. and Wadier, J. (1989) Solubility limits and formation of intermetallic precipitates in ZrSnFeCr alloys. Zirconium in the Nuclear Industry: Eighth International Symposium. American Society for Testing and Materials.

[246]Donaldson, A. T. (1991) Growth in Zircaloy-4 fuel clad arising from oxidation at temperatures in the range 623 to 723 K. Zirconium in the Nuclear Industry: Ninth International Symposium. American Society for Testing and Materials.

[247]Bouvier, P., Godlewski, J., Lucazeau, G. (2002) A Raman study of the nanocrystallite size effect on the pressure–temperature phase diagram of zirconia grown by zirconium-based alloys oxidation. *Journal of Nuclear Materials* 300(2):118-126.

[248]Thorpe, W. R., Smith, I. O. (1978) Creep properties of Zr-1wt.%Nb alloy. *Journal of Nuclear Materials* 75(2):209-219.

[249]Blat-Yrieix, M., Ambard, A., Foct, F., Miquet, A., Beguin, S. and Cayet, N. (2009) Toward a better understanding of dimensional changes in zircaloy-4: what is the impact induced by hydrides and oxide layer? Zirconium in the Nuclear Industry: Fifteenth International Symposium. American Society for Testing and Materials.

[250]Tejland, P., Andrén, H. (2014) Oxidation induced localized creep deformation in Zircaloy-2. *Journal of Nuclear Materials* 444(1):30-34.

[251]Hood, G. M. and Schultz, R. J. (1989) Diffusion of 3D transition elements in α-Zr and zirconium alloys. Zirconium in the Nuclear Industry: Eighth International Symposium. American Society for Testing and Materials.

[252]Bojinov, M., Hansson-Lyyra, L., Kinnunen, P., Saario, T. and Sirkiä, P. (2005) In-situ studies of the oxide film properties on BWR fuel cladding materials. Zirconium in the Nuclear Industry: Fourteenth International Symposium. American Society for Testing and Materials.

[253]Kakiuchi, K., Itagaki, N., Furuya, T., Miyazaki, A., Ishii, Y., Suzuki, S., Terai, T. and Yamawaki, M. (2005) Role of iron for hydrogen absorption mechanism in zirconium alloys. Zirconium in the Nuclear Industry: Fourteenth International Symposium. American Society for Testing and Materials.

[254]Shannon, R. (1976) Revised effective ionic radii and systematic studies of interatomic distances in halides and chalcogenides. *Acta Crystallographica Section A: Crystal Physics, Diffraction, Theoretical and General Crystallography* 32(5):751-767.

[255]Chang, S., Doong, R. (2004) The effect of chemical states of dopants on the microstructures and band gaps of metal-doped ZrO_2 thin films at different temperatures. *The Journal of Physical Chemistry B* 108(46):18098-18103.

[256]Couet, A., Motta, A. T., De Gabory Benoit, Cai, Z. (2014) Microbeam X-ray Absorption Near-Edge Spectroscopy study of the oxidation of Fe and Nb in zirconium alloy oxide layers. *Journal of Nuclear Materials* 452(1-3):614-627.

[257]Sabol, G. P., Kilp, G. R., Balfour, M. G. and Roberts, E. (1989) Development of a cladding alloy for high burnup. Zirconium in the Nuclear Industry: Eighth International Symposium. American Society for Testing Materials.

[258]Sabol, G., McDonald, S. (1977) The Effect of Niobium Additions on the Corrosion Behavior of Zircaloy-4. *Nuclear Science and Engineering* 63(1):83-90.

[259]Froideval, A., Degueldre, C., Segre, C. U., Pouchon, M. A., Grolimund, D. (2008) Niobium speciation at the metal/oxide interface of corroded niobium-doped Zircaloys: A X-ray absorption near-edge structure study. *Corrosion Science* 50(5):1313-1320.

[260]Otgonbaatar, U., Ma, W., Youssef, M., Yildiz, B. (2014) Effect of niobium on the defect chemistry and oxidation kinetics of tetragonal ZrO_2. *The Journal of Physical Chemistry C* 118(35):20122-20131.

[261]Bossis, P., Thomazet, J. and Lefebvre, F. (2002) Study of the mechanisms controlling the oxide growth under irradiation: Characterization of irradiated Zircaloy-4 and Zr-1Nb-O oxide scales. Zirconium in the Nuclear Industry: Thirteenth International Symposium. American Society for Testing and Materials.

[262]Markelov, V., Novikov, V., Shevyakov, A., Gusev, A., Peregud, M., Konkov, V., Eremin, S., Pokrovsky, A. and Obukhov, A. (2016) Preliminary irradiation effect on corrosion resistance of zirconium alloys. Zirconium in the Nuclear Industry: Eighteenth International Symposium. American Society for Testing and Materials (unpublished).

[263]Okamoto, H. (1993) The Sb-Zr (antimony-zirconium) system. *Journal of Phase Equilibria* 14(2):228-231.

[264]Garcia, E., Corbett, J. D. (1988) A synthetic and structural study of the zirconium-antimony system. *Journal of Solid State Chemistry* 73(2):440-451.

[265]Bell, B. D. C., Murphy, S. T., Burr, P. A., Comstock, R. J., Partezana, J. M., Grimes, R. W., Wenman, M. R. (2016) The influence of alloying elements on the corrosion of Zr alloys. *Corrosion Science* 105:36-43.

[266]Tejland, P., Thuvander, M., Andrén, H., Ciurea, S., Andersson, T., Dahlbäck, M. and Hallstadius, L. (2012) Detailed analysis of the microstructure of the metal/oxide interface region in Zircaloy-2 after autoclave corrosion testing. Zirconium in the Nuclear Industry: Sixteenth International Symposium. American Society for Testing and Materials.

[267]McDougall, G. M., Urbanic, V. and Aarrestad, O. (2000) Studies of zirconium alloy corrosion and hydrogen uptake during irradiation. Zirconium in the Nuclear Industry: Twelfth International Symposium. American Society for Testing and Materials.